

DESIGN AND IMPLEMENTATION OF AN X-RAY COLOUR DETECTION SYSTEM USING THE MEDIPIX3RX

A THESIS SUBMITTED TO THE UNIVERSITY OF MANCHESTER
FOR THE DEGREE OF DOCTOR OF PHILOSOPHY
IN THE FACULTY OF SCIENCE AND ENGINEERING

2018

Tomas Bartolome Garcia Nathan
School of Electrical and Electronic Engineering

Contents

Abstract	25
Declaration	26
Copyright Statement	27
Acknowledgements	28
List of Publications	29
Acronyms	30
1 Introduction	32
1.1 X-ray fluorescence	32
1.2 X-ray applications and detection	33
1.3 Objectives of the research	35
1.4 Research outcomes	35
1.5 Original contributions of the research	36
1.6 Project overview	37
2 The Medipix3RX hybrid detector	39
2.1 Hybrid pixelated x-ray detectors	39
2.2 Electron-hole pair creation in semiconductor diode detectors	42
2.3 The Medipix3RX sensor	43
2.4 Pixel Architecture	44
2.4.1 Amplification and discrimination of the photon pulses	45
2.4.2 Threshold offset addition to the discriminators	46

2.4.3	Pulses injection to the pixels	47
2.4.4	Masking of pixels	47
2.4.5	Pixel Counters	48
2.5	Operation modes of the Medipix3RX	48
2.5.1	Fine Pitch or Colour Mode	48
2.5.2	Single pixel or charge summing modes	49
2.6	Digital control and readout process	51
2.6.1	Operation Mode Register	51
2.6.2	Pixel matrix configuration	52
2.6.3	Frame readout	52
3	Electronic design of the LancelotRX	53
3.1	System requirements	53
3.2	Design of the printed circuit boards for the LancelotRX	56
3.2.1	Sensor board - a carrier PCB for the Medipix3RX sensor	56
3.2.2	Interface board - a PCB to condition the Medipix3RX commu- nication	59
3.2.3	Processing board - the ARMFlash heterogeneous processing board	62
3.2.4	Flexible PCB for interconnection	66
3.3	Temperature control design	67
3.3.1	Proposed cooling system	67
3.3.2	Temperature control system	68
3.3.3	Driver Design	71
3.4	Data flow design for the system	74
3.5	Summary	74
4	Gateware design for the LancelotRX	76
4.1	Gateware architecture	76
4.2	PWM_GEN - module for generating a PWM and enable lines	82
4.2.1	Generation of the PWM signal	82
4.2.2	Generation of the enable lines	82
4.3	INT_MAN - module to manage the interrupts	83
4.3.1	Controllable characteristics of the interrupts	83

4.4	MP3RX - module for control and readout of the Medipix3RX	84
4.4.1	OMR_Handler sub-module to control the Medipix3RX	85
4.4.2	Unscrambler sub-module to decode the Medipix3RX data	93
4.5	Summary	98
5	Software and firmware design for the LancelotRX	99
5.1	Server program running on the ARM processor	99
5.2	Merlin Protocol to communicate with LancelotRX over the network . .	103
5.3	Design of the client software to control LancelotRX	105
5.3.1	LabVIEW debugger client with graphical interface	106
5.3.2	MATLAB scripting client	107
5.3.3	Python client for fast data acquisition	109
5.4	Summary	111
6	Mechanical design for the LancelotRX	112
6.1	System requirements for the mechanical design	112
6.2	Housing design for the LancelotRX	113
6.2.1	Top and bottom case of the LancelotRX	113
6.2.2	Connection between the sensor chamber and the electronics chamber	114
6.3	Heat dissipation in the mechanical design	116
6.4	Summary	117
7	Equalization of the thresholds of the Medipix3RX	118
7.1	Threshold dispersion in the Medipix3RX	118
7.2	Count sources for equalization	120
7.2.1	Equalization using electronic noise	121
7.2.2	Equalization using injected pulses	123
7.2.3	Equalization with x-ray photons	125
7.3	Equalization methods for the Medipix3RX	127
7.3.1	Optimization of the I_DAC_DISC	127
7.3.2	Algorithms to determine the trim bits	130
7.3.3	Masking noisy pixels	133

7.4	Equalization methods for each operation mode of the Medipix3RX . . .	135
7.4.1	Equalization for Single Pixel Mode	135
7.4.2	Equalization for Charge Sharing Mode	135
7.4.3	Equalization for Colour Mode	137
7.4.4	Equalization for Colour Mode in CSM	137
8	Experimental results	138
8.1	LancelotRX system results	138
8.1.1	Full system assembly	138
8.1.2	Frame acquisition speed	138
8.1.3	Temperature control	140
8.2	X-ray intensity images	142
8.3	Threshold equalization results	143
8.3.1	Single Pixel Mode	145
8.3.2	Charge Sharing Mode	148
8.3.3	Colour Mode	150
8.3.4	Comparison with the energy resolution of an individual pixel . .	150
8.4	Medipix3RX temperature dependence	151
8.4.1	Threshold dispersion and noise amplitude temperature dependence	151
8.4.2	Energy calibration temperature dependence	152
9	X-ray Beam position monitor application	155
9.1	Current x-ray beam position monitoring techniques	155
9.1.1	Destructive XBPM techniques	156
9.1.2	Non-destructive XBPM techniques	157
9.2	LancelotRX as an x-ray beam position monitor	158
9.2.1	Principles of operation	158
9.2.2	Physical additions to LancelotRX system for the XBPM appli- cation	160
9.2.3	Features of the proposed XBPM	162
9.3	Experimental results with LancelotRX as an XBPM	165
9.3.1	Analysis of the spatial resolution	165
9.3.2	Analysis of beam stability	166

9.3.3	Analysis of beam flux over time	168
9.3.4	Analysis of beam energy spectrum	169
9.4	Conclusions and future work	170
10	Colour x-ray imaging application	173
10.1	Colour x-ray imaging	173
10.2	Colour band and threshold selection	174
10.3	Colour imaging test	177
10.4	Material identification	179
10.5	Conclusions and future work	181
11	Conclusions and Future Work	183
11.1	Conclusions	183
11.2	Future work	185
A	Medipix3RX information	204
B	Interface board information and FPGA configuration	208
B.1	Configuring the FPGA using the PRU-ICSS subsystem	209
B.1.1	Communication PRU to Cyclone V	210
B.1.2	Jrunner design flow and modifications for using the PRU	210
C	MATLAB functions	215
D	Medipix3RX equalization and energy calibration	219
D.1	Island phenomenon	219
D.2	Pixel parameters based equalization method	220
D.2.1	Objective of the parameters equalization	221
D.2.2	The parameters model equalization method	221
D.2.3	Results with the parameters model equalization method	224
D.3	Energy calibration	226
E	LancelotRX design for vacuum	227
E.1	Mechanical design	227
E.1.1	Heat dissipation	228

E.2	Electronics	230
E.3	System assembly	232

List of Tables

4.1	First five values LFSR decoding table for the 6-bit depth pixels. The <i>Unscrambler</i> sub-module has both a 6-bit and a 12-bit LFSR decoding LUTs, enabling the decoding in only a few clock cycles.	95
8.1	Table of the time used for each section of the acquisition and communication of data from the LancelotRX system to a client software. All the values are given in microseconds.	140
8.2	Total integration time required for the different methods and sources for equalization. The time shown in minutes corresponds only to the integration time needed, processing and communication time are not counted since they are dependent on the implementation and hardware.	145
8.3	Full Width at Half Maximum (FWHM) energy resolution, using an equalization method based on electronic noise, for all the gain modes. The Medipix3RX is used in SPM and the energy resolution is measured for the energies of 6, 8, 9, 15 and 17 keV.	146
8.4	Full Width at Half Maximum (FWHM) energy resolution, using an equalization method based on x-rays, for all the gain modes. The Medipix3RX is used in SPM and the energy resolution is measured for the energies of 6, 8, 9, 15 and 17 keV.	146
8.5	Full Width at Half Maximum (FWHM) energy resolution, using an equalization based on injected pulses. The Medipix3RX is used in SPM and the energy resolution is measured for the energies of 15 and 17 keV.	147
8.6	FWHM energy resolution, using an equalization based on electronic noise. The Medipix3RX is used in CSM and the energy resolution is measured for the energies of 6, 8, 9, 15 and 17 keV.	148

8.7	FWHM energy resolution, using an equalization based on electronic noise. The Medipix3RX is used in CSM and the energy resolution is measured for the energies of 6, 8, 9, 15 and 17 keV.	149
B.1	DIP switch configuration on the Interface board.	208
B.2	Information shown in frontal LEDs of the Interface board. The positions are given in descending order.	208
C.1	List of the individual scripts developed under the MATLAB environment as part of the client. The first column shows the name of the script as well as the arguments taken, the second column shows a brief description of the script. The argument named 'merlin' represents the TCP/IP communication object.	215
C.2	List of the individual scripts developed under the MATLAB environment as part of the client. The first column shows the name of the script as well as the arguments taken, the second column shows a brief description of the script. The argument named 'merlin' represents the TCP/IP communication object.	216
C.3	List of the individual scripts developed under the MATLAB environment as part of the client. The first column shows the name of the script as well as the arguments taken, the second column shows a brief description of the script. The argument named 'merlin' represents the TCP/IP communication object.	217
C.4	List of the individual scripts developed under the MATLAB environment as part of the client. The first column shows the name of the script as well as the arguments taken, the second column shows a brief description of the script. The argument named 'merlin' represents the TCP/IP communication object.	218
D.1	Energy calibration results. The gain and offsets were obtain by a linear fitting with measurements from energies of 6.4, 8, 9.7, 15.7 and 17.4 keV.	226

List of Figures

2.1	Cross-sectional view of one pixel of a hybrid pixel detector. The sensing layer and the ASIC chip are connected by a bump. The signal generated on the sensing layer flows to the ASIC where it is processed. Figure modified from [1].	41
2.2	Block diagram of one channel's circuitry for a typical hybrid pixel detector. Figure modified from [2].	41
2.3	Physical shape of the Medipix3RX. 1) detector area of 256 x 256 pixels, 2) chip periphery and TSV, 3) pads for wire-bonding extension, 4) TSV power pads and 5) wire-bonding extension. The sections A, B and C show the different options for in-chip dicing [3].	44
2.4	Pixel schematic of the Medipix3RX. Signal names in blue represent values or features that can be controlled by the user [4].	45
2.5	The 5-bit current DAC used on each discriminator of the Medipix3RX pixels. The current DAC is used in order to reduce the threshold dispersion between pixels [5].	46
2.6	Distortion of the energy spectrum generated by charge sharing on the Medipix3RX. (top) Scan of the threshold DAC for a 12 keV monochromatic x-ray signal. (bottom) Differential scan of the threshold DAC showing the comparison of energy spectrum with and without charge sharing effects.	50
2.7	Illustration of the CSM process. (a) Shows the charge of one photon being shared in four pixels, the outputs of the comparisons with $TH_{allocation}$ are used to determine which pixel the count will be allocated to. (b) Shows the summing nodes where the total charge of the photon is reconstructed and compared with TH_{energy} . Modified from [6].	51

3.1	External connections of the LancelotRX system. The data acquired by the Medipix3RX can be accessed through client software by a network connection. The LancelotRX system uses analog inputs and outputs to communicate with other electronic devices, for example a motor controller.	54
3.2	A block diagram of the electronics for the LancelotRX system. All the required electronics are distributed between three PCBs, the ‘Processor board’, the ‘Interface board’ and the ‘Sensor Board’.	55
3.3	Block diagram showing the main components on the Sensor board.	57
3.4	Top and Bottom views of the Sensor board design used in LancelotRX. The board contains a voltage regulator, temperature, pressure and humidity sensors and the required pads to wire-bond the Medipix3RX. A cut-out under the Medipix3RX allows a copper block (not shown) to contact directly the back of the sensor for better thermal conductivity.	58
3.5	On the left, the temperature sensor is shown on the Sensor board PCB. On the right the assembly of the Sensor board PCB and the copper block is depicted with the sensor board being in direct contact with the copper block.	59
3.6	Block diagram of the Interface board. LVDS receivers and transmitters are used to transform the LVDS connections used by the Medipix3RX to the single-ended signals used by the processing board. The generation of the high voltage for the sensor, as well as the Peltier driver, are present on this board.	60
3.7	Top and Bottom views of the Interface board for the LancelotRX design. The LVDS transmitters and receivers are placed as close as possible to the ERNI connector to the Processor board to maximize the noise protection of the LVDS signals. The connectors for the input and output signals (Lemo connectors) as well as the status LEDs, power connection and the power switch are all placed on one edge of the PCB for easy access.	62
3.8	Block diagram of the the Processor board.	63

3.9	Top and Bottom views of the Processor board used in the LancelotRX design. An ARM processor and a Cyclone V FPGA are the two processing devices of the design. Two DDR3 memories are used to store volatile data and a NAND memory and an SD card are used to store the OS and non-volatile data. A power management IC is used to generate and distribute all the required voltages.	65
3.10	Flexible board designed to interconnect the Interface and Sensor boards on the LancelotRX design. The flexible PCB is 25mm wide and between the two copper layers 49 different signals are routed. Hatched copper pours have been used to decrease electrical resistance on the power lines while still maintaining flexibility on the PCB.	66
3.11	Block diagram of the main elements in the temperature control loop. The Peltier driver is controlled by a PWM signal generated in the FPGA, the PWM required duty cycle is calculated by the ARM processor and sent to the FPGA. The control loop takes into account the Medipix3RX temperature and the heatsink temperature.	69
3.12	Basic circuit of a Buck SMPS converter. A Buck SMPS is used on the LancelotRX system to control the cooling capacity, Q , of the Peltier cooler in order to maintain a stable temperature for the Medipix3RX. .	70
3.13	Linear approximation and experimental data of the steady state temperature increase in the proposed heatsink for the Peltier. The data was taken at a room temperature of 25 °C. The obtained parameters are used to determine the Peltier working point.	71
3.14	Peltier performance graph with annotations, taken and modified from the manufacturer datasheet [7]. The mark S_w is the original suggested working point at 2.4 A and 6 V. The mark W_{C1} is the current of the first iteration obtained working point of 1.6 A with a δT of 46.806 °C. The mark W_{V1} is the voltage of the first iteration obtained working point of 4.3 V and a δT of 46.806 °C.	73

3.15	Block diagram of the data flow on the LancelotRX system. A client software runs on a PC and connects to the LancelotRX through the network. A server program running on the ARM processor is used to handle the network communication. On the FPGA, the gateway system controls the Medipix3RX and generates the PWM for the Peltier driver.	74
4.1	Main blocks of the gateway system implemented on the FPGA. The main tasks of the gateway system can be divided into communication with the processor, interrupts generation, PWM signal generation and control and process of the data acquired from the Medipix3RX sensor. .	77
4.2	Qsys modules that form the FPGA system. The data flow direction can be seen with the direction of the arrows. The communication from internal blocks to external devices outside of the FPGA are shown. . .	78
4.3	Block diagram of the data flow from the Medipix3RX sensor to the DDR3 memory. The <i>MP3RX</i> module reads the data from the sensor and generates a pixel stream, which passes a <i>Splitter</i> module, converting the stream into two parallel streams that feed the <i>Profiler</i> and <i>Frame_Storer</i> modules. Both the <i>Profiler</i> and <i>Frame_Storer</i> modules save the obtained data into the DDR3 memory.	80
4.4	Block diagram of the sub-modules used in the <i>MP3RX</i> module. The sub-modules are <i>OMR_Handler</i> , which accesses the sensor's control lines and the DDR3 memory, and the <i>Unscrambler</i> , which has access to the sensor's data lines and generates the pixel stream that is used by the <i>Frame_Storer</i> and the <i>Profiler</i> modules.	85
4.5	Main state diagram for the <i>OMR_Handler</i> sub-module on the <i>MP3RX</i> . The bits of the OMR written into the registers is used to decode which set of actions the <i>OMR_Handler</i> has to execute, as well as to send the OMR bits to the sensor to control its operation.	86

4.6	Flowcharts in the <i>OMR_Handler</i> sub-module for setting the DACs (a) and the CTPR (b) into the sensor. The same process is used to read the DACs and CTPR. Waiting for an acknowledgement from the sensor is used to ensure that the communication is correct and that protocol timings are kept.	87
4.7	Memory map for the DDR3 memory used by the gateway design. The memory is used to store the values of the DACs, the CTPR and the matrix configuration for the Medipix3RX. The last block of memory is used to store read images.	88
4.8	Flowchart of the <i>OMR_Handler</i> sub-module actions to upload the configuration matrix into the Medipix3RX. The configuration data is read from the DDR3 where the processor has set it. The configuration data is read using two buffers, while data from the DDR3 is moved into buffer B, the buffer A data is sent to the sensor. The implemented method sends the configuration data using 2 data blocks.	89
4.9	Timing of the matrix configuration data being readout from DDR3 memory and sent into the sensor. The signals show the behaviour of single bit flags used to illustrate the timings of the process. Data ready signals are high when data is being transferred.	90
4.10	Flowchart for the process of acquiring one image from the Medipix3RX in non-continuous mode. When the acquisition starts, the <i>OMR_Handler</i> sub-modules activates the <i>Unscrambler</i> sub-module, to start reading data from the data lines and generate the pixel stream.	91
4.11	Timing Diagram of the continuous acquisition. The <i>Shutter</i> line stays down while images are being taken and <i>Shutter CS</i> line is used to alternate which counter is used for readout and which one for counting the incoming x-ray photons. The <i>Image readout</i> line shows that the time used for readout must be shorter than the integration time. . . .	92
4.12	Graphical representation of the data output format on the Medipix3RX for the 6-bit pixel mode.	94

4.13	Flowchart of the image acquisition in the <i>Unscrambler</i> sub-module. Once the sub-module has been activated, the buffer A starts being filled with sorted incoming data from the data lines of the Medipix3RX. Once the buffer A has been filled with an entire row, the new incoming data is stored in the buffer B while the data from the buffer A is decoded by the LFSR LUT and sent into the pixel stream. Filling one buffer and decoding the data in the other is done in parallel, as depicted by the parallelization bars, where an arrow flow is divided into two arrows. . .	96
4.14	Timings of the pixel readout process and generating the pixel stream. The figure shows the first 3 rows of pixels sent from the Medipix3RX and converted into a stream. The signal <i>Sensor output ready</i> is high when the sensor is transferring data into the FPGA. The signal <i>Pixel stream ready</i> is high when pixels are being sent down the Avalon stream. The <i>Pixel stream ready</i> show bursts, this is generated by the timing difference between the data transfer speed of the sensor to the <i>Unscrambler</i> sub-module and the <i>Unscrambler</i> sub-module to the DDR3 memory. . .	97
5.1	Flow diagram of the main tasks of the C server application for the LancelotRX system. At the start, the program checks that all the required hardware is present on the system, then the default settings are read from system files and set into the LancelotRX system. The control loops start being executed if they are enabled, and the network connection is checked for new commands from the client.	100
5.2	Flowchart of the initialization steps for the C server. The initialization procedure checks that the hardware needed is available and working on the system. The descriptor file contains the address for the FPGA configuration file, the needed sensors, ADCs and DACs. The configuration is written to the FPGA by the processor. Finally, the I^2C devices on the Interface board and Sensor board are checked.	102
5.3	Examples of the structure of commands used in the communication protocol on the LancelotRX system. The commands are sent in human readable ASCII characters, and the image data is sent in binary format.	105

- 5.4 Main LabVIEW client window. The images obtained by the system are shown in real time in the middle window of the GUI. The two profiles for the image can be seen on the right side of the screen. The profiles are not calculated on the client, but calculated and sent by the LancelotRX. Error codes for both command and image channels are displayed in real-time to aid in debugging of the system. 107
- 5.5 LabVIEW client window for changing the values of the configuration matrix. The values are displayed both graphically and numerically. The buttons on the top part of the screen allow the reading of the configuration matrix from a file, or to save the current configuration to a file. A small window in the bottom right shows the error status and communication codes to aid debugging of the system. 108
- 5.6 LabVIEW client temperature control window. The Peltier and PID control can be enabled or disabled from this window. It is also possible to change the PID parameters. On the right side of the screen, plots of the temperature and Peltier voltage changes over time are displayed. The temperature threshold to start the fan, and the temperature range over which the fan speed changes, can be modified from the lower left corner on the screen. 109
- 5.7 Flow diagram of the Python client for the LancelotRX system. The IP of the LancelotRX is requested from the user at the start of the program. The acquisition parameters set by the client are integration time, threshold values and amount of frames or profiles to be taken. Both frames and profiles are stored as individual files in ASCII format. 110

6.1	Housing of the LancelotRX system. The housing is divided into two pieces, a top and bottom enclosure. The bottom enclosure has four holes for screws that keep the housing closed. The top enclosure has spacers screwed into it to hold the Processor and Interface boards. Four threaded holes on the top enclosure are used to fix the Sensor board in place, and another four are used for the sensor cover. A slit and two holes on the top enclosure are used for communication between the Sensor board and the Interface board, and to connect the Peltier and high voltage line to the Interface board.	114
6.2	Cross-section view of the connection from the Sensor board to the Interface board for the LancelotRX system. The connecting segment crosses the vacuum chamber floor through a slit which is later sealed with vacuum grade epoxy. The connecting segment has been painted on red for this figure to enhance visualization. The JMD connector on the Interface board is shown inside the electronics chamber. The flexible PCB shows a small bend, this is caused by the flexible PCB being longer than the distance between the sensor chamber and the Interface board. The flexible PCB has been designed longer so it's possible to assemble the LancelotRX system.	115
6.3	Cross section of the relevant parts for the temperature control. The heat generated by the Medipix3RX is removed through the copper block by the Peltier and dissipated into the top enclosure. The electronics chamber, holds a centrifugal fan situated under the air vents of the top enclosure. The airflow generated cools down the Interface and Processor boards, as well as the top enclosure.	116
7.1	A block diagram of the pixel circuitry, the outputs of DISCH and DISCL go to the processing logic. Both discriminators have the option to add an offset to its TH input, in order to compensate for pixel-to-pixel threshold variation. Modified from [8].	119

7.2	A) Differential TH scan of a 16 keV x-ray signal flooding the sensor, using SPM in an equalized sensor. The peak of the energy can be clearly detected. B) Differential TH scan of a 16 keV x-ray signal flooding the sensor, using SPM and no equalization. It is impossible to reconstruct the energy peak due to the threshold dispersion.	120
7.3	Average pixel count for a scan of the threshold DAC, using no equalization. The response is generated by the electronic noise floor that has a Gaussian distribution with a mean around 0.	121
7.4	Profile of a scan of threshold DAC using 70 test pulses and dividing the average pixel value by 70, using a sensor with no equalization.	125
7.5	Scan of the Threshold DAC of a pixel for a non-equalized sensor in SPM showing double and under counts , for x-rays of energy 14 keV. The plot also shows a simulated one pixel profile of a scan of the threshold DAC for non-equalized sensor without charge sharing effect.	126
7.6	Averaged profile of a scan of the threshold DAC for one single pixel, the set value of 5 is used to determine the position of th^*	127
7.7	Histogram of th^* for three different values of LDAC_DISC and the maximum negative added offset.	129
7.8	Histogram of the th^* for a non-equalized sensor, setting all the pixels trim bits to a value of -15 and an LDAC_DISC of 100 to set the mean of the Gaussian response away from the origin. The response is fitted to obtain the standard deviation.	129
7.9	Histogram of th^* using the optimum LDAC_DISC value to ensure that the mean of the th^* Gaussian distribution is located at 3.2σ from the target value, which for this example is a value of 10 in threshold DAC steps.	130
7.10	Plot of the th^* distribution for different values of the trim bits, showing the shift of the mean of the distribution across the threshold spectrum. In this case the same trim bits are applied to all the pixels. The measure of th^* was done using electronic noise as a source.	131
7.11	Histogram of the th^* displacement factor, using noise as a source and a trim bits swing of 5 DAC units.	132

7.12	Comparison of the histograms of the trim values after an equalization with the Stripes method using electronic noise as a source, for different values of the LDAC_DISC DAC.	134
8.1	Exploded view of the full system components of the LancelotRX system.	139
8.2	Plot of the temperature of the Medipix3RX chip on the LancelotRX system while performing a constant acquisition of images. The top plot shows the different temperature response with and without the temperature control. The bottom plot shows the speed at which the sensor's temperature reaches the target temperature, using 15 °C in this example, once the temperature control is enabled.	141
8.3	Images obtained with the LancelotRX using traditional x-ray absorption imaging. A flat field of 12 keV was used and direct imaging of the objects. a) Microprocessor Atmega32U4 [9] with a TQFP package. The wire bonding from the silicon chip to the integrated circuit pins can be detected. b) SD card memory, a hatched copper pour on the PCB can be clearly seen.	143
8.4	Energy spectrum of copper x-ray fluorescence, K_{α} =8.05 keV, in both SPM and CSM. a) Scan of the threshold DAC in SPM. b) Scan of the threshold DAC in CSM. c) Differential scan of the threshold DAC in SPM, the charge sharing effects are notable before the energy peak. d) Differential scan of the threshold DAC in CSM.	144
8.5	Comparison of the Noise counts on a scan of the Threshold DAC values for a non-equalized sensor, a noise linear equalization and a noise stripes equalization.	145
8.6	Differential scan of the Threshold DAC in CSM for the x-ray characteristic fluorescence of different elements.	149

8.7	Noise amplitude and threshold dispersion dependence on temperature on the Medipix3RX. a) The noise amplitude average in DAC units for different temperatures. b) The threshold dispersion standard deviation for a non-equalized Medipix3RX at different temperatures, the threshold dispersion is measured using electronic noise as a source of counts. c) Response of the noise in a scan of the threshold DAC for a non-equalized Medipix3RX at different temperatures. As the temperature increases the dispersion of the noise response decreases, but the mean of the response does not change significantly.	153
8.8	Erroneous change of the detected energy peak based on temperature changes of the Medipix3RX. The calibration was performed for a Medipix3RX at 20 °C and a 16 keV monochromatic x-ray flat field was used to detect the energy peak. The Medipix3RX was operating in single pixel mode, and the energy peak was calculated by applying Gaussian fittings to the scans of the threshold DAC.	154
9.1	Schematic of the principle of operation of the XBPM (not drawn to scale). Some of the photons will be scattered by the foil held at an angle α and pass through the pinhole generating a deformed cross-sectional image of the beam on the sensor. A displacement of δ on the beam results in a Δ displacement of the cross-section image on the sensor. If the angle α is constant, then the magnification is given by the ratio L/D [10].	159
9.2	Example of the image obtained with the Medipix3RX of the deformed cross-section of the x-ray photon beam using the LancelotRX as an XBPM. The graphs represent the profiles for rows and columns of the acquired image by the Medipix3RX. The profiles are fitted with a Gaussian function and the mean (μ) is used to determine the position of the beam.	161

9.3	Plot of the transmission curve of a 127 μm -thick Kapton foil. The working energy spectrum range for the LancelotRX as a XBPM is from 10 keV to 25 keV. For the working range the transmission of Kapton is higher than 0.95, therefore, less than 5% of the photons will be absorbed by the foil [11].	162
9.4	XBPM mount used for the XBPM application with the LancelotRX. On the left side, a closed view of this system is shown, while on the right side, a cross-section image shows the position of the Kapton foil, the pinhole sheet and the Medipix3RX. The dimensions D and L that control the magnification ratio are shown in the cross-section image. . .	163
9.5	The top plots show δz and δx , which are the centroid displacements from the mean on the z and x axis. The integration time used was 10 milliseconds, obtaining a frame rate of 83 images per second. The bottom plots show the Fourier power spectral densities of the centroid displacements. It's interesting to note that there is a big spike at approximately 21 Hz, this same spike has been found in a similar analysis of the beam stability of beamline I19, suggesting that the position instability might come from the source.	167
9.6	Plot of the intensity acquired per frame in the XBPM over a long run at Diamond Light Source beamline I24. The changes in intensity are generated by the top-up cycle of the photon beam at 10 minutes intervals. The acquisition frame rate is 0.1 frames per second and the integration time is 200 ms.	168
9.7	Differential energy profile obtained by the XBPM system on beamline I24, tested with different photon energies. The tail of the response is fitted to a Gaussian function, the mean of the fitted Gaussian is used to determine the photon beam's energy.	169
9.8	Relation of the energy threshold DAC value to the energy of the incident photon. The points are extracted from the mean of the fitted Gaussian functions from the differential profiles obtained by the XBPM system on beamline I24.	169

10.1	Energy spectrum of copper (k_α of 8.05 keV) and molybdenum (k_α of 17.48 keV) x-ray fluorescence. a) SPM profile of the energy spectrum of both energies. b) CSM profile of the energy spectrum of both energies. The sections limited by the red dotted lines show the ‘transition segments’. The points T_1 , T_2 and T_3 show the proposed energy threshold values needed to reconstruct the signal.	175
10.2	Diagram of the experimental setup used for the colour imaging test (not to scale). The sample holder is at an angle α from the LancelotRX, and holds the sample centred to the pinhole aperture in front of the LancelotRX. The magnification is determined by the ratio L/D	178
10.3	Colour x-ray imaging test. a) The sample used for the imaging, a copper strip with a pattern on top of a zirconium plate. The imaged section is shown with a dotted square. b) Obtained colour x-ray image of the target. The energy bins corresponding to copper and zirconium are shown in red and green respectively. To create the image, the target was scanned using a 1 x 5 mm 20 keV photon beam. The images from the scan were stitched together to form the final image, no other image processing was applied.	179
10.4	Experimental setup for the material identification test . a) Experimental setup used for the test, the x-ray fluorescence generated by the elements on the spinning wheel is detectable by the LancelotRX. The wheel was set to spin at 17.5 RPM. b) The spinning wheel is made out of 0.3 mm acrylic and has copper strips and iron pebbles attached to it.	180
10.5	X-ray intensity per colour band. Copper fluorescence is depicted in green, iron fluorescence in red and the 12 keV scatter in blue. The plot shows one revolution of the spinning wheel.	181
A.1	Checker board pattern of the test pulses in the Medipix3RX matrix. [8]	204
A.2	Table of DACs used in the Medipix3RX. [8]	205
A.3	First section of the Operation Mode Register of the Medipix3RX. Default column shows the bit value after a reset. [8]	206
A.4	Second section of the Operation Mode Register of the Medipix3RX. Default column shows the bit value after a reset. [8]	207

A.5	Configuration bits per pixel in the Medipix3RX. The configuration matrix is the combination of the configuration bits for all the pixels. [8] . .	207
B.1	Block diagram of the connections necessary to control the pins from PRU core without the use of Enhanced GPIO.	210
B.2	Block diagram of Jrunner software [12].	211
B.3	Original Jrunner program flow [12].	212
B.4	Modification to the program flow of Jrunner to use the PRU core for the bit banged communication.A) Image is the original program flow, and B) shows the modification made to use the PRU core. Modified from [12].	213
B.5	Program flow of the C program	214
D.1	Island phenomenon generated by the CSM if the thresholds of the low discriminator are not correctly equalized. The sporadic black pixels are either non responsive pixels or masked ones.	220
D.2	Profiles of one pixel for a scan of the threshold DAC on a non-equalized sensor, using pulses to generate counts. The profiles are repeated for different amplitude values of the pulses.	222
D.3	th^* values per pulse amplitude for a specific pixel. The response is shown without an added threshold offset, with a positive offset and with a negative offset. The values of th^* lines have been fitted to obtain its parameters.	223
D.4	th^* to pulse amplitude line for 9 neighbouring pixels. No correction has been added and it is possible to see the gain mismatch and original threshold dispersion.	223
D.5	th^* to pulse amplitude lines for 9 neighbouring pixels after equalization. The equalization has been done for a pulse amplitude of 100 and 300, respectively.	225
E.1	Housings and mechanical design of the vacuum system for the XBPM vacuum application.	229

E.2	Cylindrical copper piece used to hold the sensor electronics into position and to aid the heat dissipation. The copper puck is hold into position by 3 screws.	230
E.3	Flexible board designed to interconnect the Interface and Sensor boards on the vacuum design. The flex part of the board is attached to the FR4 rigid material parts of the PCB.	231
E.4	Placement of the flexible board used to interconnect the Interface and Sensor boards on the vacuum LancelotRX system. The flexible segment of the PCB has been coloured in red to help visualization.	231
E.5	Cross section of the relevant parts for the temperature control in the vacuum design. The heat generated by the Peltier is dissipated into the copper puck.	232
E.6	Full system explode for the components of the vacuum LancelotRX system.	233

The University of Manchester

Tomas Bartolome Garcia Nathan

Doctor of Philosophy

DESIGN AND IMPLEMENTATION OF AN X-RAY COLOUR DETECTION SYSTEM USING THE MEDIPIX3RX

March 27, 2018

In this work the design and implementation of an x-ray imager system is presented. The design features a direct x-ray detection scheme by making use of a hybrid pixel detector (Medipix3RX). Taking advantage of the capabilities of the Medipix3RX, such as a high resolution, zero dead-time, single photon detection, charge-sharing mode and colour mode. The imager has a better resolution and higher sensitivity compared to using traditional indirect detection schemes.

A detailed description of the design process and implementation of the system is presented, which consists of a vacuum chamber containing the sensor, an electronic board for temperature management, conditioning and readout of the sensor and a data processing unit which also handles network connection and communication with clients by acting as a server. A field programmable gate array (FPGA) device is used to implement the readout protocol for the Medipix3RX. Apart from the readout, the FPGA can perform complex image processing functions such as histogram, profiling and image compression at high speeds. The temperature of the sensor is monitored and controlled through a PID algorithm making use of a Peltier cooler, improving the energy resolution and response stability of the sensor. Without implementing data compression techniques, the system is capable of transferring 680 profiles/s or 240 images/s in a continuous mode.

A detailed analysis of equalization procedures and tests for all the operation modes of the sensor are presented in this work. Different equalization methods were tested, such as using electronic noise, injected pulses and x-ray photons to perform the equalization. The results of the trade-off of equalization time versus energy resolution are analysed and discussed.

One of the tested applications of the system is as an x-ray beam position monitor (XBPM) device for synchrotron light source experiments. The XBPM allows a non-destructive real time measurement of the beam position, size and intensity. A Kapton foil is placed in the beam path scattering radiation towards a pinhole camera setup that allows the sensor to obtain an image of the beam. By using profiles of the synchrotron x-ray beam, high frequency movement of the beam position can be studied.

Experiments testing the characteristics of the Medipix3RX are shown in this work. The colour mode capability and its limitations were tested and found to be able to recognize elements by their characteristic x-ray fluorescence. The Medipix3RX dependence to temperature was measured, showing the necessity of controlling the sensor's temperature.

Declaration

No portion of the work referred to in the thesis has been submitted in support of an application for another degree or qualification of this or any other university or other institute of learning.

Copyright Statement

- i. The author of this thesis (including any appendices and/or schedules to this thesis) owns certain copyright or related rights in it (the “Copyright”) and s/he has given The University of Manchester certain rights to use such Copyright, including for administrative purposes.
- ii. Copies of this thesis, either in full or in extracts and whether in hard or electronic copy, may be made **only** in accordance with the Copyright, Designs and Patents Act 1988 (as amended) and regulations issued under it or, where appropriate, in accordance with licensing agreements which the University has from time to time. This page must form part of any such copies made.
- iii. The ownership of certain Copyright, patents, designs, trade marks and other intellectual property (the “Intellectual Property”) and any reproductions of copyright works in the thesis, for example graphs and tables (“Reproductions”), which may be described in this thesis, may not be owned by the author and may be owned by third parties. Such Intellectual Property and Reproductions cannot and must not be made available for use without the prior written permission of the owner(s) of the relevant Intellectual Property and/or Reproductions.
- iv. Further information on the conditions under which disclosure, publication and commercialisation of this thesis, the Copyright and any Intellectual Property and/or Reproductions described in it may take place is available in the University IP Policy (see <http://documents.manchester.ac.uk/DocuInfo.aspx?DocID=2442>), in any relevant Thesis restriction declarations deposited in the University Library, The University Library’s regulations (see <http://www.manchester.ac.uk/library/about/regulations>) and in The University’s Policy on Presentation of Theses.

Acknowledgements

I would like to thank everyone at the University of Manchester that supported me throughout the course of this PhD. This work would have been impossible without the financial support of the Mexican Council for Science and Technology(CONACyT).

“We should not trust the masses who say only the free can be educated, but rather the lovers of wisdom who say that only the educated are free”

-Epictetus, Discourses, 2.1.21-23a

List of Publications

T.B. Garcia-Nathan, A. Kachatkou, C. Jiang, D. Omar, J. Marchal, H. Chagani, N. Tartoni and R.G. van Silfhout, “Compact and portable X-ray imager system using Medipix3RX,” *Journal of Instrumentation*, October 2017

H. Chagani, T.B. Garcia-Nathan, C. Jiang, A. Kachatkou, J. Marchal, D. Omar, N. Tartoni, R.G. van Silfhout and S. Williams, “Performance of the Lancelot Beam Position Monitor at the Diamond Light Source,” *Journal of Instrumentation*, December 2017

Acronyms

ASCII	American Standard Code for Information Interchange
ASIC	Application-Specific Integrated Circuit
CCD	Charge Coupled Device
CERN	European Organization for Nuclear Research
CM	Colour Mode
CMOS	Complementary MetalOxideSemiconductor
CSA	Charge Sensitive Amplifier
CSM	Charge Sharing Mode
DAC	Digital to Analog Converter
DDR3	Dual Data Rate generation 3
DIP	Dual In-line Package
EMI	Higher Electromagnetic Interference
FP	Fine Pitch
FPGA	Field Programmable Gate Array
GPMC	General Purpose Memory Controller
GUI	Graphical User Interface
HPD	Hybrid Pixel Detector
I/O	Inputs or Outputs
I²C	Inter-integrated Circuit
JTAG	Joint Test Action Group
LED	Light-Emitting Diodes
LFSR	Linear Feedback Shift Registers
LHC	Large Hadron Collider

LVDS	Low-Voltage Differential Signal
MAPS	Monolithic Active Pixel Sensor
MB	Mega Bytes
MOSFET	MetalOxideSemiconductor Field-Effect Transistor
OMR	Operation Mode Register
OS	Operating System
PCBs	Printed Circuit Boards
PFM	Pulse Frequency Modulation
PHY	Physical Layer
PID	ProportionalIntegralDerivative
PMIC	Power Management Integrated Circuit
PRU	Programmable Real-time Unit
PWM	Pulse Width Modulation
RAM	Random Access Memory
RPM	Revolutions Per Minute
SD	Secure Digital
SMPS	Switched Mode Power Supply
SNR	signal-to-noise-ratio
SOC	System On a Chip
SPI	Serial Peripheral Interface bus
SPM	Single Pixel Mode
SSH	Secure Shell
TCP/IP	Transmission Control Protocol/Internet Protocol
TSV	Through-Silicon Vias
UART	Universal Asynchronous Receiver-Transmitter
USB	Universal Synchronous Bus
XAS	X-ray absorption spectroscopy
XBPM	X-ray Beam Position Monitor
XPCS	X-ray Photon Correlation Spectroscopy

Chapter 1

Introduction

X-rays were discovered by Conrad Wilhelm Roentgen, on the 8th of November 1895, when he noticed that the radiation emitted by one of his experiments could penetrate matter. After observing the x-rays for the first time, Roentgen spent eight weeks in his laboratory doing experiments. In his notes, he temporally named the new rays ‘x-rays’, with the mathematical designation of ‘x’ representing an unknown value. He kept on working on the x-rays, until he published his famous first report “Eine neue Art von Strahlen” [13].

Roentgen’s experiments were highly limited by both the technology he had available and the physics knowledge at that time. Nevertheless, he made important discoveries about the nature of these rays, starting by verifying that attenuation depends not only on the physical arrangement of the material (thickness and density) but also on the nature of the absorber. Elements with different atomic numbers will generate different attenuation. In his third publication, he noted more major observations, including that by modifying the voltage used in this experiment, it was possible to modify the energy of the x-rays, and with this, to modify the depth in which it penetrates into the absorbers.

1.1 X-ray fluorescence

If a material is bombarded with charged particles, that have a greater energy than the ionization energy of the material, ionization may occur. When ionization happens, an electron is knocked out of its orbital. The probability of this interaction is directly

proportional to the cube of the atomic number (Z) of the absorbing material. When an electron in a lower orbital is knocked out, the electronic structure of the atom becomes unstable, forcing another electron from a higher orbital to take the place of the missing electron. In the moment when the electron falls into the lower orbital, an x-ray photon is emitted with an energy equals to the energy difference between the two orbitals. The emitted photon is known as x-ray fluorescence.

The x-ray fluorescence can only have discrete values, because the electrons can only be in specific orbitals. Different elements have electrons in different orbitals, so the radiation generated is characteristic to the element and to the orbital from where the vacancy was filled. The characteristic x-ray radiation can be associated a series K , L and M , depending on which orbital the electron filled the vacancy in. For a transition from L to K , the fluorescence is named K_α , for M to K it's called K_β and for M to L it's called L_α .

In this work, x-ray fluorescence is repeatedly used, both as a source of a known x-ray energy and as a method to identify materials. The advantages of using x-ray fluorescence as a source, is the facility with which the energy can be changed by changing the element used for the fluorescence. The x-ray fluorescence can be used to identify between different materials as long as the energy between their main fluorescence contributions, usually K_α , is bigger than the detector's energy resolution.

1.2 X-ray applications and detection

The medical applications for x-rays, became evident after Roentgen imaged his wife's hand. It is remarkable, to say the least, that x-rays became a main-stream diagnostic procedure, and was adopted by most major hospitals in Europe, within the first decade since its discovery [14]. Sadly, the effects of x-rays on the human body were not yet fully understood, and soon it became obvious the danger in their use. With the lack of dosimetry, dermatitis and deeper tissue damage were caused to patients and x-ray operators. However, x-ray imaging was still the only method to see images from inside the body for the next half century [14].

Currently, the x-ray radiation is used in a varied amount of applications, dispersed

between several fields of knowledge. The medical applications using x-rays have increased since their discovery, now x-rays are used not just for diagnostic purposes, but for treatment as well [14]. Thanks to the creation of x-ray radiation from synchrotron light, many experimental techniques have been developed, for example, X-ray Photon Correlation Spectroscopy (XPCS) or X-ray Absorption Spectroscopy (XAS). Another scientific field where the x-rays have had a big impact is material science, where methods like x-ray diffraction have allowed to study the arrangement of atoms in materials.

Following technological development, the detection of x-rays has entered the digital era. In modern detectors, the information of the detected photons is processed and stored digitally. The detection process can be done by two methods, direct and indirect detection. Indirect detection requires an extra step between the x-ray photons and the detector, for example, a scintillator screen can be used to generate visible light photons from the interaction with x-ray photons. In the direct detection method, the detection is generated from the interaction between the x-ray photons and the detector. Direct detection methods yield higher detection efficiency than indirect detection methods.

Several direct x-ray detector Application-Specific Integrated Circuits (ASIC) have been developed to meet the requirements for modern x-ray experiments. Some examples of these ASICs are: Pilatus [15], XPAD [16], ChromAIX [17], Nexis detector [18], and Medipix [19]. These detectors have similar characteristics, with pixel pitches ranging from 50 to 100 μm and with several energy comparators per pixel, ranging from 2 to 8. The Medipix3RX offers a great combination of pixels with a size of 55 μm per side and 8 energy comparators per pixel. Based on these characteristics, the Medipix3RX is the direct hybrid pixel detector to be used in this thesis.

Many detectors using the Medipix3RX ASIC, and other versions of the Medipix detectors family, have been developed, and a few of them are worth noting. Quatum detectors, a spin-off from Diamond Light Source, developed the Merlin system for Medipix3 and Medipix3RX [20]. Merlin is capable of a frame rate of 1200 frames per second, in bursts, and 100 frames per second in continuous mode. The MARS spin-off have developed a small computerized tomography scanner using the Medipix3RX called MARS-CT, with a frame readout of 2 ms [21]. The MARS-CT has been used for colour 3D imaging reconstruction of biological samples [22]. SMARTPIX is a detector

with four Medipix3RX chips and a high frame rate of 6000 frames per second , using four 8Gbit/s links [23].

Apart from the improvement on the capabilities of the detector's ASIC, some of the experimental methods require complex processing of the raw data at fast rates. One example is the XPCS method, which can be implemented by fitting the raw data into correlation functions [24]. Another example is an X-ray Beam Position Monitor (XBPM), where the position of the beam is calculated by fitting image profiles to a Gaussian function [25]. To solve these requirements, new detectors must be developed with complex in-situ processing capabilities.

1.3 Objectives of the research

The objective of this work is to design and implement an x-ray imager, using the Medipix3RX ASIC, with flexible capabilities for fast raw data processing. The designed system must explore all the possibilities from the Medipix3RX. As part of the work, characteristics and the performance of the Medipix3RX will be tested and analysed.

Currently, there are no detector systems, using the Medipix3RX, available in the market, that would allow the required data processing. All the existing systems are sold as black boxes, without the possibility of modifying the Medipix3RX driver or to add new processing features. For this reason, in this work a new imager with the Medipix3RX was designed and implemented.

1.4 Research outcomes

This section outlines the contribution to knowledge achieved by this research work.

- **Design and implementation of an x-ray colour imager using a Medipix3RX:** The electronics, firmware and software for an x-ray imager were specifically designed for this project. A detailed explanation of the design and the design choices is given.
- **Analysis of the possible equalization methods and sources for the Medipix3RX:** Different equalization methods and sources are compared and

analysed. New equalization methods are proposed and tested. The results of the existing and new methods are analysed and a discussion of the results is presented.

- **Experimental results on the temperature dependence of the threshold dispersion and energy calibration on the Medipix3RX:** The experimental results obtained show the importance of temperature control of the Medipix3RX. The results and discussion on this topic should be taken under consideration for future designs of x-ray imagers based on the Medipix3RX.
- **Experimental results using the designed imager as an x-ray beam position monitor application:** A method to monitor the position of an x-ray photon beam is presented. The principles of operation and results of the implemented x-ray beam position are described. The advantages and limits of the proposed application are discussed and future improvements are mentioned.
- **Analysis and results of colour imaging with the Medipix3RX:** The colour capabilities of the Medipix3RX were tested for colour imaging and element identification. The results of the tests are shown, and the limits of the Medipix3RX colour capabilities are discussed.

1.5 Original contributions of the research

The comparison between different equalization methodologies, presented in this work, will aid future designs in selecting the most appropriate equalization methodology for the application. A new proposed equalization methodology is presented for Colour Mode, outperforming the previous published methodology. An original equalization methodology for Charge Sharing Mode, using x-rays as an equalization source, is presented and shown to improve on the energy resolution achieved by previous methodologies.

The presented results on the behaviour dependence of the Medipix3RX to temperature have not been published before. This information allows future designs, using the Medipix3RX, to correctly select the best operational temperature.

The proposed beam position monitor application with the designed detector, outperforms previous solutions. The proposed solution include new features, such as a variable optical magnification or an independent x-ray energy measurement, while maintaining a high spatial resolution and high sampling frequency.

1.6 Project overview

This thesis is structured as follows:

Chapter 1 defines the objective of the thesis and explains the contribution to knowledge. A brief introduction of x-rays and some of its many applications is given.

Chapter 2 introduces the Medipix3RX. The chapter starts by explaining the differences between hybrid and monolithic x-ray detectors. Afterwards, an explanation of the Medipix3RX capabilities is provided.

Chapter 3 describes the requirements and the design of the electronics for the thesis. After the general requirements of the design have been explained, a description of the designed hardware and its implementation is given.

Chapter 4 explains the Medipix3RX driver design. The implementation of the driver in a Field Programmable Gate Array (FPGA) as well as the interconnections of the FPGA to the rest of the electronic system are described.

Chapter 5 presents the software and firmware designed for this thesis work. A description of the firmware implemented on the detector as well as the client software to control the detector is given. The chapter also includes a brief explanation of the network protocol used.

Chapter 6 describes the mechanical design. An explanation of the requirements from the mechanical design, as well as a description of the designed enclosure for the detector is given.

Chapter 7 explains the equalization methods for the Medipix3RX. A description of different equalization methods is given. The advantages and disadvantages of using different equalization methods are discussed.

Chapter 8 presents the experimental results obtained with the detector. Results of the designed detection system, as well as specific measurements of the Medipix3RX

behaviour are shown. A numerical comparison between the outcome of different equalization methods is shown.

Chapter 9 describes an application of the detector as a beam position monitor. This chapter shows a description of how the detection system can be applied as a beam position monitor, as well as the results of this application in two beamlines at Diamond Light Source synchrotron.

Chapter 10 describes an application of the detector as an x-ray colour imager. This chapter describes the possibility of the Medipix3RX in sorting the incoming photons into energy bands, and presents experiments using this feature of the Medipix3RX.

Chapter 11 concludes the thesis and discusses further work.

Chapter 2

The Medipix3RX hybrid detector

In this chapter, the fundamentals of a hybrid pixel detector are presented, as well as the advantages and common applications of this technology. The Medipix3RX detector is introduced and its architecture, features and usage are explained. The Medipix3RX detector is a fundamental part of the work presented in this thesis.

2.1 Hybrid pixelated x-ray detectors

The detection process for solid-state detectors can be separated into two sections: the x-ray interaction with the material, and the processing of the generated signal. These sections can be implemented in different material layers, generating a hybrid pixel detector (HPD), or in one semiconductor layer, called a monolithic active pixel sensor (MAPS). MAPSs are limited to using silicon as the absorption material, and therefore, the detection efficiency of this type of detector starts to drop at a photon energy range of 8-15 keV [1]. MAPSs can have a pixel pitch smaller than 10 μm but suffer from noise produced by dark current [26], which generates a smaller signal-to-noise-ratio (SNR) than HPDs [27].

HPDs are not limited to silicon and can use different sensing materials. This allows for a higher detection efficiency at different x-ray energies. Another advantage of HPDs is that they are more resilient to radiation effects than MAPSs, which is a necessity, specifically for high-energy physics experiments where radiation damage to the detectors is likely [28]. Different materials have been tested for the sensing layer of HPDs, incrementing the range of energies that can be detected. For example,

germanium (Ge) has been proven to be suitable to detect x-rays at 50 keV [29], while gallium arsenide (GaAs) has been tested for a range of up to 70 keV [30]. For higher energies, cadmium telluride (CdTe) has been tested for energies above 100 keV [31] [32].

There are two types of HPDs, photon-integrating and counting. Photon-integrating HPDs integrate the total signal for a user defined period. This method enables the handling of large instantaneous fluxes. The disadvantage of photon-integrating detectors is that it's not possible to discern between the dark current generated noise and photons, or between photons of different energies. An example of a photon-integrating HPD is the CSPAD developed by the Linear Coherent Light Source (LCLS) [33].

Photon-counting HPDs count each photon individually, the signal is counted as a photon only if it passes a threshold criterion. This threshold comparison grants the ability to discern between different photon energies and the dark current generated noise, allowing a practically zero-noise performance [1]. A disadvantage of the photon-counting HPDs is that they are not able to handle large fluxes of x-ray photons. An example of a photon-counting HPD in use is the Pilatus detector developed by the Swiss Light Source (SLS) at the Paul Scherrer Institute (PSI) [34].

In Figure 2.1 the cross-section of a typical HPD is shown. The sensor layer is interconnected to the readout Application-Specific Integrated Circuit (ASIC) by using a solder process called bump-bonding [35]. When an x-ray photon impinges the sensor material, its energy is transferred into electron-hole pairs via ionization. Due to the influence of an externally applied electric field, a depletion region is generated on the sensor layer. The electric field forces the electrons and holes to drift to opposite directions of the sensor material. The drift of electrons and holes under the electric field induces an electric current on the charge sensing nodes bump-bonded to the ASIC [36]. The generated current is then processed by the ASIC electronics.

A block diagram of the typical detection channel on a photon-counting HPD is shown in Figure 2.2. The signal induced in the sensor layer is read out and amplified using a charge sensitive amplifier. A band-pass filter is used to improve the SNR. Because this filter changes the time shape of the signal, it's commonly referred to as a 'Shaper'. The filtered output is compared against a threshold value in a comparator, the threshold value is set by the user. The output of the comparator is a pulse that is passed to the digital processing section of the pixel circuitry.

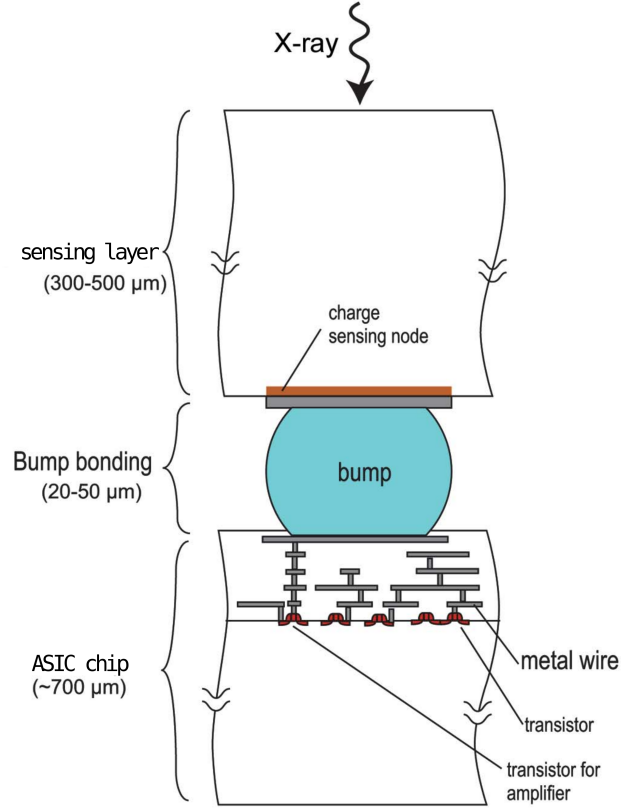


Figure 2.1: Cross-sectional view of one pixel of a hybrid pixel detector. The sensing layer and the ASIC chip are connected by a bump. The signal generated on the sensing layer flows to the ASIC where it is processed. Figure modified from [1].

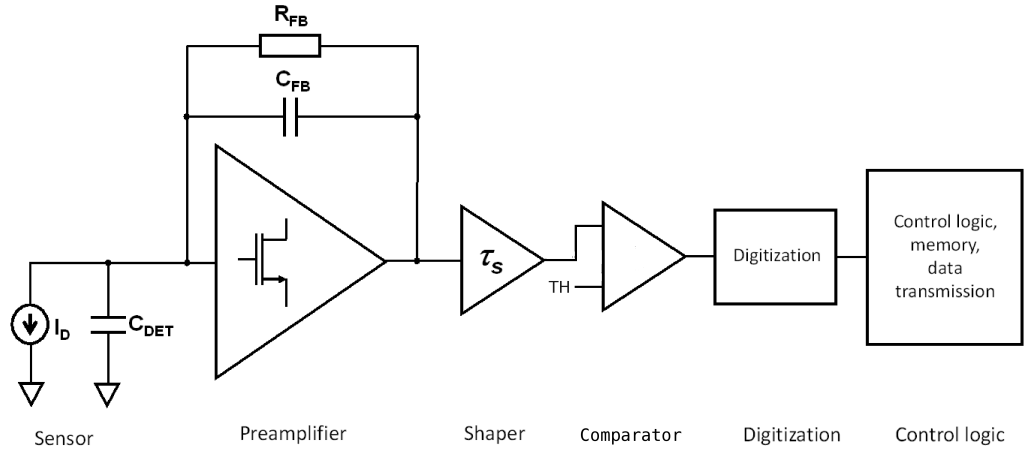


Figure 2.2: Block diagram of one channel's circuitry for a typical hybrid pixel detector. Figure modified from [2].

HPDs can have many functionalities embedded in the ASIC, from multiple comparators to smart reconstructions of the signal, but this comes at a cost of a more complex electronic design. An electronic design with more features will mean more

space to implement these circuits is required, increasing the minimum size of each pixel. More features also mean a higher power consumption. A increase in power consumption is already limited by the use of long metal wires, with a significant resistance, connected to the periphery of the chip [37]. This comes as a trade-off of functionalities versus power consumption and pixel size.

The use of detectors based on HPDs has expanded in recent decades. This technology can be found in many fields of science, including synchrotron radiation applications (for example in the crystallography technique [38]), material analysis by using the x-ray diffraction technique [39], space dosimetry [40], low energy electron microscopy [41], adaptive optics [42], medical x-ray imaging techniques [43], x-ray inspection techniques [44] and many others.

2.2 Electron-hole pair creation in semiconductor diode detectors

When the energy of an electron in the valence band is increased, the electron passes to the conduction band, leaves the specific bonding site, and drifts through the crystal. In this process, both a free electron in the conductance band and a vacancy (called hole) in the valence band are created. The combination of the two are called an electron-hole pair. Both the electron and the hole can be made to move, in opposite directions, by applying and electric field.

When a charged particle passes through a semiconductor, many electron-hole pairs are produced. The production can be the result of direct interaction between the charged particle and the semiconductor, or of indirect interaction. For indirect interaction, the charged particle generates a high energy electron, which subsequently produces more electron-hole pairs. The energy expended by the primary charged particle to create an electron-hole pair is called ionization energy. The ionization energy for silicon is 3.6 eV.

The sensor layer is a junction between n-type and p-type semiconductor materials. By applying an external bias voltage, the free electrons and the holes are moved to the sides of the material. This movement creates a depleted region, and if the bias voltage is high enough, a fully depleted region is created. New electron-hole pairs

created within the depleted region by the passage of radiation, will be moved out of the depleted region by the bias voltage, creating the electric signal used for detection of radiation.

The drift velocity of the electron-hole pair is proportional to the electric field intensity. If the electric field intensity is increased enough, a saturation velocity is reached, which becomes independent of further increases in the electric field intensity. For semiconductor materials, the drift velocity of electrons and holes are roughly of the same order, but the electrons have a higher velocity than the holes [45].

To take advantage of the higher velocity of the electrons over holes, electrons will be collected by applying a positive electric field to the sensing layer of the Medipix3RX. The saturation velocity for electrons in silicon is in the order of 10^7 cm/s. For a silicon sensor layer of $300\text{ }\mu\text{m}$, like the one used in this work, the time required to collect all the generated electrons is under 30 ns [46].

2.3 The Medipix3RX sensor

The Medipix is a family of photon-counting hybrid pixel detectors used for particle image and detection. The Medipix detectors have been developed by the Medipix Collaboration, which is an international collaboration based at the European Organization for Nuclear Research (CERN). The Medipix1 chip was the first version of this detector developed for high-energy physics to address the needs of particle tracking at the CERN Large Hadron Collider (LHC). To expand the use of this technology to new scientific fields, new versions of the detector were developed with the appearance of the Medipix2 collaboration in 1999 and the Medipix3 collaboration on 2005. In 2016, the Medipix4 collaboration was formed and the development of the new detector is currently in process.

In this work, the Medipix3RX is used, which is a corrected version of the design made by the Medipix3 collaboration. The Medipix3RX in its usual form has a size of $15.9 \times 14.1\text{ mm}$ and it is designed in eight metal layers using a $0.13\text{ }\mu\text{m}$ Complementary MetalOxideSemiconductor (CMOS) fabrication technology. The detector area is formed by a 256×256 pixel matrix, where each pixel is a $55\text{ }\mu\text{m}$ square. The analog

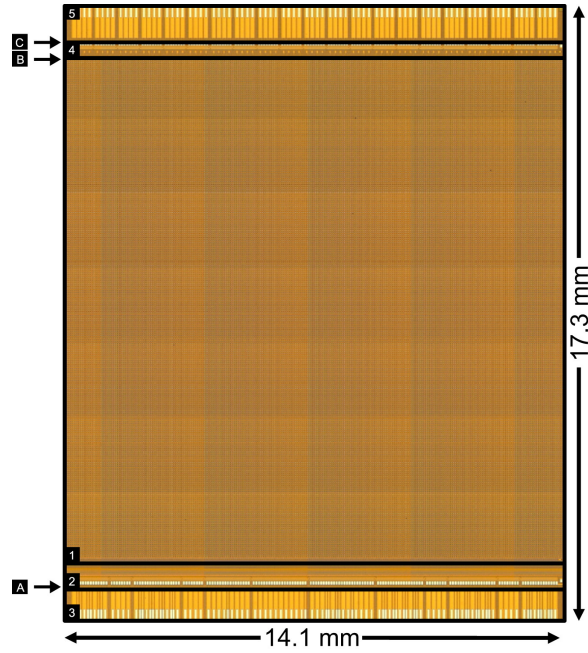


Figure 2.3: Physical shape of the Medipix3RX. 1) detector area of 256 x 256 pixels, 2) chip periphery and TSV, 3) pads for wire-bonding extension, 4) TSV power pads and 5) wire-bonding extension. The sections A, B and C show the different options for in-chip dicing [3].

power consumption of the chip is between 600 and 900 mW, depending on the operation mode used. The average digital power consumption for a 200 MHz main clock is approximately 250 mW [47]. A set of 32 fuses are available for chip identification.

In Figure 2.3 a picture of the Medipix3RX chip is shown. To connect the chip to the readout logic, it's possible to use either wire-bonding or Through-Silicon Vias (TSV). To reduce the amount of dead-area between chips in a detector array, it is possible to dice the Medipix3RX chip to remove the unused options. If only the bottom wire-bonding extensions are used, then the chip can be diced on the B line. If only the bottom TSV are used, then both the B and the A line can be diced. This allows for a maximum active area of 94.3% [3], allowing for large area detectors using tiled Medipix3RX with minimal dead-areas in between.

2.4 Pixel Architecture

Each pixel of the Medipix3RX contains the required electronics to detect the signal generated by the interaction of x-rays with the sensing layer, amplify and shape the signal, compare it with one or two thresholds and store the event in registers. Each

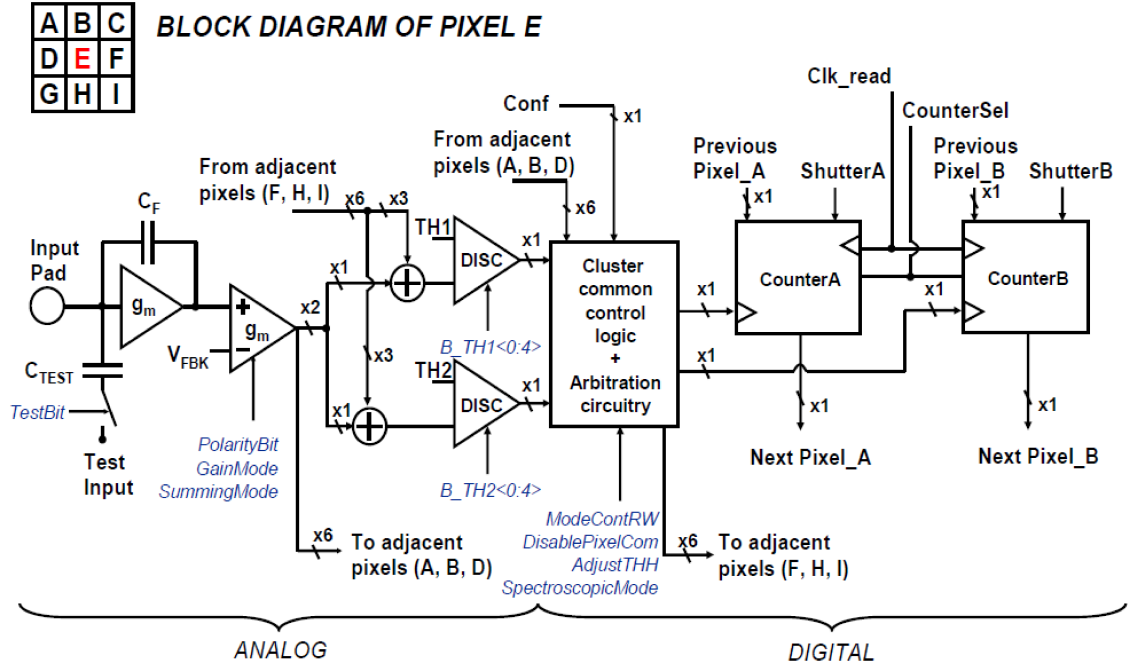


Figure 2.4: Pixel schematic of the Medipix3RX. Signal names in blue represent values or features that can be controlled by the user [4].

pixel has two discriminators, the low discriminator and the high discriminator. In Figure 2.4 a schematic diagram of the main components of the pixel circuitry is shown.

2.4.1 Amplification and discrimination of the photon pulses

Each pixel's circuitry contains an analog and a digital section as shown in Figure 2.4. The charge collected on the sensing layer is passed to, and integrated by, a Charge Sensitive Amplifier (CSA). The CSA used on the Medipix3RX chip is based on the Krummenacher [48] [49] architecture, which has the advantage of handling both negative and positive input charges. The C_F capacitor used on the CSA can have four different values, generating four gain settings that the user can select.

The output of the CSA is then passed through a shaper. The shaper acts as a first order semi-Gaussian filter [3] to remove possible noise. Another feature of the shaper is that it couples the output from the CSA to the next section of the pixel circuitry. Through coupling, the system becomes less sensitive to variations in the characteristics of the CSA. The output of the shaper is sent to summing nodes on both the pixel to which it belongs, and the neighbouring pixels. Based on the operation mode of the sensor, the summing nodes output either a sum of all the inputs, or the direct signal

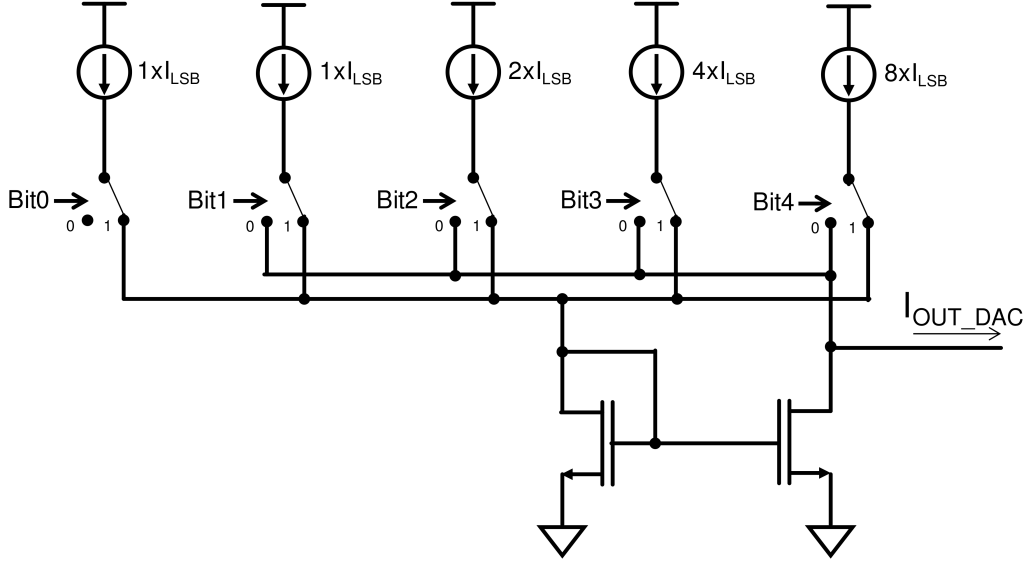


Figure 2.5: The 5-bit current DAC used on each discriminator of the Medipix3RX pixels. The current DAC is used in order to reduce the threshold dispersion between pixels [5].

from their corresponding shaper.

2.4.2 Threshold offset addition to the discriminators

The output of the summing node is sent to a zero-crossing discriminator. The discriminator compares the output signal from the summing node with a threshold value set by the user. The threshold value is set by a 9-bit Digital to Analog Converter (DAC) whose output is used by all pixels. Each pixel has two discriminators, with an individually customizable threshold setting. The output of the discriminators is sent to a logic block, which processes the inputs and determines if either of the counts in the two counters of the pixel will be incremented.

Each discriminator has a 5-bit current DAC used to reduce the threshold dispersion generated by the mismatch of the transistors used in the shaper and the summing nodes. The global dynamic range of the current DACs in the chip can be set by the user. In Figure 2.5 the schematic of the current DAC used to fix the threshold dispersion is shown. The used current DAC has the capability to add or subtract current from its output node. The current named I_{LSB} in Figure 2.5 is the current set by the global current DAC.

2.4.3 Pulses injection to the pixels

Each pixel circuitry has the option of using an injected pulse, as shown in Figure 2.4. The injected pulse passes through the C_{TEST} capacitor and then follows the entire pixel circuitry. Two different pulses can be generated simultaneously on the pixel matrix, TP_1 and TP_2 , but each pixel has access to only one of the generated pulses. The access to TP_1 or TP_2 is arranged in a chessboard pattern in the pixel matrix, shown in Appendix A.1. The duration of the pulses TP_1 and TP_2 is controlled by the user, as well as the amplitude of the pulses. The amplitude of the pulses is controlled by setting the value of three 9-bit DACs. The total charge injected in the preamplifier is proportional to the amplitude of the pulse set by the DACs and to the value of the capacitance of C_{TEST} .

A set of 27 on-chip DACs are used to set many parameters in the Medipix3RX including, but not limited to, the amplitude of the pulses, different bias conditions, and reference voltages. The on-chip DACs are of either 8-bit or 9-bit resolution. Both current and voltage DACs are present on the system with different DAC ranges. The output of each DAC can be channelled to a physical pin of the Medipix3RX to monitor the value of the generated current or voltage. A complete list of the DACs used on the system can be found in Appendix A.2.

2.4.4 Masking of pixels

Due to imperfections in the manufacturing of the chip or the sensor layer, some pixels could behave unpredictably. This behaviour can either be generating counts that are not related to a real input signal, or having a huge threshold offset in comparison to the rest of the pixels. Both behaviours are undesired since they can reduce the SNR or the energy resolution of the detector. To fix the potential problem, the pixel circuitry has the possibility of masking specific pixels. The masking is done on the logic block of the pixel circuitry and stops the pixel from incrementing the values on the pixel's counters.

2.4.5 Pixel Counters

Each pixel has two 12-bit counters, which are associated to the two discriminators on the pixel, simultaneously allowing two different energy thresholds in each acquisition. The counters can be configured to have different pixel depths, meaning the maximum amount of bits the counter can use. The counters can be used as 1-bit, 6-bit or 12-bit counters, or both counters can be united and used as a 24-bit depth. Using a 24-bit depth allows for longer integration times, but then only one threshold can be used per integration. Another functionality of the two counters, is to use one counter for registering incoming photons while the second counter is being readout. This features allows no dead time operation on the Medipix3RX.

To save space on the pixel circuitry, the counters have been implemented using Linear Feedback Shift Registers (LFSR), which use less gates than a normal binary counter. As shown in Figure 2.4, each counter is connected to the similar counter of its direct neighbours in the same column. For readout of the chip, the shift registers pass their values serially to the counter of the next pixel, generating a chain of counters whose values can be shifted out from one output.

2.5 Operation modes of the Medipix3RX

The operation modes of the Medipix3RX are different ways in which the incoming photons are processed. The operation modes can be divided into two categories, the amount of energy thresholds available per pixel input and the use of shared charge reconstruction. Each category has two options generating four possible combinations or operation modes.

2.5.1 Fine Pitch or Colour Mode

For the Fine Pitch (FP) operation mode, the circuitry of the pixel operates as the one shown in Figure 2.4. In FP, the signal input of each pixel is compared against two energy thresholds and the size of the pixels is $55\ \mu\text{m}$. For the Colour Mode (CM), four pixels will be grouped into a super-pixel having all the outputs of the four Shapers added in the summing nodes of each pixel. The inputs to the eight comparators of

the super-pixel will be the same signal, which is the addition of the four outputs of the Shapers. This enables eight different energy threshold comparisons for each super-pixel in CM. The disadvantage of colour mode is that the pixel pitch is now $110\ \mu\text{m}$ and the matrix is only 128×128 pixels. The CM is a new feature on the Medipix family, starting with the Medipix3.

2.5.2 Single pixel or charge summing modes

A problem present on the semiconductor detectors is that the charge of an incoming x-ray photon can be diffused through different pixels, generating a distortion on the energy spectrum [50]. If an x-ray photon impinges in the boundary between two pixels, the charge generated on the sensor material will be collected by the circuitry of different pixels, generating an erroneous detection of two photons of a lower energy than the original one. This phenomenon distorts the energy spectrum by generating detections of inexistent lower energy photons.

The charge sharing effects in the measured energy spectrum are shown in Figure 2.6. The top plot represents a scan of the threshold DAC for energies from 0 to 18 keV. For each threshold DAC value, a frame is acquired and the average pixel value is calculated from the pixel matrix. The input signal is a 12 keV monochromatic x-ray flat field covering the entire sensor. If there were no charge sharing effects, then the response to the threshold DAC scan should be a flat signal all the way up to 12 keV, and then an abrupt fall to zero. Due to the effects of charge sharing, the obtained response is a slope showing extra counts for low energies and missing counts for higher energies. The bottom plot of Figure 2.6 shows the differential version of the threshold DAC scan. The differential is obtained by subtracting the current scan value to the previous one. In the differential scan, the energy peak can be clearly seen for the response without the charge sharing effects, but with the charge sharing effects, the energy peak is not so evident.

Simulations and tests on the early prototypes of the Medipix3 show that it is possible to reduce the effects of the charge sharing by using the Charge Sharing Mode (CSM) implemented on the Medipix3 chip [6] [51] [52]. Nevertheless, practical tests on the final design of the Medipix3 showed a higher level of threshold dispersion than expected, which stopped the CSM from working correctly [53]. The double and under

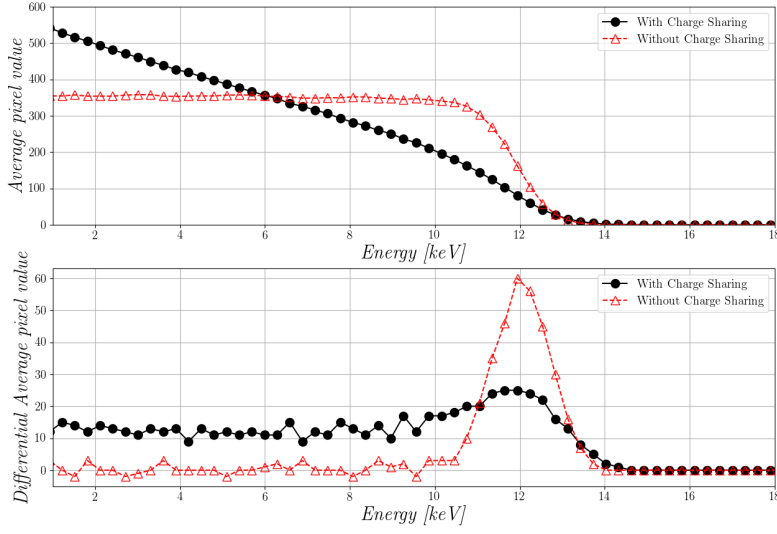


Figure 2.6: Distortion of the energy spectrum generated by charge sharing on the Medipix3RX. (top) Scan of the threshold DAC for a 12 keV monochromatic x-ray signal. (bottom) Differential scan of the threshold DAC showing the comparison of energy spectrum with and without charge sharing effects.

counts were solved on the Medipix3, but the high threshold dispersion generated a misallocation of the hits. To solve this problem, the new Medipix3RX has an improved CSM algorithm and a new method to reduce the threshold dispersion.

Two thresholds are needed for the CSM, one to allocate in which pixel the photon impinged ($TH_{allocation}$) and one to determine if the reconstructed energy is higher than the energy threshold (TH_{energy}). In Figure 2.7, a photon sharing its charge in four pixels is shown. The signal generated in the four pixels is compared with $TH_{allocation}$, which should be set to $1/4$ of TH_{energy} . The logic will use the output of these comparisons to determine which pixels has the highest charge. At the same time, the signals of each block of 4 pixels are summed together in the summing nodes. A photon count will be generated in a pixel if two conditions are met, the arbitration logic assigns the highest charge in the neighbourhood to belong to that pixel, and one of the summing nodes in the corners of the pixel has a reconstructed energy higher than TH_{energy} .

The Medipix3RX chip can be used in CSM, where the internal electronics of the detector allocate and reconstruct the charge of photons arriving at the edges of the pixels, or it can be used in Single Pixel Mode (SPM) where the charge sharing feature

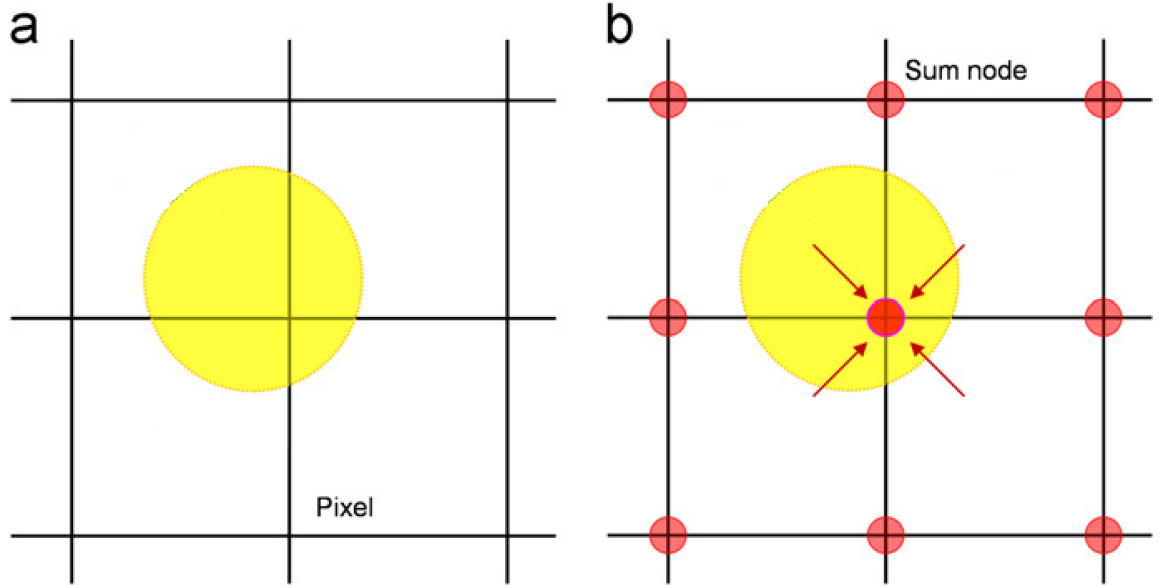


Figure 2.7: Illustration of the CSM process. (a) Shows the charge of one photon being shared in four pixels, the outputs of the comparisons with $TH_{allocation}$ are used to determine which pixel the count will be allocated to. (b) Shows the summing nodes where the total charge of the photon is reconstructed and compared with TH_{energy} . Modified from [6].

is disabled. The disadvantage of using CSM is that the amount of available thresholds is divided by two.

2.6 Digital control and readout process

The Medipix3RX uses 16 Low-Voltage Differential Signal (LVDS) lines for communication. The chip requires a clock input, which is used as the main clock of the system and as the sampling clock for the input data lines. The output data lines are sampled to an output clock generated by the Medipix3RX. The chip can be used to a maximum operating frequency of 500 MHz.

2.6.1 Operation Mode Register

The Medipix3RX uses an Operation Mode Register (OMR) to determine the operation to be realized by the chip. Every action of the Medipix3RX starts by the control electronics sending the 32-bit OMR, followed by a ‘Start Operation’ command to execute the action selected on the OMR. A table with the description of all the bits on the OMR is shown in Appendix A.3.

2.6.2 Pixel matrix configuration

For each pixel on the Medipix3RX there are four individual settings that have to be configured, these are the masking bit, the test bit, the added threshold for the low discriminator and the added threshold for the high discriminator. The masking and the test options are 1-bit configurations, either enable or disable. The added thresholds require 5 bits each, making a total 12 bits per pixel. The configuration matrix is the sum of all the configuration bits per pixel, with a total size of 786,432 bits. The configuration matrix is sent serially to the Medipix3RX, which allocates the data in each pixel by shifting the configuration bits through the pixel's counters. To reduce the requirements on the control logic, the configuration matrix can be sent in sections, removing the need for the control logic to store the entire configuration matrix at once. A table of the pixel's 12-bit configuration is shown in Appendix A.5.

2.6.3 Frame readout

The image data can be sent from the Medipix3RX using 1, 2, 4 or 8 data lines. Reducing the amount of data lines to use reduces the I/O requirements on the control logic but, also increases the readout time. The required time for the readout of a frame is dependent on the amount of data lines used, the clock frequency sent to the Medipix3RX and the pixel depth that has been selected for the pixel's counters.

Chapter 3

Electronic design of the LancelotRX

In order to control and readout the Medipix3RX sensor, manage network communications, distribute power, and solve all the other requirements of a fully functional detector, an electronic system has been designed and implemented. This chapter describes the design process of the electronic system for the LancelotRX. The chapter starts by explaining the requirements of the electronic design, then explains how the system has been divided into different Printed Circuit Boards (PCBs) and explains each one. Finally, there's a description of the designed temperature control system.

3.1 System requirements

LancelotRX is the name of the x-ray colour detection system that has been designed using the Medipix3RX sensor. As shown in Figure 3.1, the LancelotRX system contains the sensor and it's capable of outputting the processed readout data either by an Ethernet network communication, or by analog voltage outputs. The objective is to design a detector system capable of using all the features from the Medipix3RX sensor, in order to test its limits, analyse possible future applications and use the resulting system in specific applications.

The aim is to use the system as a standalone device or to obtain the readout data from the sensor and process it externally. To transmit the data from the sensor, an Ethernet connection to a client computer on the network will be used. The Ethernet

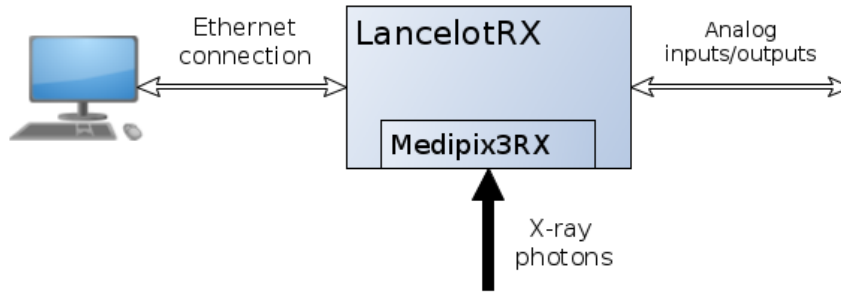


Figure 3.1: External connections of the LancelotRX system. The data acquired by the Medipix3RX can be accessed through client software by a network connection. The LancelotRX system uses analog inputs and outputs to communicate with other electronic devices, for example a motor controller.

connection will also be used to control and configure the LancelotRX system from a client software. Another objective is that the frame acquisition by the system can be triggered by digital inputs.

The requirements for the design are, to be able to control and readout the Medipix3RX, and perform internal processing of the raw data. The internal processing required is to generate column and row profiles from the acquired images. A connection to a client software is needed, to both control the system, and to be able to send the acquired data.

The frame rate objective in the LancelotRX system is to achieve 1k frames per second. The system should also be able to perform internal processing of the raw data, this enables extracting specific features from the raw sensor data. Apart from the network communication, analog outputs and inputs are required to work as triggers. To increase reliability of the sensor, the design has as an objective to implement a real-time temperature control of the sensor, since the literature reveals that the sensors' behaviour can be dependent on the temperature [54] [55].

Three PCBs are used in order to fit the electronics into the designed enclosure and to facilitate the ability to expand the system features by having a modular approach. These three PCBs are, the main processing board, called 'Processor board', an interconnection and sensors board called 'Interface board', and the board containing the Medipix3RX which is called 'Sensor board'. A system block diagram of this

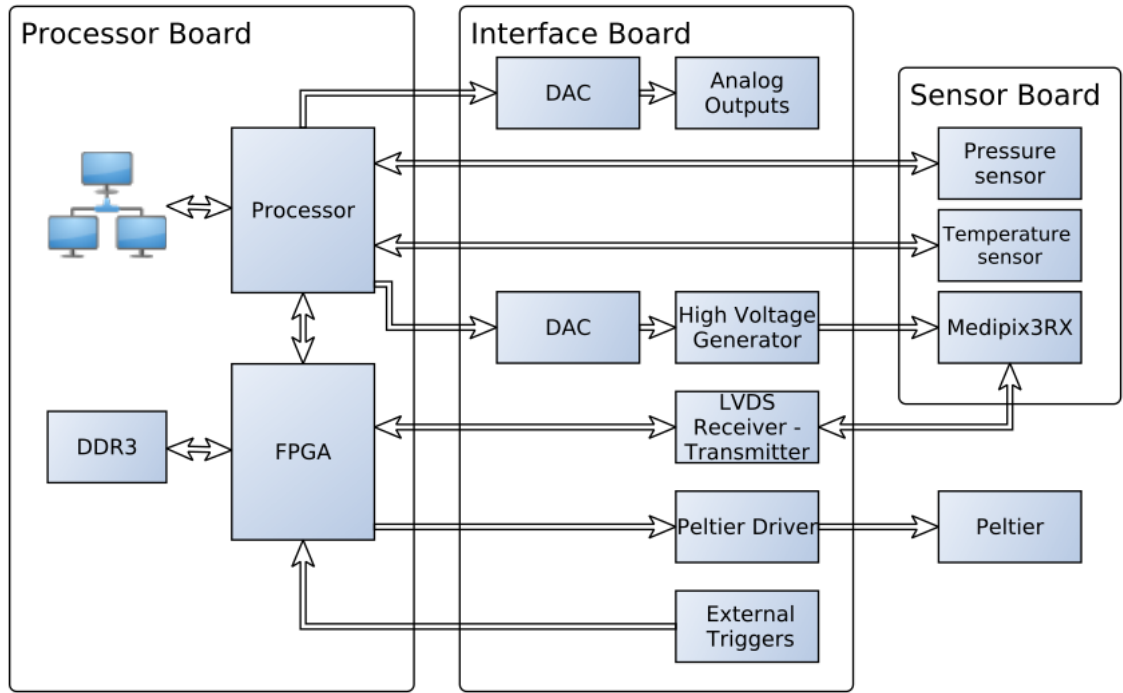


Figure 3.2: A block diagram of the electronics for the LancelotRX system. All the required electronics are distributed between three PCBs, the ‘Processor board’, the ‘Interface board’ and the ‘Sensor Board’.

architecture can be seen in Figure 3.2. The main processing blocks are a Field Programmable Gate Array (FPGA) to drive the Medipix3RX and a processor to control the communication.

The electronics design and assembly was completed in-house. The exception was the manufacture of the PCBs, which was done by a specialist supplier because of the lack of manufacturing facilities for multi-layered PCBs at the university. The population of the electronic components on the PCBs was done in-house, either by hand for the first prototypes or with the help of a Pick and Place machine for the final design.

3.2 Design of the printed circuit boards for the LancelotRX

3.2.1 Sensor board - a carrier PCB for the Medipix3RX sensor

The Sensor board is the carrier PCB for the Medipix3RX sensor. A requirement of the design of this board is to be as small as possible in space so it can fit in a small enclosure. The need for a small enclosure is rooted in having the option to use the Medipix3RX in vacuum, setting the entire LancelotRX in vacuum isn't necessary, therefore setting a small chamber in vacuum containing only the Medipix3RX was considered more appropriate. It's desirable to minimise the volume to be set in vacuum, to do this, the sensor will be mounted on the smallest PCB possible. The pressure value from the vacuum chamber, as well as the temperature of the sensor, have to be monitored with the required sensors placed inside the vacuum chamber.

To drive the Medipix3RX chip, the Sensor board has the required electronics to power and connect the data and control lines of the chip. The board also contains a temperature and a pressure sensor. The main components of the Sensor board can be seen in Figure 3.3.

The Medipix3RX uses three power domains on the proposed application, an analog 1.5 V, a digital 1.5 V and a digital 2.5 V [8]. All the communication and control lines of the sensor are routed to the Interface board connector on the PCB. Although the sensor can be readout using only one data line, the design has routed all 8 data lines in order to allow the maximum speed of the readout process. The Medipix3RX is connected to the PCB using wire-bond. In Figure 3.4, the design of the Sensor board is shown.

For the sensor to detect x-ray photons with as little electronic noise as possible, the analog supply voltage (1.5 V), must be as stable as possible. Minimising the heat generation in the voltage regulator is a priority since it is placed close to the sensor, but maintaining a low voltage variation and a small footprint are also key points. A low-noise and low-drop out voltage regulator was selected to address the requirements. The selected voltage regulator ensures a 1.5 % voltage accuracy under load changes

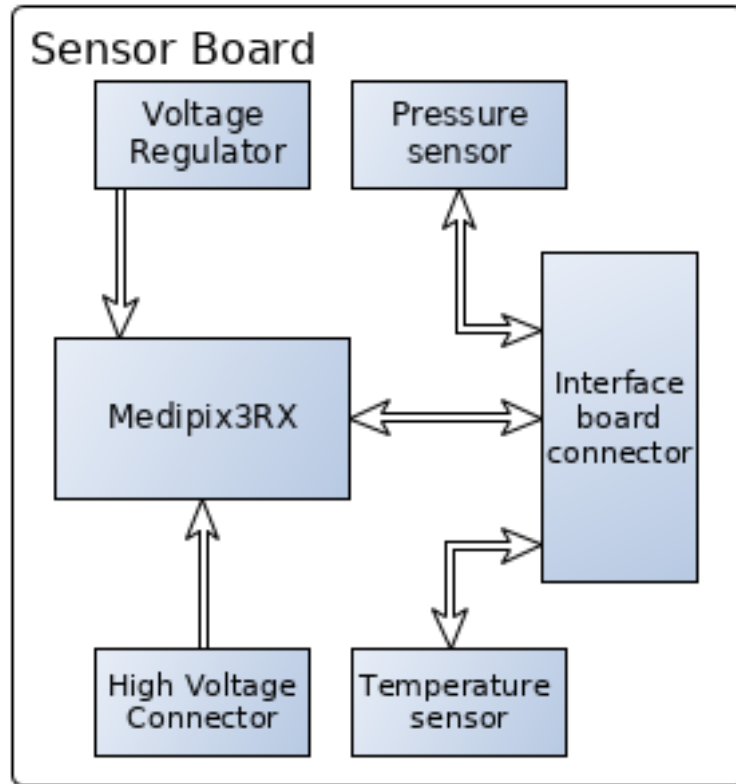


Figure 3.3: Block diagram showing the main components on the Sensor board.

and has a 180 mV dropout voltage for a current up to 2 A [56].

To sample the state of the vacuum or air pressure surrounding the sensor, a pressure sensor is used. An interrupt capable pressure sensor has been selected, with the possibility to configure the pressure threshold at which the interrupt will be activated. To control the pressure and temperature sensors on the Sensor board, the Inter-integrated Circuit (I²C) protocol will be used. The I²C communication protocol is selected in order to reduce the amount of communication lines that are required, using only 2 lines and having the feature of allowing multiple addressable slaves in the same bus.

The sensor board uses a female 80 pin board-to-board JMD connector with a 0.5 mm pitch for interconnecting the Medipix3RX lines, the I²C communication protocol lines and the power lines. This connector was selected for its high pin density. The design of the Sensor board can be seen in Figure 3.4.

The PCBs use a 4-layer stack of copper planes, with ground pours on both the top and bottom layer. The Sensor board is manufactured using RO4350B, which is a woven

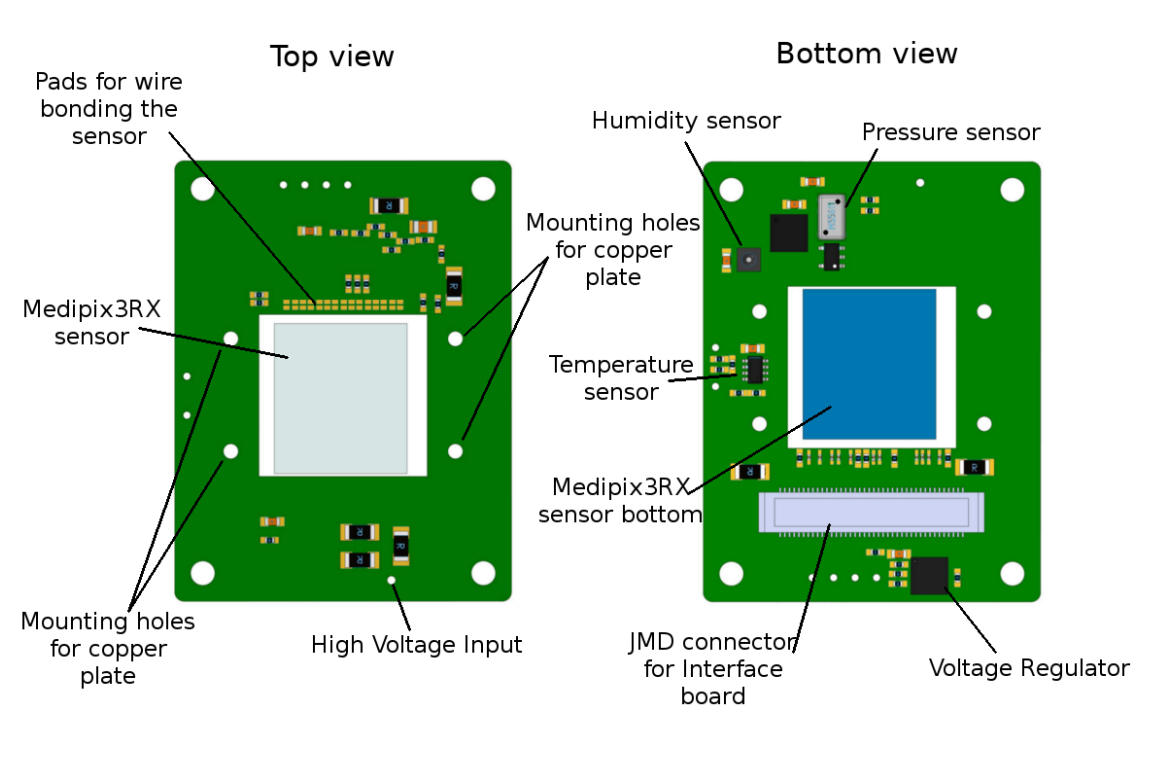


Figure 3.4: Top and Bottom views of the Sensor board design used in LancelotRX. The board contains a voltage regulator, temperature, pressure and humidity sensors and the required pads to wire-bond the Medipix3RX. A cut-out under the Medipix3RX allows a copper block (not shown) to contact directly the back of the sensor for better thermal conductivity.

glass reinforced hydrocarbon/ceramic, as a dielectric material for the PCB. This material was selected primarily for its low outgassing rate as measured by the NASA test procedure SP-R-0022A [57] and validated recently by the Rogers manufacturing company [58]. Other useful characteristics are a superior high frequency performance than FR4 and a higher thermal conductivity, with a reported $0.69 \text{ W}/(\text{m}^\circ\text{K})$ for RO4350B [59] while FR4 has a thermal conductivity around $0.25 \text{ W}/(\text{m}^\circ\text{K})$ [60] [61].

To control the temperature of the sensor, a closed loop control algorithm is used, making it necessary to have an accurate measurement of the sensor's temperature. It is necessary to have a high heat transfer between the sensor and the temperature controlling element, to increase the speed of the control response. The thermal conductivity of a PCB is not ideal since the base material tends to have a low thermal conductivity [62], using vias is a common approach to improve the thermal conductivity on a PCB [63] but a better solution would be to have an entirely different material. The solution used is to have a cut out section on the PCB, where a block of copper can

be inserted to be in direct contact with the Medipix3RX sensor, improving the heat transfer. The measurement of the sensor's temperature is read from the copper block with which the temperature sensor is in direct contact. As it is shown on Figure 3.5, there is direct contact from the temperature sensor placed on the back side of the PCB to the copper block, this allows a precise temperature measurement.

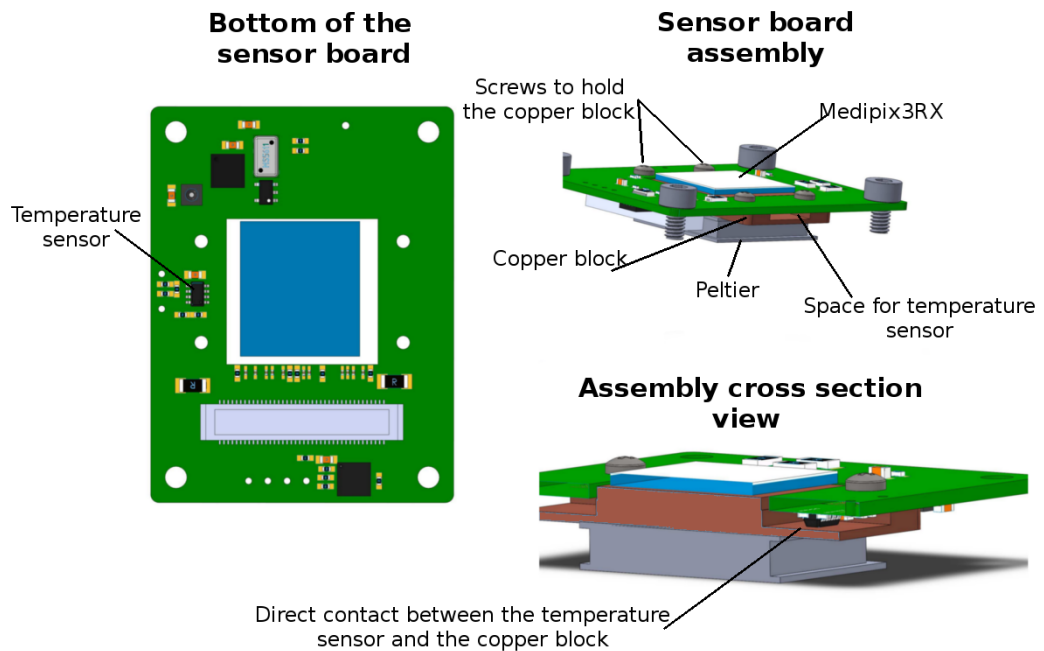


Figure 3.5: On the left, the temperature sensor is shown on the Sensor board PCB. On the right the assembly of the Sensor board PCB and the copper block is depicted with the sensor board being in direct contact with the copper block.

3.2.2 Interface board - a PCB to condition the Medipix3RX communication

The Interface board has been designed to act as a bridge between the Processor board and the Sensor board, it also contains all the extra required electronics that are not used for processing information. The Interface board is not placed in vacuum, so there is not a requirement to minimise its size. The main power regulation and voltage generation is performed on this board, as well as the conditioning of the communication and data lines with the sensor. The electronics needed to drive the temperature control are placed in this board. A block diagram of the main components of the Interface board is shown in Figure 3.6.

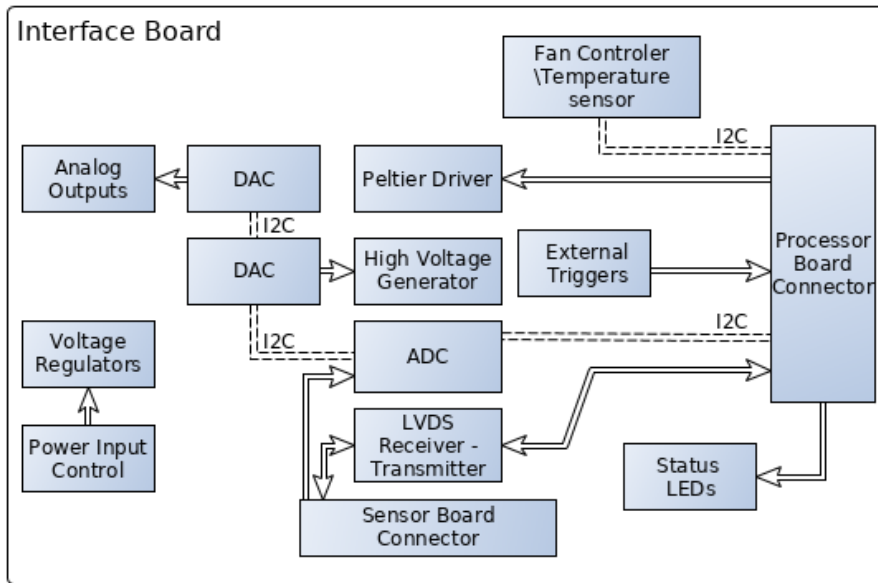


Figure 3.6: Block diagram of the Interface board. LVDS receivers and transmitters are used to transform the LVDS connections used by the Medipix3RX to the single-ended signals used by the processing board. The generation of the high voltage for the sensor, as well as the Peltier driver, are present on this board.

The Interface board must interconnect the Sensor board to the Processor board. The connection to the Processor board is done by an 80 pin AMP connector designed for direct connection between PCBs. The connector for the Sensor board is a female 80 pin JMD connector, which is a surface mount connector with a pitch of 0.5 mm. The same female connectors are used in the Sensor board and the Interface board, a segment containing two male connectors is used to interconnect the two boards.

The Medipix3RX has a total of 18 digital lines for control and data, all of which are Low Voltage Differential Signals (LVDS). An LVDS interface could be implemented on the FPGA [64], but this would use 36 Inputs or Outputs (I/O) pins of the FPGA and 36 pins of the connector between the Interface board and the Processing board. To reduce the amount of I/O pins of the FPGA needed to communicate with the sensor, transmitter and receiver chips that transform between LVDS and single-ended signals have been selected. The connection between the Interface board and the Sensor board is where most of the communication noise could be picked up. By placing the LVDS transmitter and receivers on the Interface board, the signals through the connection are less vulnerable to noise.

The electronics needed to implement the temperature control for the sensor are on

the Interface board. The temperature control electronics consists of a Switch-Mode Power Supply (SMPS) and a digital fan driver. The digital fan driver has an external temperature probe, which is used to determine the temperature of the Interface board and the Processing board. The connection from the SMPS to the Peltier driver is done through a two pin connector on the Interface board, as shown in Figure 3.7.

Three different voltages are required to power the Medipix3RX, as discussed in Section 3.2.1 the analog voltage is generated on the Sensor board, two further voltages of 1.5 V and 2.5 V that supply the digital parts of the Medipix3RX are generated on the Interface board and sent to the Sensor board through the main connector between these boards. A voltage of 3.3 V is also sent through the same connector to power the temperature and pressure sensors. Apart from these voltages, the Medipix3RX sensor requires a high voltage to generate the depletion region on the sensing layer, for this application the sensing layer used is Silicon, so a high voltage module with an output of 0-200 V has been chosen. In Figure 3.7, the design of the Interface board is shown.

Analog inputs and outputs are used on the LancelotRX to either trigger the acquisition of data, or to output a control signal generated by processing the Medipix3RX data. For the output signals, a combination of DACs and bipolar instrumentation amplifiers has been selected, this allows for the generation of a -10 to +10 V signal. The type of signal, bipolar or unipolar, as well as the range of voltages, can be selected through a Dual In-line Package (DIP) switch. The position of the switch can be seen in Figure 3.7 and the table of possible configurations is showed in Appendix B.1. For the analog inputs an optocoupler has been selected in order to protect the circuit and to increase signal compatibility with external hardware.

The Interface board has the main manual power switch for the LancelotRX system, as well as 4 Light-Emitting Diodes (LED) used to show the system status. The parameters shown by the LEDs can be seen in Appendix B.2. A dual colour LED is used to indicate the power status, displaying colour red when the system is off but power is connected, and displaying green colour when the system is on.

The circuit design is implemented on a 6-layer PCB using FR4 material for the substrate between copper layers. As shown in Figure 3.7, the power connector, the power switch, analog connections and the status LEDs are all on the same edge of the board, so they can be accessed from one face of the mechanical enclosure.

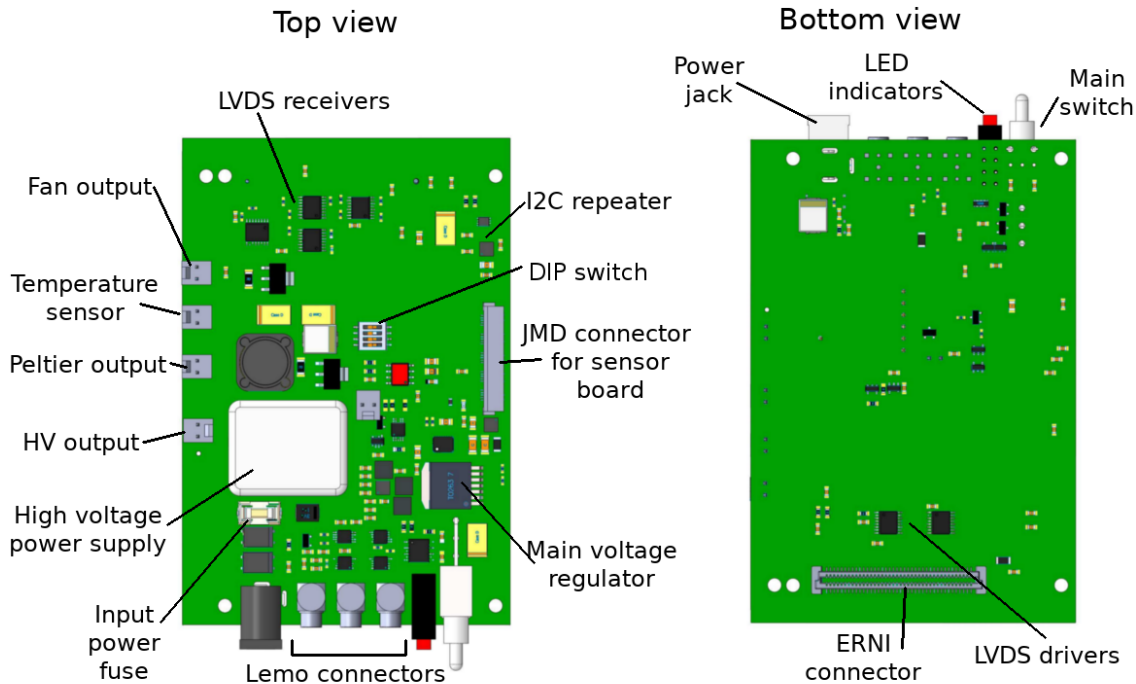


Figure 3.7: Top and Bottom views of the Interface board for the LancelotRX design. The LVDS transmitters and receivers are placed as close as possible to the ERNI connector to the Processor board to maximize the noise protection of the LVDS signals. The connectors for the input and output signals (Lemo connectors) as well as the status LEDs, power connection and the power switch are all placed on one edge of the PCB for easy access.

3.2.3 Processing board - the ARMFlash heterogeneous processing board

The Processor board was not specifically designed for this project, a general purpose heterogeneous processing board named ‘ARMFlash mini C5’ was used. This board has been designed by the research group and is also used in different applications. Multiple iterations of the design have been used and for this specific project the newest version of the board, using a Cyclone V FPGA [65], was selected. As part of the LancelotRX design, debugging and development of the ARMFlash mini was done.

For the sensor readout an FPGA was selected, this allows for a readout implementation capable of handling the maximum speed of the sensor. By using an FPGA, some of the data processing can be done in parallel. The sensor sends data in a format that requires decoding and bit arranging, this can be implemented using a pipe line on the FPGA. Another advantage of using an FPGA is that it grants flexibility to the

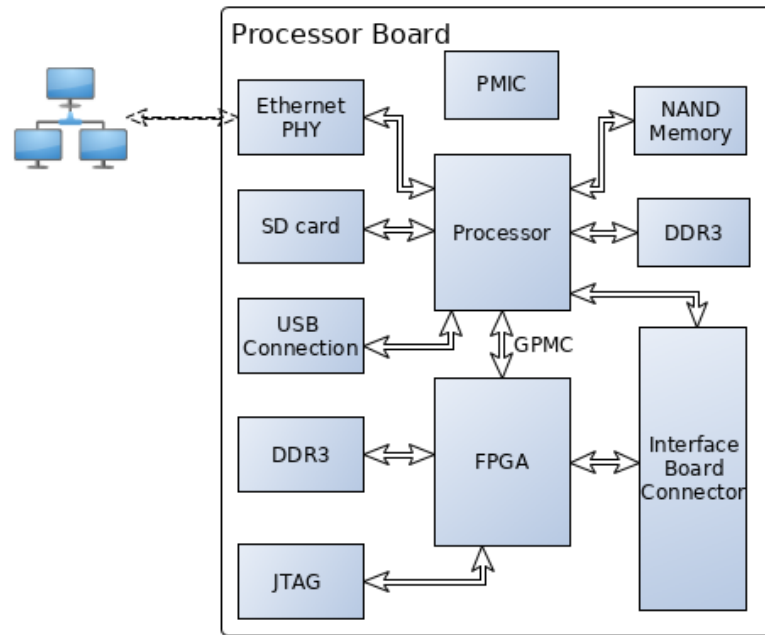


Figure 3.8: Block diagram of the the Processor board.

design, particularly allowing further processing of the raw images. For the first design, the intention was to use an Altera Cyclone III FPGA with 25k logic elements, but after the final FPGA system was developed it was evident that there were not enough logic elements. The selected FPGA changed to an Altera Cyclone V with 150k logic elements, to ensure that even if new features are added, there will be enough logic gates to implement the design. The FPGA can be configured by using a Joint Test Action Group (JTAG) protocol which can be accessed via a direct connection to the board, as shown in Figure 3.9, or directly by GPIO of the processor. In the debugging stage, the FPGA was configured through the JTAG connector using an Altera USB-Blaster connected to a computer, which is the fastest method to send the configuration data. For the working system, the FPGA will be configured by the processor as part of the initiation process. More information on the configuration of the FPGA can be found in Appendix B.1, including a proposed method to increase the configuration speed when the FPGA is configured by the processor.

To handle the FPGA (control and image transfer/formatting), the Ethernet connection and the communication protocol, a Texas Instruments AM335x processor with an ARM Cortex-A8 core [66] was selected. The used features of the processor in the design are the Serial Peripheral Interface bus (SPI), the Universal Asynchronous

Receiver-Transmitter (UART) and I²C communication interfaces, the Ethernet controller and the General Purpose Memory Controller (GPMC) interface. The selected processor also has two Programmable Real-time Unit (PRU) cores. The PRU cores can be used to implement a faster configuration process of the FPGA, this is explained in the Appendix B.1. To facilitate the development of a server program to which external clients can connect and control the LancelotRX system, a Linux operating system is used.

As shown in Figure 3.8, the processor is connected to three different memory devices, a Dual Data Rate generation 3 (DDR3) memory, a NAND flash memory and a Secure Digital (SD) card. The DDR3 memory is used as Random Access Memory (RAM) for the processor, and it is necessary to run the Linux Operating System (OS). A DDR3 memory of 512 Mega Bytes (MB) size was selected. For the development process, the OS was stored on the SD card in order to have a faster way to change the contents of the root file system and of the Linux kernel image. Having the possibility of booting from a system on an SD card also allows a simple and fast way to restore the system to a previously saved working state. On the final working system, the OS and the server program is stored into the NAND flash memory, this way an external SD card is not needed. Data corruption is more common on a SD card than on a NAND flash memory, for this reason the final prototype uses the NAND flash memory to store the OS.

The amount of data taken from the sensor is too big to be stored into memory blocks on the FPGA. To solve, this a DDR3 memory of 512 MB is used, the memory is connected only to the FPGA but its contents could be accessed from the processor by using the FPGA like a bridge. To allow both the processor and the FPGA to access the memory contents of the DDR3, arbitration has been implemented on the FPGA. The selected memory has enough space to store up to three full 16-bit Medipix3RX images and other data required by the FPGA system.

To allow the system to communicate through Ethernet, a Physical Layer (PHY) chip was selected. The processor can use the Ethernet protocol with 10, 100 and 1000 Mbps mode of operation. To power all the devices on the Processor board, different power supplies and voltage values are required. A Power Management Integrated Circuit (PMIC) was selected to coordinate all the power supplies and generate some

of the required voltage levels.

A UART to Universal Synchronous Bus (USB) converter chip is used to access the serial terminal of the processor from a USB connection on a computer. Accessing the processor from this interface is required on the early stages of development, once an OS has been booted and the network interface configured, it is possible to use Secure Shell (SSH) protocol to access the system.

Figure 3.9 shows the PCB design of the Processor board. Due to the density of the signals required by the FPGA and processor, an eight layer PCB was used. The top and bottom planes have a ground pour and the intermediate layers are used for a mixture of power and signal planes. An 80 pin Tyco/AMP connector is placed on the bottom of the board, containing signals from the processor and the FPGA. This is the connector that will be used to connect with the Interface board.

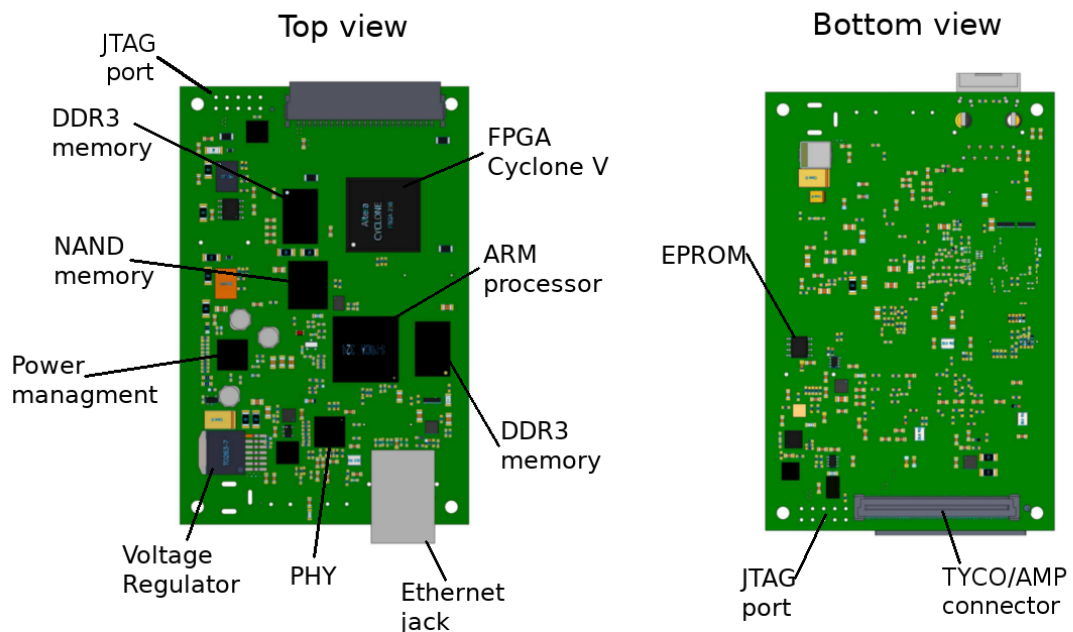


Figure 3.9: Top and Bottom views of the Processor board used in the LancelotRX design. An ARM processor and a Cyclone V FPGA are the two processing devices of the design. Two DDR3 memories are used to store volatile data and a NAND memory and an SD card are used to store the OS and non-volatile data. A power management IC is used to generate and distribute all the required voltages.

3.2.4 Flexible PCB for interconnection

The Medipix3RX sensor is placed on an individual PCB, and the communication and control lines have to travel from the Interface board to the Sensor board. A total of 49 different signals, including voltages and communication with the sensors, are required. The connectors selected are 80 pin connectors, these connectors were selected in order to have extra pins to use in parallel for the voltages and ground signals, reducing their equivalent resistance. This forces the communication between boards to have a cable of at least 49 different signals in a tight footprint of 25 mm wide. To achieve the required number of lines in a 25 mm wide segment a flexible PCB has been chosen.

Flexible PCBs are copper layers placed into a flexible dielectric material, allowing the final board to flex up to some degree, without breaking the copper paths. In this case, Kapton was selected as a base material, due to its resistance to high temperatures allowing soldering components to the copper layers without burning the base material.

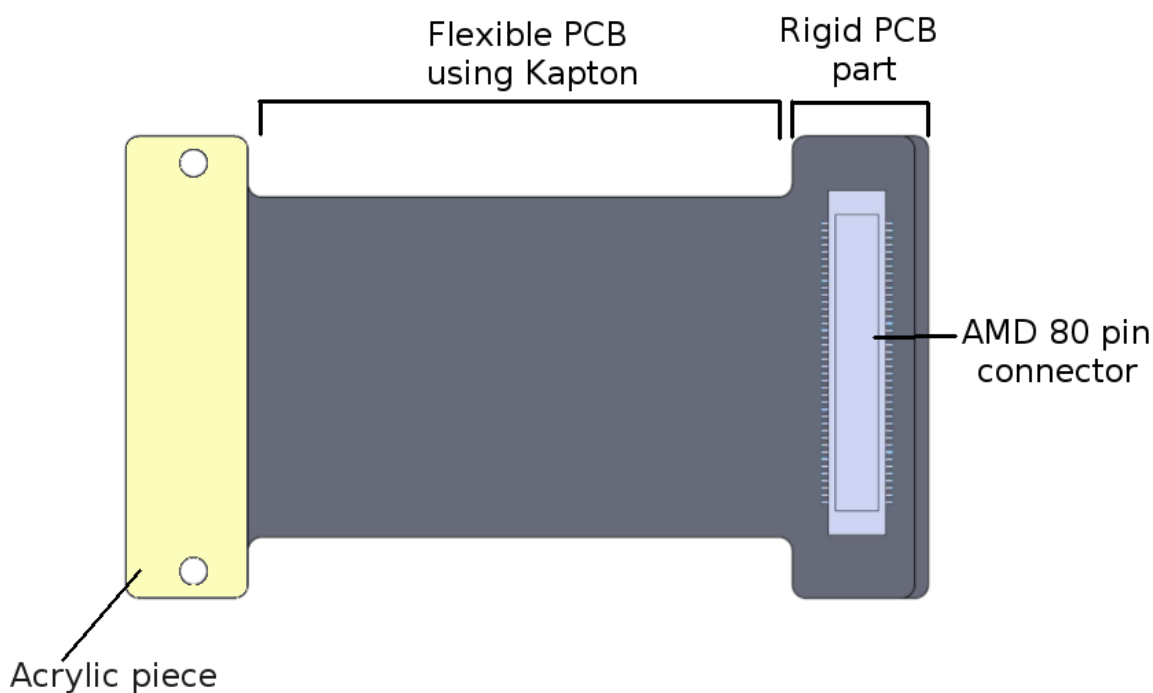


Figure 3.10: Flexible board designed to interconnect the Interface and Sensor boards on the LancelotRX design. The flexible PCB is 25mm wide and between the two copper layers 49 different signals are routed. Hatched copper pours have been used to decrease electrical resistance on the power lines while still maintaining flexibility on the PCB.

A two layer fully flexible PCB is used to communicate the Interface and Sensor

boards. A connector is placed at every extreme of the flexible PCB, one is placed on the top layer and one on the bottom as shown in Figure 3.10. The side of the flexible PCB that will connect to the Sensor board is pasted against the bottom of the vacuum chamber. The connector used for the Interface board has a rigid acrylic piece pasted on the other side of the connector to the Interface board, to avoid the flexible PCB bending near the connector and breaking one of the soldered pins. The connector to the sensor board has a rigid standard FR4 PCB segment to protect the connector pins.

3.3 Temperature control design

The Medipix3RX chip can consume up to 1W [8] of power which will cause a temperature rise on the chip, this can generate a temperature rise on the sensor material as well [67]. With an increase of the sensor's temperature, there is an increase in the rate of degradation of pixel response [54], apart from the increased rate of degradation, the high temperatures can cause an increase in the sensor leakage current, reported to be an increase of up to 26 times [67]. These two factors will generate a high noise level and a decrease in pixel response, negatively affecting the signal to noise ratio [67].

The need to control the temperature of the Medipix3RX sensor has been approached through different options. Systems like the Smartpix use water cooling to control the temperature [23], other designs use fans to cool down the sensor [67] or even let the sensors cool down by using a big heatsink like the design used by Merlin [68]. For the design of LancelotRX, the use of a Peltier cooler is proposed. The objective is to create a temperature control system that will allow the user to set a constant target temperature for the sensor which the system will be able to maintain for long periods of time under system operation.

3.3.1 Proposed cooling system

To control the temperature of the sensor, a system using a Peltier cooler has been chosen. A Peltier cooler, or Thermoelectric cooler, uses the Peltier effect to create a heat flux between its two sides, generating a hot and a cold side. The heat flux on the Peltier cooler is controlled by the current flow through the device. A Peltier cooler was selected to cool the sensor because of its small form factor and its long utility life.

A Peltier cooler does not have any moving parts, which allows the device to safely operate for long periods of time. Other cooling methods require larger equipment, external elements like liquids or gases, and are more prone to mechanical failures or leaks.

In order to allow the heat transfer from the sensor to the Peltier cooler, a copper block was used. The Medipix3RX sensor is glued to the copper block, creating a direct contact with the copper block to optimize heat transfer to the Peltier cooler. The space between the copper block and the Peltier cooler is filled with heat transfer paste, in order to maximize the heat transfer between these elements. A fan is used to cool down the Processing board and the Interface board. Temperature sensors are placed on both the Sensor board and the Interface board to control both the Peltier cooler and the fan.

Temperature sensors are used to know the temperature at several key places in the system and provide readings to the temperature control loop. Three sensing points are used on the design for the control loop: the temperature of the sensor, the temperature of the Peltier hot-side heatsink and the temperature of the electronics on the Processor and Interface boards. The temperature of the sensor is read from the copper block and is the same temperature as the cold side of the Peltier cooler. The temperature of the heatsink is read right under the hot side of the Peltier cooler. The third temperature is read on the Interface Board and represents the temperature of the electronics on the Processor and Interface boards.

Tests completed with the Medipix3RX, in the temperature range of 12 to 24 C, show that lower temperatures result in an improvement in the stability of the pixel response for Medipix3RX using a sensing layer of CdTe [54]. However, reducing the working temperature of the sensor increases the probability of generating condensation on the Medipix3RX. In order to maximize the stability of the pixel response, whilst reducing the risk of condensation, the temperature of 20 C has been selected as the target temperature for the Medipix3RX sensor in the LancelotRX system.

3.3.2 Temperature control system

A closed loop control is needed to maintain a stable temperature, as the power consumption of the Medipix3RX sensor is not constant and depends on the sensor's mode

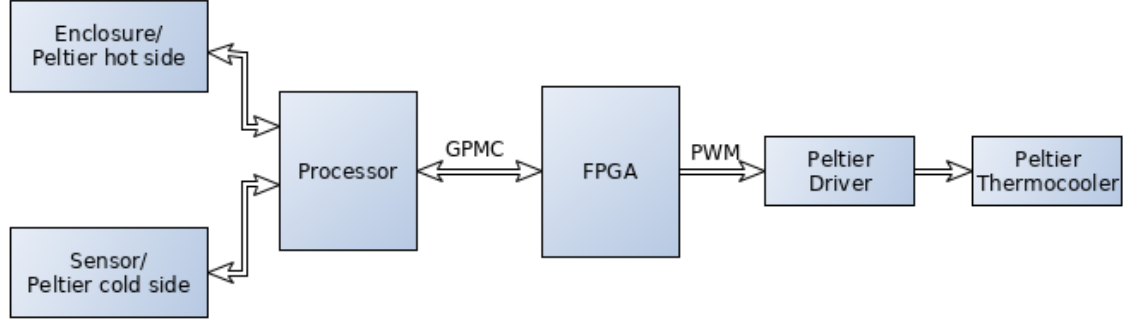


Figure 3.11: Block diagram of the main elements in the temperature control loop. The Peltier driver is controlled by a PWM signal generated in the FPGA, the PWM required duty cycle is calculated by the ARM processor and sent to the FPGA. The control loop takes into account the Medipix3RX temperature and the heatsink temperature.

of operation. To achieve this, a ProportionalIntegralDerivative (PID) control has been selected. The PID control is implemented in software using the ARM processor, with temperature sensors as inputs and the power control for the Peltier driver as the output. As it is shown in Figure 3.11, the Peltier driver is controlled by a Pulse Width Modulation (PWM) signal generated by the FPGA, the duty cycle for the PWM is written in a register of the FPGA by the ARM processor.

To control the temperature on the Medipix3RX sensor, the energy sent to the Peltier cooler has to be controlled. The direct approach is to set an intermittent power supply, to power the Peltier cooler by a power supply enabled by a PWM signal, but this method is not recommended by the manufacturer. Controlling a Peltier by PWM is always less efficient than using DC current. It is shown, that the achievable temperature difference δt and cooling capacity Q are bigger for the constant current method, at the same average power consumption [69].

In order to generate a constant current control, it's possible to use either a linear transformer, or a Switched Mode Power Supply (SMPS). The use of a SMPS has the main advantage of having, in most instances, a greater efficiency than linear regulators [70] based on the ability of the switching transistor to dissipate little power when acting as a switching element. The linear regulator will transform the extra energy into heat, causing the system to heat up. This extra energy transformed into heat is a major disadvantage for controlling the temperature of the system.

To reduce the heat generation, the proposed solution uses a SMPS in a buck topology. The buck converter transforms a high input voltage into a lower output voltage. The classic buck converter can be seen in Figure 3.12. The topology consists of two switches, usually a controlled one, i.e. a MetalOxideSemiconductor Field-Effect Transistor (MOSFET) and an uncontrolled switch, such as a diode. These two switches are used to obtain unidirectional power flow from the input to the output [71]. An inductor and a capacitor are placed on the output of the circuit to store and transfer energy, and to filter the output voltage and current.

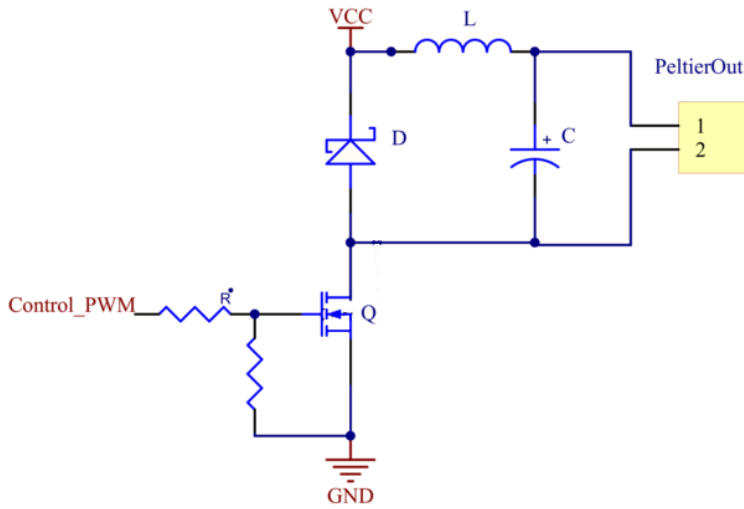


Figure 3.12: Basic circuit of a Buck SMPS converter. A Buck SMPS is used on the LancelotRX system to control the cooling capacity, Q , of the Peltier cooler in order to maintain a stable temperature for the Medipix3RX.

To control the amount of energy sent to the load by the Buck converter, a control signal is used to allow the MOSFET to pass current or not. One approach is to use a PWM for this signal, where the signal has a constant frequency but the time the signal has a high value and a low values changes, this is called its duty cycle. Another option is to use Pulse Frequency Modulation (PFM), where the time the signal is high is always constant, but the time the signal is low is variable, making the frequency of the signal variable as well.

PFM can have an energy advantage for applications of low energy transmission. In cases where the main energy loss of the MOSFET happens due to switching losses (instead of having the main energy loss as the conductive losses), using a PFM method can increase the converters efficiency [72]. For this application the converter will not be

working on low energy transmission, so the increased efficiency of PFM over PWM does not exist. Apart from this, using PFM has the disadvantages that it requires a more complex circuit, it generates Higher Electromagnetic Interference (EMI) than using PWM [73] and the design process is more complex since a wide range of frequencies is used. For all these reasons, PWM has been selected to drive the switches in this design.

3.3.3 Driver Design

To select the correct Peltier cooler and to know the required power, an analysis of steady state has been made to obtain the working point of the Peltier. For this analysis, the plots associated with the Peltier are used to determine the behaviour of the cooler element. The heatsink used for the analysis corresponds to the bottom of the sensor chamber where the Medipix3RX will be placed, which is the main element to dissipate the heat generated by the Medipix3RX and the Peltier. To understand the behaviour of the heatsink, simulations on SolidWorksTM were used and experimental tests were conducted to verify the simulation results. In Figure 3.13, the plot of the steady state temperature rise near the Peltier on the proposed heatsink, for each heat power load is shown.

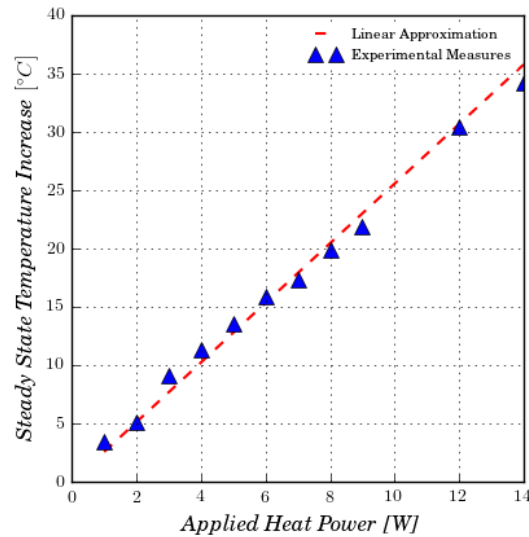


Figure 3.13: Linear approximation and experimental data of the steady state temperature increase in the proposed heatsink for the Peltier. The data was taken at a room temperature of 25 °C. The obtained parameters are used to determine the Peltier working point.

The parameters for the working point computation is a target stabilization temperature of 20 °C for the Medipix3RX sensor, with a proposed tolerance of 0.5 °C. The thermal resistance $R_{heatsink}$ for steady state of the proposed heatsink linearization of 2.556 C/W is used. Figure 3.13 shows the difference between the linearized value and the experimental data. The rest of the used parameters are: the maximum power consumption of the sensor of 1.5 W and denoted as $Sensor_{MaxPower}$, a maximum ambient temperature of 30 °C, denoted as $T_{ambient_Max}$, and a suggested working point for the Peltier of 6 V at 2.4 A using a total of 14.4 W, denoted as $Peltier_{WP_power}$. The suggested working point was obtained from the Peltier performance graph in Figure 3.14, this point is denoted with a S_w mark. With this information, it's possible to calculate the total power dissipated, denoted as $Power_{dissipated}$, with the following equalization:

$$Power_{dissipated} = Peltier_{WP_power} + Sensor_{MaxPower} = 14.4 + 1.5 = 15.9[W]$$

Once the total dissipated power has been calculated, it is possible to obtain the temperature rise of the heatsink, denoted $Heatsink_{T_rise}$ by using the previously obtained thermal resistance. With the temperature rise of the heatsink, the final temperature of the heatsink, denoted $Heatsink_{T_final}$, can be calculated in the following form:

$$Heatsink_{T_rise} = Power_{dissipated} * R_{heatsink} = 14.4 * 2.556 = 36.806[^\circ C]$$

$$Heatsink_{T_final} = T_{ambient_Max} + Heatsink_{T_rise} = 30 + 36.806 = 66.806[^\circ C]$$

The amount of energy needed by the Peltier to maintain a desired Heat flux (Q_c) is dependent on the temperature difference between its cold side and hot side, where the hot side is the heatsink temperature and the cold side is the sensor's target temperature denoted as T_{target} . To obtain the temperature difference (δT) :

$$\delta T = Heatsink_{T_final} - T_{target} = 66.806 - 20 = 46.806[^\circ C]$$

With a δT of 46.806 °C and a needed Q_c of 1.5 W, which is the needed Q_c for steady state since this is the maximum power dissipation by the Medipix3RX sensor, the intersection of these two values in the performance graph in Figure 3.14 is marked with a W_{C1} and shows a current of 1.6 A on the Peltier. With the calculated current value for the Peltier of 1.6 A and the temperature difference of 46.806 °C, it is possible to obtain the voltage of the Peltier using the performance graph, this point is denoted as W_{V1} in Figure 3.14 and it represents a voltage of 4.3 V.

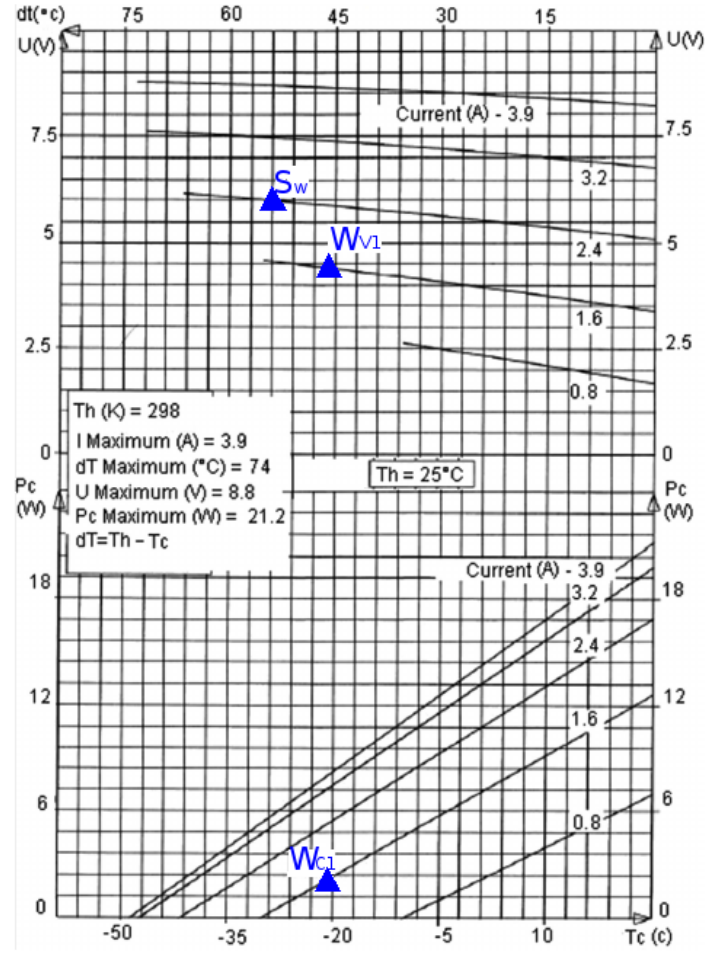


Figure 3.14: Peltier performance graph with annotations, taken and modified from the manufacturer datasheet [7]. The mark S_w is the original suggested working point at 2.4 A and 6 V. The mark W_{c1} is the current of the first iteration obtained working point of 1.6 A with a δT of 46.806 $^{\circ}C$. The mark W_{v1} is the voltage of the first iteration obtained working point of 4.3 V and a δT of 46.806 $^{\circ}C$.

With the new obtained possible working point for the Peltier of 1.6 A and 4.3 V, it's clear that the energy used by the Peltier to obtain the thermal equilibrium desired is less than the original estimate. Using these values as input data, the previous process is repeated until the difference between the heatsink temperatures of two consecutive iterations is smaller than a threshold of 0.5 $^{\circ}C$. The threshold of 0.5 $^{\circ}C$ was chosen as it is the proposed tolerance for the target temperature. By using the proposed threshold, the obtained working point for the Peltier is 0.5775 A and 1.5 V.

3.4 Data flow design for the system

The data flow in the LancelotRX system can be divided into three main sections, the gateway on the FPGA, a server running on the ARM processor and a client running on a personal computer (PC). The FPGA acts as a controller of the Medipix3RX sensor, implementing the readout from the sensor as well as some basic processing of the data. The server running on the ARM processor processes the control loops, controls the FPGA system and communicates with the client program over the network. The client program is how the user can control the LancelotRX system and obtain data from it. Figure 3.15 shows a block interconnection depicting the data flow.

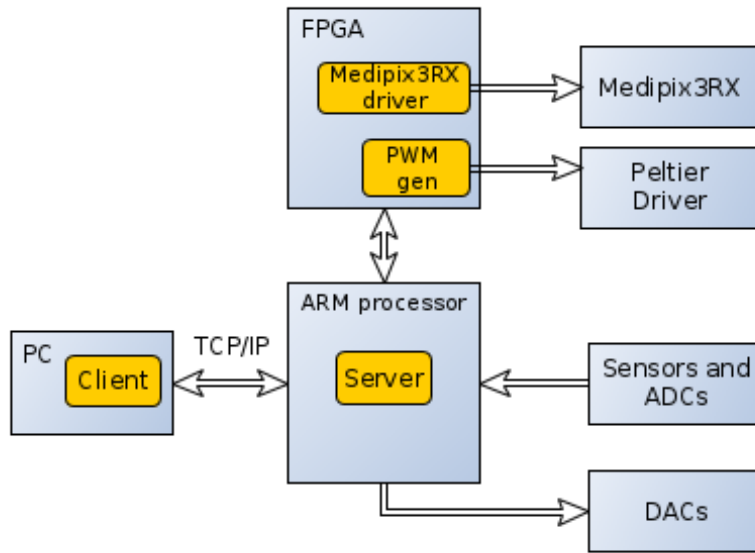


Figure 3.15: Block diagram of the data flow on the LancelotRX system. A client software runs on a PC and connects to the LancelotRX through the network. A server program running on the ARM processor is used to handle the network communication. On the FPGA, the gateway system controls the Medipix3RX and generates the PWM for the Peltier driver.

3.5 Summary

The design of the required electronic system for the LancelotRX system has been presented. The electronics are divided between three PCBs, one for the sensor, one for interconnection and one for the digital processing. The Medipix3RX is placed on a small PCB facilitating the operation of the sensor inside a vacuum chamber. The

use of an FPGA and ARM processor have been selected to implement all the control and readout of the sensor, the processing of the sensor's data and the communication protocol over the network. A temperature control system making use of a Peltier cooler has been presented, as well as the design of a Peltier driver. The electronic architecture presented in this chapter is the platform where the gateware and the software, discussed in Chapter 4 and Chapter 5 respectively, is implemented.

Chapter 4

Gateway design for the LancelotRX

Gateway is the system implemented on the FPGA using a hardware description language. The gateway system is how the readout and processing of the Medipix3RX data is implemented, as well as generating a PWM signal and interrupts. In this chapter, a full description of the gateway is presented. The chapter starts by explaining the main blocks of the gateway and its interconnections, afterwards, each block is explained in detail. The chapter finishes by explaining the signals' timing to control the sensor, as well as the data processing of the acquired images.

4.1 Gateway architecture

A FPGA is used to control and communicate with the Medipix3RX sensor. The FPGA has been chosen with the intention of achieving a faster communication rate and processing speed of the obtained images, for a high frame rate. A complex logic design is required with different processing stages and actions to be performed in parallel. To facilitate this design process, an Altera Quartus tool called Qsys is used. Qsys generates a system by building blocks or modules, some modules are available from a standard Altera library, but the majority of the modules used in this design have been developed specifically for this application.

The logic design implemented using a FPGA will be referred to as 'gateway' to differentiate it from the executable software or firmware and from the electronics. The

gateway can be divided into four principal blocks: a block for communication between the ARM processor and the FPGA, a block for generating a PWM signal and enable lines, a block for interrupt management and a block to handle communication with the Medipix3RX sensor and processing of the sensor's data. The main blocks and their connection to physical devices outside the FPGA are shown in Figure 4.1.

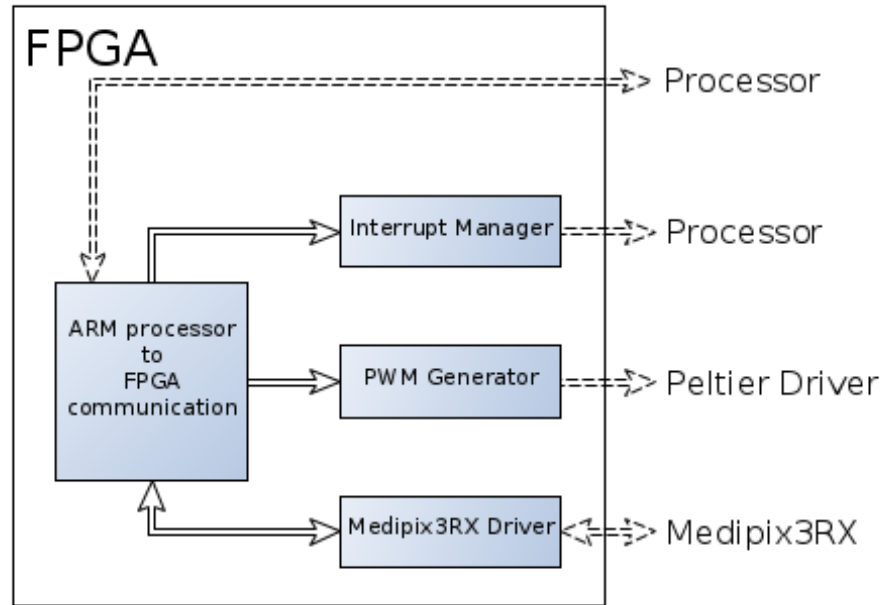


Figure 4.1: Main blocks of the gateway system implemented on the FPGA. The main tasks of the gateway system can be divided into communication with the processor, interrupts generation, PWM signal generation and control and process of the data acquired from the Medipix3RX sensor.

The processor uses the communication block to control the Interrupt Manager, PWM Generator and Medipix3RX Driver blocks. The processor controls the Medipix3RX throughout the Medipix3RX Driver block. The data from the Medipix3RX is read by the Medipix3RX Driver, processed and stored into memory. The Interrupt Manager notifies the processor when the Medipix3RX Driver has finished an operation. After the processor has been notified, the processor retrieves the processed data from the memory. The processor sets the PWM signal used for the Peltier driver through the PWM Generator block. These principal blocks are implemented in the gateway as Qsys modules.

All the modules on the gateway are designed with the same standard and have common characteristics, this allows for a flexible system design that can be used for different applications and platforms. All the modules have a unique id number that

the processor uses to identify the modules available on the system. There is a status register and a control register on all the modules, with the same offset address, in order to make the control of the modules from the processor a standard method. The processor handles the gateware as if it was memory. The access to the modules are memory mapped, enabling the processor to access specific modules on the gateware by using different memory addresses. All the modules are connected to a general reset master so one reset command from the processor resets all the modules simultaneously. In Figure 4.2 the gateware, represented in Qsys modules, is shown.

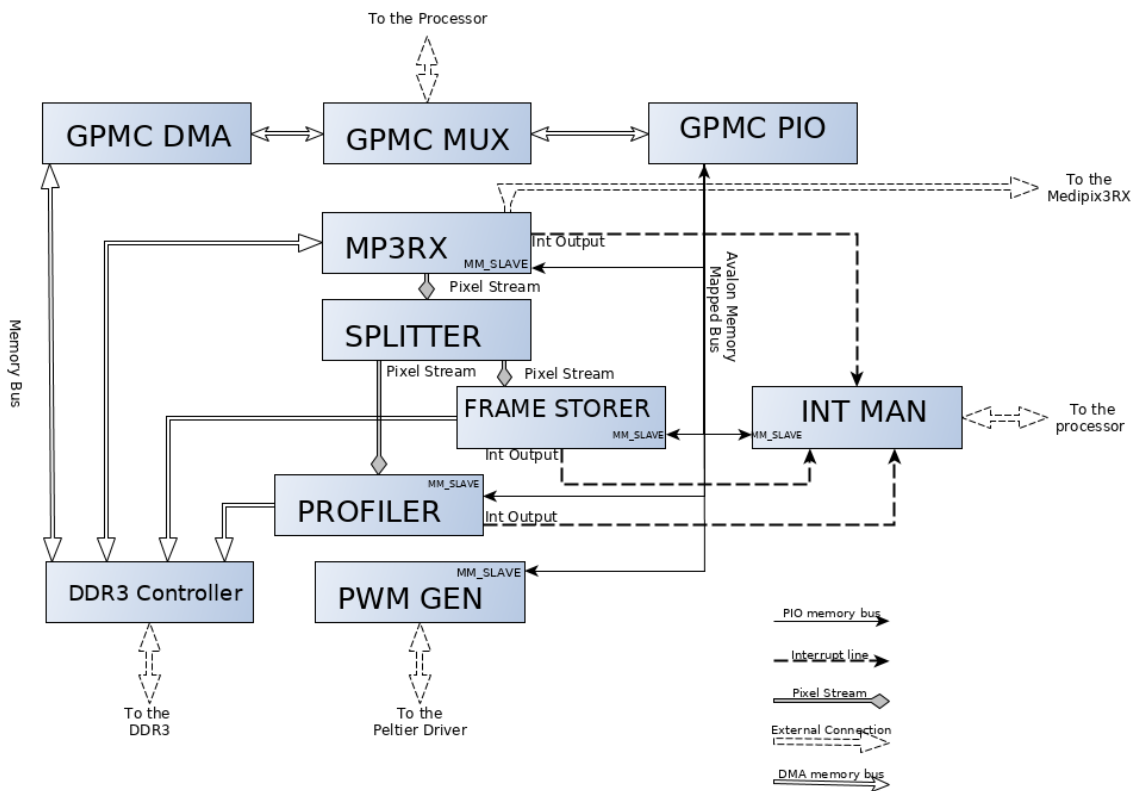


Figure 4.2: Qsys modules that form the FPGA system. The data flow direction can be seen with the direction of the arrows. The communication from internal blocks to external devices outside of the FPGA are shown.

The interface between the processor and the FPGA is achieved through the GPMC of the AM335x processor. Thus for the processor, the FPGA is behaving like a memory mapped device, where the processor can read and write data to different memory locations. On the FPGA system the communication to the processor through the GPMC is implemented using three modules, the multiplexer (*GPMC_MUX*), the programmed input/output (*GPMC_PIO*) and the direct memory access module

(*GPMC_DMA*). The interconnections between these three modules used for communication with the processor are shown in Figure 4.2. The data from the processor goes to *GPMC_MUX*, this module directs the data flow to either the *GPMC_PIO* or to the *GPMC_DMA* modules. The *GPMC_PIO* module is used for non-consecutive reads and writes to the FPGA system from the processor, setting the memory address for every read or write action. The *GPMC_DMA* module is used for consecutive reads or writes, having an improved transfer speed for big blocks of data. The *GPMC_DMA* module is connected to the DDR3 controller, used to interface to a dedicated memory buffer. The *GPMC_DMA* module provides the data path used by the processor to read and write data from the DDR3 memory. The *GPMC_PIO* module is connected to other modules allowing the processor to read and write data into the module registers.

The Medipix3RX interface module depicted in Figure 4.1 can be broken down into several sub-modules. A block diagram of these sub-modules used for the Medipix3RX sensor data acquisition and processing is shown in Figure 4.3. The module that communicates with the Medipix3RX sensor is called the *MP3RX* module. This module is used to configure the sensor, to control the actions of the sensor, to readout the images and to convert them into a stream. The streaming protocol used is the Avalon Video Stream Protocol designed by Altera and used in their modules [74]. Using a video stream allows the processing of the images to be pipelined or made parallel, by splitting the stream into two or more identical streams.

The *Profiler* and *Frame_Storer* modules work in parallel with the same image, each module takes data from one of the two identical streams going out of the *Splitter* module. The *Frame_Storer* module saves the stream image into the DDR3 memory, where the processor can read it using the *GPMC_DMA* module. In parallel to the *Frame_Storer*, the *Profiler* module processes the image and generates both the column's and row's profiles of the image.

As part of the LancelotRX system, a Peltier cooler is used for controlling the temperature of the Medipix3RX sensor, and a high voltage power supply will be used to generate the high voltage required by the sensor to work. The signals used to control the Peltier and to enable or disable the high voltage power supply are generated in the FPGA system. The module *PWM_GEN* generates the signals for the Peltier and high

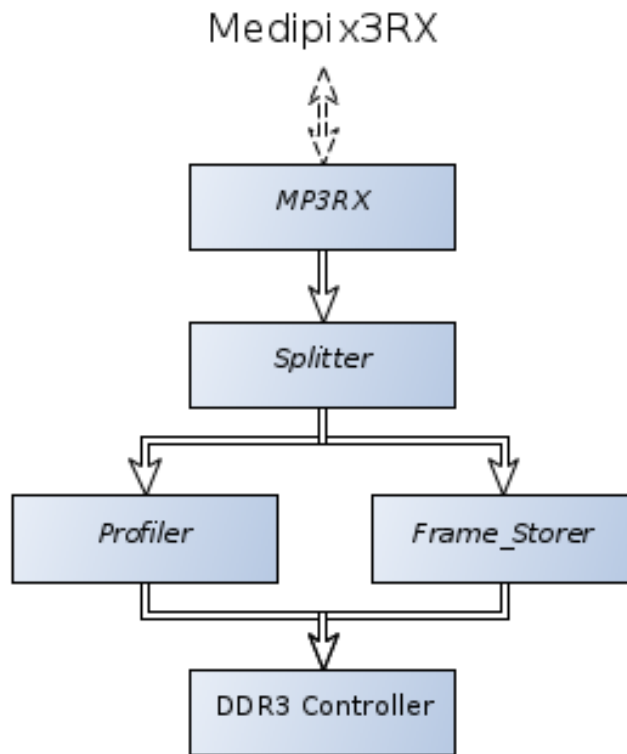


Figure 4.3: Block diagram of the data flow from the Medipix3RX sensor to the DDR3 memory. The *MP3RX* module reads the data from the sensor and generates a pixel stream, which passes a *Splitter* module, converting the stream into two parallel streams that feed the *Profiler* and *Frame_Storer* modules. Both the *Profiler* and *Frame_Storer* modules save the obtained data into the DDR3 memory.

voltage power supply and it is controlled by the processor through the *GPMC_PIO* module.

In order to achieve an efficient system running on the processor, the use of polling for status bits should be avoided and a more efficient method should be used. Constant polling increases the load on the processor reducing its ability to complete other tasks while waiting for the FPGA. If the polling is not constant, delays between polling can be generated. This delay time between the moment when a task has been finished on the FPGA and when the processor is notified, can cause speed reduction of the whole system. To improve performance, an interrupt system was implemented on the FPGA design. Using interrupts is a faster way to notify the processor that a task has ended and it allows the processor to complete other operations while the task is executed on the FPGA system.

To manage the generated interrupts and to fine tune the interrupt characteristics

in order to work correctly with the processor's interrupt subsystem, an interrupt manager module named *INT_MAN* has been developed. This module can be configured from the processor through the *GPMC_PIO* module, so the output interrupt signal characteristics can be set. The outputs of this module go directly to general purpose I/O pins of the FPGA that are connected to interrupt receiving capable pins on the processor.

There are different clock domains used on the FPGA system. There is one physical clock on the ARMFlash mini board that is a 25 MHz oscillator, which is used as an input to a Phase-Locked Loop (PLL) module, which transforms it into a 150 MHz and a 75 MHz clock. The 150 MHz clock is the one used for most of the logic and the DDR3 controller. The clock used for the communication interface with the sensor is the 75 MHz clock. This frequency was chosen so the readout is fast enough to achieve 1000 frames per second rate.

From the used modules on the system, the *Splitter* module and the *DDR3Controller* module are Altera Quartus IP, the settings for these modules have been tuned for the needs of the design, but the source code has not been changed. The GPMC modules, the *Profiler* and *Frame_Storer* modules have been written by the research group. The GPMC modules have not being modified for this project, but the *Profiler* and *Frame_Storer* module required changes to fulfil the requirements for this project. The *Frame_Storer* module required changes in order to allow an 8-bit depth for the pixel values, which was needed to enable a padded 6-bit depth pixel value, which is a feature of the Medipix3RX. The *Profiler* module was not working correctly due to some internal synchronization issues, these problems were solved for this work. The *MP3RX*, *PWM_GEN* and *INT_MAN* modules were entirely designed for this system, they are written following the control protocols and memory mapped standards used on all the research group modules, so they could be ported to other FPGA system designs. The objective is to have an FPGA design that will satisfy the requisites of this work, but also to develop a system that is capable of expansion in order to control more Medipix3RX sensors simultaneously in the future. By using the same standard as other modules developed by the research group, the modules designed in this work could be used for future projects with different sensors and new applications.

4.2 PWM_GEN - module for generating a PWM and enable lines

The *PWM_GEN* module is used to generate signals for the Peltier driver and the high voltage power supply on the interface board. The module is controlled by the processor through a control register and a status register, where the processor can read back the current operations of the module. The module uses the main 150 MHz system clock and is connected to the global reset line. After a reset pulse the module sets the outputs to the default state of logic 0.

4.2.1 Generation of the PWM signal

The module can generate a PWM signal, which is a pulsed signal where the amount of time the signal is on can be changed without changing the frequency of the signal. The module has been designed to generate a PWM signal with a frequency of 100 kHz. The duty cycle of the PWM has a range from 0 to 100% in steps of 0.067%. To control the duty cycle of the PWM signal the processor writes to the control register on the module. Once the PWM duty cycle has been changed, the effect will be set on the output signal on its next cycle. To generate the PWM signal, the output of a free running counter is compared against the duty cycle set by the processor. While the value of the set duty cycle is bigger then the free running counter, the PWM output will have a logic 1 output. An ‘enable_output’ bit on the control register grants the option of disabling or enabling the PWM output at any moment.

4.2.2 Generation of the enable lines

This module generates two enable signals that will be used on the interface board to enable the high voltage power supply and the Peltier driver. Both lines are set low by default or after a reset, turning off the Peltier and high voltage power supply. To set these lines high, the processor writes to the control register of the module.

4.3 INT_MAN - module to manage the interrupts

Some modules on the FPGA system require an interrupt output, which will be sent to the processor. These modules are the ones that execute tasks with long execution times that may directly affect the performance of the processor. An interrupt output has been implemented into the *MP3RX* module, the *Frame_Storer* module and into the *Profiler* module. All of these modules generate an interrupt every time a task is completed. The generated interrupt signal is the same for all the modules and it is a high active interrupt that lasts for 5 clock cycles of the clock that is fed into the module.

The FPGA system has three modules that generate interrupt signals, but the ARMFlash mini board only has two lines from the FPGA outputs to direct interrupt inputs on the processor. In order to solve the requirement of more interrupt lines to the processor and to generate a more versatile design that will allow an easier expansion of capabilities, an interrupt manager has been designed.

The interrupt manager module has as inputs the interrupt outputs from the other modules and allows configuration of the behaviour of these interrupts to the processor. It is important to have the capability to change the behaviour of the interrupts in order to create a flexible system. By having a flexible system, adding new features or porting the system to new hardware, becomes easier. The characteristics of the interrupts that the interrupt manager can modify are: polarity, enable/disable interrupts, duration of the interrupt, latched or non-latched, clearing mode and to summarise interrupts.

4.3.1 Controllable characteristics of the interrupts

Polarity - Set the polarity of the interrupts to the processor, if they are low-active or high-active. This feature grants versatility to the design by enabling it to work with different processors and other hardware.

Enable/disable interrupts - It is possible to enable or disable each one of the input interrupts to the interrupt manager from the processor. By doing this, the processor can select which interrupts will pass through the interrupt manager and get to the processor.

Latched or non latched - The behaviour of the interrupt can be configured to be latched or non-latched. A latched interrupt is one where the interrupt signal keeps the active value of the interrupt until the processor clears the interrupt. There is a source interrupt register where the processor can read which interrupts have been fired.

Duration of the interrupt - If the interrupts behave as a pulse (non-latched), then the duration of the pulse can be set on the interrupt manager. This feature can be useful if there is a hardware migration of the system since different processors can have a different minimal pulse duration for the interrupt triggers.

Clearing mode - The way in which the processor clears the interrupt can be set to the Interrupt manager. The interrupts can be cleared once the interrupt source register has been read, or the interrupts can be cleared after a write command to the interrupt source register.

Summarise interrupts - Because physical connection lines between the FPGA and processor can be a limitation for adding new interrupts, the interrupt manager is able to summarise any amount of the input interrupts to one of the output interrupts. This way, the same interrupt line on the processor can be used to sense several different interrupts. Once this interrupt has fired, the processor needs to read the interrupt source register to find which of the summarised interrupts was the one that was triggered.

4.4 MP3RX - module for control and readout of the Medipix3RX

The *MP3RX* module is constructed by two sub-modules, the *OMR_Handler* and the *Unscrambler*, which are shown in Figure 4.4. The *OMR_Handler* sub-module is where the main state machine is located, the sub-module has access to the control lines of the Medipix3RX and to the DDR3 memory controller. The control lines are used to configure and control the operation of the sensor, while the access to DDR3 memory is needed to move configuration data between the processor and the sensor. The *Unscrambler* sub-module is used to read the image data from the sensor, rearrange

the obtained data into pixels, decode the LFSR counter and send the pixel values down the pixel stream.

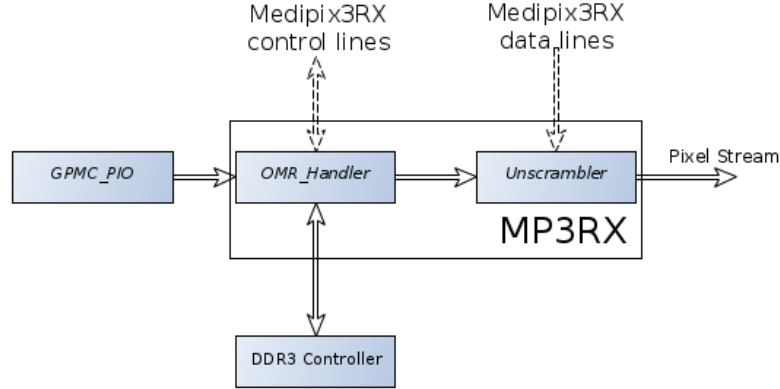


Figure 4.4: Block diagram of the sub-modules used in the *MP3RX* module. The sub-modules are *OMR_Handler*, which accesses the sensor’s control lines and the DDR3 memory, and the *Unscrambler*, which has access to the sensor’s data lines and generates the pixel stream that is used by the *Frame_Storer* and the *Profiler* modules.

4.4.1 OMR_Handler sub-module to control the Medipix3RX

The Medipix3RX sensor is controlled mainly by a 48-bit register called OMR, the configuration bits and positions of the OMR are shown in detail in the Appendix A.3. For every operation to be executed by the sensor, the OMR has to be loaded first. The values of the OMR bits are passed from the processor to two 32bit wide registers on the *OMR_Handler* through the GPMC communication, the sub-module then sends the OMR bits serially to the sensor. The values for the OMR written on the *OMR_Handler* registers are also used to control the main state machine on the sub-module, this way, the amount of data needed to control the *MP3RX* module is reduced.

As shown in Figure 4.5, to initiate an operation, after the OMR has been loaded to the OMR registers on the *OMR_Handler*, the ‘Control.Operation’ bit on the control register of the *MP3RX* is set high, which will activate the state machine on the *OMR_Handler* to do all the necessary steps to complete the operation loaded to the OMR. The *MP3RX* module also contains a status register in which a ‘Busy’ bit is set high while an operation is taking place on the module, this feature is checked by

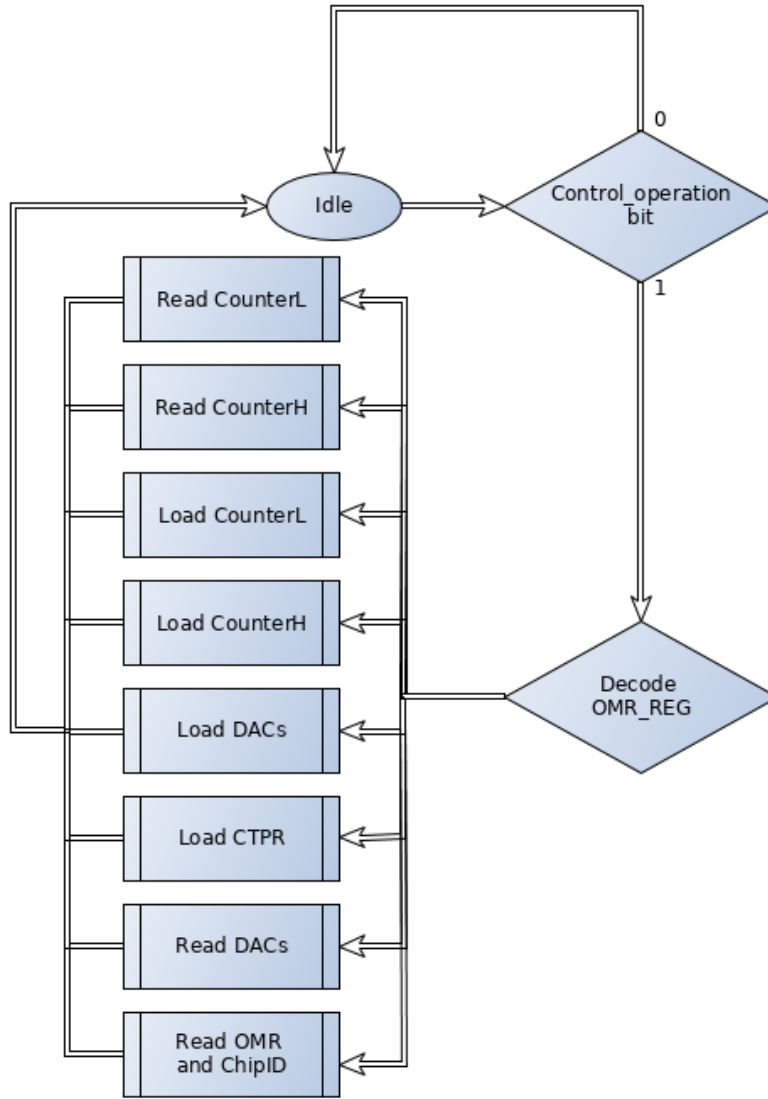


Figure 4.5: Main state diagram for the *OMR_Handler* sub-module on the *MP3RX*. The bits of the OMR written into the registers is used to decode which set of actions the *OMR_Handler* has to execute, as well as to send the OMR bits to the sensor to control its operation.

the processor before starting an action, to ensure that two action commands are not executed simultaneously.

Setting and reading the values from the DACs and CTPR

The process to configure the DAC values or the CTPR values into the sensor is shown in Figure 4.6. The values of the CTPR or DACs are written from the processor into a specific memory location on the DDR3, these memory locations can be seen on the memory map for the DDR3 in Figure 4.7. When an action to set the DACs

or the CTPR is started on the *OMR_Handler*, the sub-module reads the required information from the DDR3 memory and buffers it into a register before sending it to the sensor. Reading the DACs or CTPR is the same process, and the data read from the sensor is stored in the same locations on the DDR3 memory so the processor can access the DACs or CTPR values.

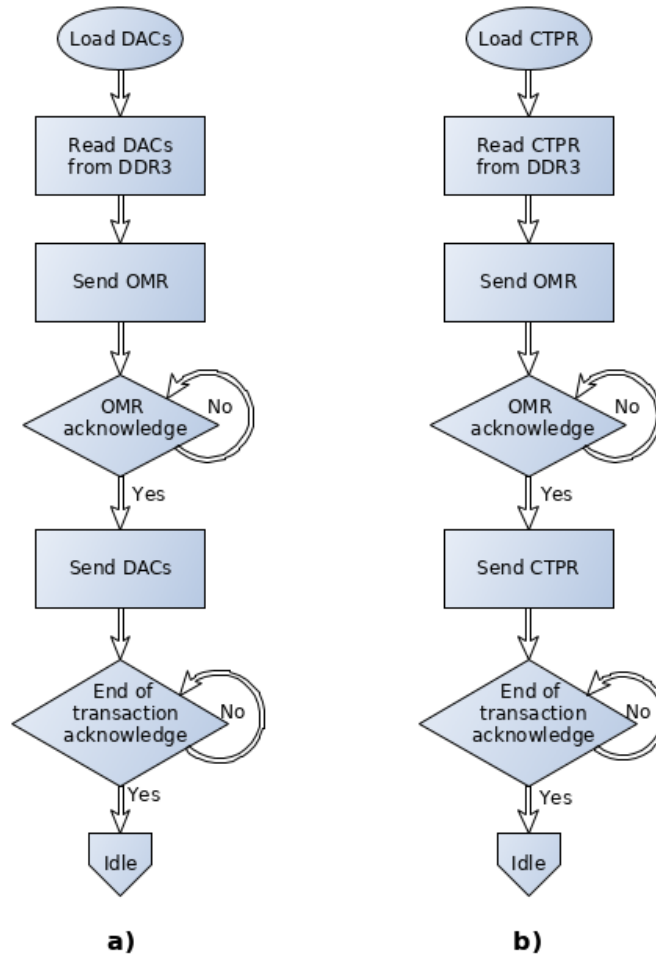


Figure 4.6: Flowcharts in the *OMR_Handler* sub-module for setting the DACs (a) and the CTPR (b) into the sensor. The same process is used to read the DACs and CTPR. Waiting for an acknowledgement from the sensor is used to ensure that the communication is correct and that protocol timings are kept.

Sending the configuration matrix to the Medipix3RX

As explained in Chapter 2, the Medipix3RX sensor requires that each pixel is configured individually. For each pixel, 12-bits are required for the configuration. The

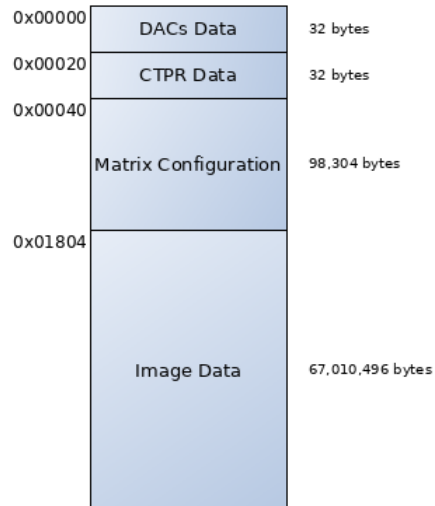


Figure 4.7: Memory map for the DDR3 memory used by the gateway design. The memory is used to store the values of the DACs, the CTPR and the matrix configuration for the Medipix3RX. The last block of memory is used to store read images.

configuration matrix is composed by all the 12 configuration bits for each pixel, creating a set of $256 \times 256 \times 12$ bits of data. This matrix is uploaded to the sensor using serial communication, and the entire matrix has to be sent at the same time, no partial changes can be done.

The communication protocol of the sensor enables the configuration matrix to be sent in parts, with a waiting time between parts defined by the driver of the sensor. The configuration matrix can be sent in blocks of 128 rows, 64, 32, 16, 8, 4, 2, and one pixel row at a time. There is a minor bug in the Medipix3RX that prevents the sending of the configuration matrix in one block to work, so the configuration matrix has to be sent in parts for it to work properly [8]. Even when the configuration matrix is sent in blocks, the entire configuration matrix has to be sent, it is not possible to modify the configuration bits of just a section of the image without sending the rest of data.

Figure 4.8 outlines the procedure required to set the configuration matrix into the sensor. The configuration matrix information is handled in the processor, this data is then stored in the DDR3 memory to a specific location from where the *OMR_Handler* sub-module is able to retrieve it. The data is rearranged in the processor as it is being written to DDR3 memory to have the bit order per pixel line that the sensor requires. After that, the *OMR_Handler* sub-module can retrieve the data from the DDR3 in

the required order and shift it out serially to the sensor without the need to rearrange it. The process starts by sending an OMR with the bits for loading a configuration matrix which also details how many blocks will be used to configure the whole pixel matrix. After that, the first block of configuration data is sent, then there is a wait state until the sensor acknowledges the transferred data. At least 5 clock cycles of the sensor clock have to pass before the next transaction is started. This process is repeated until every block of configuration data is sent. The *OMR_Handler* sub-module is designed to send the configuration data in two blocks of 128 pixel rows each. Using two blocks was selected to increase the speed of the configuration process. Each block requires a pre-sync and post-sync, making the use of more blocks a longer process.

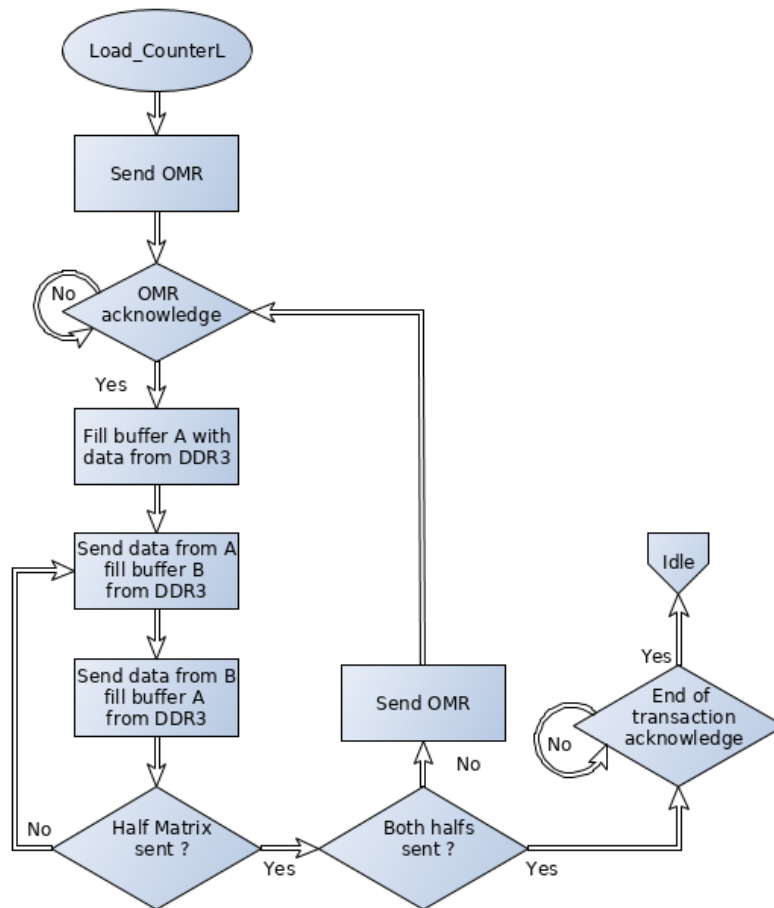


Figure 4.8: Flowchart of the *OMR_Handler* sub-module actions to upload the configuration matrix into the Medipix3RX. The configuration data is read from the DDR3 where the processor has set it. The configuration data is read using two buffers, while data from the DDR3 is moved into buffer B, the buffer A data is sent to the sensor. The implemented method sends the configuration data using 2 data blocks.

The FPGA design has two buffers to store the data from the DDR3, as one buffer is used to shift out the data in a serial communication, the second buffer is being filled with data from the DDR3. To read from the DDR3 a burst of 8 words of 32 bits each is used, getting 256 bits in each burst. This data readout requires approximately 70 clock cycles of the main clock of 150 MHz. The readout from the DDR3 is much faster than the process of sending the data serially to the sensor at the sensor clock rate (75 MHz). Therefore, there is enough time for one register to be filled while the other register is being shifted out. In Figure 4.9 the buffer filling and sending data to the sensor timings are shown.

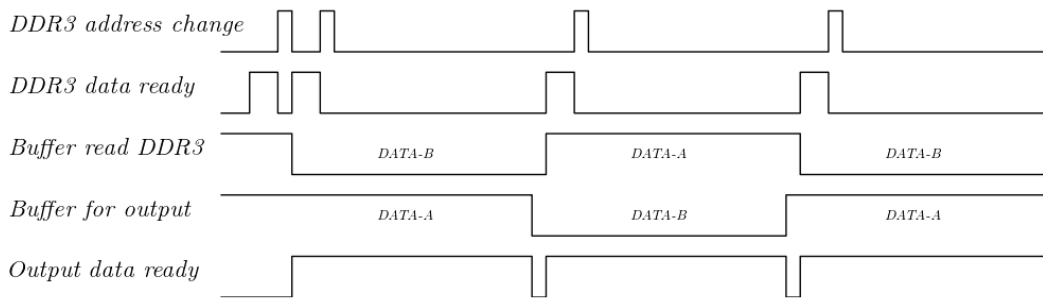


Figure 4.9: Timing of the matrix configuration data being readout from DDR3 memory and sent into the sensor. The signals show the behaviour of single bit flags used to illustrate the timings of the process. Data ready signals are high when data is being transferred.

The configuration matrix is read from the DDR3 memory, stored in two 256-bit wide buffers called DATA-A and DATA-B and then sent serially to the sensor. The signal ‘*DDR3 data ready*’ is high while a transfer of data from the DDR3 to the buffer is performed, while the signal ‘*Output data ready*’ shows the time required to move the same amount of data from the buffer on the FPGA to the sensor. The time needed to send the data to the sensor is approximately 7 times the time required to read data from the DDR3 into the buffers, this time difference is caused by the amount of lines available for the communication and the clock domain in which the communication operates. The time required to read data from the DDR3 isn’t constant due to the arbitration process done on the DDR3 PHY controller, but the time required is always less than the time used to send data to the sensor.

Continuous and non-continuous acquisition modes

In Figure 4.10, the flowchart to acquire a frame from the sensor is shown. Before the process starts, the integration time is written by the processor to a register on the FPGA design. The acquire process starts when the OMR registers are set with the bits for acquisition. After this, the processor sets the Control_Operation bit and the MP3RX module starts the process to obtain an image. The OMR is sent to the sensor and an acknowledge is read back, following this, the Shutter line on the sensor is set high, opening the digital shutter on the sensor and starting the photon counts in the pixels. Once the previously set integration time has passed, the Shutter line is cleared and a pre-sync command is sent to the sensor, which responds with the readout data. This readout data is obtained by the *Unscrambler* sub-module which buffers it, rearranges the bits and sends it in an Avalon Streaming protocol to the next modules.

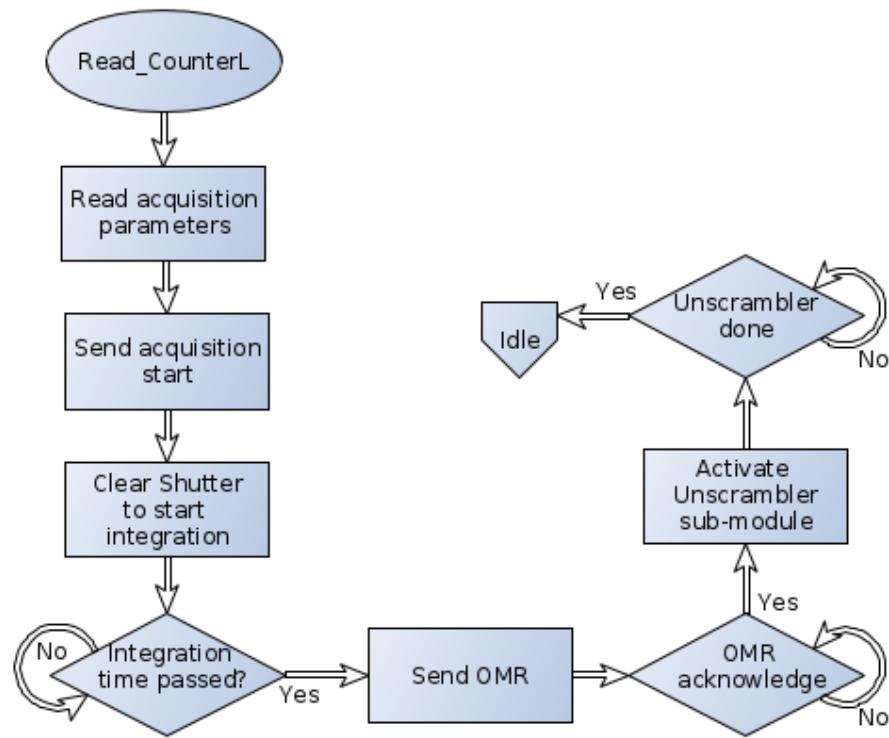


Figure 4.10: Flowchart for the process of acquiring one image from the Medipix3RX in non-continuous mode. When the acquisition starts, the *OMR_Handler* sub-modules activates the *Unscrambler* sub-module, to start reading data from the data lines and generate the pixel stream.

The Medipix3RX sensor has the option of taking continuous images. For this, the sensor uses its two individual counters of 12 bits. While one of the counters is

integrating the image, the other counter can be read out. After the integration time has passed, the role of the counters is swapped and a new image is taken. This enables a readout without dead-time between images. This feature can be useful in scenarios where the desired phenomenon appears for a very short time span, so it could be lost in the readout dead-time between two images. The maximum frame rate is still limited by the readout time, since a new image can't be taken until the old one is fully read.

In order to control the continuous acquisition, the *MP3RX* module has the option of setting the sensor to acquire an image in parallel to the readout of one of the counters on the sensor, this process is shown in Figure 4.11. The ‘*Shutter*’ signal is activated by setting it low, since it's a negated signal, and it stays like that throughout all the continuous acquisition process. Once the integration time has passed, the line ‘*Shutter CS*’ is set to low, indicating to the sensor that the incoming photons must be counted on the high counter. While the high counter is active, the *MP3RX* module sends a pre-sync command to start the readout of the low counter. When a new integration time has passed the ‘*Shutter CS*’ line is set high so the incoming photons are counted into the low counter and the readout of the high counter starts. This process gets repeated as long as the continuous acquisition is used.

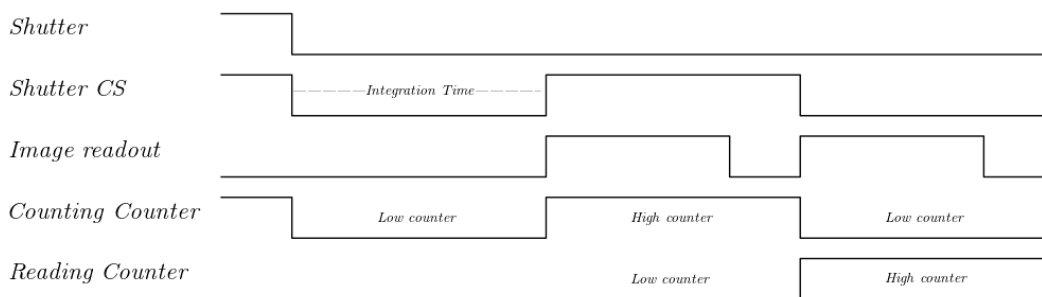


Figure 4.11: Timing Diagram of the continuous acquisition. The *Shutter* line stays down while images are being taken and *Shutter CS* line is used to alternate which counter is used for readout and which one for counting the incoming x-ray photons. The *Image readout* line shows that the time used for readout must be shorter than the integration time.

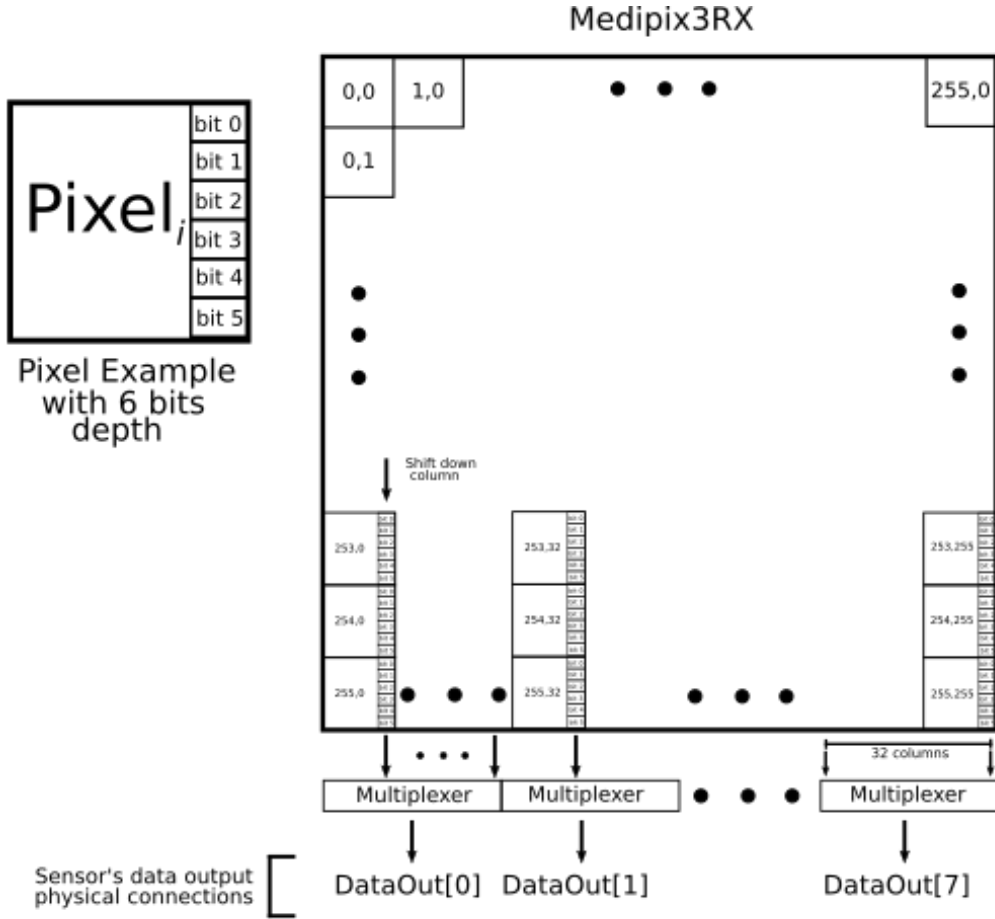
4.4.2 Unscrambler sub-module to decode the Medipix3RX data

The *Unscrambler* sub-module obtains the raw readout from the Medipix3RX sensor, sets the bits in the correct order of the pixels values and changes these values from the LFSR to hexadecimal. This module generates the timings to transform the 8 bits at 75 Mhz data-rate from the Medipix3RX sensor, to the intermittent rate of 6 or 12 bits at 150 MHz pixel values that will be sent in the Avalon Streaming Protocol.

Bit rearranging from the sensor's data lines to pixels

The Medipix3RX sensor has an uncommon data output format, the data flow is shown in Figure 4.12. The data output of the sensor is not done in pixel structure, the system has the pixels aligned in columns of shift registers, each column has only one output, and all the bits for the entire column of pixels are shifted and sent serially through this output. The pixel shift registers are wired in such a way that the first bit to come out represents the most significant bit of that pixel, then the next bit and so on until the less significant bit of the pixel is sent. After this, the most significant bit of the next pixel is sent. This process gets repeated until all the pixels have been sent. This is the procedure for each column of pixels, the sensor has 256 columns like that, but only 8 parallel lines for the data output. The output on those 8 lines is the multiplexed output of the pixels columns.

Even when the pixels are arranged into columns, the actual readout of the sensor is done in rows. Each column of pixels has only one output, and all of these outputs will be read. The first output represents all the most significant bits of the pixels of the first row, and then all the columns will shift one bit, so the second most significant bit of the first row of pixels can be read. The columns output are multiplexed through the 8 parallel lines with an offset of 32 columns between each parallel line, in such a way that at time t_0 $DataOut[7]$ has the value for $Column_0$, $DataOut[6]$ has the value for $Column_{32}$ and so on for the rest of the lines. The next clock cycle of the sensor clock t_1 , $DataOut[7]$ will have the data corresponding to $Column_1$ and $DataOut[6]$ to $Column_{33}$. To have all the most significant bits of a row, 32 clock cycles of the sensor clock are required.



Output example:

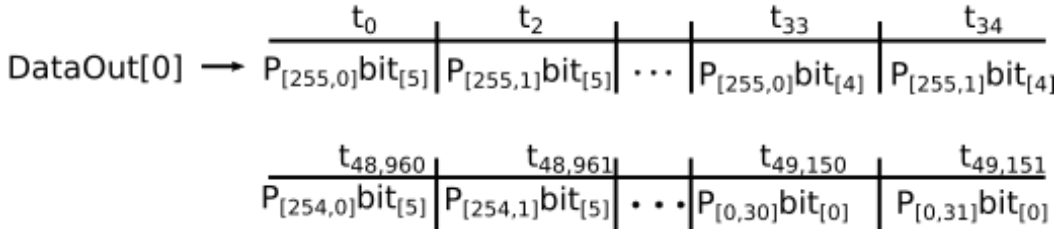


Figure 4.12: Graphical representation of the data output format on the Medipix3RX for the 6-bit pixel mode.

To obtain all the bits for a row of the sensor matrix $32 \times 6 = 192$ or $32 \times 12 = 384$ clock cycles from the sensor clock are required, depending on the pixel bit depth. The *Unscrambler* sub-module stores the incoming bits in specific positions of a data structure, so that they can be rearranged into pixel values of either 6 or 12 bits. The full value of the pixels will only be obtained when a full pixel row has been read, at this stage the pixels' values will be passed to the LFSR decoder.

Decoding the LFSR counters from the Medipix3RX

The Medipix3RX sensor uses LFSR as the counting circuit for the pixel sensor logic. The value obtained for each pixel in the bit rearranging is not on a binary numeral system, so it must be decoded from the LFSR counter to a binary numeral system. To decode the LFSR counter, two Look-Up Tables (LUT) were implemented. In this case, each pixel uses either 6 or 12 bits, therefore, there are either 64 or 4096 possible values, the two LUTs implemented are of 64 and 4096 entries. An example of the first five entries for the 6 bit LUT is shown in Table 4.1. The reason behind using LUTs is to improve the speed of the decoding process. Another option would have been to implement the LFSR counter equal to the one used on the Medipix3RX pixels. By counting the increments on the LFSR counter and comparing the output with the pixel value, it's possible to obtain the binary value of the pixel using less memory space of the FPGA, but this process requires more time than the LUT option.

LSFR Input		Output Value
6'b000000 : LUT_decode_out	<=	6'b000000
6'b000001 : LUT_decode_out	<=	6'b000001
6'b000011 : LUT_decode_out	<=	6'b000010
6'b000111 : LUT_decode_out	<=	6'b000011
6'b001111 : LUT_decode_out	<=	6'b000100

Table 4.1: First five values LFSR decoding table for the 6-bit depth pixels. The *Unscrambler* sub-module has both a 6-bit and a 12-bit LFSR decoding LUTs, enabling the decoding in only a few clock cycles.

Image acquisition timing

The image data is stored in two buffers in the *Unscrambler* sub-module, while one buffer is being filled with data from the sensor, the other buffer is decoded and sent in the pixel stream. A flowchart of the acquisition process, storing the data in buffers and decoding the pixel values to be sent into the stream is shown in Figure 4.13.

In the gateway system, a combination of three different clock domains is used. A 25 MHz oscillator is used to feed a PLL and generate a 75 MHz and a 150 MHz clock signals. The Medipix3RX sensor outputs 8 bits of data each clock cycle using a 75 MHz clock, while in the gateway system an Avalon Stream of 6 or 12 bits pixels at a rate of 150 MHz is used. Because the pixel stream rate on the gateway system is faster

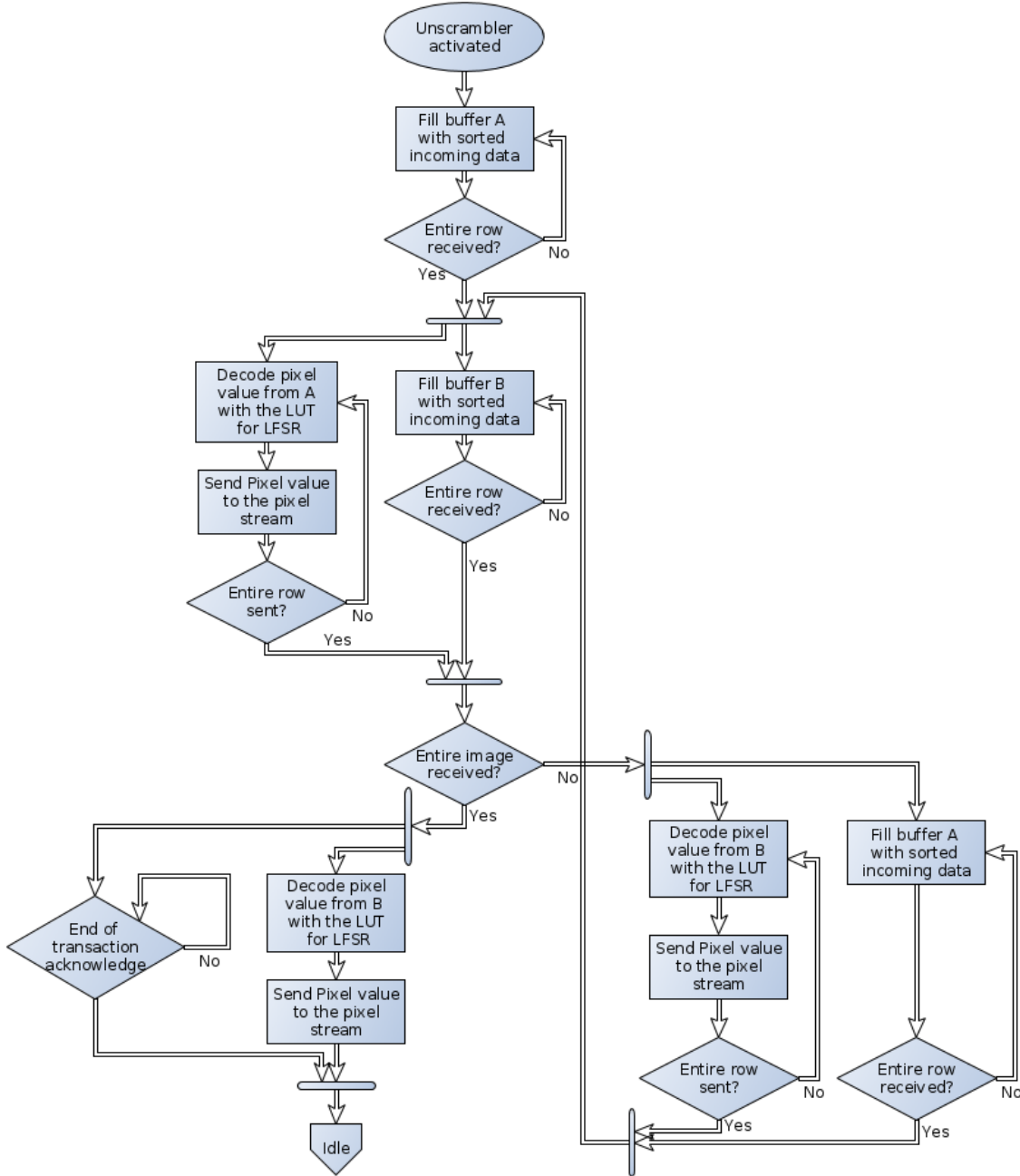


Figure 4.13: Flowchart of the image acquisition in the *Unscrambler* sub-module. Once the sub-module has been activated, the buffer A starts being filled with sorted incoming data from the data lines of the Medipix3RX. Once the buffer A has been filled with an entire row, the new incoming data is stored in the buffer B while the data from the buffer A is decoded by the LFSR LUT and sent into the pixel stream. Filling one buffer and decoding the data in the other is done in parallel, as depicted by the parallelization bars, where an arrow flow is divided into two arrows.

4.4. MP3RX - MODULE FOR CONTROL AND READOUT OF THE MEDIPIX3RX97

than the output of the Medipix3RX sensor, a system of bursts is used to synchronize both speed rates. It is not possible to have both at the same clock cycle, for example 75 MHz since the data output from the Medipix3RX sensor is 8 bit parallel and the pixel depth is either 6 or 12 bit. Inside the gateway system, the design convention is to use a stream of pixel values, all other modules are written following this convention. Using bit packing or breaking the pixel values into smaller blocks would mean that all the other modules have to be modified as well. Because of this scenario, using full pixel values for the stream and different clock domains was chosen.

The timings of the full readout process are shown in Figure 4.14. On the first stage, all the incoming bits from the sensor to the *Unscrambler* sub-module are arranged in a structure (structure A) having 256 pixels of 6 or 12 bits depth for each pixel. After the first 256 pixels have been read, the incoming data is stored in structure B, until the equivalent bits to 256 pixels have been read. This means that while one structure is being filled, the other is ready for LFSR decoding and sending the pixels on the Avalon Stream. This part of the system works in a pipeline manner, after the first row of pixels has been sent from the Medipix3RX sensor, obtaining the data output from the sensor and sending pixels to the Avalon stream is done in parallel.

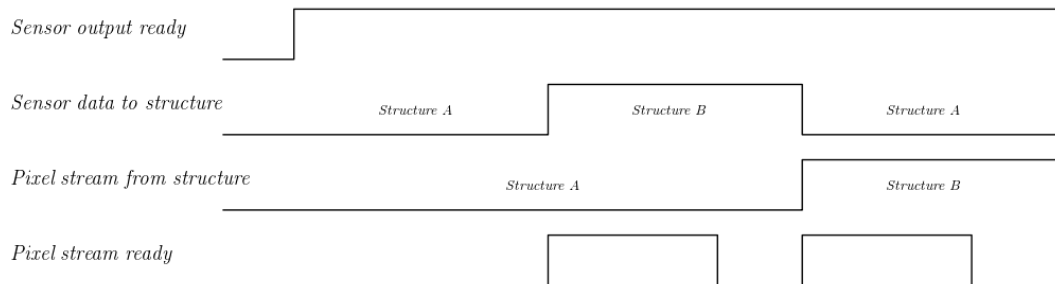


Figure 4.14: Timings of the pixel readout process and generating the pixel stream. The figure shows the first 3 rows of pixels sent from the Medipix3RX and converted into a stream. The signal *Sensor output ready* is high when the sensor is transferring data into the FPGA. The signal *Pixel stream ready* is high when pixels are being sent down the Avalon stream. The *Pixel stream ready* show bursts, this is generated by the timing difference between the data transfer speed of the sensor to the *Unscrambler* sub-module and the *Unscrambler* sub-module to the DDR3 memory.

There are 256 pixels of either 6 or 12 bits each, which are sent to the Avalon stream at a rate of one pixel per clock cycle of the main gateway system clock, which

is 150 MHz. At the same time, the pixel values pass through the LUT for decoding the LFSR counter. To send an entire row of pixels into the Avalon Stream takes $256 \cdot (1/150,000,000) = 1.707 \mu s$ for either 6 or 12 bits, which is less than the time it takes to read the sensor for the same data. The time required to read an entire row of pixels from the sensor is $(256 \cdot 6)/8 \cdot (1/75,000,000) = 2.56 \mu s$ for 6-bit and $(256 \cdot 12)/8 \cdot (1/75,000,000) = 5.12 \mu s$ for 12-bit. Once the pipeline is full, after the first full row of pixels have been read from the Medipix3RX sensor, both processes, reading from the sensor and sending to the stream, happen at the same time. Sending a row of pixels to the Avalon Stream takes either 0.853 or 3.41 μs less than reading a row of pixels from the sensor. In the time difference between reading and sending, the Avalon Stream is halt until the next pixels row has been read. The pixels are then sent to the Avalon Stream inside the FPGA in bursts of 256 pixels at a time, with a wait of either 0.853 or 3.41 μs between bursts. The total time to read a frame from the sensor and send it through the Avalon Stream is 657.067 μs for the 6-bit depth frame and 1312.427 μs for the 12-bit depth frame.

4.5 Summary

The presented gateware system is capable of controlling and reading data from the Medipix3RX as well as generating a PWM signal and interrupts. The system allows the processor to control all the actions for the Medipix3RX as well as accessing the DDR3 memory through the GPMC module. The gateware system is capable of decoding the image data from the sensor and calculating profiles from the images. A server program, explained in detail in Chapter 5, running on the ARM processor of the ARMFlash, controls the gateware system through a set of registers.

Chapter 5

Software and firmware design for the LancelotRX

A combination of two software projects are used in the LancelotRX system, these are a server program running on the ARM processor and a client running on a PC. The server program running on the ARM processor is in charge of handling the network communication with the clients, processing the control loops, and controlling the gateway system on the FPGA. The client program is how the user can control the LancelotRX system and obtain data from it. In this chapter, a description of both software projects is presented. The chapter starts by explaining the server program, then an overview of the communication protocol is given, and finally, an explanation on the client software is presented.

5.1 Server program running on the ARM processor

A server program running on the ARM processor and written in C and C++ is used to control the LancelotRX system. The server receives commands from a client application through an Ethernet connection using a Transmission Control Protocol/Internet Protocol (TCP/IP) protocol. Based on the received commands, the C server executes different tasks. These include controlling the gateway system, setting the value of the DACs and reading data from the sensors and ADCs. Apart from commands, configuration and image data is sent and received by the server. The top-level operations from the C server can be seen in Figure 5.1. The absence of an end state is because

the C server is intended to run continuously while the LancelotRX system is powered on. The majority of the tasks performed by the C server involve obtaining data and sending it through the Ethernet. The only processing done on the server is the option of fitting the image profiles with a Gaussian function to obtain its parameters.

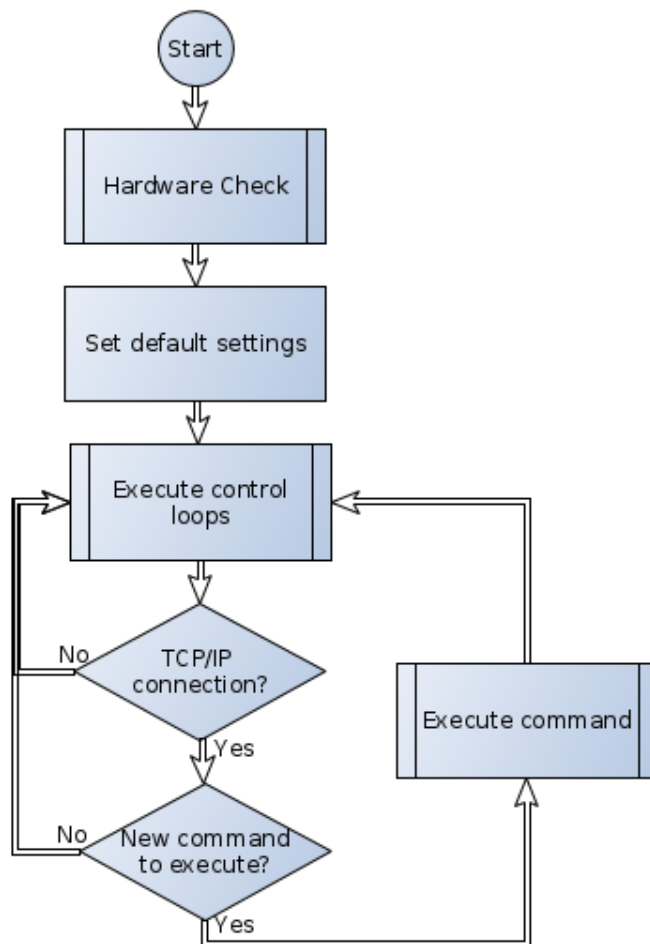


Figure 5.1: Flow diagram of the main tasks of the C server application for the LancelotRX system. At the start, the program checks that all the required hardware is present on the system, then the default settings are read from system files and set into the LancelotRX system. The control loops start being executed if they are enabled, and the network connection is checked for new commands from the client.

The C server is initiated at boot-up of the system. During the booting sequence, the C server starts after all the network infrastructure has been initialized on the Linux system. The booting process is shown in Figure 5.2. It starts by reading the hardware descriptor structure, which includes the information of the amount of devices to be checked and how to localize them. For the FPGA, the path to the FPGA configuration file is parsed and for the sensors, the I^2C addresses are read from the descriptor file.

Each device has an internal identifier used by the C server to obtain the correct drivers.

After the hardware descriptor file has been parsed, the C server writes the configuration file to the FPGA. After the file is written, the GPMC module is used to read the ID registers from the gateway system. This process is used to ensure that the correct configuration data has been written to the FPGA and the GPMC communication is working properly. The C server checks which modules are available on the gateway system by reading their ID registers, based on the available modules, certain functions will be enabled or disabled. As an example, if the C server on initialization does not find the *Profiler* module on the gateway system, then when a profile acquisition command is sent by the client, the server will respond with an error message specific to the module not being enabled. This structure provides system flexibility, allowing the C server to adapt quickly to changes in the gateway system without the need for a new compilation. If the GPMC communication module is not found on the gateway system, the C server exits with an error message printed to the serial terminal.

The rest of the hardware to be checked in the system before initialization is the I^2C devices, which include sensors, ADCs, DACs and a fan controller. The driver to be used for the sensors, ADCs and DACs, as well as their I^2C addresses, are stored in the hardware descriptor file. Small changes in different versions of the prototypes used for the development of LancelotRX make it an impossibility to use a rigid hardware check for all the systems. Using a file descriptor, the C server code can quickly accommodate for changes on the hardware without the need of a new compilation for every change. This flexible solution generates a better development environment, as well as facilitating the future addition of new features and hardware.

The C server reads a default environment settings descriptor to obtain the initial state in which the system is going to be configured. This feature is especially important when the system is deployed as a general detector or as any other possible applications in a Synchrotron experimental setup. Once the system is powered on, and after the time it takes to initialize, the LancelotRX has to be ready to perform the desired task. To make this feature available, a default settings environment descriptor is used, in which the configuration data for the sensor, the temperature control parameters and the operation mode of the sensor is recorded. The descriptor is saved as a file using American Standard Code for Information Interchange (ASCII) characters, and can

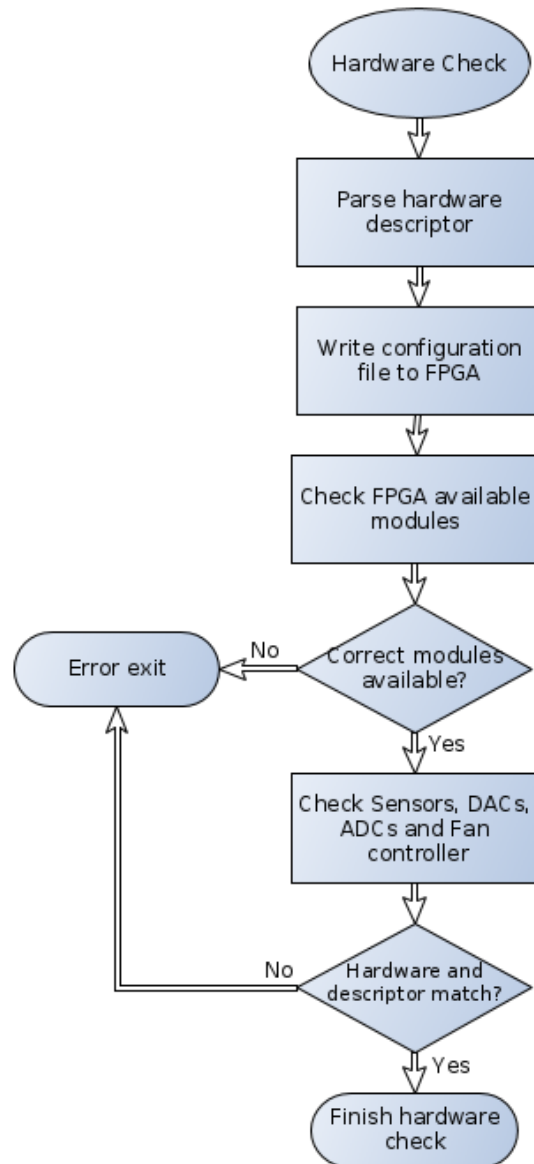


Figure 5.2: Flowchart of the initialization steps for the C server. The initialization procedure checks that the hardware needed is available and working on the system. The descriptor file contains the address for the FPGA configuration file, the needed sensors, ADCs and DACs. The configuration is written to the FPGA by the processor. Finally, the I^2C devices on the Interface board and Sensor board are checked.

be modified through the C server by commands from the client, or directly as a file accessed by the Linux system.

The C server can perform two control loops while receiving and executing commands. The first control loop is a temperature control using the Peltier cooler. The second control loop is a position tracker in the images, where the difference between the current position to a target position can be output as an analog signal. Both

control loops are implemented as PID controllers whose variables have been tuned by experimental procedures. The PID parameters and target values can be configured through commands to the server and are stored in the default environment settings descriptor. Apart from the inputs needed for the two control loops, the other input that the C server can monitor constantly is the status of a latched interrupt output from the pressure sensor on the Sensor board. This can be used as an alarm for a change in the pressure state of the Medipix3RX chamber.

Two threads are used on the C server to control the communication which is divided into different channels, a control and a data channel. The communication is implemented on two channels to allow commands to be sent to the LancelotRX while the system is acquiring and sending images to the client. The processes that are not control based, for example acquiring images, are executed as long as there is a connection on both the data and control channel. If the connection breaks, then the data acquisition process is stopped and the system returns to a wait state for an incoming connection. Only one connection to a client is permitted at once. The C server blocks all other connections once one client has successfully connected to the system. For the developing stage, the serial terminal of the processor was used to interact with the C server.

5.2 Merlin Protocol to communicate with LancelotRX over the network

The communication protocol between the LancelotRX and the client software is called Merlin protocol. Merlin protocol has been designed by the detectors group of Diamond Light Source and is currently being used by different detector systems using the Medipix3RX sensor. The main advantage of using this protocol is that it allows for faster deployment and testing of the LancelotRX system in the Diamond Light Source beamlines. Most of the protocol has been implemented without changes, but extra commands have been added in order to control specific features of the LancelotRX system.

The communication protocol is implemented using TCP/IP stream sockets, each LancelotRX system requires two sockets. Different connection streams are established

for commands and for data. This model enables indefinite streaming of data on the data channel, while listening to the command channel for a stop command. Streaming data continuously is the common usage for these type of detectors in a Synchrotron experimental setup. For this reason, the dual-channel communication protocol Merlin, is selected.

The communication protocol uses human readable ASCII characters to implement all the commands and system replies. For the image data, a binary system is used to minimize the communication length. An example of the communication protocol is shown in Figure 5.3, where a command example is shown together with the structure in which image data is sent by the LancelotRX system. When data is acquired, the system sends both the image data and the working parameters of the system. The information of the parameters is sent in two sections, an ‘Acquisition header’ and an ‘Image header’. The ‘Acquisition header’ contains the information that will remain constant for the entire acquisition. Examples of the data sent in the ‘Acquisition header’ are: integration time, masks used, data storage path, etc. This information is sent once per acquisition set. The ‘Image header’ contains data that can change from frame to frame. An example of the ‘Image header’ data are the values of the threshold DACs, which can be set to vary through the acquisition process. The ‘Image header’ is sent with every frame.

The length of the incoming data is encoded at the beginning of each message to ensure that all the data has been received. The binary data of the image is encoded in big-endian data order in the communication protocol. There is no difference between big-endian and little-endian when the pixel bit depth used on the sensor is 6 bits since it can be written in one 8-bit word. However, when larger pixel bit depths are used, the data order creates a difference. The client software written for this project transforms the data order from big-endian to little-endian as part of decoding the received communications.

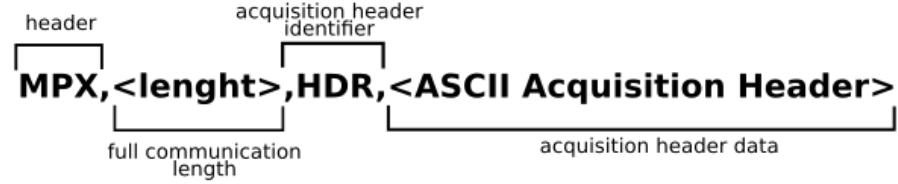
General command :Acquisition header :Image header :

Figure 5.3: Examples of the structure of commands used in the communication protocol on the LancelotRX system. The commands are sent in human readable ASCII characters, and the image data is sent in binary format.

5.3 Design of the client software to control LancelotRX

Multiple client programs were developed to control and obtain data from the LancelotRX system. There is no third-party client software available to interact with LancelotRX due to the communication protocol used, which is proprietary from the research groups at Diamond Light Source. As part of this project, client software was developed to test and use the LancelotRX. During the development stage of LancelotRX, a client implemented using LabVIEWTM was used to test and debug the system. After the development phase, a second client was implemented using a series of scripts to run in the MATLABTM environment. A third client, with reduced control over the LancelotRX system, has been written in python, with the intention of solving compatibility issues present with the LabVIEW and MATLAB environments.

5.3.1 LabVIEW debugger client with graphical interface

The client developed in the LabVIEW environment was designed to be an aid for the debugging of the system. The client was developed in parallel to the C server and gateway system. It was the tool used to test each feature of the system and to debug possible errors. The debugger client was implemented in LabVIEW for the speed of development that this programming environment provides, and for the simplicity in which data can be displayed in a graphical form. The Graphical User Interface (GUI) generated by LabVIEW was used to ensure the image information from the Medipix3RX was readout and processed correctly on the system. The current LabVIEW client is a modification of a previous version of a client developed by the research group.

Figure 5.4 shows the main control panel of the LabVIEW client. At the centre of the GUI, there is space for the acquired images to be displayed. Visualizing only specific regions of the acquired images is possible with the GUI. At the bottom of the screen, the Merlin protocol commands that are sent and received are displayed to facilitate debugging for communication errors. On the top part of the screen, status indicators from the system are displayed. These status indicators are internal flags used by the C server to check if everything is working correctly on the system. At the left of the screen, drop down menus are used to select commands to be sent.

For the configuration matrix of the sensor, a window with a graphical display of the data is used, this is shown in Figure 5.5. The configuration matrix can be either loaded from a file or generated on the client. Generating this data on the client by using the mouse is not the most efficient way to control the configuration matrix, but it allows an understandable and precise visualization of the data, which proved to be of key importance while debugging this setting from the sensor. There is also the possibility to download the current configuration data from the system to the client. This was an important tool to ensure that the sent configuration data had been correctly uploaded to the sensor.

Another key feature of the LabVIEW client for the development stage of the system was the control of the Peltier driver. From the control panel shown in Figure 5.6 the Peltier cooler can be directly controlled. The output voltage from the SMPS can be set from this window if the PID temperature control is not enabled. The PID control

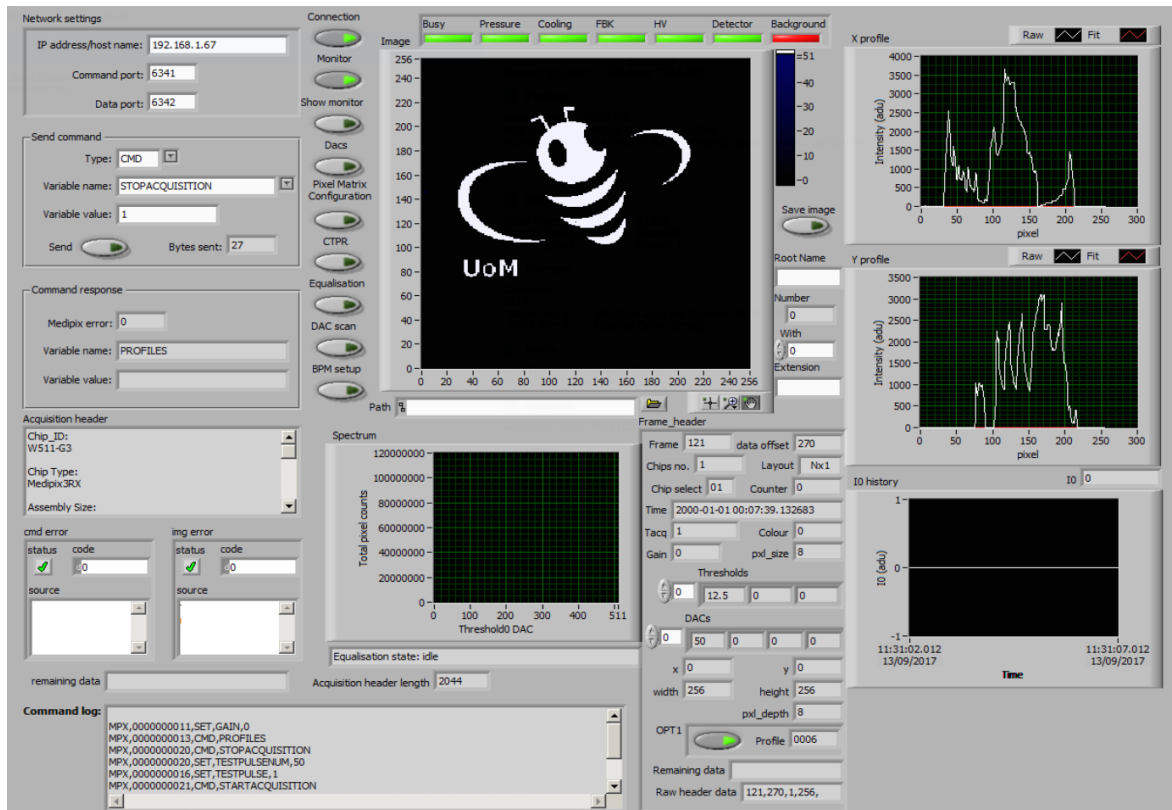


Figure 5.4: Main LabVIEW client window. The images obtained by the system are shown in real time in the middle window of the GUI. The two profiles for the image can be seen on the right side of the screen. The profiles are not calculated on the client, but calculated and sent by the LancelotRX. Error codes for both command and image channels are displayed in real-time to aid in debugging of the system.

algorithm can be enabled or disabled, the constants for the PID can also be modified. The changes over time of the temperatures of the system, as well as the voltage of the Peltier, are plotted on the right side of the window. This feature was important when the PID constants of the control algorithm were tuned.

5.3.2 MATLAB scripting client

In order to perform the analysis of the data generated by the LancelotRX system, a wide variety of numerical procedures on matrices was needed. The MATLAB environment was selected for this purpose, taking advantage of the digital image processing features, the plotting libraries and the scripting options. By using the shared Java libraries, a TCP/IP socket is implemented on the MATLAB environment. This feature is used to communicate with the LancelotRX system.

The client implemented on MATLAB stores the incoming data into a structure.

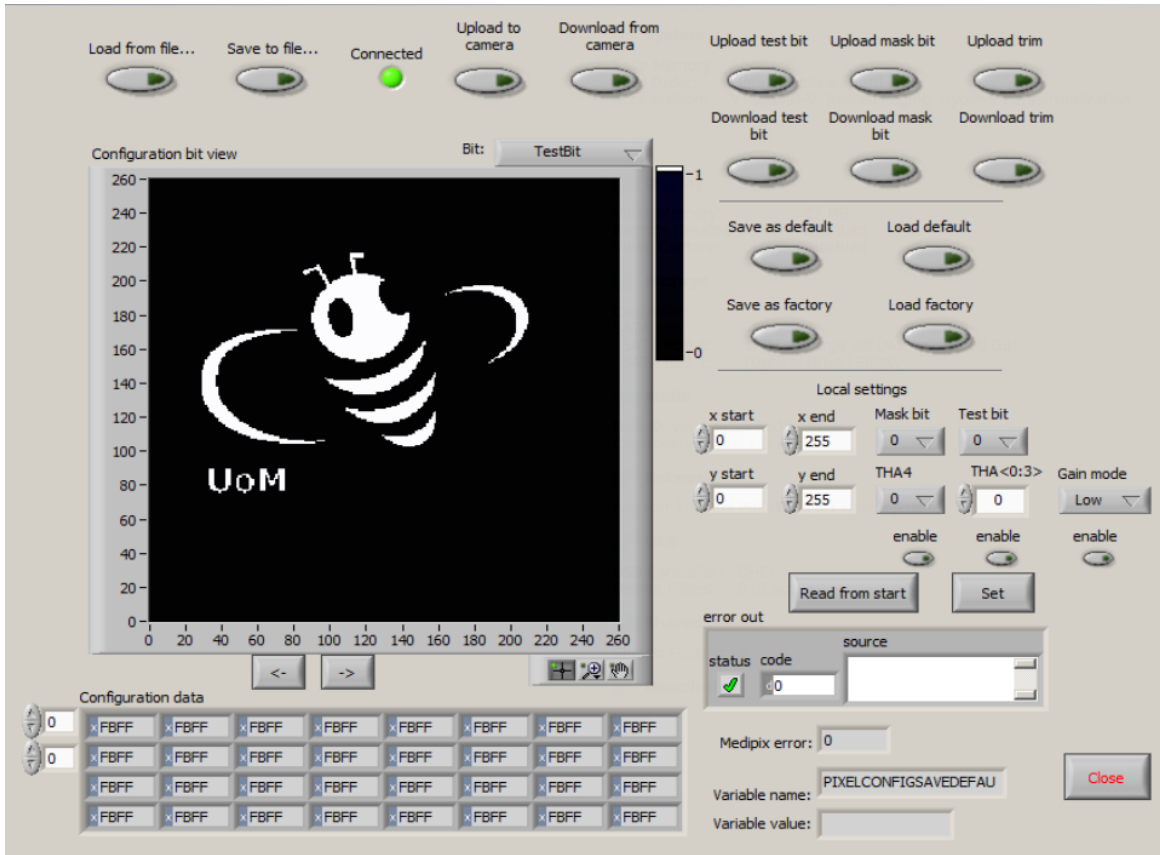


Figure 5.5: LabVIEW client window for changing the values of the configuration matrix. The values are displayed both graphically and numerically. The buttons on the top part of the screen allow the reading of the configuration matrix from a file, or to save the current configuration to a file. A small window in the bottom right shows the error status and communication codes to aid debugging of the system.

The client stores for each frame, the image data, and the header acquisition information. This allows a precise correlation between the obtained data and the system parameters used to obtain the data. In order to handle fast acquisition of frames, the client is written so the incoming data gets stored in RAM memory until the full acquisition sequence has finished. Following this, the information is decoded and stored. The information can be stored as text, as a MATLAB environment variable, or as images.

The client is implemented as a series of individual scripts that perform a specific task. In order to communicate with the LancelotRX system, a socket object is created, which is passed as an argument to each script. This allows each script to send and receive data from the system. Each script can be called as a function from another script. This allows the creation of macro scripts. The macro scripts are used to perform a task that requires several specific actions. In Appendix C.1 a table of all

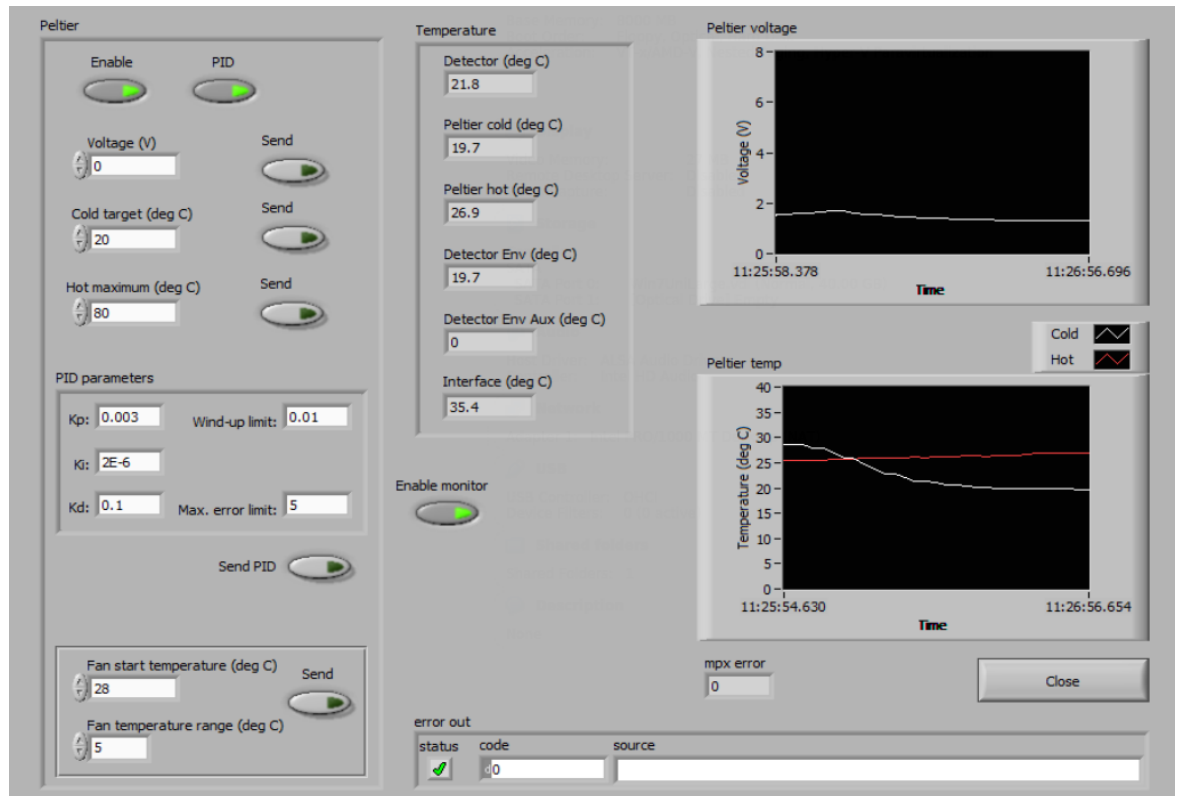


Figure 5.6: LabVIEW client temperature control window. The Peltier and PID control can be enabled or disabled from this window. It is also possible to change the PID parameters. On the right side of the screen, plots of the temperature and Peltier voltage changes over time are displayed. The temperature threshold to start the fan, and the temperature range over which the fan speed changes, can be modified from the lower left corner on the screen.

the single function scripts implemented for the client is shown. Calling these scripts as functions is done in the macro scripts. This client implementation in the MATLAB environment was the one used for all the calibration procedures with the LancelotRX system presented on this work.

5.3.3 Python client for fast data acquisition

The need for a client that could be shared with other research groups was not satisfied by the clients implemented using either the MATLAB or LabVIEW environments due to version compatibility issues and licencing. A simple data acquisition client has been implemented using Python language. This language was selected for its wide usage and portability.

The client is implemented without a GUI, only a simple command line interface is used. The obtained data is stored in text format as independent files. For each

acquired frame, two files are generated, an acquisition header file and a frame data file. The image data is stored in text format to avoid the requirement of external libraries to generate a file in image format. A flow diagram of the python client is shown in Figure 5.7.

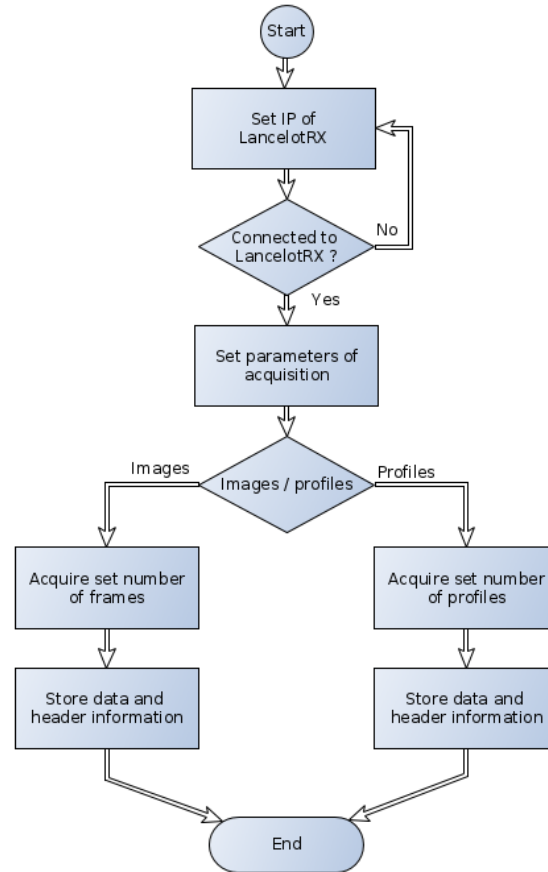


Figure 5.7: Flow diagram of the Python client for the LancelotRX system. The IP of the LancelotRX is requested from the user at the start of the program. The acquisition parameters set by the client are integration time, threshold values and amount of frames or profiles to be taken. Both frames and profiles are stored as individual files in ASCII format.

The python client has the feature of requesting images and profiles from the LancelotRX system and storing the obtained data locally. The amount of frames, integration time and threshold values can be set using this client. These limited commands are sufficient to obtain information from a LancelotRX system.

5.4 Summary

A server running on the ARM processor and three different clients have been presented. The server is capable of controlling the gateway system on the FPGA, reading the sensors and ADCs on the system, processing two control loops and handling communication with the client. The Merlin protocol has been implemented for the communication with the LancelotRX. This protocol is implemented over two TCP/IP ports, allowing the flow of data and the control commands to work in parallel. A client implemented in LabVIEW has been used to debug the LancelotRX during the development stages. A client implemented in MATLAB has been used to configure the system and to acquire the data shown in the experimental results of this work. Finally, a client implemented in Python language has been presented with the purpose of having good portability, and allowing external research groups to acquire data from the LancelotRX.

Chapter 6

Mechanical design for the LancelotRX

The previously presented electronics, gateway and firmware for the LancelotRX are placed inside a mechanical enclosure. The mechanical enclosure is designed to both protect the electronic hardware, as well as to act as a heatsink for the temperature control of the Medipix3RX. This chapter describes the design of the mechanical enclosures and the physical arrangement of the elements required for the temperature control.

6.1 System requirements for the mechanical design

The enclosure is designed to protect the electronics and the Medipix3RX sensor. The enclosure was designed with the aim of making the LancelotRX system as small as possible, resulting in a versatile x-ray detector. A small form-factor is preferred because a smaller detector is easier to install in an experimental beamline setup. The enclosure was designed to allow direct access to the Medipix3RX sensor.

The mechanical enclosure has to create two separated chambers, one for the sensor and one for the electronics. The electronics chamber will contain the Interface board and the Processing board, while the sensor chamber will contain the Sensor board. In order to remove undesired x-ray interaction with air, the sensor chamber must hold the capacity to be set in vacuum.

The LancelotRX enclosure is required to work as a heatsink for the heat generated

by the Peltier cooling system described in Chapter 3.3. To cool down the electronics chamber, a fan is used. The mechanical design must allow airflow on the electronics chamber to maximize the cooling effect of the fan.

6.2 Housing design for the LancelotRX

A metal alloy has been selected for the LancelotRX enclosure to ensure protection of the system by a strong material. Using a metal alloy also allows the enclosure to work as a heatsink. The principal material used in the housings is anodized aluminium for its properties of corrosive resistance, good thermal conductivity and its characteristic of being non-conductive. The designs have been manufacture by an external manufacturer.

6.2.1 Top and bottom case of the LancelotRX

The individual parts for the LancelotRX enclosure design are shown in Figure 6.1. The LancelotRX, using the designed enclosure, has a base footprint of 88x120 mm, and a height of 70 mm. The enclosure design is divided into two chambers, a chamber for the electronics and a chamber for the sensor. The division is done in order to create a separate chamber for the Medipix3RX sensor that can be set in vacuum. The electronics chamber is contained between the base of the enclosure and the top of the enclosure. The sensor chamber is contained between the top of the enclosure and the sensor cover. Different sensor covers can be used to enable the LancelotRX to be adapted to different applications. The most common cover is an aluminium plate with a Kapton window in the middle.

In the top enclosure four threaded holes are placed for screws that will keep the Sensor board PCB in position. An engraved space is used to paste in position the connector for the Sensor board. The top enclosure has a groove around the sensor chamber to set an elastomer O-ring in order to create a seal for the vacuum. The sensor cover also requires to have a groove to compress the O-ring, generating a seal. The sensor cover is held in position by four threaded holes. Inside the electronics chamber, spacers are screwed into the top enclosure to hold the PCBs in position.

The bottom and top of the enclosure are held in position by four screws that pass

through the bottom enclosure and reach threaded perforations in the top enclosure. An opening on the side of the electronics chamber is used to access the connectors for power, Ethernet and analog signals. A face plate is used to enclose the connectors and label them. This plate is clamped in position by grooves in the walls of the top and base enclosure.

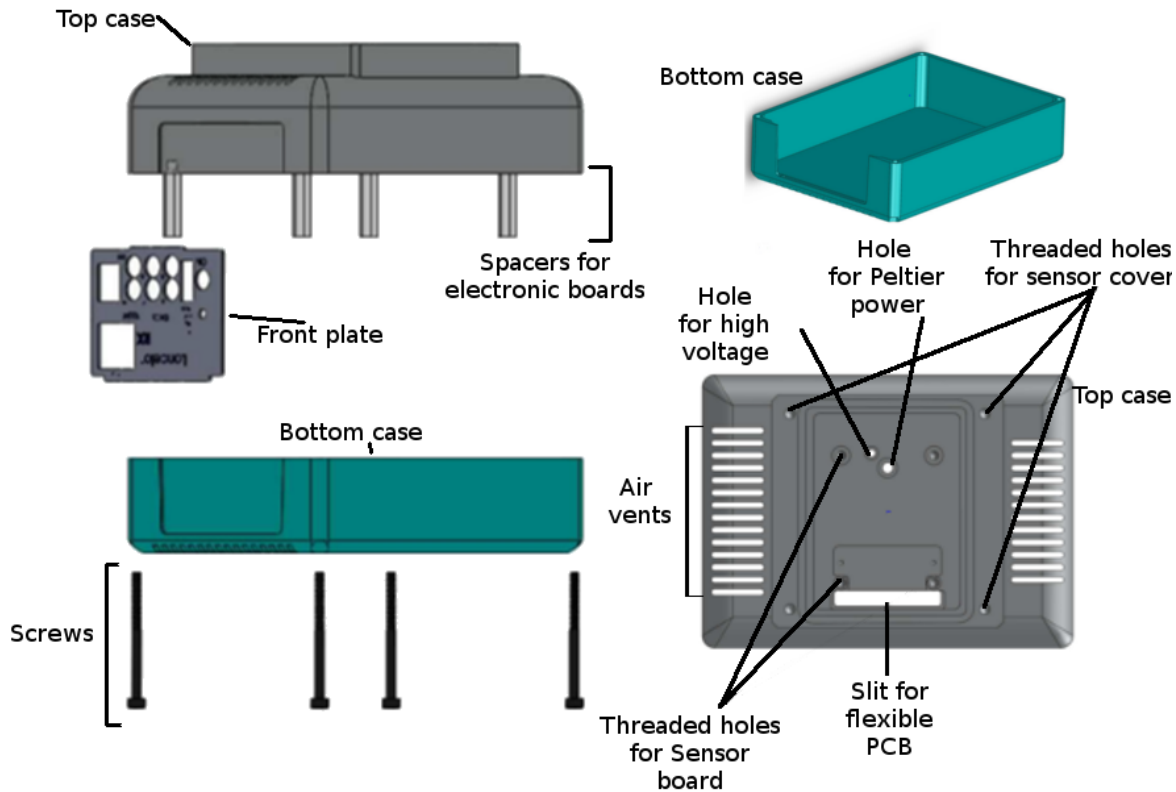


Figure 6.1: Housing of the LancelotRX system. The housing is divided into two pieces, a top and bottom enclosure. The bottom enclosure has four holes for screws that keep the housing closed. The top enclosure has spacers screwed into it to hold the Processor and Interface boards. Four threaded holes on the top enclosure are used to fix the Sensor board in place, and another four are used for the sensor cover. A slit and two holes on the top enclosure are used for communication between the Sensor board and the Interface board, and to connect the Peltier and high voltage line to the Interface board.

6.2.2 Connection between the sensor chamber and the electronics chamber

The Sensor board and the Interface board are held in different chambers. In order to connect the Sensor board with the Interface board, a thin slit is cut through the floor of the sensor chamber and the flexible PCB, which has been described in Chapter 3.2.4,

is passed through the slit. Two circular holes in the floor of the sensor chamber are used to pass cables to connect the Peltier cooler and to feed the high voltage required by the sensing layer of the Medipix3RX. The slit and the holes are the minimum necessary size and will be sealed using vacuum grade epoxy once the connections have been placed. The holes and the slit are shown in Figure 6.1.

The side of the flexible PCB that will connect to the Sensor board is pasted against the bottom of the vacuum chamber, as shown in Figure 6.2. The flexible interconnection board is passed through the slit between the vacuum chamber and the main electronics chamber to interconnect both boards. When the connector for the Sensor board on the flexible PCB has been pasted into position, a vacuum grade epoxy is used to seal the gap.

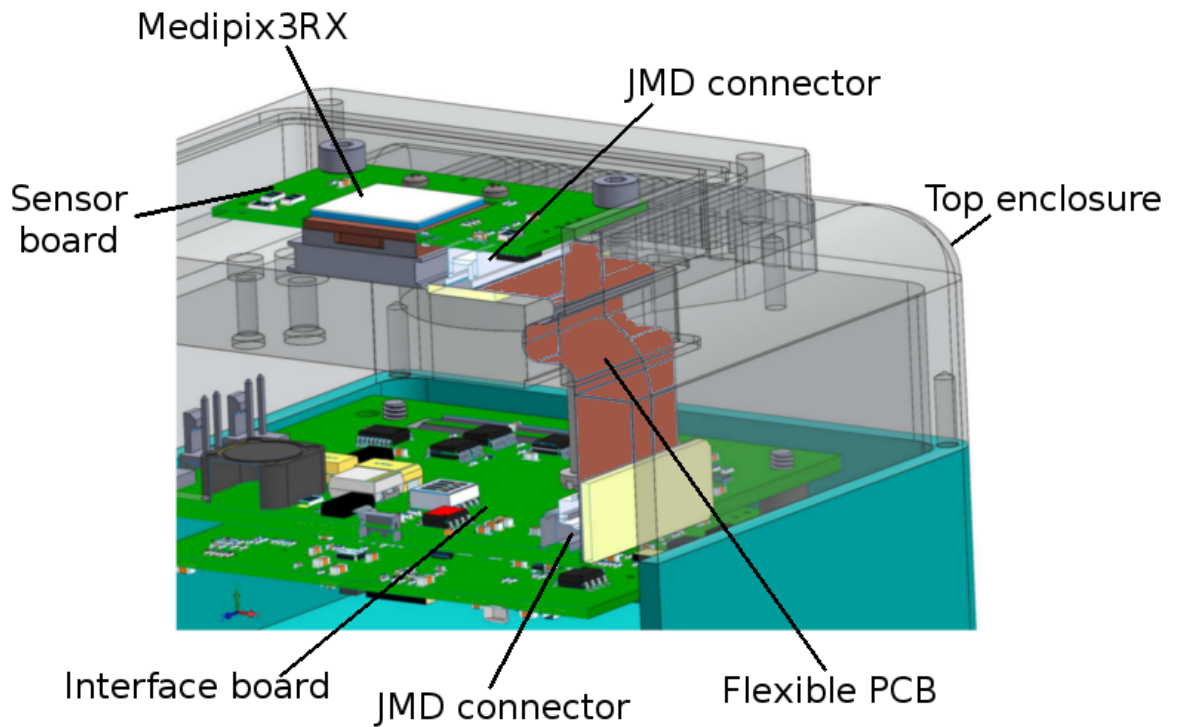


Figure 6.2: Cross-section view of the connection from the Sensor board to the Interface board for the LancelotRX system. The connecting segment crosses the vacuum chamber floor through a slit which is later sealed with vacuum grade epoxy. The connecting segment has been painted on red for this figure to enhance visualization. The JMD connector on the Interface board is shown inside the electronics chamber. The flexible PCB shows a small bend, this is caused by the flexible PCB being longer than the distance between the sensor chamber and the Interface board. The flexible PCB has been designed longer so it's possible to assemble the LancelotRX system.

6.3 Heat dissipation in the mechanical design

The top enclosure has been designed to act as a heatsink for the temperature control system. The Peltier cooler removes heat from the sensor through a copper block and dissipates the heat by using the top enclosure of the system as a heatsink. A cross section of the position of the Medipix3RX, the copper block, the Peltier and the top enclosure is shown in Figure 6.3. Temperature sensors placed on both the sensor chamber and the electronics chamber are used as inputs to the temperature control loop.

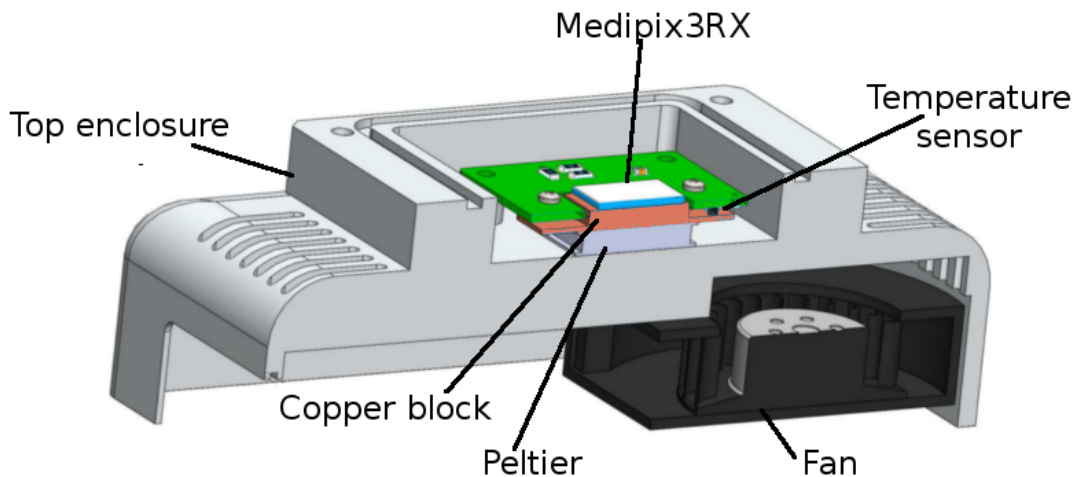


Figure 6.3: Cross section of the relevant parts for the temperature control. The heat generated by the Medipix3RX is removed through the copper block by the Peltier and dissipated into the top enclosure. The electronics chamber, holds a centrifugal fan situated under the air vents of the top enclosure. The airflow generated cools down the Interface and Processor boards, as well as the top enclosure.

The top enclosure is used as a heatsink for the heat generated by the sensor. The heat generated in the electronics chamber can be dissipated through the top and bottom chassis. To ensure the temperature in the electronics chamber does not rise over the recommended working limits of the electronic components, a fan is used to generate an air flow. The top chassis has air vents at both sides of the base of the sensor chamber to generate an air flow. As shown in Figure 6.3, a centrifugal fan is

placed under the air vents generating a current flow that will cool down the electronics and the bottom of the sensor chamber, where most of the heat generated by the sensor is transferred.

6.4 Summary

The designed mechanical enclosure is able to hold and protect the electronics from the LancelotRX system, while maintaining a small form factor allowing the system to be fitted in small spaces. The enclosure is designed using anodized aluminium, allowing the top enclosure to be used as a heatsink by the temperature control system. The mechanical design generates a sealable sensor chamber where the Medipix3RX is placed, allowing the sensor to be used in vacuum.

Chapter 7

Equalization of the thresholds of the Medipix3RX

The Medipix3RX has the option of adding an individual offset to the energy thresholds of the pixels. The process to obtain the values of the added offsets, that would generate a unified response from the pixels, is described in this Chapter. Different methodologies are described and compared, and two new methods are proposed.

7.1 Threshold dispersion in the Medipix3RX

The Medipix3RX contains two energy thresholds per pixel. This enables specific counting of photons that are within an energy range, or to obtain spectral information of the arriving x-rays. A large pixel-to-pixel threshold variation is observed in the Medipix3RX. The root of this issue has been attributed to transistor thin oxide degradation during circuit manufacturing caused by transistor gates not being protected by tie-down diodes [75]. The sensor presents gain and offset variation between pixels, generated specifically by the mismatch on the Shaper transistors.

In order to fix this issue, the Medipix3RX has the option of adding a configurable positive or negative offset to the thresholds of each individual pixel. The process of finding the correct offset value for each pixel is called the equalization process, ensuring that the effective threshold of the pixels is as similar as possible to the ideal threshold. This process requires the setting of the right values for the global DACs and the individual per pixel DACs to get a uniform response from the sensor pixels.

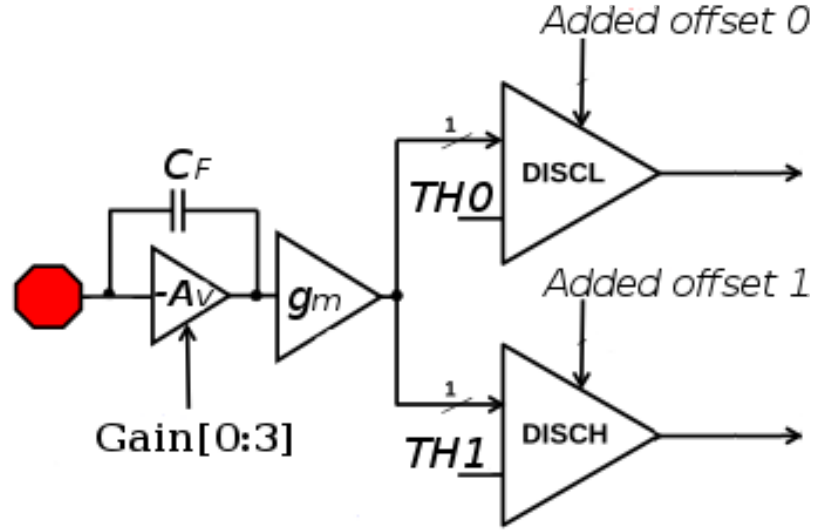


Figure 7.1: A block diagram of the pixel circuitry, the outputs of DISCH and DISCL go to the processing logic. Both discriminators have the option to add an offset to its TH input, in order to compensate for pixel-to-pixel threshold variation. Modified from [8].

Figure 7.1 shows a diagram of the circuitry for one pixel which has two discriminators, DISCL and DISCH. Both discriminators show an added offset input, that is used to add a positive or negative offset to the TH input of the discriminator. The effective threshold of the discriminator is the sum of the TH input and the added offset, where the added offset for an arbitrary pixel i is determined by:

$$added_offset_i = 16 * trim_bits_i * I_DAC_DISC$$

The trim bits are a 5-bit value from -15 to 16 and I_DAC_DISC is a 9-bit value from 0 to 511. The trim bits represent the value of the individual DAC per discriminator. The I_DAC_DISC value represents the global current source. There are two global current sources in the Medipix3RX, one for all the DISCL discriminators and one for all the DISCH. The global current sets the least significant bit current, allowing to configure the dynamic range of the added offsets [8]. For a correct equalization, the value of the DAC I_DAC_DISC has to be optimized. If the I_DAC_DISC is set to a large value, it will be possible to equalize more pixels but the equalization of each pixel will be coarser. If it's set to a lower value, the equalization for each pixel will have a

finer control but it will be possible to equalize less pixels. To correctly equalize the sensor, the value of the global DACs has to be set, as well as specific DACs per pixel.

In order to use the Medipix3RX to obtain spectral information of x-rays, equalization is needed. The effects of the equalization are shown in Figure 7.2, where the sensor has been flooded by 16 keV x-ray field. As shown in Figure 7.2a, by using a sensor that has been equalized, it's possible to detect the peak of the signal and reconstruct the energy of the x-ray field. As shown in Figure 7.2b, if the sensor is not equalized then the peak of the signal is lost in the threshold dispersion and the energy of the x-ray field can't be reconstructed.

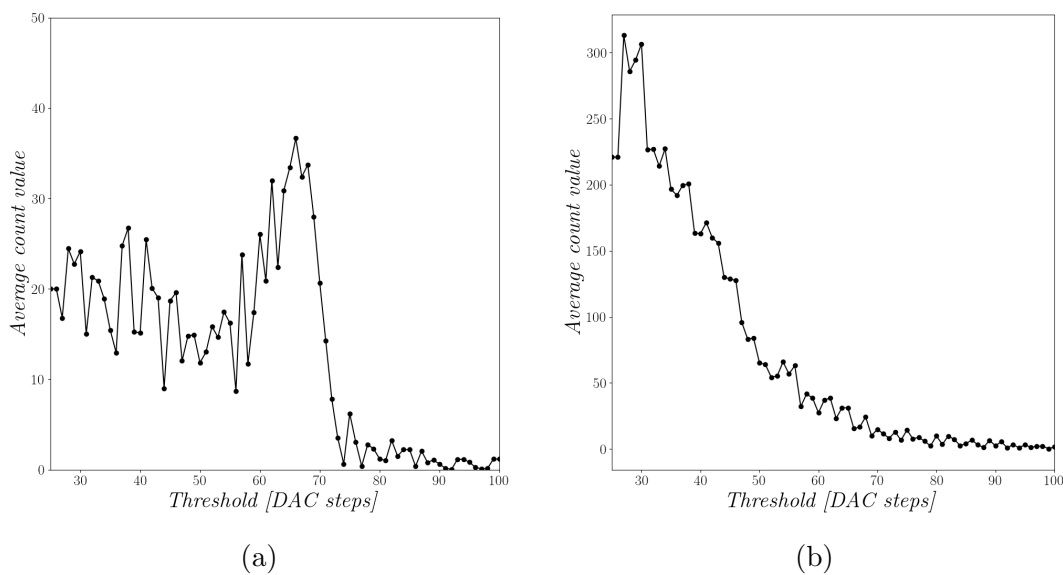


Figure 7.2: A) Differential TH scan of a 16 keV x-ray signal flooding the sensor, using SPM in an equalized sensor. The peak of the energy can be clearly detected. B) Differential TH scan of a 16 keV x-ray signal flooding the sensor, using SPM and no equalization. It is impossible to reconstruct the energy peak due to the threshold dispersion.

7.2 Count sources for equalization

For the equalization procedures it's needed to measure the response of each pixel, in order to determine the required added offset. The response of each pixel can be measure by different sources that generates counts on the pixel. The sources available in the Medipix3RX are: the presence of electronic noise, injected test pulses and x-ray photons.

7.2.1 Equalization using electronic noise

A possible source of counts to the sensor, and the simplest to use, is electronic noise present on the Medipix3RX. When there is no energy input to the pixel and the threshold is set to the lowest value, then both inputs of the discriminator have the same value. If both inputs have the same value, small electronic noise will generate the zero-crossing discriminator to have an output similar to pulses from photons, causing the logic to interpret it as photons and to increment the counters.

A method to observe how the sensor responds to electronic noise, when it's not equalized, is to use a scan of the values for the threshold DAC, and process the average pixel value for all the pixels in the matrix for each value of threshold DAC selected. This will give a graph of average pixel value vs threshold, as shown in Figure 7.3. The counts observed by this method are the 'electronic noise floor' of each pixel, this is the point where the value of the threshold DAC and the input signal to the pixel have close values and small noise is able to trigger the zero-crossing discriminator. Ideally, all the pixels should have this noise floor triggering at the same threshold DAC value, but in practice there is a big dispersion among the pixels at which value of threshold DAC the noise floor is present.

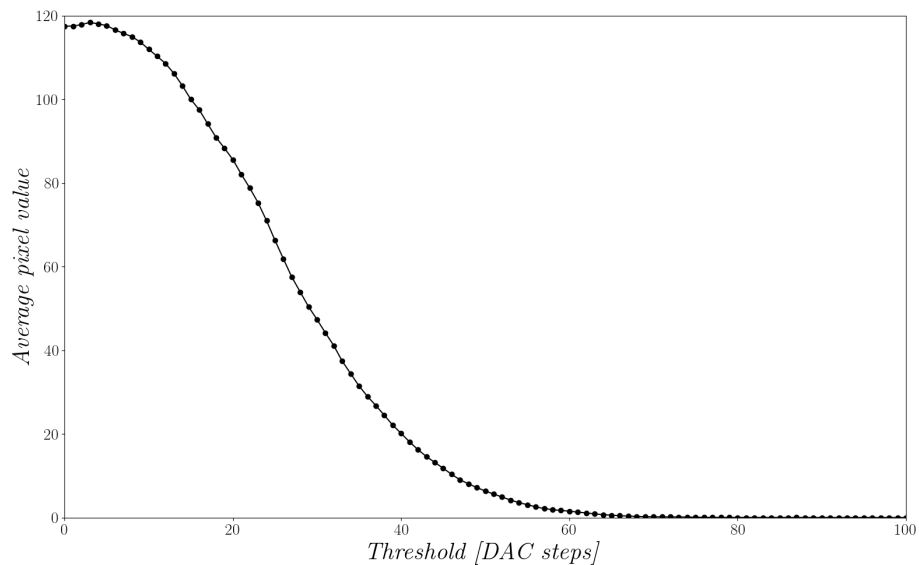


Figure 7.3: Average pixel count for a scan of the threshold DAC, using no equalization. The response is generated by the electronic noise floor that has a Gaussian distribution with a mean around 0.

It's possible to implement an equalization procedure by measuring at what threshold DAC values the pixel shows noise floor counts. Ideally, all the pixels should have this zero level at the same value of the threshold DAC, but as shown in Figure 7.3, there is a big dispersion of the zero level. Adding either a positive or a negative threshold offset to the pixel, it's possible to move closer all the zero levels to the same threshold DAC value. The process of equalization with noise, uses the value of this zero level per pixel, to assign a correcting offset to each pixel. A method to quantify the threshold dispersion on the sensor matrix after equalization, is to have a scan of the threshold DAC and obtain the standard deviation from fitting the response with a Gaussian curve. A perfect equalization should have standard deviation of zero, with all the pixels zero level aligned to the same threshold value.

Using the electronic noise as a source of counts for the equalization, the pixel-to-pixel threshold dispersion can be determined. The Medipix3RX sensor presents both a threshold offset and a gain mismatch. When the equalization is made by using the zero level variation, visible with the electronic noise, it is possible to reduce the zero level variation, but not the gain mismatch. As the detected energy increases the response dispersion between pixels will be larger caused by the gain mismatch. The primary disadvantage for the equalization procedures using electronic noise, is that the gain mismatch can't be determined or corrected. The advantage for this source of counts, is that it can be implemented without the need of an x-ray source.

Definition of th^* for electronic noise

A global threshold value is set into the sensor matrix, but as explained previously, each pixel will have a variation of this value. The effective threshold of each pixel, which is different from the global threshold, will be referred as th^* , where the effective threshold of pixel i is th_i^* . In order to equalize the sensor, the values of th^* of the matrix are required. When electronic noise is used as a count source, the th^* is defined as the centre of gravity of the response generated in a pixel by the electronic noise in a threshold DAC scan. The mathematical definition used is the value of the threshold DAC for which an integration of the response from 0 to the centre of gravity is equal to half the value of the integration of the whole response.

$$\int_0^{\text{centre_of_gravity}} f(th) = \frac{1}{2} \int_0^{\text{max_th}} f(th) \quad (7.1)$$

The center of gravity approach for obtaining th^* is implemented to solve the problem of non-symmetrical responses. Using a method to find the middle-point from the range where the response is bigger than a determined value would be less computationally expensive, but some of the responses appear to be non-symmetrical.

7.2.2 Equalization using injected pulses

In order to solve the problem of the gain mismatch, as explained in using electronic noise as a counts source, it is possible to use injected test pulses as a source of counts for the equalization. When the equalization is made using test pulses or real x-rays photons, it is possible to equalize for a specific energy. Both gain mismatch and threshold offset can be corrected for the specific energy or pulse amplitude. This method has been reported to generate a more precise equalization for a given energy than using electronic noise [76].

The use of injected pulses

The Medipix3RX sensor has the capability to inject test pulses into the pixels, this is done by using a test capacitor connected to the input of the pixels circuitry. The test capacitor is connected to the input of the pixel before the gain amplifier in the circuit [8]. Two different pulse amplitudes can be generated simultaneously in the sensor, this is created by having three general voltages controlled by DACs. The DACs used are V_{Tp_ref} , which will act as the lower value of the pulses, and V_{Tp_refA} and V_{Tp_refB} , which will be the high value of the pulses. Each pixel will have only one test pulse high amplitude voltage, either A or B, and this is dependent on the spatial position of the pixel in the matrix. The matrix is arranged in a chessboard style, alternating pixels with RefA and RefB in both vertical and horizontal directions, as showed in Appendix A.1.

A disadvantage of using injected pulses to do the equalization, is that the behaviour of the pulses becomes unstable when a large area of the pixel matrix is used, bigger than one ninth of the matrix (85 pixels by 85 pixels). When a large area of the

Medipix3RX is set for injected pulses, a saturated response is found, where most of the pixels in the matrix exhibit the maximum count. This behaviour of the Medipix3RX has been corroborated by collaborators . The source of this behaviour seems to be based in power requirements. A large amount of pulses require current spikes, that may interfere with logic of the Medipix3RX. This characteristic of the sensor forces the equalization process with injected pulses to be done in tiles, using only a section smaller than one ninth of the matrix. For the experimental verification of the injected pulses equalization method obtained in this thesis, the matrix was divided in 16 sections, equalizing one at a time and then stitching the results together. This method dramatically increases the equalization time.

Definition of th^* for injected pulses

To find the th^* of all the pixels, the pulses are set such that a known quantity of pulses are sent into the pixels in the integration time. A scan of the threshold DAC is processed and a profile of the scan is computed. The profile of a scan can be seen in Figure 7.4, the obtained average pixel value of each frame is divided by the number of pulses that were sent, generating a flat region with the value of 1.

Figure 7.4 shows the characteristic ‘S’ curve, where the electronic noise region of the threshold DAC generates very high counts, then there is a flat region of value 1, and after that, there is a fall to 0. The length of the fall between 1 and 0 is the th^* spread in the sensor.

The method used to calculate the th^* is to use a differentiation and Gaussian fitting of the pixel response to the threshold DAC scan. The differential of the pixel response is obtained by subtracting the pixel value from the next threshold DAC value frame to the pixel value of the current threshold (TH_i) DAC frame , $Pixel_value[TH_i] - Pixel_value[TH_{i+1}]$. The differential response is then fitted to a Gaussian function. The mean of the fitted Gaussian response is used as the value of th^* . Using this method a large amount of points are used and the result th^* value is consistent. This method has the disadvantage of being computationally expensive.

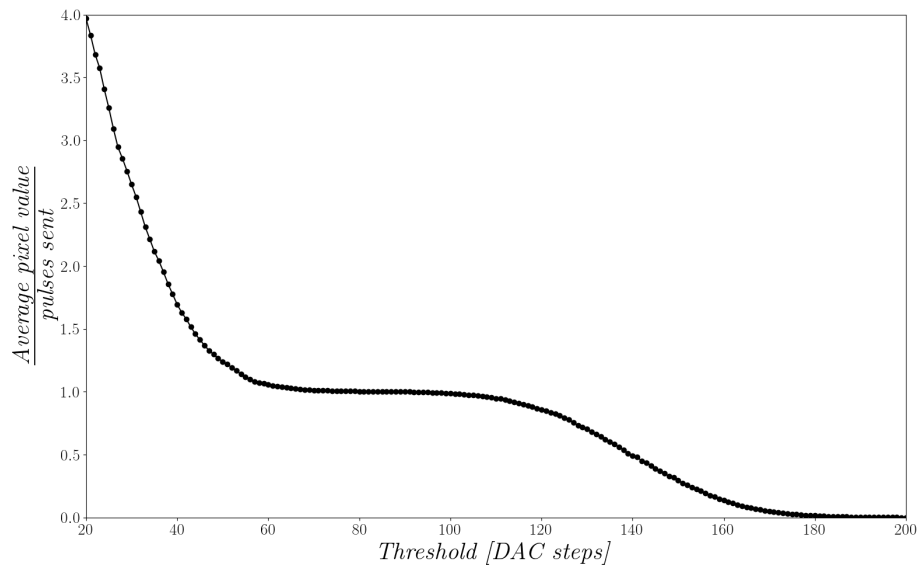


Figure 7.4: Profile of a scan of threshold DAC using 70 test pulses and dividing the average pixel value by 70, using a sensor with no equalization.

7.2.3 Equalization with x-ray photons

Equalizing the Medipix3RX with x-rays has the practical disadvantage of requiring a monochromatic x-ray source with a high flux. A flat field of x-rays is required, which is usually achieved by setting the sensor at a relatively large distance from the x-ray source. This will reduce the flux of the x-ray photons that arrive to the sensor, requiring longer integration times, and increasing the process length. A high count rate is needed in order to average the Poisson distribution of the arriving photons.

The second problem with equalizing using x-rays, is the charge sharing between pixels. If the sensor is configured in SPM, then the photons that hit the borders of the pixel will spread their charge with the neighbouring pixels, this will generate either double counts or missing counts. This phenomenon will generate a decreasing response from the pixel to a threshold scan, rather than a flat response with a quick fall as would be expected. Figure 7.5 shows a comparison between these two responses. It's possible to see how the real response of the sensor makes it difficult to determine a cut-out energy.

The combination of needing an x-ray source and requiring longer integration times due to low fluxes, make the equalization with x-rays an impractical approach. The only advantage of using x-rays to equalize is that it can take into account both threshold offset and gain dispersion.

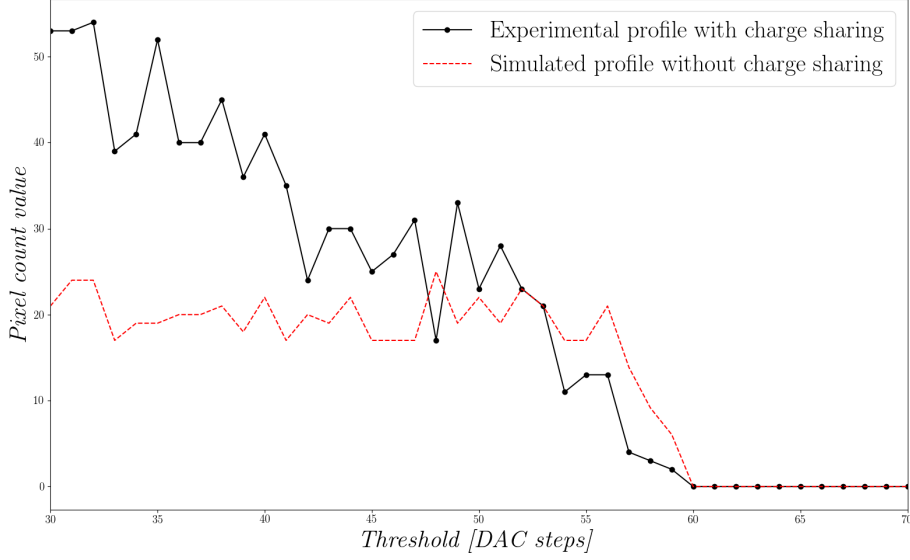


Figure 7.5: Scan of the Threshold DAC of a pixel for a non-equalized sensor in SPM showing double and under counts , for x-rays of energy 14 keV. The plot also shows a simulated one pixel profile of a scan of the threshold DAC for non-equalized sensor without charge sharing effect.

Definition of th^* for x-rays

To determine where the cut-out voltage is in every pixel, while minimizing the instability caused by the photon Poisson distribution of arrival and the charge sharing, a long integration time is used. The th^* for each pixel is defined as the first threshold DAC value, in an increasing order, that has an average value of less than a set reference. Figure 7.6 shows an averaged pixel profile, and the set value used to define th^* is denoted with a dashed red line, for this example the value of 5 pixel counts was used.

Using a differential profile and a fitting of a Gaussian, similar to the method used for injected pulses, is not a viable method. The big changes on the profile values generate several peaks on the differential response, making the fitting of one peak difficult.

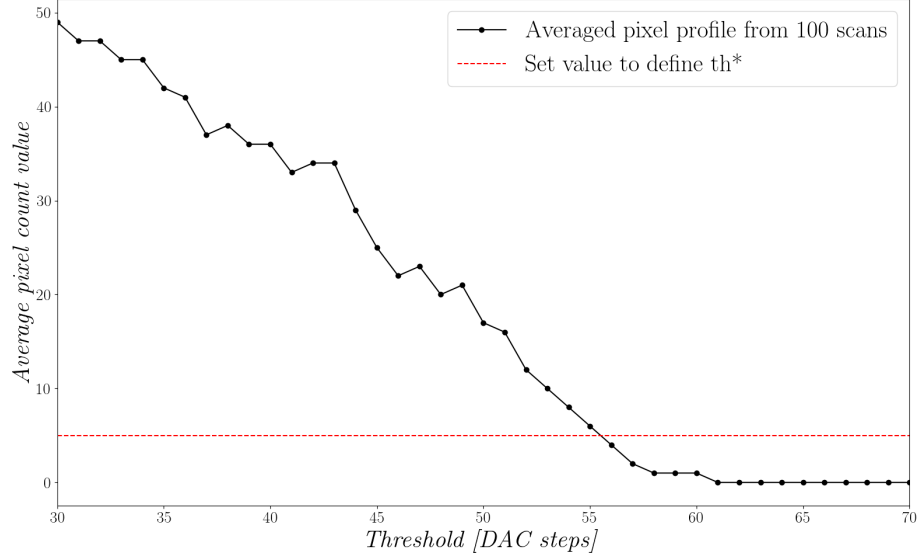


Figure 7.6: Averaged profile of a scan of the threshold DAC for one single pixel, the set value of 5 is used to determine the position of th^* .

7.3 Equalization methods for the Medipix3RX

The presented equalization methods are implemented using one of three different sources of pixel counts: pixel counts generated by the noise floor, injected pulses by the testing mechanism of the Medipix3RX or using x-rays from a monochromatic source. All of these sources generate counts on the pixels of the matrix, using those counts the th^* of each pixel can be found and used to equalize the sensor. Depending on the algorithm used and the source from the counts, the precision of the equalization and the amount of images required from the sensor or computational process of the images data differ. The equalization process is divided into three parts, setting the value of the global `I_DAC_DISC`, setting the value of the trim bits per pixel and masking noisy pixels.

7.3.1 Optimization of the `I_DAC_DISC`

As explained previously the value of both `I_DAC_DISC` will determine the dynamic range of the added offsets to the pixels of the matrix. To have a precise equalization these values have to be optimized, as using a non-optimized value will result in either having pixels that can't be equalized or in having an equalization with a wide th^* spread.

Without equalization the th^* values of the matrix have a Gaussian dispersion in a histogram of th^* in the threshold axis. This response can be seen in Figure 7.8, regardless of the source used to obtain the th^* the dispersion always have a Gaussian response. In order to equalize the response of the pixels, the trim bits and LDAC_DISC were set to move all the th^* closer to a target value on the threshold spectrum. The target value used was different based on the source of the counts. In the specific case of using the noise floor as a source, the ideal would be to use a target of zero but in practice a positive value was used in order to see both sides of the response curve. Choosing zero as a target would generate pixels that have the th^* at negatives threshold DAC values, which can't be measured and, therefore, can't be corrected.

The process to obtain the optimal value of the LDAC_DISC DAC starts by obtaining the amount of threshold DAC counts, that the mean of the th^* distribution is moved by each DAC step of LDAC_DISC. This means the rate of change in the position of the mean of th^* in threshold steps to the change of LDAC_DISC.

$$noise_displacement_ratio = \frac{\nabla \mu_{th^*}}{\nabla LDAC_DISC} \quad (7.2)$$

To obtain the noise displacement ratio three values of LDAC_DISC were used and a scan of the values of the threshold DAC to obtain th^* for each value of LDAC_DISC was obtained. The trim bits are set to add the highest negative threshold offset, which is the value of -15 for the trim bits, so the response of the th^* increases in the threshold DAC spectrum. Figure 7.7 shows the overlap of three histograms of th^* for the values of 40, 90 and 140 of LDAC_DISC with trim bits of -15.

The next step was to obtain the standard deviation of the histogram of th^* . The LDAC_DISC was set at a value of 100 DAC steps and the trim values of all the pixel matrix are set to -15 for the maximum negative added threshold offset. This offset was used in order to move the mean of the Gaussian response of the th^* to a higher threshold DAC value and have a better fit. Keeping the Gaussian response with a mean of approximately zero would generate less points to use for the fit, and therefore a less accurate fit result. By adding the same offset to all the pixels, the standard deviation of the th^* dispersion remains the same. As shown in Figure 7.7, the histogram of th^* is obtained and the data is fitted to a Gaussian curve. The fitting process allows to acquire the standard deviation of the th^* dispersion of the non-equalized sensor.

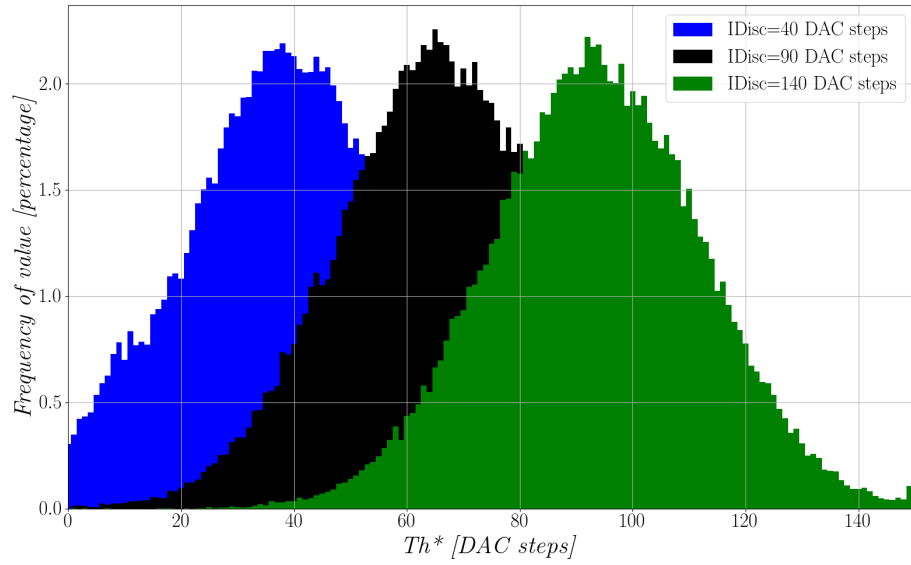


Figure 7.7: Histogram of th^* for three different values of I_DAC_DISC and the maximum negative added offset.

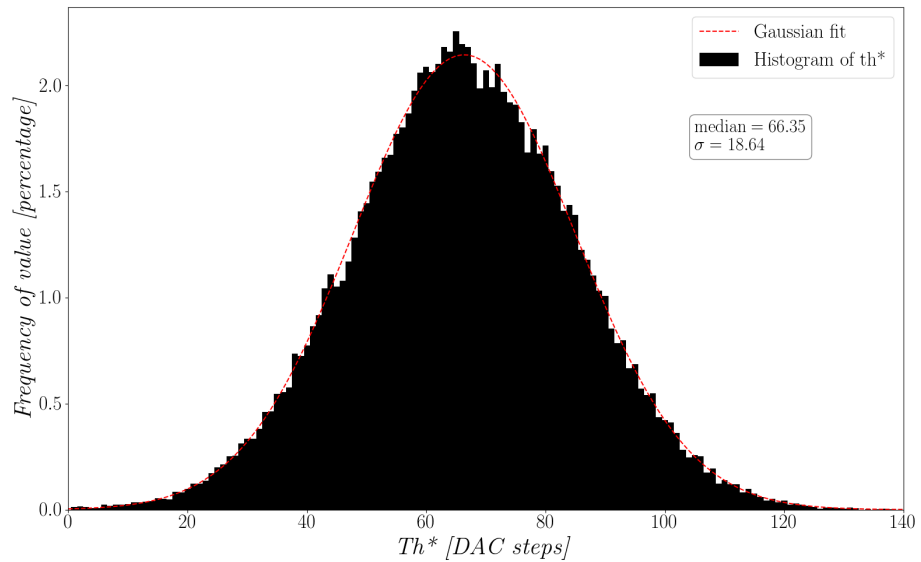


Figure 7.8: Histogram of the th^* for a non-equalized sensor, setting all the pixels trim bits to a value of -15 and an I_DAC_DISC of 100 to set the mean of the Gaussian response away from the origin. The response is fitted to obtain the standard deviation.

The ideal value for LDAC_DISC is the minimal value for which all the pixels' th^* can be moved by the trim bits to the target th position. To obtain this ideal value, the mean of the distribution (when all the pixels' th^* have been moved to higher values of threshold DAC spectrum) should be located at 3.2σ DAC steps from the target value. Were σ represents the standard deviation of the Gaussian curve. This will ensure that the dynamic range in which the mean of the th^* can be moved using the trim bits, goes from -3.2σ to 3.2σ from the target value. In Figure 7.9 an example of this positioning of the Gaussian response for a target value of 10 is showed.

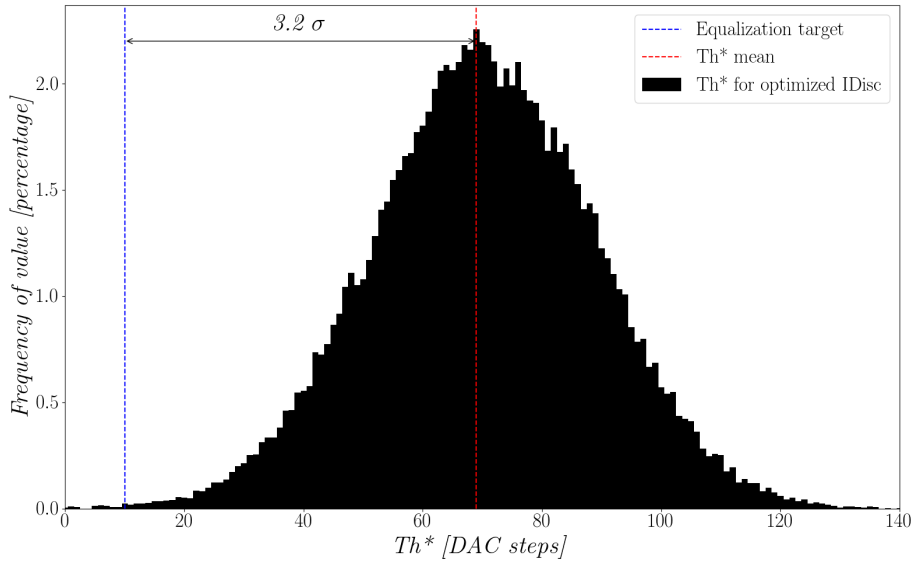


Figure 7.9: Histogram of th^* using the optimum LDAC_DISC value to ensure that the mean of the th^* Gaussian distribution is located at 3.2σ from the target value, which for this example is a value of 10 in threshold DAC steps.

To obtain this minimum value the formula used is:

$$Optimum_I_DAC_DISC = \frac{3.2 * \sigma_{th^*} + Eq_Target}{Noise_Displacement_Ratio} \quad (7.3)$$

7.3.2 Algorithms to determine the trim bits

After obtaining the th^* of the pixel matrix and having optimized the value of LDAC_DISC to be used, the next step is to align all the th^* as close as possible to the threshold target th . This alignment is done by changing the value of the trim bits, which will determine the added threshold offset per pixel.

Linear Method

The first step, to calculate the trim values, is to move the pixels' th^* to one of the extremes of the shift range. For this, the value of -15 will be used for all the trim bits, moving the mean of the th^* distribution as much as possible to higher values in the DAC threshold spectrum, as it is shown in Figure 7.10. The new th^* values are calculated and a comparison between the old th^* values and the new ones is made. Comparing the two values and dividing it by the change on the trim bits, a th^* displacement factor for pixel i or $th^*_displacement_i$, is obtained. The formula for the th^* displacement factor for pixel i is:

$$th^*_displacement_i = \frac{th^*_trim_{i,A} - th^*_trim_{i,B}}{trim_{i,B} - trim_{i,-A}} \quad (7.4)$$

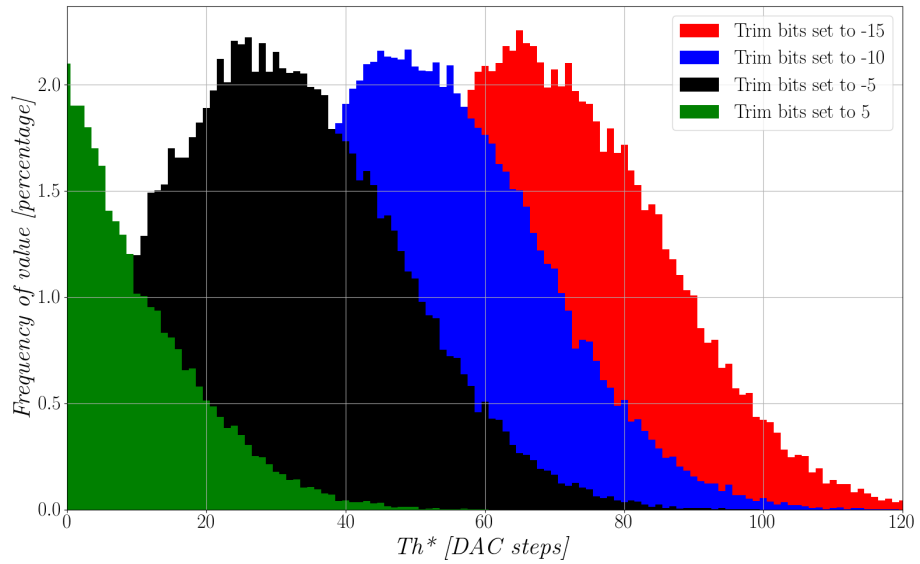


Figure 7.10: Plot of the th^* distribution for different values of the trim bits, showing the shift of the mean of the distribution across the threshold spectrum. In this case the same trim bits are applied to all the pixels. The measure of th^* was done using electronic noise as a source.

Where $trim_{i,A}$ and $trim_{i,B}$ are two different values of the trim bits for pixel i . Ideally, these values have to be as far apart as possible, but depending on the source of the counts, this might push some pixels to have their th^* in what would be negative values of the Threshold DAC. The values for $trim_{i,-A}$ and $trim_{i,B}$ have to be chosen dependent on the counts source. In order to obtain the best possible equalization with this method, the th^* displacement factor has to be used as a matrix, not as an

individual value. Figure 7.11 shows the spread of the th^* displacement factor values per pixel.

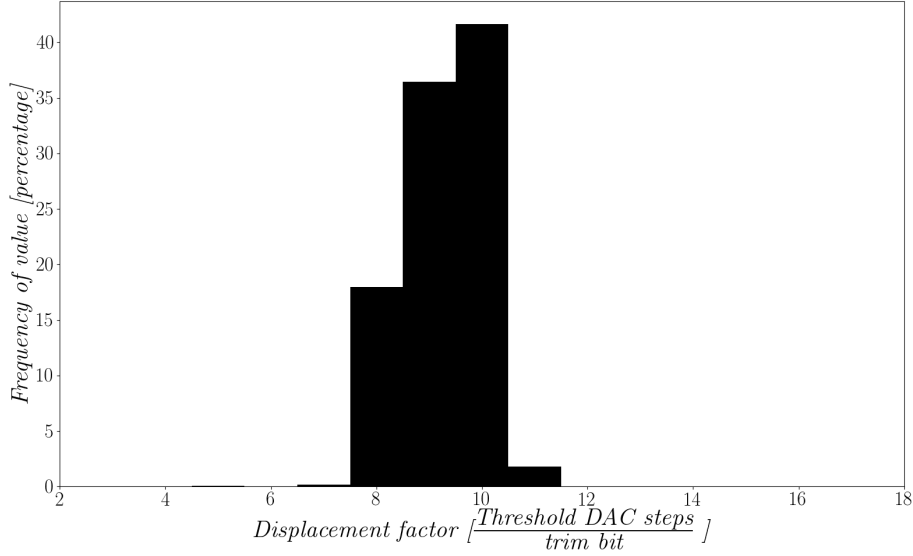


Figure 7.11: Histogram of the th^* displacement factor, using noise as a source and a trim bits swing of 5 DAC units.

To calculate the trim bits offset for each pixel, the difference between the th^* and the target th is calculated when all the pixels are configured to have no added threshold offset. The resulting value in threshold DAC units is divided by the th^* displacement factor. This can be expressed per pixel as:

$$trim_bits_{[i]} = \frac{th_{[i]}^* - th_{[i]}}{th^*_displacement_{[i]}} \quad (7.5)$$

The generated matrix of trim values is the new equalization matrix, which will bring all the th^* values closer to the target threshold value. This method considers the movement of the th^* value on the threshold spectrum to be perfectly linear with the trim bits, which is not true, but its a usable approximation. The linear method has the advantage of requiring very low computational power and it does not require further data from the sensor.

Stripes Method

To take into account that the movement of the th^* value on the threshold spectrum by the trim bits is not perfectly linear, the stripes method implements a different approach. The stripes method tests all combinations of the trim bits. Using the 5-bit

value for this configuration, 32 possible combinations exist per pixel. One of those 32 possible combinations will give the best response alignment for each pixel. The best response alignment per pixel is defined as the trim bits value for which the th^* value is closer to the target th value.

In order to avoid all the pixels of the Medipix3RX generating high counts in the same frame, which has been found to generate saturation in the sensor, a structure of ‘stripes’ is used. The stripes structure is generated by setting the first pixel to the trim bits value of -15, the second pixel to the value of the previous pixel value plus one and so on, so neighbour pixels have different trim bits values. All the trim bits values are tested for each pixel and for each value of the trim bits the th^* is calculated for all the pixels. The data obtained for each th^* position is processed, and the difference between the th^* value and the equalization target th is obtained. The trim bits value, which gave the lowest difference to the target th , is used for the final equalization matrix. This method generates the best results in the final equalization, but it requires a large amount of data taken from the sensor and it is computationally heavy.

If the equalization is done correctly, the distribution of the histogram of trim bits values in the sensor matrix should be a Gaussian with a mean of approximately 0. However, it’s usually a lower value to compensate for the equalization target being a larger value than 0. The standard deviation of the Gaussian is directly proportional to the value of `LDAC_DISC` and can be seen in Figure 7.12. A larger value of `LDAC_DISC` will generate a smaller standard deviation and vice versa. A large amount of pixels with a trim bit value on the limits, suggest that the equalization method was not able to align a large amount of pixels, suggesting that the value of `LDAC_DISC` is too low.

7.3.3 Masking noisy pixels

The Medipix3RX sensor has noisy pixels, that either do not respond to the added threshold offset, or that have such a big offset that is not possible to equalize them. Pixels which generate counts all the time also exist, independent of the input energy to the pixel or the value of the threshold. These types of pixels are undesired and must be masked. Failure to mask noisy pixels can result in images with artefacts, and the inability to reconstruct the energy peak of an x-ray source. In experiments where

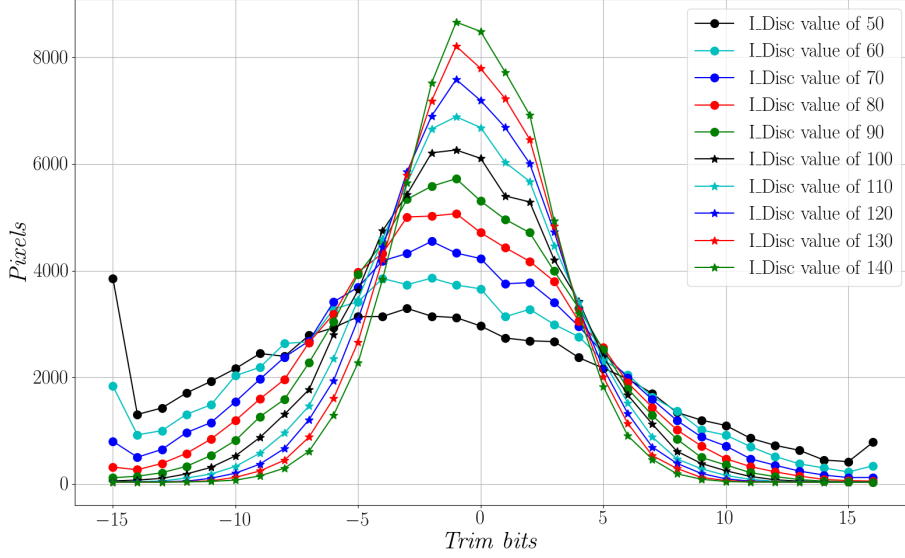


Figure 7.12: Comparison of the histograms of the trim values after an equalization with the Stripes method using electronic noise as a source, for different values of the LDAC_DISC DAC.

the energy flux is low, generating pixel counts with an average below 10, noisy pixels with saturated values of over 4000 (for 12 bit images), can create a signal to noise ratio so low that the signal cannot be reconstructed. Ideally, the pixels to be masked should be found automatically through the equalization process, without the need for a manual inspection from a user.

The process of finding noisy pixels is done after the equalization has been processed, and the sensor is configured with an equalization matrix. Depending on the source of the counts, the methodology for finding noisy pixels can differ. In general terms, the sensor has to be configured to a state, in which a correctly working pixel would not generate counts.

In the case of using electronic noise as a source, the masking is implemented by obtaining pixels that show counts outside the electronic noise band in a scan of the threshold DAC. A similar method can be implemented using injected pulses or x-rays, by setting the threshold value to be considerably higher than the input energy, with pixels that show counts marked as noisy. Another approach to find noisy pixels is to make use of the th^* after equalization. The th^* for the matrix is calculated and the extremes of the th^* distribution can be marked as noisy. By doing this, the overall energy resolution of the sensor can be improved, at the cost of losing pixels.

The pixels selected as noisy pixels are masked in hardware by the sensor. This is

done by setting the mask bit of the selected pixels which will stop the logic block of those pixels to signal the counters.

7.4 Equalization methods for each operation mode of the Medipix3RX

7.4.1 Equalization for Single Pixel Mode

For the single pixel mode operation, all the previous equalization methods can be directly applied. For each pixel, there are two discriminators which have to be equalized individually. The method is repeated identically for both discriminators, equalizing one discriminator at a time. Once a discriminator output has been selected, the algorithm should modify only the trim bits related to that discriminator.

7.4.2 Equalization for Charge Sharing Mode

When using the CSM, two discriminators must be used simultaneously. As explained in Chapter 2.4, the signal arriving to the low discriminator is the direct output of the amplifier stage of that pixel so the same equalization matrix as the one used for SPM can be used for the low discriminator. The signal arriving to the high discriminator is a mix of the summed outputs of all the neighbouring amplifier stages and the specific pixel. This results in the need for a specific equalization for the high discriminator on CSM.

The equalization procedure for the high discriminator in CSM is similar to the procedures used for SPM. The only difference is the use of the CSM for the equalization. Before starting the equalization procedure, the Medipix3RX is set into CSM. The equalization procedure with noise is then executed, and the signals arriving to the high discriminator are the sum of the output of the amplifier stage of that pixel plus the outputs of the amplifier stages from the neighbour pixels. This procedure will generate the high discriminator equalization matrix, and the full equalization for this mode will be the SPM equalization matrix for the low discriminator and the newly obtained CSM high discriminator equalization matrix.

Proposed equalization fine-tuning using x-rays

The main difficulty of equalizing with x-rays comes from the charge sharing effect on the sensor, generating double and under counts. This problem can be avoided by using the sensor in CSM. A disadvantage of performing an equalization using this mode, is that the sensor has an incorrect response if there is no equalization. If the sensor isn't equalized and it is set into CSM, then the pixel with the lowest threshold in the neighbourhood will get all the counts assigned to it, this is called the 'island phenomenon' and it is explained in Appendix D.

The equalization process can't be done in CSM mode alone, but once an equalization using a source like electronic noise has been realized, the sensor can be configured in CSM and the equalization can be fine-tuned using x-rays. As it has been explained previously, equalizing with noise will not take into account the gain mismatch. A fine-tuning equalization can be performed under energy to improve the total equalization.

The assumption is that the fine-tuning equalization will require a small movement in the offset of the pixels, to correct for the gain mismatch, which is smaller than the threshold offset. The change is small and the total range of added threshold offset will not vary, therefore, the value of `LDAC_DISC` can be kept to the optimized value calculated by the `LDAC_DISC` optimization method.

After an equalization in CSM mode has been realized, a monochromatic x-ray signal is used to flood the sensor entirely in a flat-field. Under these conditions, a scan of the threshold DAC is performed and the obtained data is used to determine the th^* value for every pixel. This obtained th^* value per pixel, is subtracted from the ideal th value, and a starting error matrix is generated. The next step is to add an offset to the value of all the trim bits of -5 and repeat, obtaining a scan of the threshold DAC and obtaining the th^* value for each pixel. These new th^* values are subtracted to the target th value, and if the error is smaller than the corresponding value on the starting error matrix, then the old trim bits are substituted by the new trim bits. This process is repeated until a range of -5 to +5 of the trim bits has been tested. In the tested range, the trim bits value per pixel that gave the closest response to the target th value is stored, and these new values generate the improved equalization.

7.4.3 Equalization for Colour Mode

In the CM, four pixels are grouped into one cluster that acts as one pixel. This architecture enables to have four energy comparisons for the same energy input. In theory, the four discriminators from one cluster are the same discriminators for individual pixels when the sensor is used in FPM, therefore, the same equalization matrix could be used between FPM and CM [8]. Nevertheless, when this was tested both with electronic noise and x-rays count sources, the results showed that this simplification generates undesired results. Using this method, only the output of one of the discriminators was equalized, the other discriminators gave a non-equalized response.

The equalization method proposed is based in using the electronic noise to equalize, and to use one discriminator at a time. The value of `LDAC.DISC` used is the optimized one for FPM. One discriminator is selected to be equalized, starting with the second discriminator, since the first one is already equalized in the FPM equalization matrix. The rest of the discriminators are set to a high threshold to remove their contribution. The stripes equalization method is used on the selected discriminator and the computed equalization matrix is stored. This process is repeated for all of the discriminators, with the partial equalization matrices mixed into one final equalization matrix.

7.4.4 Equalization for Colour Mode in CSM

For this mode, all the discriminators are used simultaneously, the even discriminators (0, 2, 4, 6) are used to assign which cluster the photon arrived, and the odd discriminators (1,3,5,7), are used to compare the reconstructed charge. It is necessary to have all the discriminators equalized to use this mode. The equalization for the even discriminators is the same equalization matrix as for the colour equalization in SPM, while the equalization for the odd discriminators is different from all other modes. Similar to the method described for the CSM mode, the same equalization method as used in the colour equalization in SPM must be followed for the odd discriminators, with the change that the CSM has to be enabled. By enabling the CSM the signal arriving to the odd discriminators will be the sum of the signals from the neighbour clusters.

Chapter 8

Experimental results

The results obtained with the fully assembled system are shown and discussed in this chapter. The chapter starts by showing the fully assembled system, discussing the maximum frame rate and testing the temperature control. Next, an analysis and discussion of the results of the equalization methods is presented. Experimental verification of how the temperature of the Medipix3RX affects its behaviour are given.

8.1 LancelotRX system results

8.1.1 Full system assembly

A full assembly with all the parts of the LancelotRX system is presented in Figure 8.1. The completed design has been fully tested and every part of the design has been integrated into a working system. Each part of the system was tested individually, using either test data or development electronic setups.

8.1.2 Frame acquisition speed

The maximum frame rate achieved with the LancelotRX system is 240 full frames per second, and 680 profiles per second. This frame rate is constant and can be maintained for an indefinite amount of time. In Table 8.1, the time required for every specific part of the process is shown. The presented times are for a 6-bit depth image acquisition, and these time values do not include the integration time.

Taking into account the image data and the merlin protocol overhead, the network

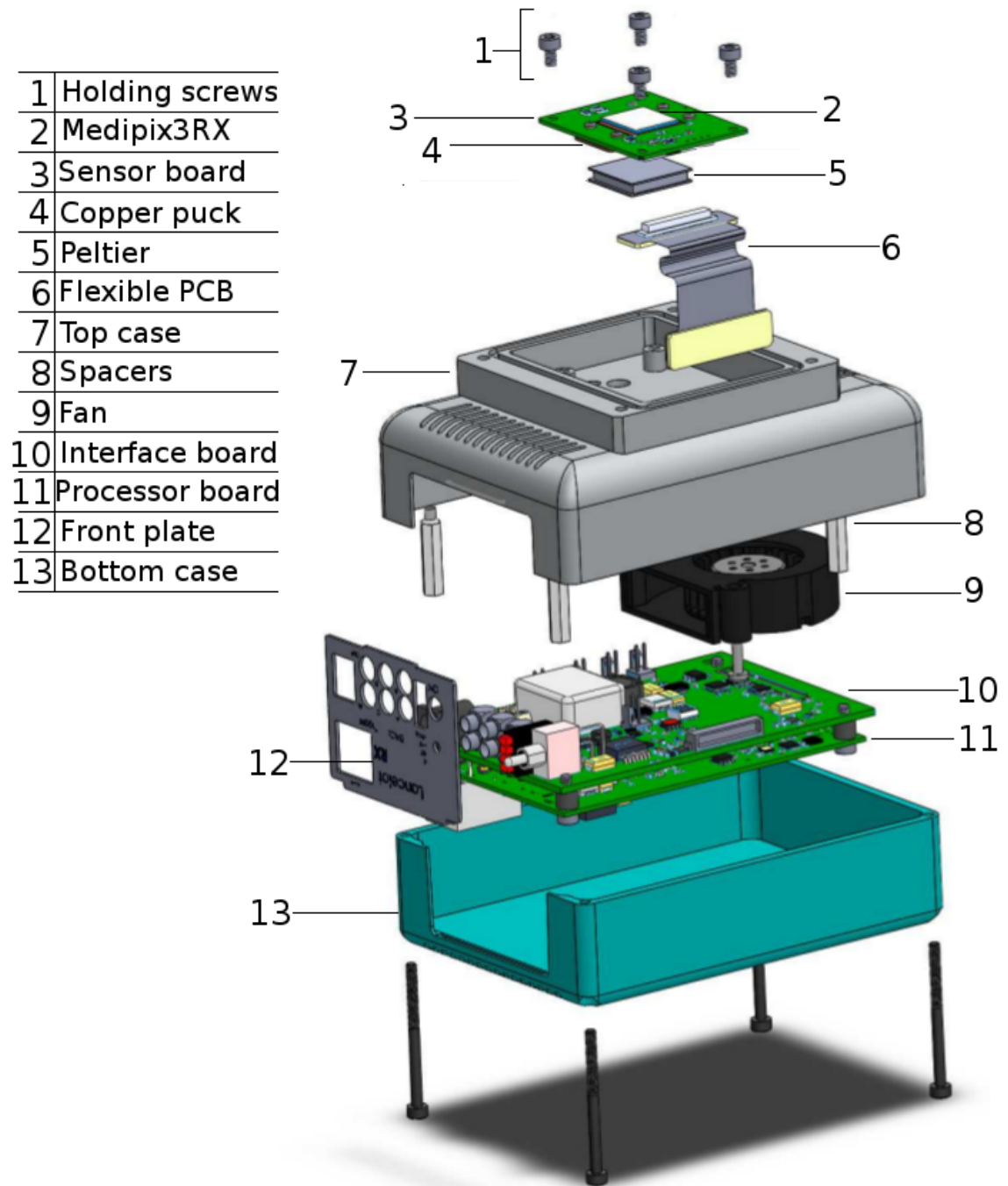


Figure 8.1: Exploded view of the full system components of the LancelotRX system.

	Full image [μs]	Profile [μs]
Loading data and triggering acquisition	64.2	69.6
Wait for pipeline readout to finish	655.7	655.7
Read Data from DDR memory	648.4	180.4
Clear finished flags for next acquisition	12.1	14.1
Generate and send header data	218.3	218.3
Send image/profile data	2432.5	310.6
Total Time	4031.4	1449.1

Table 8.1: Table of the time used for each section of the acquisition and communication of data from the LancelotRX system to a client software. All the values are given in microseconds.

transfer speed obtained is 127 Mbits/s. The LancelotRX hardware is capable of 1Gb/s bandwidth for the network, which seem to suggest that the network bandwidth is not the frame rate limitation of the system. Copying data from the DDR3 memory of the FPGA to the processor is the second more time consuming task for the images and the third for the profiles.

8.1.3 Temperature control

The designed temperature control system is able to maintain a constant operation temperature for the Medipix3RX. As shown in Figure 8.2, the temperature of the Medipix3RX sensor can be stabilized at a target temperature, for this example 15 °C Celsius is used. In Figure 8.2, the bottom plot show the temperature of the sensor when the temperature control is enabled. It takes less than 60 seconds to achieve the target temperature of 15 °C. The top plot of Figure 8.2 shows the temperature response of the sensor with and without the temperature control. The response with temperature control disabled was taken using the LancelotRX under the worst case scenario. The worst case scenario was obtained on the LancelotRX by placing the system in a thermally isolated box, disabling the internal fan, disabling the Peltier and taking continuous images with the sensor. The heating curve for the sensor on the system can be modelled using:

$$T_{sensor}(t) = T_{init} + T_{stabilization}(1 - e^{-\frac{t}{\tau}}) \quad (8.1)$$

Where T_{init} is the initial temperature, $T_{stabilization}$ is the maximum temperature at which the sensor will stabilize and τ is the time constant. The experiment was run

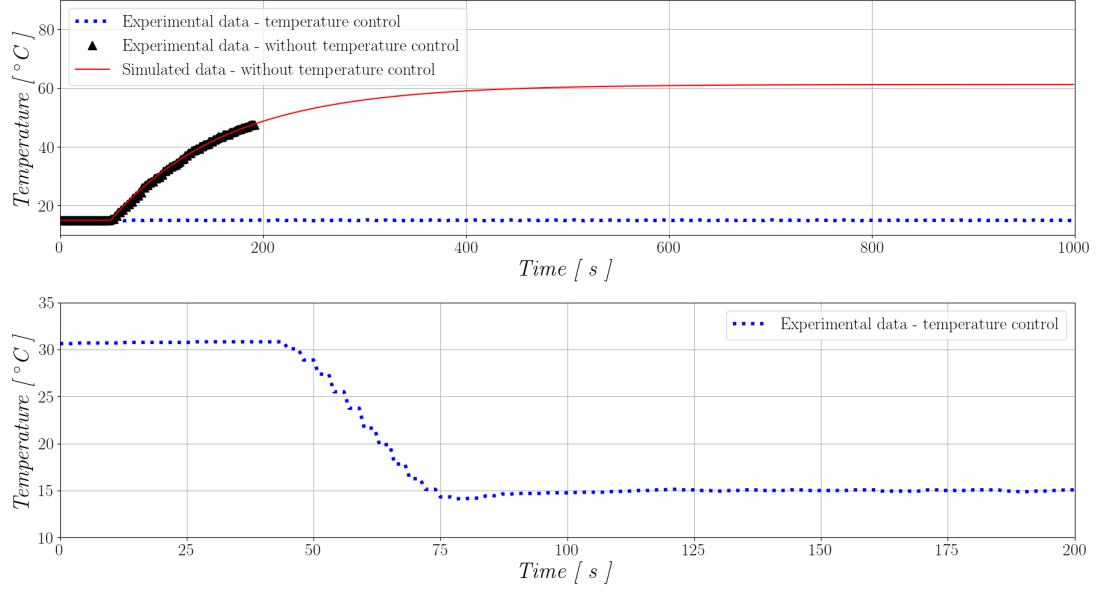


Figure 8.2: Plot of the temperature of the Medipix3RX chip on the LancelotRX system while performing a constant acquisition of images. The top plot shows the different temperature response with and without the temperature control. The bottom plot shows the speed at which the sensor’s temperature reaches the target temperature, using 15 °C in this example, once the temperature control is enabled.

until the sensor reached a temperature near to 50 °C, at this point, the experiment was stopped to protect the Medipix3RX. The electronics chamber, where the Processor and Interface board are located, reported a temperature of over 80 °C when the experiment was stopped. Allowing the FPGA’s temperature to increase further could generate erroneous data as the FPGA used is designed to work within a max temperature of 85 °C [65]. Using the measured data a response could be fitted, with parameters of a $T_{stabilization} = 62.5$ °C and a time constant of 115 seconds.

The heat generated by the sensor is dependent on the activities that the sensor performs. When the sensor is not obtaining images, the heat it generates is reduced. If the system is used in intervals of image acquisition followed by periods of no activity, then the temperature of the sensor will vary. The amplitude of the temperature change in this case will depend on the operation mode and the length of the time intervals, but swings of 5 °C in the temperature of the sensor are common when the temperature control is not being used. The changes in the temperature of the sensor through the operation time will affect the sensor’s precision [67]. When the temperature control is enabled, the maximum change on the sensor is of 0.5 °C while the operation mode of the sensor is changing.

The temperature control has been tested for target temperatures as low as 10 °C. Colder temperatures have not been tested to avoid the possible problem of water condensation on the sensor. However, while controlling the temperature to this target of 10 °C, the power required for the Peltier thermoelectric cooler corresponded to around half of the maximum power consumption allowed, which suggests that lower temperatures could be reached.

The limit on the lowest possible temperature target is set by the maximum temperature difference between the cold and hot faces of the Peltier, that for the currently used Peltier is 72 °C. Based on experimental tests using a resistor dissipating the maximum heat that the Medipix3RX can dissipate, the hot face of the Peltier will have a temperature of around 60 °C when the cold side is at -10 °C. This sets the limit of the lowest possible target temperature for the Medipix3RX on the LancelotRX to -10 °C.

8.2 X-ray intensity images

Images have been taken using the traditional x-ray absorption imaging technique, without energy spectral information. The images are formed by the different absorption rate of the imaged targets' materials. This method has been tested in SPM and in CSM, without any noticeable difference in the images produced by these methods, similar to other published work [47].

In Figure 8.3, traditional x-ray absorption images obtained with the LancelotRX are shown, a) shows a microprocessor in a TQFP package and b) an SD card memory. The images were taken using a flat field of 12 keV, whilst placing the components in front of the Medipix3RX. No pinhole camera setup was used. The resolution corresponds to 55 μm , the square size of the pixels.

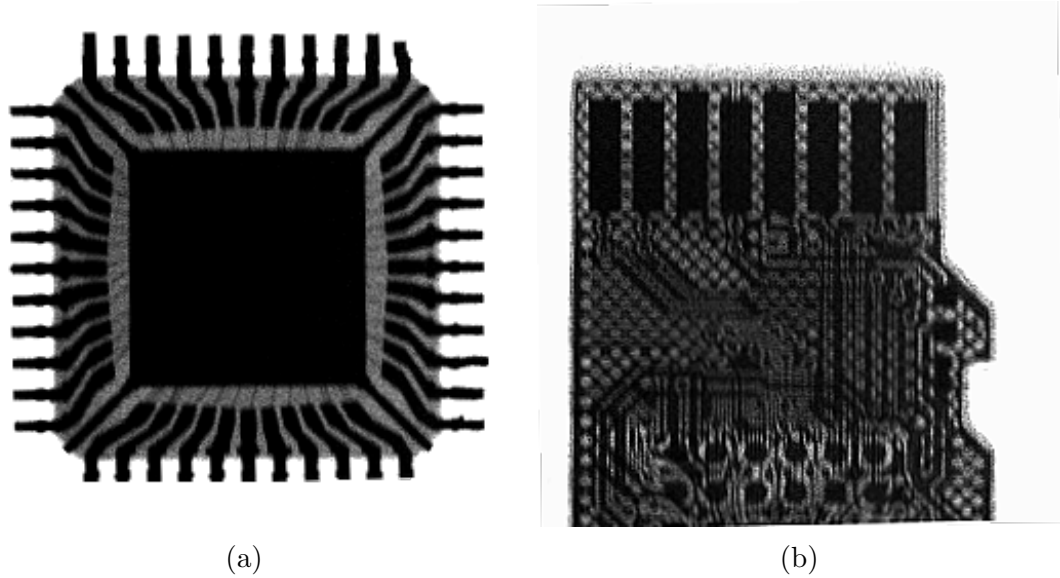


Figure 8.3: Images obtained with the LancelotRX using traditional x-ray absorption imaging. A flat field of 12 keV was used and direct imaging of the objects. a) Microprocessor Atmega32U4 [9] with a TQFP package. The wire bonding from the silicon chip to the integrated circuit pins can be detected. b) SD card memory, a hatched copper pour on the PCB can be clearly seen.

8.3 Threshold equalization results

Both SPM and CSM have been equalized and used for energy measurements after equalization. In Figure 8.4, the analysis of the energy spectrum using both SPM and CSM is shown. The x-ray signal measured is the fluorescence of a copper strip, with a K_α of 8.05 keV. The energy of the fluorescence can be obtained from the spike response in the differential scan. It is possible to identify the energy peak in both in the SPM and CSM. To measure the energy resolution, the Full Width at Half Maximum (FWHM) will be used. The FWHM is obtained by fitting a Gaussian function to the energy peak and multiplying σ by $2\sqrt{2\ln 2} \approx 2.3548$.

The selection of which source to use for equalization ends up being a compromise, either time and source practicality, or energy resolution have to be selected. To compare the time needed between sources and methods the total integration time is used. The total integration time is the amount of time the electronic shutter of the Medipix3RX has to be opened for the equalization procedure. This amount of time is independent of the way the equalization method is implemented or the processing speed of the results, which is why it's selected for comparison of the results. The integration time for the image used for equalization with electronic noise is 10 ms, 50

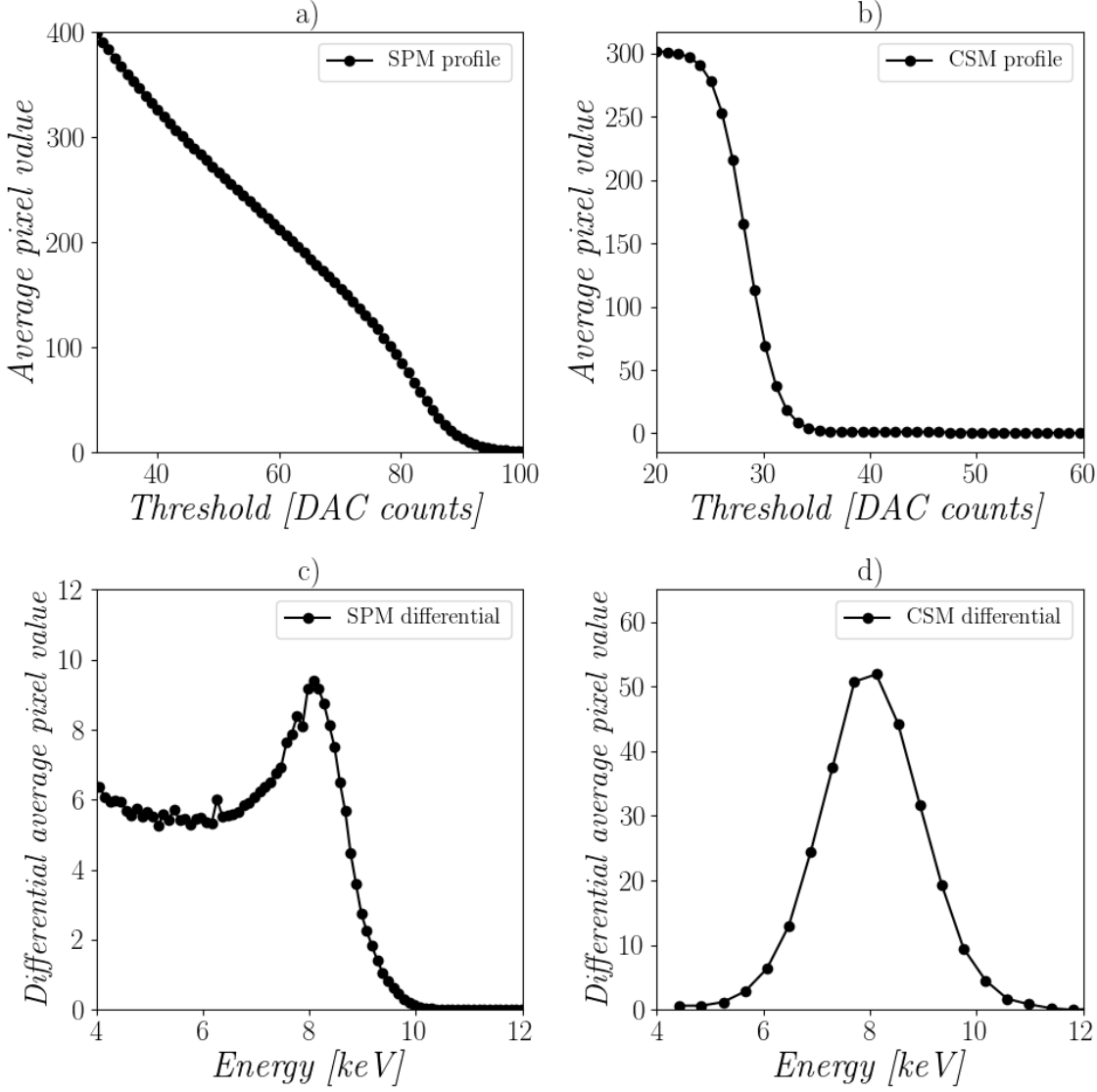


Figure 8.4: Energy spectrum of copper x-ray fluorescence, $K_{\alpha}=8.05$ keV, in both SPM and CSM. a) Scan of the threshold DAC in SPM. b) Scan of the threshold DAC in CSM. c) Differential scan of the threshold DAC in SPM, the charge sharing effects are notable before the energy peak. d) Differential scan of the threshold DAC in CSM.

ms for injected pulses and 500 ms for x-rays. The integration times were selected to ensure enough counts in the pixels. As it is possible to see from the data on Table 8.2, the linear equalization method is the fastest method to implement, since it requires the least amount of images taken.

	Total integration time required for equalization methods					
Source	Noise		x-rays		Pulses	
Method	Linear	Stripes	Linear	Stripes	Linear	Stripes
Time [min]	0.20	0.35	15	27	18	32

Table 8.2: Total integration time required for the different methods and sources for equalization. The time shown in minutes corresponds only to the integration time needed, processing and communication time are not counted since they are dependent on the implementation and hardware.

8.3.1 Single Pixel Mode

The results obtained by the FWHM of the fitted energy response show that the stripes equalization method gives a better energy resolution than the linear one, with an average of a 22% decrease on the FWHM. In Figure 8.5, a comparison of the linear and stripes equalization methods on noise is shown. The response of a non-equalized Medipix3RX is given for comparison. Based on the improved energy resolution given by the stripes method, the following experiments comparing different counts sources are given for the stripes method.

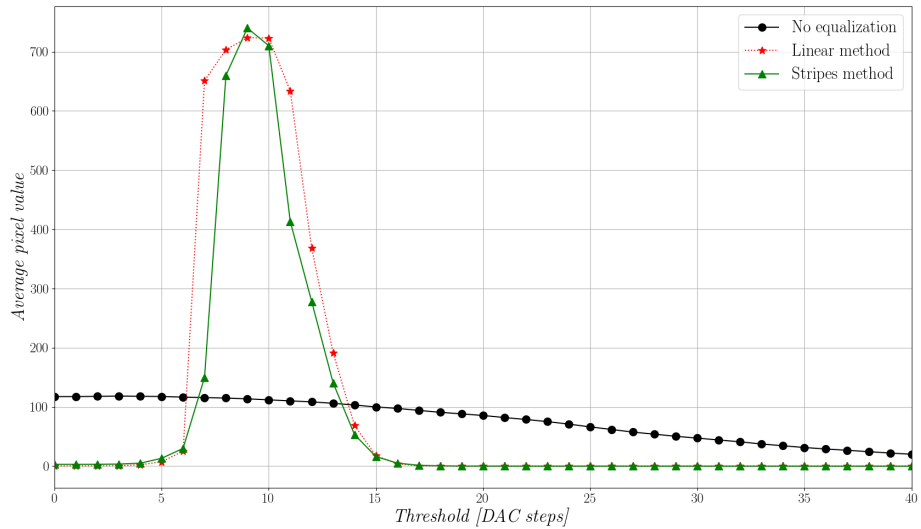


Figure 8.5: Comparison of the Noise counts on a scan of the Threshold DAC values for a non-equalized sensor, a noise linear equalization and a noise stripes equalization.

Electronic noise

The energy resolution obtained in SPM using electronic noise as a source is shown in Table 8.3. The energy resolution is measured with the FWHM and shown for different

	FWHM (keV) using Noise				
Gain Mode	6 keV	8 keV	9 keV	15 keV	17 keV
SLGM	2.20	2.11	2.26	2.58	2.70
LGM	2.11	1.67	1.94	2.35	2.68
HGM	1.80	1.58	1.77	2.14	2.53
SHGM	1.63	1.53	1.63	1.92	2.40

Table 8.3: Full Width at Half Maximum (FWHM) energy resolution, using an equalization method based on electronic noise, for all the gain modes. The Medipix3RX is used in SPM and the energy resolution is measured for the energies of 6, 8, 9, 15 and 17 keV.

	FWHM (keV) using x-rays				
Gain Mode	6 keV	8 keV	9 keV	15 keV	17 keV
SLGM	1.92	1.95	2.12	2.03	2.04
LGM	1.87	1.98	2.09	2.08	2.06
HGM	1.47	1.50	1.84	1.63	1.59
SHGM	0.99	1.35	1.17	1.11	1.25

Table 8.4: Full Width at Half Maximum (FWHM) energy resolution, using an equalization method based on x-rays, for all the gain modes. The Medipix3RX is used in SPM and the energy resolution is measured for the energies of 6, 8, 9, 15 and 17 keV.

energies. All the gain modes of the Medipix3RX have been tested and, as expected, the best energy resolution has been achieved using the Super High Gain Mode (SHGM). The worst energy resolution is found for the Super Low Gain Mode (SLGM). It is important to note that the FWHM increases as the tested energy increases, this is caused because of the gain mismatch. The equalization is done at the zero level, and as the energy increases, the gain mismatch generates a higher threshold dispersion, increasing the FWHM.

X-ray photons

Table 8.4 shows the obtained energy equalization resolution using x-rays as a source. As with electronic noise, the best energy resolution is obtained for the highest gain of the Medipix3RX. There is a small increment of the FWHM as the energy increases. In difference to the equalization using electronic noise as a source, the equalization using x-rays takes into consideration the gain mismatch and therefore the energy resolution stays similar across different energies.

The best energy resolution achieved for SPM has a FWHM of 0.99 keV, using x-rays as a source and equalized using photons with an energy of 6 keV. For the same

	FWHM (keV) using Pulses	
Gain Mode	15 keV	17 keV
SLGM	4.41	4.75
LGM	4.59	3.82
HGM	4.26	3.91
SHGM	3.88	3.58

Table 8.5: Full Width at Half Maximum (FWHM) energy resolution, using an equalization based on injected pulses. The Medipix3RX is used in SPM and the energy resolution is measured for the energies of 15 and 17 keV.

energy using electronic noise, a FWHM of 1.63 keV was obtained. Using x-rays as an equalization source a better energy resolution is obtained than using electronic noise, but it requires an x-ray source and over 70 times more total integration time than using electronic noise.

Injected pulses

The equalization methods based on pulses showed promising results when tested with injected pulses, but the results obtained when tested with x-rays were not as expected. Table 8.5 shows the FWHM energy resolution obtained by the stripes method using pulses as a source. An increased range of zero-level noise in the threshold DAC spectrum made the reconstruction of the energy peak difficult for lower x-ray energies, only the energies of 15 keV and 17 keV could be correctly reconstructed.

As shown in of Table 8.5, the energy resolution obtained with pulses is the worst of the tested sources. The FWHM obtained with pulses are almost double the values obtained with electronic noise. This problem could be caused by a mismatch in the value of the capacitors used to inject the test pulses. As reported by Ballabriga [47], the technology parameters used for the manufacture of the Medipix3RX have a tolerance of $\pm 20\%$ of capacitance values. Any mismatch in the value of capacitors could be the cause of why the equalization using pulses gave good results when tested against injected pulses but bad ones when tested against x-rays. On the other hand, Rinkel [76] reports a FWHM of 0.79 keV using an equalization based on pulses, whose results could not be duplicated on the LancelotRX. Further analysis and testing on the injected pulses capacitor value variance is needed, as well as in the effects of this variance in equalization procedures.

	FWHM (keV) using Noise in CSM				
Gain Mode	6 keV	8 keV	9 keV	15 keV	17 keV
SLGM	2.37	2.73	2.74	3.62	3.88
LGM	1.94	2.34	2.35	3.01	3.34
HGM	2.09	2.01	2.07	2.74	2.97

Table 8.6: FWHM energy resolution, using an equalization based on electronic noise. The Medipix3RX is used in CSM and the energy resolution is measured for the energies of 6, 8, 9, 15 and 17 keV.

Another equalization method, based on injected pulses, was tested. The method is named ‘Pixels parameters’ and it is described in Appendix D.2. For this method, the effect of the capacitance mismatch was worse, making it impossible to reconstruct the energy peak.

8.3.2 Charge Sharing Mode

In Table 8.6, the obtained energy resolution using noise equalization for CSM is shown. In general, the obtained values show a better energy resolution by using higher gain modes of the Medipix3RX. As expected, by the equalization made using noise as a source, the FWHM increases as the tested energy increases. The obtained FWHM values for CSM are larger than the ones obtained for SPM, this degraded energy resolution response is caused by the sum of the uncorrelated electronic noise between four pixels in the CSM [77].

Equalizing for the SHGM in CSM gave an unexpected response from the Medipix3RX. By using the same method as applied to all the other gains, the sensor gave a ‘saturated’ response, in which all the pixels showed the maximum count value, stopping the algorithm generating a working equalization. This problem does not seem to be a bug in the sensor since others have reported of been able to equalize for SHGM in CSM [78]. It’s possible there is a problem in the way the algorithm is implemented. Walsh reports a similar finding, by stating that when the Medipix3RX is set into the SHGM and CSM, the electronic noise on the threshold DAC behaves in a non-linear fashion [79], which can be solved by using the HGM instead of the SHGM.

	FWHM (keV) using fine tuning in CSM				
Gain Mode	6 keV	8 keV	9 keV	15 keV	17 keV
HGM	1.69	1.70	1.79	2.24	2.48

Table 8.7: FWHM energy resolution, using an equalization based on electronic noise. The Medipix3RX is used in CSM and the energy resolution is measured for the energies of 6, 8, 9, 15 and 17 keV.

Fine-tuning using x-rays

Using the proposed fine-tuning method on x-rays is possible to improve the energy resolution in CSM. Table 8.7 shows the results of the FWHM response for the tested energies. Only the High Gain Mode (HGM) was tested due to time constraints. On average, an improvement of the energy resolution by a 16.3% reduction of the FWHM was obtained.

The process can be significantly time consuming. In the completed experiments, the process took between 90 to 120 minutes to be executed. These values are determined by the range of threshold DAC to be scanned and the required integration time per image necessary to ensure enough photon counts. To use this method for practical experiments, the used energy must remain constant, otherwise, the proposed fine tuning equalization must be processed every time the experiment energy is changed.

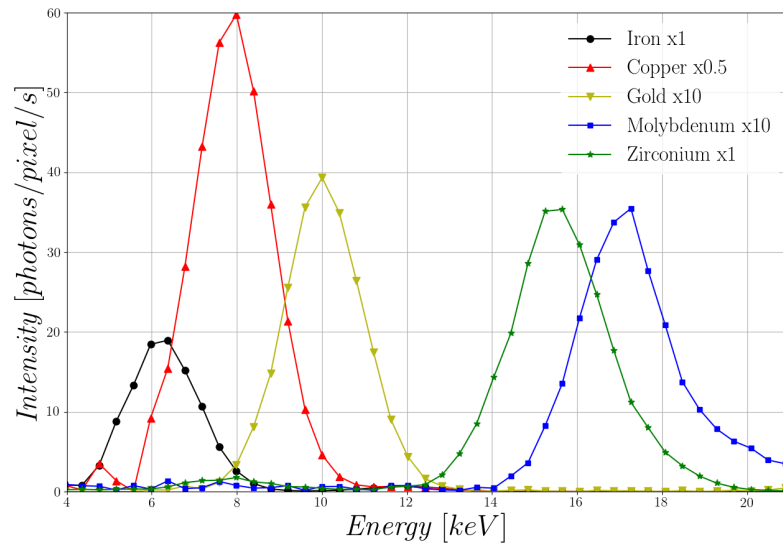


Figure 8.6: Differential scan of the Threshold DAC in CSM for the x-ray characteristic fluorescence of different elements.

Tested x-ray fluorescence

In Figure 8.6, a plot of the measured characteristic x-ray fluorescence from different elements is shown. This plot shows that different elements can be correctly discerned by their characteristic x-ray fluorescence by using a scan of the threshold DAC in CSM. A 20 keV photon beam was used to hit the target elements and generate the x-ray fluorescence. Each element fluorescence was measured individually.

8.3.3 Colour Mode

The suggested method in the Medipix3RX manual [8] to equalize the sensor in CM was found to give poor results, equalizing correctly only one of the four thresholds used. In contrast, the proposed method in this work generates a correct equalization, where all the thresholds present a similar response to electronic noise or x-rays. The energy resolution shows no difference to the one from the SPM, whose results are shown in Table 8.3.

8.3.4 Comparison with the energy resolution of an individual pixel

Using the HGM and an energy of 8 keV, the average energy resolution obtained in FWHM for one individual pixel is 1.17 keV for SPM and 1.25 keV for CSM. These values show a better energy resolution than the one obtained for the entire matrix, that is 1.5 keV for SPM and 1.7 keV for CSM (as shown in tables 8.34 and 8.7 respectively). The increment of the FWHM is to be expected, caused by a non-perfectly equalized sensor.

The FWHM energy resolution for an individual pixel is affected by different factors, also called peak broadening factors, and can be divided in three categories:

- The amplitude of the electronic noise generated by the combination of the preamplifier-amplifier, denoted as δ_{EN}
- Incomplete charge collection and variations of the energy lost by the particle in dead layers of the detector, denoted as δ_{INC}

- The statistical error created by the variance in the number of charge carriers (electron-hole pairs) created by an incident x-ray photon, denoted as δ_X .

All the mentioned sources of peak broadening are normally independent, so the total energy resolution, δ_T , can be calculated as:

$$\delta_T^2 = \delta_{EN}^2 + \delta_{INC}^2 + \delta_X^2$$

The δ_T represents the theoretical single pixel resolution limit. The biggest contribution to the energy resolution for this application is given by the electronic noise, which for SPM, the Medipix3RX at 20 °C and HGM is ≈ 1.1 keV.

8.4 Medipix3RX temperature dependence

The temperature control implemented on the LancelotRX was used to test the temperature dependence of the Medipix3RX. Three aspects of the Medipix3RX were tested for temperature dependence, the electronic noise present on the chip, the threshold dispersion between pixels and the energy calibration. A explanation of the energy calibration procedure is given in Appendix D. The noise and threshold dispersion were tested without x-rays and the energy calibration was tested using x-rays at the beamline BM26A at the European Synchrotron Radiation Facility (ESRF).

8.4.1 Threshold dispersion and noise amplitude temperature dependence

To measure the amplitude of the electronic noise of the Medipix3RX, a scan of the threshold DAC was used. As explained in Chapter 7, in subsection 7.3.1, the electronic noise can be used to generate counts on the Medipix3RX. Considering only the response of one pixel in a scan of the threshold DAC, the shape of the scan plot will be a pulse, where the width of the pulse, in DAC steps, is dependent on the amplitude of the noise. For this experiment, the average width of the pixel's pulse generated by noise on a scan of the threshold DAC is used as a measure of the noise amplitude on the Medipix3RX.

The threshold dispersion is measured by the standard deviation (σ) of the noise response obtained by a scan of the DAC threshold. For this experiment, no equalization

procedure was used, the Medipix3RX was used in its default state to measure the raw threshold dispersion. The results of the scans of the threshold DAC were fitted to a Gaussian function to find the σ .

Both noise amplitude and threshold dispersion tests were done for a range of temperatures starting at 10 °C and finishing at 40 °C. The maximum temperature was set by a technical limit with the LancelotRX. After 40 °C there is not a stable control of the temperature, the temperature increases if the Medipix3RX is operating constantly, and decreases if the detector is not in use. Particularly, the scans of the threshold DAC are not a constant operation, because communication to change the value of the threshold DAC is needed between each frame. To complete this experiment up to a higher temperature, a different setup would be needed, one that can controllably and stably heat up the Medipix3RX.

The obtained results are shown in Figure 8.7. In a) the average value of the noise amplitude is shown to decrease as temperature increases for the tested range. A similar behaviour is shown for the threshold dispersion in b), decreasing the dispersion of the threshold as the temperature increases. A plot of different noise response scans of the threshold DAC are shown in c), showing that for the temperature of 40 °C the noise response has the smallest dispersion of the set.

Based on these temperature experiments and the ambient temperature of the Synchrotron light experimental facilities, a temperature of 20 °C was chosen as a target temperature. The room temperature in various experimental facilities is between 20 °C and 25 °C, forcing the target temperature to be under this range if constant temperature control is desired. The equalization procedures were done at this target temperature.

8.4.2 Energy calibration temperature dependence

To test how dependent the energy calibration is to the temperature of the sensor, a test was executed at the ESRF. Monochromatic x-ray flat fields flooding the detector at different energies were used to calibrate the detector. The sensor was equalized using noise for SPM. Both the equalization and the energy calibration were done at a controlled temperature of 20 °C for the Medipix3RX.

After a calibration procedure, a monochromatic 16 keV x-ray was used to flood

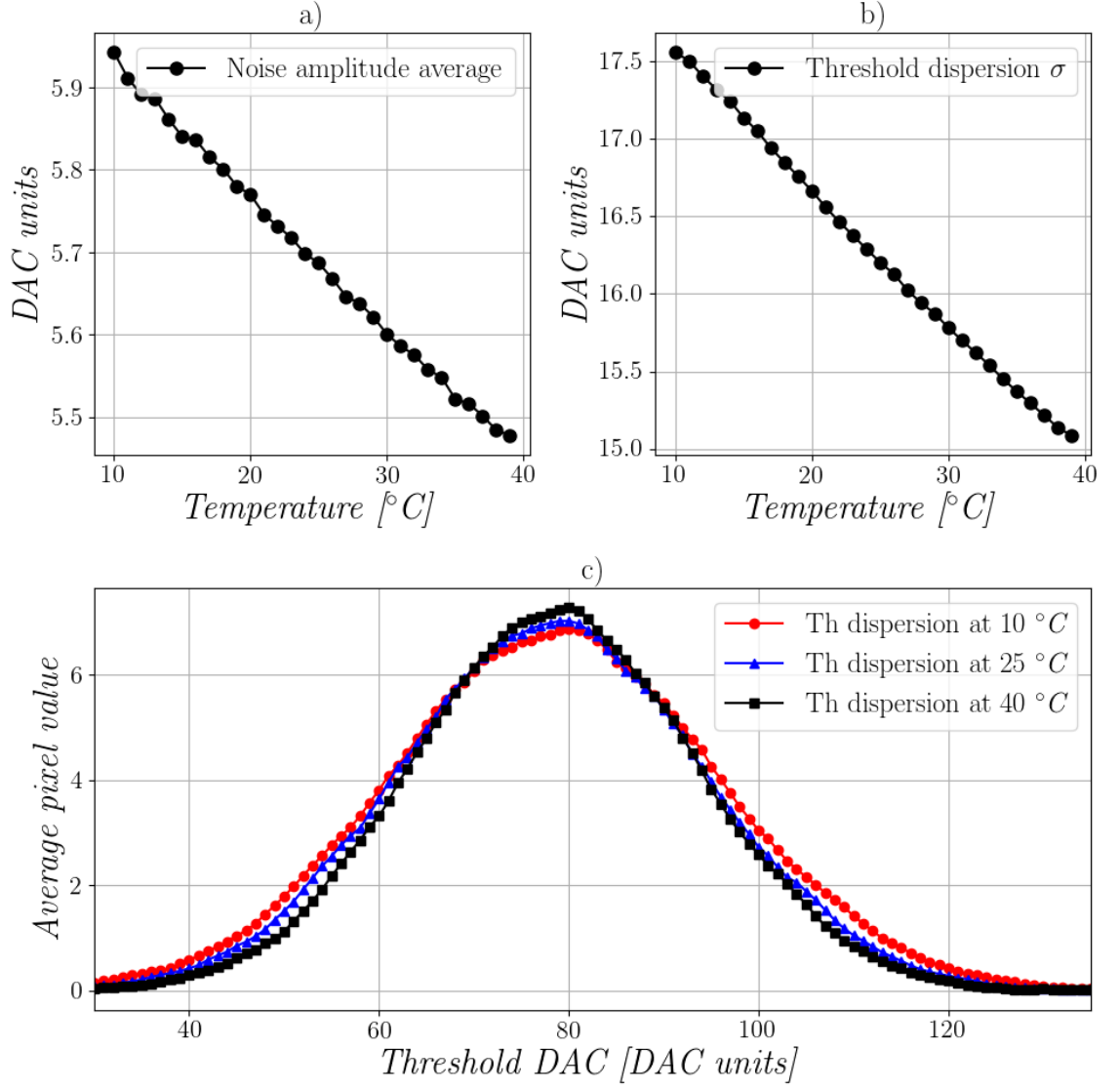


Figure 8.7: Noise amplitude and threshold dispersion dependence on temperature on the Medipix3RX. a) The noise amplitude average in DAC units for different temperatures. b) The threshold dispersion standard deviation for a non-equalized Medipix3RX at different temperatures, the threshold dispersion is measured using electronic noise as a source of counts. c) Response of the noise in a scan of the threshold DAC for a non-equalized Medipix3RX at different temperatures. As the temperature increases the dispersion of the noise response decreases, but the mean of the response does not change significantly.

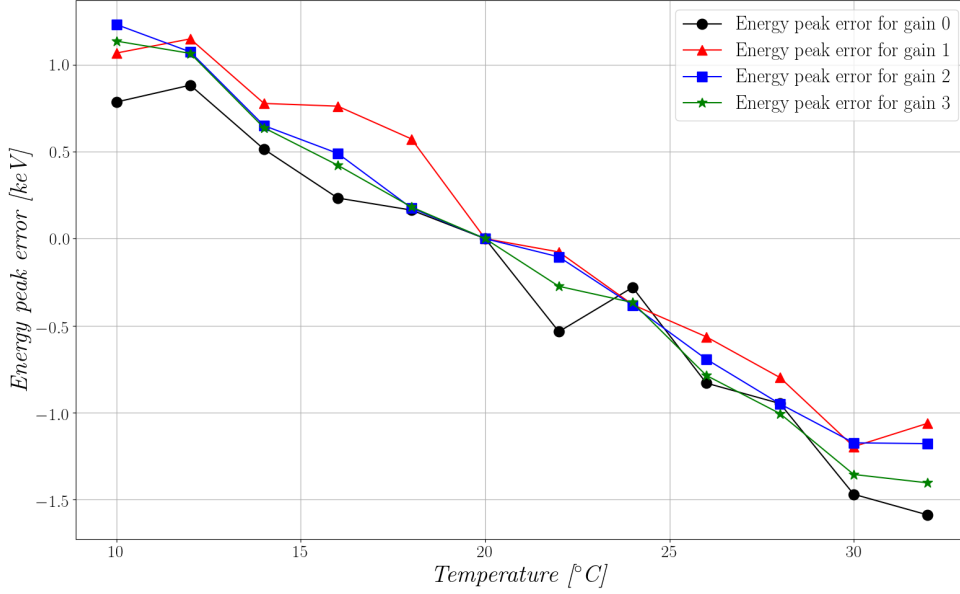


Figure 8.8: Erroneous change of the detected energy peak based on temperature changes of the Medipix3RX. The calibration was performed for a Medipix3RX at 20 °C and a 16 keV monochromatic x-ray flat field was used to detect the energy peak. The Medipix3RX was operating in single pixel mode, and the energy peak was calculated by applying Gaussian fittings to the scans of the threshold DAC.

the detector. For each temperature in the range of 10 to 32 °C, in increments of two, a scan of the threshold DAC was used to find the energy peak. The obtained energy peaks at different temperatures did not match the 16 keV, an error between the measured energy peak and the real energy peak was found. In Figure 8.8 the error of the obtained energy peaks for each temperature tested are shown. The measurement is repeated for all the gain modes of the Medipix3RX. For each gain and temperature increment, one measurement was completed. The maximum error swing is of 2.45 keV for the highest gain mode in the tested temperature range. All the errors are zero at 20 °C, since this is the temperature used for the equalization and calibration procedures.

Chapter 9

X-ray Beam position monitor application

An application of the LancelotRX system is as an x-ray beam position monitor (XBPM) for an x-ray photon beam generated at a Synchrotron light source. This chapter describes the application of the LancelotRX system as an XBPM. The chapter starts by discussing the current solutions to implement an XBPM, with their advantages and disadvantages analysed. The proposed implementation of an XBPM using LancelotRX is presented and the physical principle is explained, then the features of the proposed implementation are discussed. The chapter concludes with experimental results of the XBPM application obtained at Diamond Light Source in beamlines I19 and I24.

9.1 Current x-ray beam position monitoring techniques

A common application for the microfocused and monoenergetic x-ray photon beams used in third-generation synchrotron light source facilities is to probe and image materials at a molecular scale. The non-destructive procedure enables the discovery of the tested material structure, which has proved to be highly valuable for many scientific disciplines as well as industrial applications [80].

The electromagnetic radiation is generated in the storage ring of the Synchrotron

light source and passed to each beamline, where the beam will pass different optical devices that will modify its shape, photon flux and bandwidth. The different optical devices used to control and modify the beam can introduce small errors or uncertainties. Other factors like the temperature of the devices, for example the temperature of the monochromator used to ensure the beam is monoenergetic, will change the way the device interacts with the beam and the final beam position. The combination of all the devices' errors or uncertainties in the beam path, plus the effect of external factors like temperature, mechanical tolerances or vibration results in an unstable position of the x-ray beam.

In order to effectively characterize the molecular structure of materials, or realize other experiments requiring similar spatial scale resolution, and as the size of the tested sample approaches the size of the beam's cross-section, it is necessary to control in real-time the position of the beam. The position of the beam must be known before the experiment starts to ensure the correct reconstruction of the data. To accomplish this, an x-ray Beam Position Monitor (XBPM) and the ability to move the beam position are essential.

Different methods to monitor the position of the photon beam have been implemented in synchrotron facilities. The methods can be divided into two groups, the methods that are destructive for the beam and the non-destructive. A destructive method is one that does not allow the beam to pass through, while a non-destructive method behaves as transparent to the beam allowing it to continue on its path. The advantage of the non-destructive methods is that they can be used simultaneously to an experiment taking place, commonly named 'in-situ'. This grants the ability to know the position of the beam throughout the experiment and correct it in real time.

9.1.1 Destructive XBPM techniques

A common and simple destructive method used to align the x-ray photon beam is to use a luminescent screen [81], for example a phosphor screen [82], a material that generates visible light when it interacts with the x-ray photons. These type of screen in conjunction with a visible light camera, are used to align the position of the x-ray photon beam previous to the experiments. When the position of the beam is correct,

the fluorescent screen is removed and the experiments are run. This method is inexpensive and simple, but has an inaccurate position resolution. An other disadvantage is that the phosphor screens deteriorate as they are exposed to high flux x-ray photon beams for long periods [83], reducing the ability of the screen to generate visible light.

9.1.2 Non-destructive XBPM techniques

Several implementations of non-destructive methods have been developed and a few are worth noting. The first is the use of a gas chamber to monitor the position of the beam [84], based on photoluminescence generated by the ionization of the gas atoms when an interaction with the x-ray photons occur. The visible light is detected using a Charge Coupled Device (CCD) camera next to the beam line. This method has the disadvantage of requiring different gasses and the obtained spatial resolution is approximately $1\text{ }\mu\text{m}$. Other position sensitive implementations based on ionization chambers have been used for specific applications [85] [86].

A common XBPM method consists of placing an array of thin blades in the path of the x-ray photon beam and sensing the small current generated on the blades by the loss of electrons with the interaction with the x-ray photon beam [87]. The difference in the current between the blades is analysed to determine the position of the beam. The blades can be manufactured from different elements, with tested applications using tungsten [87] or aluminium [88]. This method generates a small area where the beam's position can be correctly measured, however, an estimation of the shape of the beam can't be performed and some of the designs can require complex water-cooling systems [89].

An other positioning method reported, is to use a metal foil in the path of the x-ray photon beam to generate characteristic fluorescence x-rays. The fluorescence x-rays are then detected by an array of four photodiodes which are placed around the metal foil [90]. The output of the four photodiodes is used to determine the position of the centre of gravity of the beam. Some of the disadvantages of this method include the fact that several metals foils are required to work in different energy bands and still have fluorescence, as well as the anomalies that the system can introduce to the experiment if energies close to the absorption edges of the foil material are used.

Another approach to create an XBPM is to use polycrystalline diamond synthesized using a technic called chemical vapour deposition (CVD). CVD diamond has the features of a high electron-hole pair mobility, an excellent resistance to harsh conditions and radiation exposure [91] and a low absorption at low x-ray energies [92]. Using an approach of four-quadrant electrodes, detecting the centre of gravity of the beam can be computed [92] [93]. The disadvantages of this method include having a small area where the centroid of the beam can be fully determined, and an inability to reconstruct the cross-section shape of the beam.

9.2 LancelotRX as an x-ray beam position monitor

9.2.1 Principles of operation

The principle of operation is to obtain a cross-section image of the beam within an area of reference, and to use the cross-section image to determine the position of the beam. In order to obtain a cross-section image of the x-ray photon beam a thin scattering foil of a low-Z material is placed in the path of the beam. The scattering foil will scatter a fraction of the x-ray photons and allow the rest to keep their original path. From the scattered photons, some of them will pass through a pinhole forming an image that is detected by the Medipix3RX sensor on the LancelotRX system. In Figure 9.1 the basic principle of operation is depicted, the image formed on the Medipix3RX is a deformed cross-sectional image of the beam.

As shown in Figure 9.1, a change in the position of the beam will generate a change in the position of the cross-sectional image on the sensor. The plane of the detector will be referenced as x' and y' and the displacements of the beam from the midpoint of the sensor will be referenced as δx and δz for the planes x and z respectively. To model the movement of the image formed on the Medipix3RX, the footprint of the beam will be considered small and the thickness of the pinhole sheet will be considered negligible. With these considerations the model can be expressed as:

$$\frac{\Delta x'}{\delta x} = \frac{L}{D} \quad (9.1)$$

$$\frac{\Delta y'}{\delta z} = \frac{L}{D} \frac{1}{\tan \alpha} \frac{1}{(1 + \frac{\delta z}{D})} \quad (9.2)$$

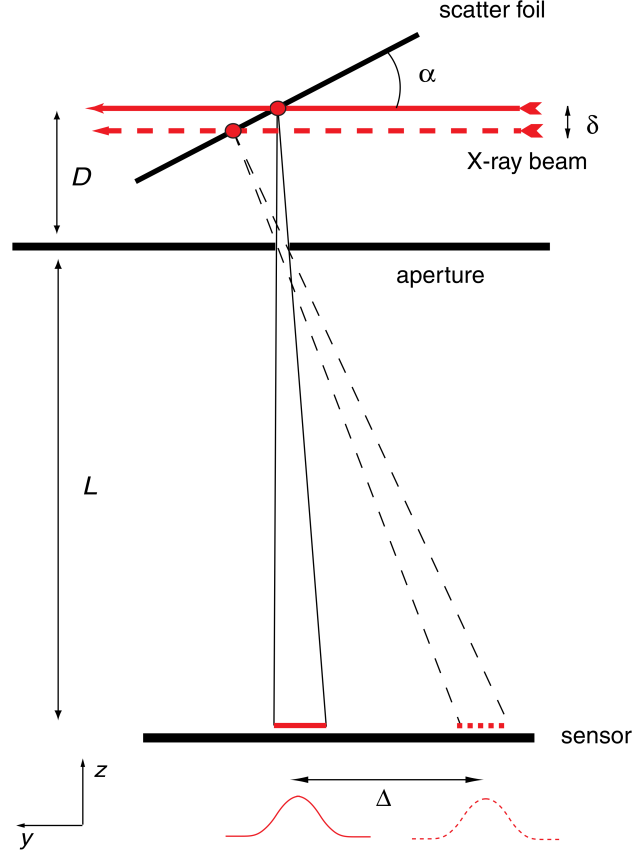


Figure 9.1: Schematic of the principle of operation of the XBPM (not drawn to scale). Some of the photons will be scattered by the foil held at an angle α and pass through the pinhole generating a deformed cross-sectional image of the beam on the sensor. A displacement of δ on the beam results in a Δ displacement of the cross-section image on the sensor. If the angle α is constant, then the magnification is given by the ratio L/D [10].

Where $\Delta x'$ and $\Delta y'$ are the values of the position shift of the cross-section image on the sensor, the tilt angle of the foil is referenced as α , and as shown in Figure 9.1, L is the distance from the detector to the pinhole and D is the distance from the pinhole to the scattering foil. In Eq. 9.2, the third term on the right hand is used as a correction of the variation in distance between the footprint of the beam on the foil and the pinhole.

Considering that the movement on z , as denoted by δz , is of a very small value in comparison with the value of D , then the whole third term on the right hand of Eq. 9.2 can be neglected. If the tilt angle of the foil is considered as $\alpha = 30^\circ$, solving Eq. 9.2 shows that the magnification on the y' axis is a factor $\sqrt{3}$ bigger than the magnification along the z' axis. This difference of magnification is what generates the

distorted representation of the beam's true cross-section.

The magnification of the beam cross-section is determined by the L/D ratio, which is dependent on the mechanical design for the XBPM application. Using a higher magnification creates a better pixel resolution of the beam's deformed cross-section. The disadvantage of using a higher magnification is that the detected intensity spreads over a larger area generating fewer counts in each pixel, which can translate into poor quality fittings to find the centroid of the beam. The overall spatial resolution of the beam's position is dependent on magnification, image intensity and signal to noise ratio (SNR) [94]. Another disadvantage of using a high magnification is that it reduces the range of movement of the photon beam on the scattering foil in which a cross-sectional image will still be formed on the sensor.

To calculate the real location of the beam, the measured vertical and horizontal positions of the generated image are used. There are several methods proposed in the literature to obtain real position based on pinhole cameras and pixelated detectors [95] [96] [97], but the method to be implemented will be based on vertical and horizontal profiling of the obtained image. Reducing the data in the 2D images to two segments of 1D profiles significantly simplifies and increases the processing speed of the system. Using profiles instead of the 2D image will increase the SNR of the obtained data [98]. Figure 9.2 shows an example of the image formed on the Medipix3RX of the beam's deformed cross-section. The profiles of the image will be used by fitting a Gaussian function and finding its mean (μ). The quality of the fitting will be dependent on the SNR of the acquired image.

9.2.2 Physical additions to LancelotRX system for the XBPM application

To implement the proposed XBPM system, a thin foil to act as a scatter is required. It is common for diagnostic purposes to use a Low-Z material to scatter the beam [99]. Based on this, the foil selected is a polyamide foil (Kapton $C_{22}H_{10}N_2O_5$). This material has primarily been selected for two reasons. The first, is a low absorption for the desired energy range (10 keV to 25 keV), and the second is that the transmission curve is smooth and presents no irregularities, which is needed to ensure that no

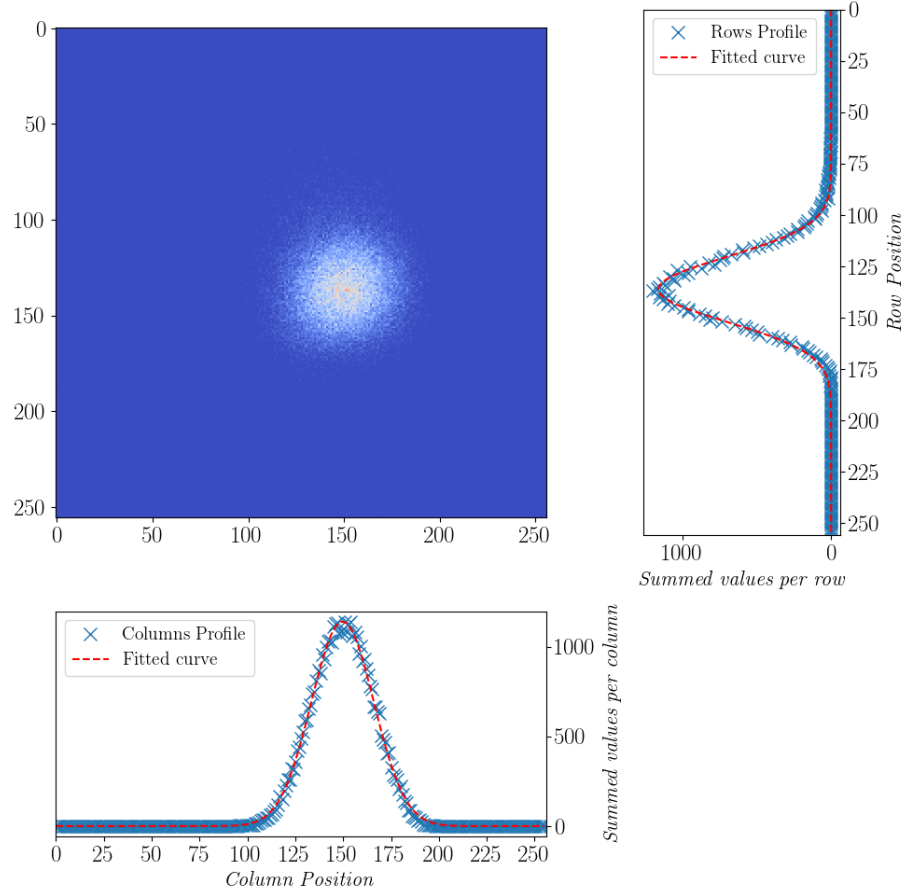


Figure 9.2: Example of the image obtained with the Medipix3RX of the deformed cross-section of the x-ray photon beam using the LancelotRX as an XBPM. The graphs represent the profiles for rows and columns of the acquired image by the Medipix3RX. The profiles are fitted with a Gaussian function and the mean (μ) is used to determine the position of the beam.

artefacts will be introduced into the beam images across the desired range of energies [94]. These two points are shown in Figure 9.3, which is the transmission curve for a $127\text{ }\mu\text{m}$ -thick Kapton foil. In previous designs other materials like aluminium, beryllium and carbon as scatterers have been tested [100] but this option have de disadvantage of introducing non constant behaviour around the absorption edges of the used materials and higher absorption rates.

The image resolution of a pinhole camera is determined by the size of the aperture of the pinhole [83]. The ideal aperture can be determined using the equations presented by Rayleigh [101], but for the magnification ratio of the design, and the energy spectrum to be used, the resulting optimal size is less than $1\text{ }\mu\text{m}$. Such a small value would cause a reduction in the intensity detected on the sensor, forcing the integration

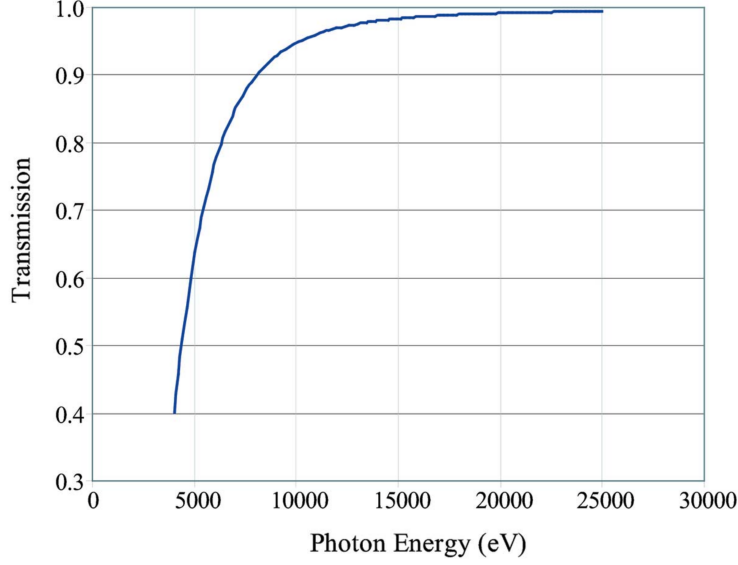


Figure 9.3: Plot of the transmission curve of a 127 μm -thick Kapton foil. The working energy spectrum range for the LancelotRX as a XBPM is from 10 keV to 25 keV. For the working range the transmission of Kapton is higher than 0.95, therefore, less than 5% of the photons will be absorbed by the foil [11].

time to increase. In order to have a short integration time, a higher transmission is needed, and therefore, a bigger aperture for the pinhole. For this design, the used aperture is a 50 μm diameter pinhole.

To fit all the previously detailed parts in place, an XBPM mount is used on top of the LancelotRX. As shown in Figure 9.4, the mount has two Kapton windows to allow the x-ray beam to travel through. Inside the mount, there is a ring used to hold the Kapton foil in position, setting the α angle. Under the Kapton foil, a clamp keeps the pinhole sheet in the correct position, ensuring that the aperture is centred to the sensor and the Kapton foil. The Medipix3RX is located directly beneath the aperture inside the LancelotRX.

9.2.3 Features of the proposed XBPM

Data speed acquisition

The maximum acquisition frequency for the LancelotRX system is 240 full frame images or 680 profiles per second, as explained previously for the XBPM application the use of profiles is preferred. The acquisition of images can be of interest to study the shape of the beam cross-section, but for position of the beam centroid, monitoring

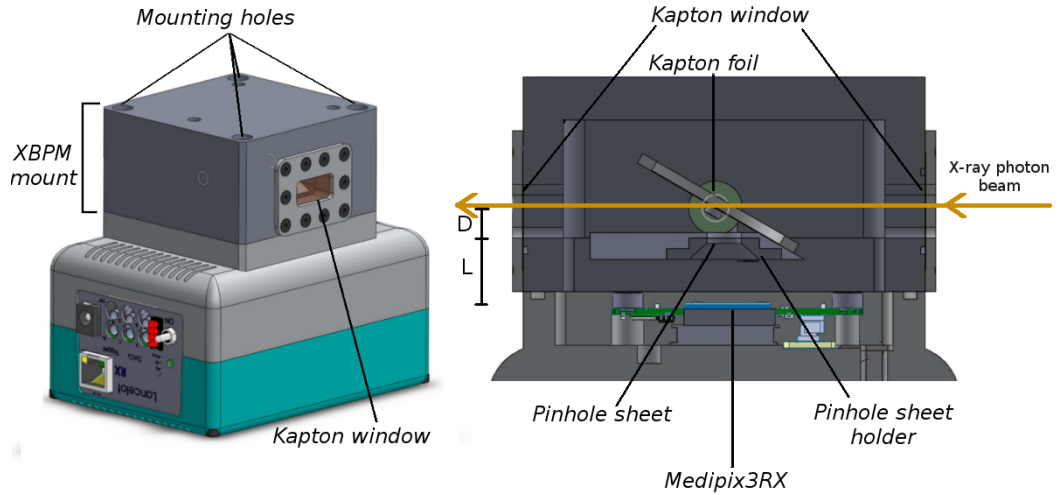


Figure 9.4: XBPM mount used for the XBPM application with the LancelotRX. On the left side, a closed view of this system is shown, while on the right side, a cross-section image shows the position of the Kapton foil, the pinhole sheet and the Medipix3RX. The dimensions D and L that control the magnification ratio are shown in the cross-section image.

profiles contain all the information needed.

Spatial resolution

As explained in Section 5.2.1, incrementing the magnification will reduce the intensity received by the sensor, and therefore the quality of fitting. This means that increasing the magnification will increase the total resolution up to certain value, after this, further increasing the magnification will only decrease the achieved resolution. Based on the calculations of [10], the D and L distances have been designed at 4.5 mm and 11.55 mm respectively, achieving a magnification ratio of 2.56.

Beam intensity measurement

With the proposed XBPM it is possible to compute an estimate of the beam intensity. By tracking the total number of counts in the sensor's pixels per image acquisition, changes in the beam intensity can be detected. To have a correct relation between the measured intensity in the XBPM and the total photon beam flux, the scattering efficiency of the Kapton foil has to be considered. This value is dependent on the x-ray energy and can be obtained from the transmission curve shown in Figure 9.3.

A measure of the beam intensity is a useful tool for the experimental setup, the

beamline scientist can observe to this measurement to ensure the mirrors are correctly aligned, that there are no obstacles on the beam's path, or ensuring that the beam absorption by gas compounds on the beam's path is not too high.

Independent Energy measurement

A novel characteristic of the LancelotRX system being used as an XBPM is the ability to have an independent measure of the beam energy. This feature is granted by the programmable energy threshold capability of the Medipix3RX sensor. The elastic scattered photons by the Kapton foil maintain the same energy as the photon beam, so by completing a comparison between the energy of the arriving photons to the sensor, and the programmable energy threshold, the photon beam's energy can be obtained.

A differential energy profile is produced by obtaining the average pixel count in the sensor for different values of the energy threshold and differentiating the response, this principle is explained in Chapter 2. Having an independent energy measure could be of great help to ensure that the output of the monochromator is the desired one. This feature could also be used to find undesired x-ray energies generated by x-ray fluorescence.

Beam position control

Small drifts in the position of the photon beam are common in synchrotron applications, this can be caused by changes in temperature, by uncertainties in the position control of different equipment, or changes in the source. The position drift can be a problem for experiments working with small samples, or with experiments that require a long period to be completed.

The LancelotRX has implemented a beam position error signal output that can be used to correct the beam position in real time. The profiles of each frame are fitted to a Gaussian function on the processor to find the beam position on both axis, the current position is compared with a programmed target position by the user, and the difference between these positions is output as an analog signal from the LancelotRX. The output is generated by a PID control loop, where the parameters of the PID can be modified by the user. The analog signal can be used by other electronic control

modules to correct the beam position. This feature enables position correction in real time of the beam, ensuring the position stability of the beam over long periods.

9.3 Experimental results with LancelotRX as an XBPM

The XBPM application with LancelotRX is currently being used at two beamlines in Diamond Light Source, beamlines I24 and I19. For the I24 beamline, a different mechanic design was made, this is because the beamline setup required that both the scattering foil and the Medipix3RX were enclosed inside a vacuum chamber. The only difference between the systems is the mechanical design and the feature of the I24 design to modify the L/D ratio up to a magnification of 29. A detailed description of the I24 XBPM design for vacuum can be found in the Appendix E.

Currently both I24 and I19 XBPM with LancelotRX systems are deployed and in use, but the I19 system is being used in air. The LancelotRX sensor chamber together with the XBPM mount generate a sealed chamber that can be set in vacuum, nevertheless, it has been decided to use the system in air. The interaction between the scattered x-ray photons and the air, lower the intensity received by the Medipix3RX sensor, reducing the fitting quality and generating a bigger error when the position of the centroid is computed. To increase the counts, a coded aperture in the form of a cross, is used instead of the pinhole in the I19 XBPM. Two slits of 100 μm width and 3 mm length form the cross aperture. By allowing more scattered photons to impinge the sensor, this method increases the counts and allows for a higher quality in the fitting of profiles, but has the disadvantage of losing the information on the cross-sectional shape of the beam.

If not stated otherwise, the experimental results shown in this chapter correspond to the I24 beamline since there is no attenuation of the x-ray intensity by air.

9.3.1 Analysis of the spatial resolution

The spatial resolution of the XBPM LancelotRX vacuum design has been tested experimentally. The system has been placed on a movable stage with movements of 20

μm in respect to the beam position. The movements took place in an area of $100 \times 100 \mu\text{m}$ centred in the midpoint of the sensor, 100 images were taken in each position and their profiles fitted to a Gaussian function to obtain the centroid of the beam. The obtained position in pixel values can then be correlated to the known position of the beam in relation to the XBPM. A combination of 100 images per position and 25 different positions were used to minimize the error generated by uncertainties in the motors movement. The maximum L/D ratio tested on the I24 design was 17.6 and the obtained resolution was $3.12 \pm 0.02 \mu\text{m}/\text{pixel}$ in x and $1.59 \pm 0.15 \mu\text{m}/\text{pixel}$ in z . As explained in Section 5.2.1, the resolution is different in x and z directions caused by the different amplification. The larger error on the z -axis seems to be generated by a deformation on the Kapton foil, probably caused by radiation damage to the foil.

9.3.2 Analysis of beam stability

Taking advantage of the high frame rate achieved in the system, a frequency analysis of the beam stability has been realized in both I19 and I24 beam lines. Figure 9.5 shows the frequency analysis for beamline I24. In order to have enough photon counts for a good quality of the Gaussian fittings, the integration time used is 10 milliseconds. This integration time sets an acquisition rate of 83 images per second, allowing a frequency analysis using a Fourier fast transform (FFT) up to 41 Hz. The position of the centroid of the beam is measured as a displacement from the mean position, and the units have been transformed from pixels to μm . A set of 1000 images have been used for the frequency analysis.

Both beam stability analysis for I19 and I24 show a peak at approximately 21 Hz in the power spectral frequency. The fact that the same peak can be found in two different beamlines suggests that the beam motion comes from the source and not from equipment on the beamlines. Different elements of the instrumentation and equipment used on the beamline can generate small vibrations, a large amount of motors and pumps are used that can introduce these unwanted effects on the experimental setup. The measured RMS noise is $1.1 \mu\text{m}$ for the centroid displacement of the beam in δz and $1.3 \mu\text{m}$ for δx .

An analysis at higher frequencies could not be done due to the low intensity received by the Medipix3RX. Integration times under 5 milliseconds have been attempted to

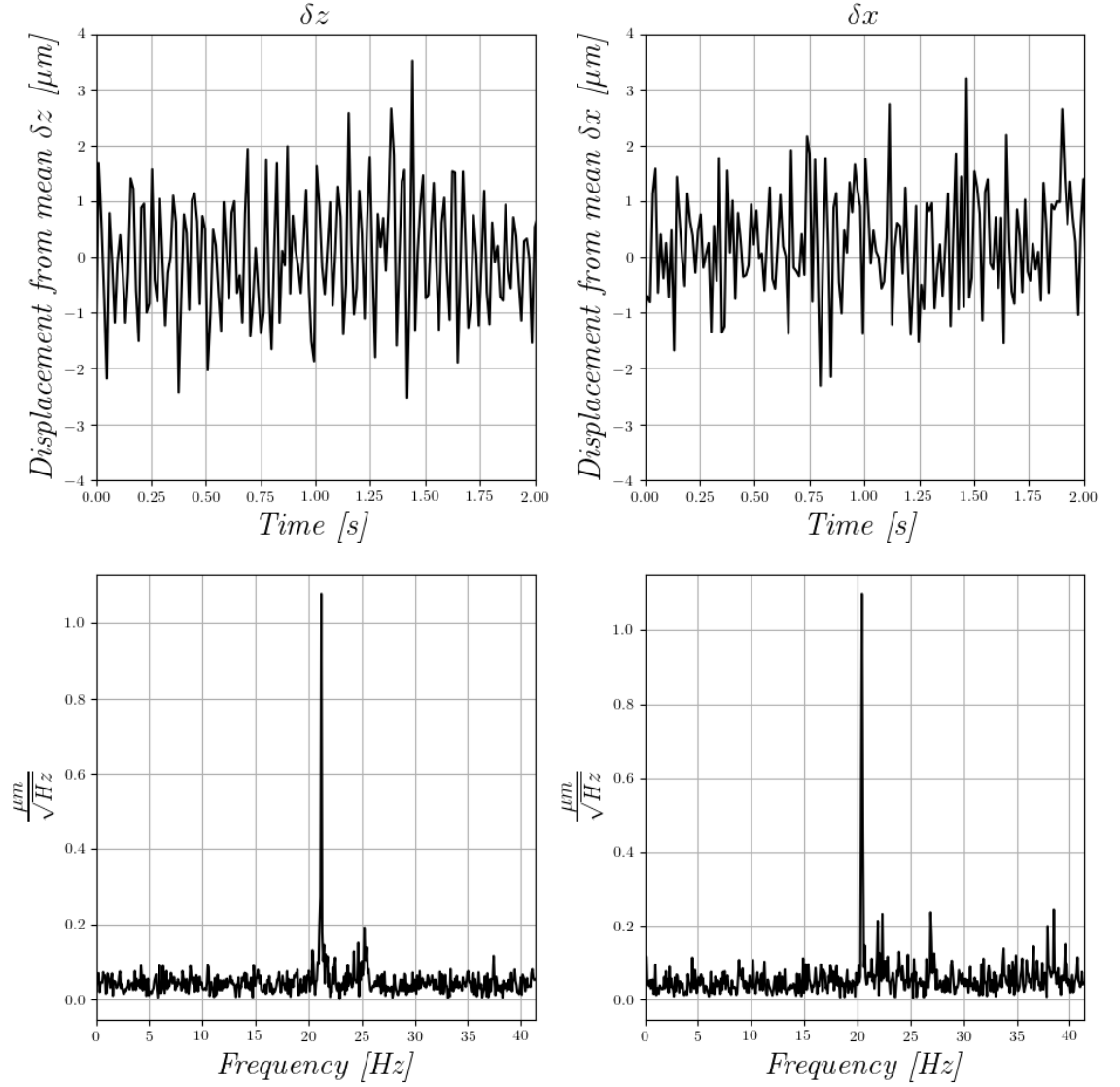


Figure 9.5: The top plots show δz and δx , which are the centroid displacements from the mean on the z and x axis. The integration time used was 10 milliseconds, obtaining a frame rate of 83 images per second. The bottom plots show the Fourier power spectral densities of the centroid displacements. It's interesting to note that there is a big spike at approximately 21 Hz, this same spike has been found in a similar analysis of the beam stability of beamline I19, suggesting that the position instability might come from the source.

generate cross-sectional images, but not enough counts were observed to have a good quality of the Gaussian fitting of the profiles. As the counts per acquired frame decrease, the quality of the fit decreases, and the signal to noise ratio increases.

9.3.3 Analysis of beam flux over time

An example of the beam intensity change is shown in Figure 9.6, where the total counts were tracked in a period of one hour on the I24 beamline. The changes in intensity of the beam reflect the storage ring top-up method used at Diamond Light Source, which has a frequency of 10 minutes.

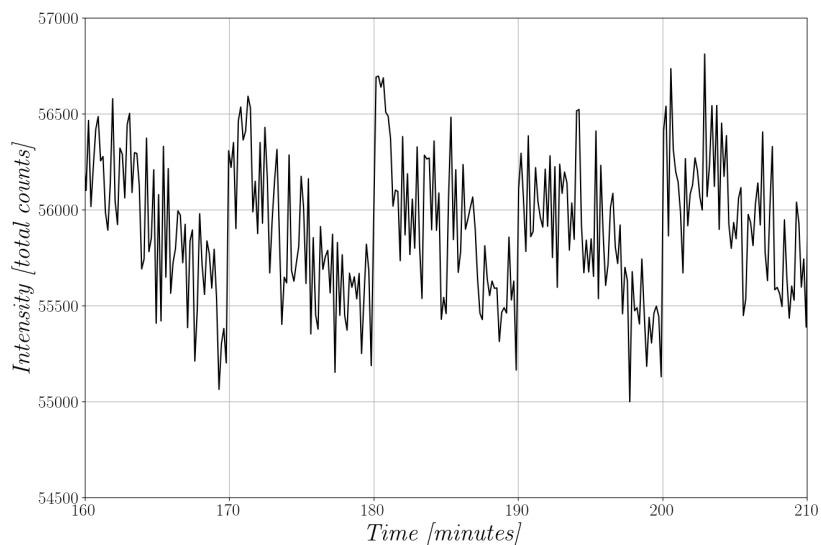


Figure 9.6: Plot of the intensity acquired per frame in the XBPM over a long run at Diamond Light Source beamline I24. The changes in intensity are generated by the top-up cycle of the photon beam at 10 minutes intervals. The acquisition frame rate is 0.1 frames per second and the integration time is 200 ms.

A relative intensity of the beam can be known by tracking the total counts over time, as shown in Figure 9.6, but an absolute measure of the beam intensity requires additional calculations since the scattering efficiency of the Kapton foil is dependent on the energy of the incident photons, as shown in Figure 9.3.

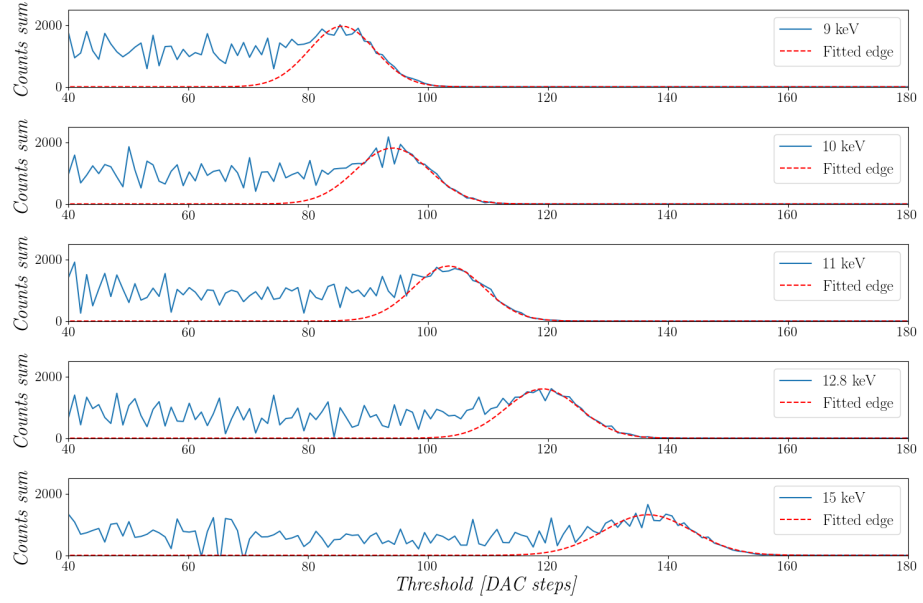


Figure 9.7: Differential energy profile obtained by the XBPM system on beamline I24, tested with different photon energies. The tail of the response is fitted to a Gaussian function, the mean of the fitted Gaussian is used to determine the photon beam's energy.

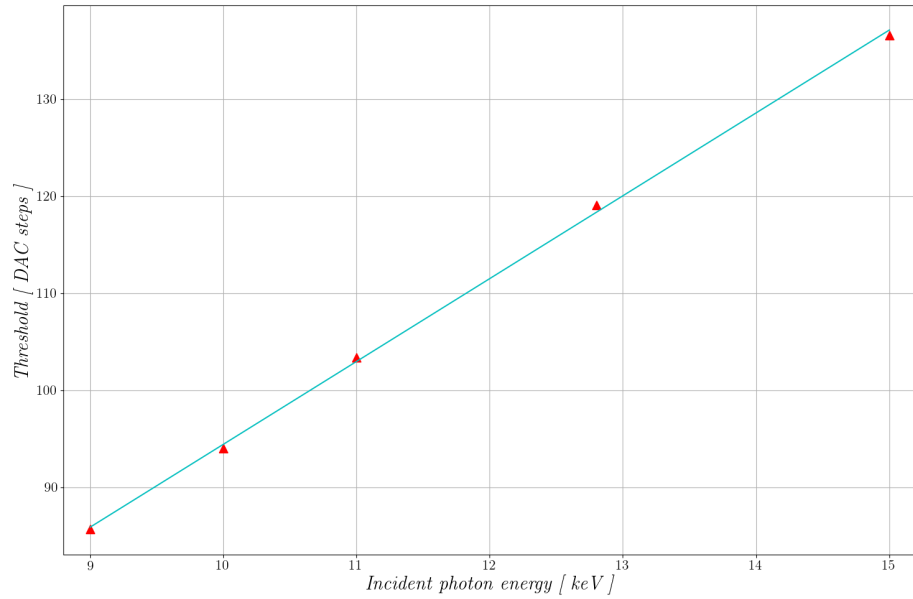


Figure 9.8: Relation of the energy threshold DAC value to the energy of the incident photon. The points are extracted from the mean of the fitted Gaussian functions from the differential profiles obtained by the XBPM system on beamline I24.

9.3.4 Analysis of beam energy spectrum

Currently, the SPM is used on the Medipix3RX for the XBPM application, which as explained in Chapter 2 results in a spectral response polluted by charge sharing between neighbouring pixels. Figure 9.7, shows the differential energy profile of different

photon beam energies, the tail of the response is used to obtain the energy of the photons by fitting a Gaussian. Models of the differential energy profile, including the contribution of the charge sharing effect, beam flux and electronic noise, have been developed for Pilatus detectors [15] and can be used to determine the energy of the photon beam from the differential energy profile.

Figure 9.8 shows the linear fitted relation between the energy threshold values on DAC units (DACu) and the energy of the incident photons. The response is clearly linear and a gain of 8.45 DACu/keV with an offset of 11.5 DACu has been obtained. The energy resolution of the system is dependent on the Medipix3RX mode and equalization used, as explained on Chapter 7.

The CSM mode of the Medipix3RX could be used to obtain a response without the effects of charge sharing, but at the moment when the XBPM application was deployed the SPM was the only operational mode of the sensor that had been implemented into LancelotRX.

9.4 Conclusions and future work

A non-destructive x-ray beam position monitor application was developed with the LancelotRX system. The XBPM has a maximum sub-micron resolution and a maximum frame rate of 240 full frames per second or 680 profiles per second. Apart from the photon beam position, the XBPM has been shown to track the shape of the photon beam cross-section and its intensity. The XBPM application developed with the LancelotRX system has the novel feature of an independent measurement of the photon beam's energy. An analog voltage output from the system can be used to correct in real time the photon beam position, ensuring position stability for long periods of time. Both the mechanical designs for beamlines I19 and I24 have been shown to work as an XBPM.

When measuring the vacuum design spatial resolution, an area with a higher position error was found, later on, it was determined that this problem was generated by radiation damage on the Kapton foil. Radiation damage on the foil is caused by the flux of the beam and the energy of the beam, it is possible that for a specific beamline setup, Kapton is not a suitable material and a more radiation-hard material should

be used. Different materials could be used to avoid radiation damage, for example beryllium or CVD diamond.

Based on the presented experiments, it is clear that the maximum rate of data points of the photon beam position per second obtained by the system is limited by low photon flux arriving to the sensor. In order to obtain a good quality fit of the Gaussian function on the beam cross-section profiles, higher counts on the sensor's pixels are required. This issue generates a limit below the maximum frame rate of the LancelotRX system. For future designs, this problem has to be taken into consideration before attempting to generate a system with a higher frame rate. Possible solutions to this issue would be to use a photon beam with a higher flux, using a different aperture for the pinhole camera setup, or using a foil with a higher scattering efficiency. All of these solutions present disadvantages as well, for example, losing the option to reconstruct the beam shape or reducing the beam intensity after the BPM by using a foil with a higher scattering efficiency.

As explained previously, the Medipix3RX sensor is currently used in SPM in the XBPM applications. The use of this mode presents charge sharing effects between the pixels, forcing a more complex analysis of the differential energy profiles. The charge sharing effects can be avoided by using the sensor in CSM, reducing the complexity of processing the photon beam energy. Using the CSM could also improve the beam position measurement by eliminating erroneous multiple counts. For future implementations of an XBPM using the Medipix3RX sensor, the CSM should be considered as it presents advantages over the SPM.

A measure of the photon beam's flux, incident to the XBPM, has many practical applications for the experimental setup on a beamline. This feature could be further improved if processing the total counts of the acquisition, the relative beam flux measure, was done on the LancelotRX system. The output of this measure could be sent to the client or directly output as an analog voltage. By outputting this measure as an analog voltage, other electronic devices on the beamline instrumentation could use the analog signal as a feedback. An example of this application is to use the analog voltage proportional to the beamflux to optimize the mirrors' positions, a task that is normally done manually by the beamline scientist when the experiment is being set up. By using an analog voltage, the optimization of the mirrors' position could be

done automatically, or corrected in real time.

The proposed XBPM system presents many advantages over other techniques. In comparison with the ionization gas or metal foils solutions, the proposed XBPM system can be used in the range of 10 to 25 keV without the need to change foils or gasses. The proposed XBPM system has a larger area of beam position detection than the four-quadrant electrodes systems. The disadvantage of requiring a complex water-cooling system presented on the solutions based on blades is not present on the proposed XBPM. The feature of an independent energy measure from the XBPM system is unique to the proposed design.

Chapter 10

Colour x-ray imaging application

One of the features of the Medipix3RX is the ability to operate in Colour mode, in which four pixels work together as a super pixel. The resulting super pixel can have up to eight threshold comparators, granting the possibility of generating an image with up to eight x-ray energy bins or colours. This chapter describes the colour mode option of the Medipix3RX as well as its limitations. Possible applications are discussed and two experiments using this mode are shown. The possibility of using LancelotRX as an x-ray colour imaging system is discussed.

10.1 Colour x-ray imaging

X-ray colour imaging, also known as spectroscopic x-ray imaging, is an imaging method capable of resolving the energy components of incident x-ray photons. An image can be formed with different colour bands, also called energy bins, resulting in the ability to obtain more information than with traditional x-ray intensity imaging. This method can be implemented by hybrid pixel detectors using one or several tuneable energy thresholds. The use of colour imaging techniques with hybrid pixel detectors has been reported in many medical applications, such as luminal depiction in blood vessels [102], targeted gold nanoparticle imaging [103] and atheroma imaging [104]. Colour imaging techniques are also common in material science, for example in Computed Tomography (CT) [105] or to reduce beam hardening effects [106].

A substantial amount of the applications of x-ray colour imaging are in the CT field. For CT applications, it's common to use a broad spectrum x-ray source [107],

instead of using monochromatic energies as is more common in synchrotron applications. By combining the information from x-ray intensity with the information from the energy of the photons, it's possible to identify different materials from their x-ray attenuation. The information obtained is used to reconstruct a three dimensional representation of the scanned sample. The CT applications tend to use high-resistivity cadmium telluride (CdTe) or cadmium zinc telluride (CdZnTe), due to their favourable absorption properties in the desired x-ray energies range [108]. Colour imaging has also been performed successfully using silicon as a sensor layer [109] [110].

By using CdTe and CdZnTe as sensing layers, the absorption energy range enables experiments to be performed at energies relevant to biomedical applications, even to human imaging [107]. In order to resolve between materials, the CT spectrum imaging makes use of the specific measurable x-ray spectrum that each material has. By simultaneously detecting different x-ray colours, or x-ray energy bins, it is possible to track several biomarkers of biological processes. Different materials or biomarkers with a high Z can be identified by methods like K-edge imaging [111] [112] [113] or by its characteristic x-ray fluorescence. It is common to use high Z contrast materials in biological samples, for example iodine [114], barium [115] or gold [116], but it is also possible to identify soft tissue, with a relative low Z , using colour CT [107]. All of these options predict that x-ray colour imaging will have a big significance in the biomedical and material sciences in the near future.

The x-ray colour imaging method presented in this chapter, is based on detecting specific monochromatic x-ray energies, in difference to detecting a specific absorption spectrum. Both methods can be used to resolve between different materials. The method presented in this chapter relies on the x-ray fluorescence of elements, which generates x-ray photons at specific energies. This method was selected in order to work with a monochromatic x-ray source. The experiments were conducted at the beamline BM26A of the ESRF.

10.2 Colour band and threshold selection

As explained in Chapter 2, the Medipix3RX can be configured in colour mode (CM), where each super pixel has up to eight individual energy thresholds. The thresholds

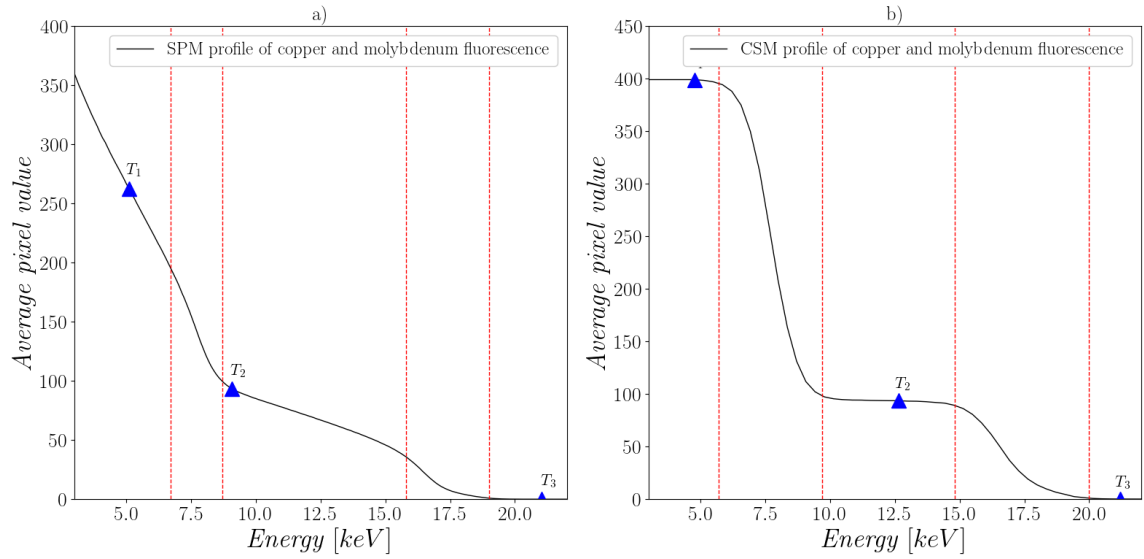


Figure 10.1: Energy spectrum of copper (k_α of 8.05 keV) and molybdenum (k_α of 17.48 keV) x-ray fluorescence. a) SPM profile of the energy spectrum of both energies. b) CSM profile of the energy spectrum of both energies. The sections limited by the red dotted lines show the ‘transition segments’. The points T_1 , T_2 and T_3 show the proposed energy threshold values needed to reconstruct the signal.

can be used to create energy bins, separating the detected photons into specific energy bands. By using the eight thresholds, up to nine energy bins can be used to sort the detected photons. This energy bins division is similar to the colours division in the visible light spectrum, and therefore can be considered as colour bands.

Even with the larger super pixels used in CM (110 μm per side), charge sharing between super pixels can occur and degrade the signal energy spectrum. In Figure 10.1, the energy spectrum of an x-ray signal with two monochromatic energies is shown. The signal is generated by an x-ray photon beam of 20 keV hitting a target of a combination of molybdenum and copper. Both elements show x-ray fluorescence, with values of a k_α of 8.05 keV for copper and a k_α of 17.48 keV for molybdenum. By using the Medipix3RX CM, these elements can be differentiated in the same frame, and the fluorescence photons of both elements can be counted independently.

In Figure 10.1 the energy spectrum of the copper-molybdenum target is shown in both the SPM and the CSM operation modes of the Medipix3RX. Between the red dotted lines, the ‘transition segments’ are shown, which are the segments of the energy threshold spectrum in which a monochromatic x-ray energy transitions from being detected to not being detected. The width of the ‘transition segments’ is dependant

on the energy resolution achieved through the equalization process. The width of the ‘transition segments’ can be defined as $1.35 \times \text{FWHM}$ of the energy resolution, as presented in Chapter 8.3.

The colour bands are defined as the energy in-between two threshold values, for example, a colour band of 5-12.5 keV could be defined by subtracting the detected photons at T_1 from the ones from T_2 from Figure 10.1b. The colour band width limit, before the incoming photons are assigned to an incorrect energy bin, is determined by the energy resolution achieved in the equalization.

The methodology to determine the value of the energy thresholds differs in the SPM to the CSM. In the CSM the energy thresholds should be placed at any point inside the plateaus, in-between ‘transition segments’, as shown for T_1 , T_2 and T_3 in Figure 10.1b. Placing the energy thresholds in the ‘transition segments’ will generate the photons to be incorrectly assigned.

In comparison to CSM, placing the energy thresholds in SPM has one extra complication that needs to be taken into account. In SPM, the energy thresholds should be placed outside the ‘transition segments’ and as close as possible to half the value of the expected energy. Due to the charge sharing effect, under and over counts of photons is present in the SPM, with the most accurate photon count approximately at half the energy value of the signal. If the half value can not be selected to place the energy threshold, due to a ‘transition segment’ or to the half value being outside of the detectable spectrum, then the closest value should be selected. An example of this selection is T_1 , T_2 and T_3 in Figure 10.1a, where the values 5 keV and 9 keV were selected for T_1 and T_2 respectively.

One of the disadvantages of using the CSM is that, as shown in Chapter 8.3, the energy resolution obtained is lower than the one for SPM. This lower resolution results in a wider ‘transition segment’, making it difficult to detect correctly between elements whose x-ray fluorescence have similar energies. Another disadvantage of CSM is that two comparators are required per effective threshold, one for energy reconstruction and the other for hit allocation, which means that in this mode only four energy thresholds are available. The advantage of using CSM is that every photon gets correctly counted and sorted into the right colour band.

The disadvantage of using SPM is that charge sharing between pixels will generate

an incorrect photon count, and that some photons will be sorted into the incorrect colour band. In this mode, the lower energy bands will have counts from miss-sorted photons of higher energies. The advantages of SPM are a better energy resolution and the possibility of using eight different energy thresholds.

The equalization procedure tested for CM and CSM gave erroneous results. The expected result was to obtain an x-ray energy spectrum clear of charge sharing effects, nevertheless, the obtained spectrum was polluted with charge sharing miscounted photons. This seems to be a problem with the implemented equalization procedure, as other sources have cited correctly using this operation mode [117] [118]. Based on this problem, the SPM was used for the tests presented in this chapter.

10.3 Colour imaging test

To test the colour imaging capabilities of the LancelotRX, an image of two elements was taken. The two elements were identified by their characteristic x-ray fluorescence. For a correct identification of the elements, their characteristic x-ray fluorescence should be separated in the energy spectrum for at least 1.35 times the FWHM of the energy resolution. With this requirement, copper and zirconium were selected.

In Figure 10.2 the diagram of the experimental setup is shown. The sample, made of zirconium and copper, is fixed in the sample holder over the Medipix3RX. A pinhole aperture was used so a defined image could be formed, without the pinhole camera setup only a blurry image could be acquired. The pinhole aperture, of 300 μm , was set in between the sample and the Medipix3RX in the LancelotRX. The use of a pinhole camera setup generated an image magnification controlled by the L/D ratio. The test was set with an L of 21 mm and a D of 9 mm, generating a magnification of 2.1.

A photon beam of 20 keV and with a cross-section of 1 x 5 mm was used. The used photon beam was smaller than the area of the sample to be imaged, so a scanning process was used. Images were taken at different positions of the photon beam over the sample, and then stitched together. The sample used is shown in Figure 10.3a. A copper strip with a slits pattern was placed on top of a zirconium plate. Three thresholds creating two colour bands were used to discern both elements, T_1 , T_2 and T_3 were set to 5, 9.5, 18 keV respectively. The first colour band is created by $T_3 - T_2$

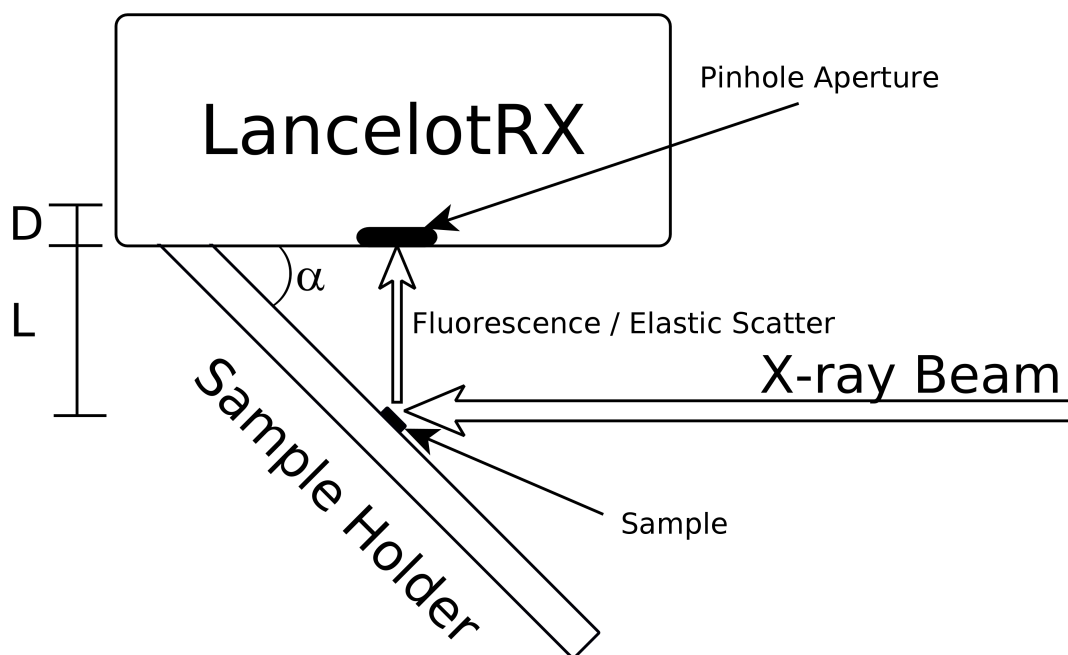


Figure 10.2: Diagram of the experimental setup used for the colour imaging test (not to scale). The sample holder is at an angle α from the LancelotRX, and holds the sample centred to the pinhole aperture in front of the LancelotRX. The magnification is determined by the ratio L/D .

and contains the photons from the zirconium fluorescence. The second band is created by $T_2 - T_1$ and contains the photons from the copper fluorescence. The obtained image is shown in Figure 10.3b, where the colour band for the zirconium fluorescence has been depicted in green and the colour band for copper in red.

Due to the angle α at which the sample is held, the x-ray beam hits the sample at an angle, causing the copper to cast a shadow over the zirconium. The shadow created by the copper makes the zirconium fluorescence intensity higher on the left side of the image and lower on the right side. The angle α also generates a perspective on the image, where the copper slits seem bigger on the right side of the image in comparison with the slits on the left side.

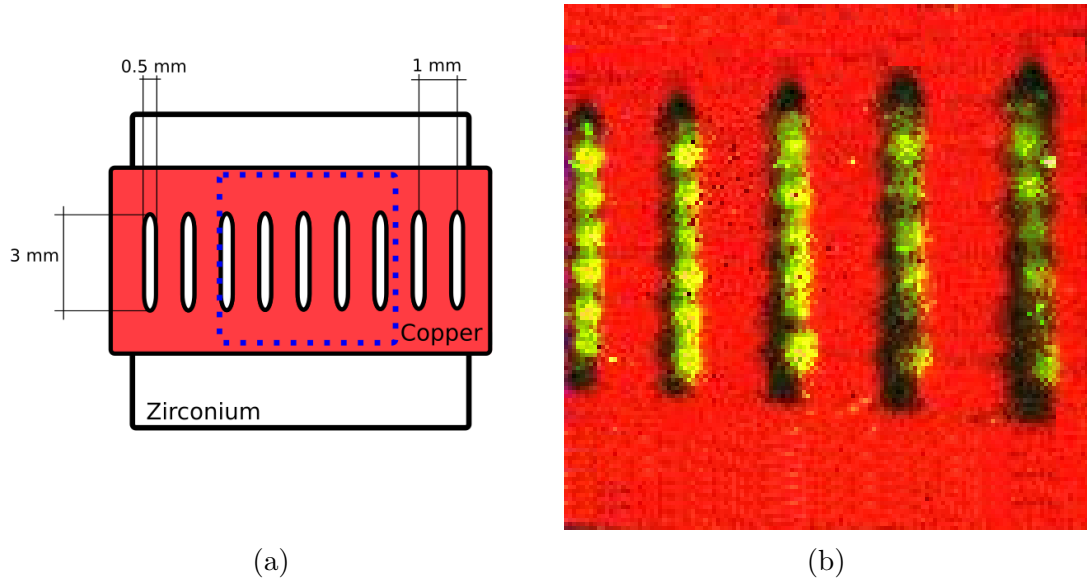


Figure 10.3: Colour x-ray imaging test. a) The sample used for the imaging, a copper strip with a pattern on top of a zirconium plate. The imaged section is shown with a dotted square. b) Obtained colour x-ray image of the target. The energy bins corresponding to copper and zirconium are shown in red and green respectively. To create the image, the target was scanned using a 1 x 5 mm 20 keV photon beam. The images from the scan were stitched together to form the final image, no other image processing was applied.

10.4 Material identification

The colour mode of the Medipix3RX has a clear advantage in medical applications, since by using multiple thresholds the amount of images required is reduced, which also reduces the radiation dose to the patient or sample. Another advantage of the colour mode is the speed of acquisition. Thanks to using multiple thresholds in the same frame, the effective time resolution can be improved. This advantage could be used in industrial applications that use x-rays to detect specific materials and have a short amount of time for the detection process, for example, searching for undesired materials in a food production line or in a water stream.

To test the possibility of having a fast identification of materials with the LancelotRX system, an experiment has been conducted in which three different elements of a moving target are individually detected. The elements used are iron, with a k_{α} of 6.4 keV and copper, with a k_{α} of 8.05 keV. The x-ray photon beam used is of 3 mm x 1 mm cross-section beam with an energy of 12 keV. Acrylic is used to generate elastic scattering of the beam, which will have the same energy as the beam's photons.

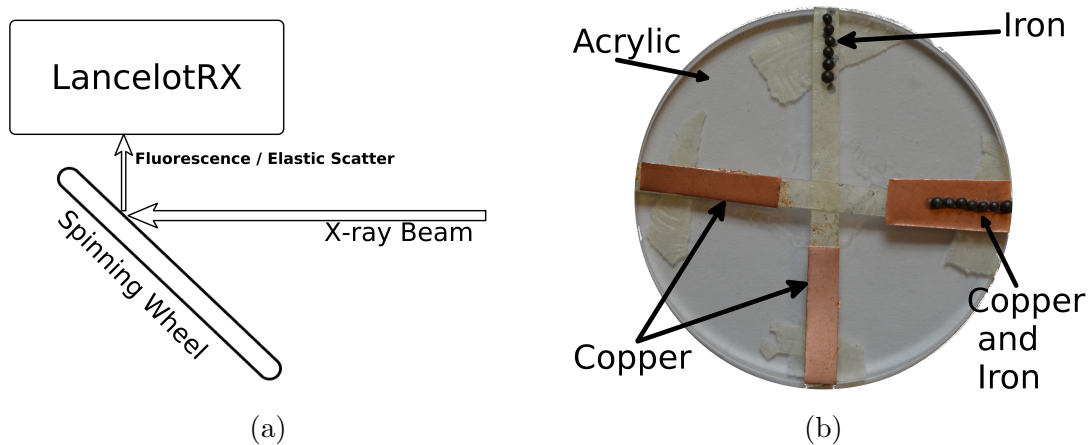


Figure 10.4: Experimental setup for the material identification test . a) Experimental setup used for the test, the x-ray fluorescence generated by the elements on the spinning wheel is detectable by the LancelotRX. The wheel was set to spin at 17.5 RPM. b) The spinning wheel is made out of 0.3 mm acrylic and has copper strips and iron pebbles attached to it.

In Figure 10.4a, the experimental setup is shown. In Figure 10.4b an acrylic wheel, which was used in the experiment, is shown. The wheel has four sections, two of them with copper strips, one with iron pebbles, and one with both a copper strip and iron pebbles. As the wheel spins at 17 Revolutions Per Minute (RPM), and because the x-ray photon beam only hits a small fraction of the wheel, the generated fluorescence or elastic scattering changes. These changes of the energy of the x-rays detected by the LancelotRX are used to identify the materials.

The frames acquisition was done at 100 frames per second, this acquisition speed was selected to ensure enough photon counts per frame. Three colour bands were set, using four thresholds. The thresholds T_1 , T_2 , T_3 and T_4 were set at 5, 7.2, 9.5 and 13.5 keV respectively. The colour band for iron is set by $T_2 - T_1$, the colour band for copper is set by $T_3 - T_2$ and the colour band for the elastic scattering is set by $T_2 - T_1$. The intensities of each colour band were processed from all the frames in the experiment. In Figure 10.5, a time plot of the intensity of each colour band is shown. The time plot corresponds to one revolution of the wheel.

As explained in Section 2 of this chapter, the use of SPM generates erroneous photon counts. Even with the photons being assigned to an incorrect energy band, the three elements can be detected with high precision. But the incorrect assignment of photons of lower energies can be seen in the iron colour band. Between the seconds 2 and 3 of the plot, the iron band shows counts that correspond to the copper band.

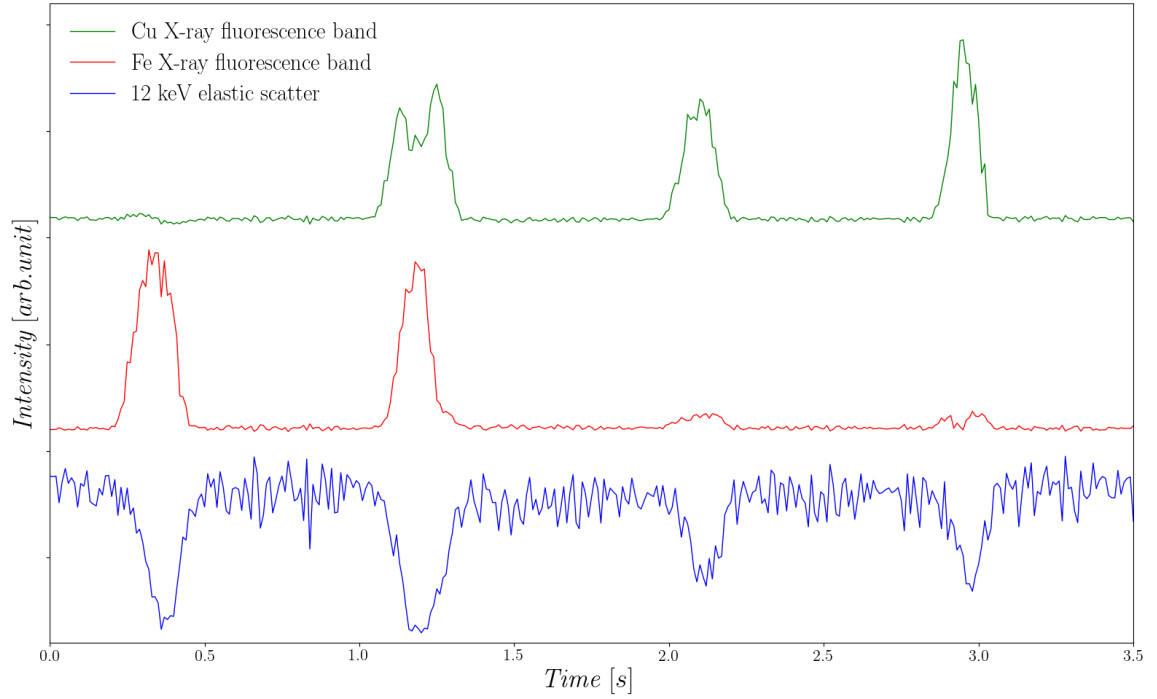


Figure 10.5: X-ray intensity per colour band. Copper fluorescence is depicted in green, iron fluorescence in red and the 12 keV scatter in blue. The plot shows one revolution of the spinning wheel.

10.5 Conclusions and future work

It has been shown that the LancelotRX is capable of using the colour mode of the Medipix3RX, and that the LancelotRX system could be used for medical or industrial applications. The limitation on the minimum width of the colour bands is set by the energy resolution achieved by the equalization. Even when the CSM equalization for colour mode did not work, it has been shown in this chapter that the SPM mode can be used for colour imaging and materials detection.

The LancelotRX can be used for colour imaging with fine detail. The limitation of space resolution with the $110\ \mu\text{m}$ pixels can be fixed by using a pinhole camera setup with magnification. As shown in the imaging test, colour sub-millimetre details can be correctly detected using the pinhole camera setup.

Material identification has been shown to work using the LancelotRX. The system can be used for fast element detection by their characteristic x-ray florescence, where the limit of the presented experiment was set by the photon flux. By having a higher photon flux, the material identification could be done at the 280 frames per second

maximum frame rate, that the LancelotRX is capable of.

As shown in Chapter 8, using x-rays as a source for the equalization procedures yields a better energy resolution. This method could be used for colour mode, as long as a monochromatic x-ray source, whose energy can be changed, is available. For each threshold value used for the colour bands, a calibration of that threshold can be done in x-rays. This approach would allow for more specific colour bands, or detection at higher precision of elements whose x-ray fluorescence lines are close to each other. The downside is that the equalization procedure would take very long, and it would only work for a specific set of threshold values.

Chapter 11

Conclusions and Future Work

The outputs from this research project are presented in this chapter. A summarised description of the important conclusions of this work is discussed. Possible future work is suggested in the hope of helping to promote future research in this area.

11.1 Conclusions

The conclusions are presented in the same order of the proposed research outcomes shown in Chapter 1.2.

Design and implementation of an x-ray colour imager using a Medipix3RX.

A fully functional x-ray colour imager has been developed and tested. The system, named LancelotRX, is capable of fast processing of the Medipix3RX raw data in-situ, an example of this is the calculation of image profiles. A continuous maximum frame rate of 240 frames per second or 680 profiles per second has been achieved with the system. A temperature control maintains a constant temperature for the Medipix3RX in a tested range of 10 to 30 °C. Control and data transfer with the LancelotRX is done through the network using a client software developed for this project. All the operation modes of the Medipix3RX can be used in the LancelotRX system.

Analysis of the possible equalization methods and sources for the Medipix3RX.

Different equalization methods and sources have been analysed and tested. The existence of a trade-off between energy resolution and required equalization time, has been experimentally verified. It was found that the energy resolution is better for the

SPM than for the CSM, and that the best energy resolution was achieved using x-ray energy as an equalization source. Poor results were obtained with the equalization based on injected pulses, with the suspected cause being the capacitance dispersion between the injected pulse capacitors. The proposed pixels parameters method was shown to perform poorly, while the proposed energy fine tuning on CSM yielded an improvement of 16.3% on the energy resolution.

Experimental results on the temperature dependence of the threshold dispersion and energy calibration on the Medipix3RX.

A relation between the threshold dispersion and the temperature of the Medipix3RX was found. In the range of 10 to 40 °C, it was found that both the threshold dispersion and the noise amplitude have lower values for higher temperatures. Contrary to what was expected, lowering the Medipix3RX temperature did not improve its energy resolution. For the energy calibration, it was shown that temperature changes can generate an erroneous energy measurement. Based on these findings, to have a reliable energy resolution and calibration, the temperature of the sensor must be kept constant and close to 40 °C.

Experimental results using the designed imager as an x-ray beam position monitor application.

The LancelotRX, applied as an XBPM, has been proven to calculate the position of the beam with sub-micron precision. The XBPM application has the same maximum frame rate as the LancelotRX, with 240 frames per second or 680 profiles per second. The XBPM application has also been shown to be able to track the beam's cross-section shape and the beam's relative intensity. This XBPM design has the ability to take an independent measurement of the photon's beam energy. The proposed design has been proven to work as a reliable XBPM, showing advantages over other methods.

Analysis and results of colour imaging with the Medipix3RX.

It has been shown that the colour mode can be used on the LancelotRX. It was found that the limitation on the minimum size of the energy bins, before misallocation of photons occur, is set by the energy resolution achieved through the equalization procedures. A methodology to determine the threshold values has been proposed and tested. It has been shown that using the SPM for colour mode, it is possible to differentiate between materials based on their x-ray fluorescence.

11.2 Future work

The maximum obtained frame rate is 240 frames per second for images and 680 profiles per second. To improve this frame rate a few options are available. The current communication protocol, Merlin protocol, is not efficient for speed since it does not support bit-packing and requires the pixel's data to be sent in either 8 or 16-bit format. Apart from this, the header information sent as part of the protocol, is a big limiting factor for the profiles acquisition. If a faster frame rate is desired, the communication protocol should be changed to allow the header information not to be sent, to allow bit-packing of the pixels and to support compression techniques.

The current implementation of the GPMC driver on the ARM processor, is copying data between user and kernel space in the Linux OS. Better implementations of the driver could remove the unnecessary data copying, reducing the load on the ARM processor. Another alternative could be to use a System On a Chip (SoC), where an FPGA and a processor are implemented in the same chip. The SoC architecture allows the FPGA and the processor, to share the same memory. This implementation would remove the necessity of copying data between the FPGA memory and the processor memory.

Data compression techniques could be implemented to reduce the amount of data transferred between the LancelotRX and the client software. To have higher frame rates, the integration time has to be reduced, and with it, the amount of counts per image. This results in images whose pixel's values are primarily zero. A variable data length compression method could be implemented, for example Huffman coding. Future designs could implement a Huffman compression using a LUT in the FPGA, creating a fast and simple compression that could reduce the amount of data transferred.

As shown in the results of Chapter 8.3, the best equalization method is a compromise between the time the equalization procedure takes and the energy resolution. The best energy resolution is obtained when equalizing with x-rays at the experiment's energy, but this tends to be an impractical method. For most applications, especially for imaging applications, the noise equalization yields a sufficient energy resolution. The x-rays equalization should be used only for cases when high energy resolution is

needed, for all other cases the noise equalization is a better solution. Further work testing the injected pulses capacitance dispersion, and how this dispersion affects the possibility of using pulses as an equalization source, is needed.

As explained in Chapter 8.3, the Medipix3RX behaved unstably for the highest gain mode in CSM, which stopped the equalization algorithm from working. Other systems using the Medipix3RX report equalizing correctly for this operation mode, which seems to suggest that the problem is caused by some of the settings on the Medipix3RX. Further tests are required to understand what settings are causing the instability and how it can be overcome.

The calculated minimum temperature at which the Medipix3RX can be set in LancelotRX, is -10 °C. To decrease the sensor temperature further, a different Peltier with a larger maximum temperature difference could be used, or the heat dissipating capabilities of the LancelotRX system could be improved by using a larger fan. If the Medipix3RX temperature is further decreased, the different expansion coefficients of the silicon and copper, have to be taken into account.

An experimental test could be conducted to find the temperature at which the threshold dispersion and the noise amplitude have the minimum value in the Medipix3RX. It would be necessary to repeat the experiment shown in Chapter 8.4, but with a larger temperature range. The results of the energy calibration temperature dependence, suggests that the amplifiers used on the Medipix3RX pixels are not temperature compensated. This would explain why the x-ray energy to threshold DAC ratio changes with the temperature of the Medipix3RX.

The results of the energy calibration temperature dependence show the importance of maintaining a stable temperature when the energy spectrum of the x-rays is measured. To ensure a reliable measurement, the temperature of the Medipix3RX has to be stable, or equalization and calibration procedures have to be routinely executed. In practical terms, requiring to repeat the calibration procedure every time the temperature changes is not ideal. A detector system that uses passive temperature control, for example by using a large heatsink, will not provide reliable measures until the stable temperature has been reached. Future designs should aim for an active temperature control.

Given the results of the threshold dispersion and noise amplitude dependence to

temperature, as shown in Chapter 8.4, future designs must aim to maintain the temperature of the Medipix3RX at a higher target temperature. The optimal temperature seems to be over 40 °C, which is difficult to achieve only through active cooling, especially for cooled environments like a synchrotron beamline. The temperature controller for future designs must be able to heat up and cool down. A Peltier cooler could be used with a bipolar power supply, allowing heat to be extracted from the electronics chamber and pumped into the Medipix3RX.

References

- [1] Hatsui Takai and Heinz Graafsma. X-ray imaging detectors for synchrotron and xfel sources. *IUCrJ*, 2(3), May 2015. doi: 10.1107/S205225251500010X.
- [2] R. Ballabriga, J. Alozy, M. Campbell, E. Frojdh, E.H.M. Heijne, T. Koenig, X. Llopart, J. Marchal, D. Pennicard, T. Poikela, L. Tlustos, P. Valerio, W. Wong, and M. Zuber. Review of hybrid pixel detector readout asics for spectroscopic x-ray imaging. *Journal of Instrumentation*, 11(01):P01007, 2016. URL <http://stacks.iop.org/1748-0221/11/i=01/a=P01007>.
- [3] R. Ballabriga, M. Campbell, E. Heijne, X. Llopart, L. Tlustos, and W. Wong. Medipix3: A 64k pixel detector readout chip working in single photon counting mode with improved spectrometric performance. *Nuclear Instruments and Methods in Physics Research Section A: Accelerators, Spectrometers, Detectors and Associated Equipment*, 633(Supplement 1):S15 – S18, 2011. ISSN 0168-9002. doi: <https://doi.org/10.1016/j.nima.2010.06.108>. URL <http://www.sciencedirect.com/science/article/pii/S0168900210012982>.
- [4] Medipix3 collaboration. Technical specifications for the medipix3. *CERN*, 2010.
- [5] R. Ballabriga and X. Llopart. *Differences between the Medipix3.0 and the Medipix3RX chips*. CERN, 2014.
- [6] D. Pennicard, R. Ballabriga, X. Llopart, M. Campbell, and H. Graafsma. Simulations of charge summing and threshold dispersion effects in medipix3. *Nuclear Instruments and Methods in Physics Research Section A: Accelerators, Spectrometers, Detectors and Associated Equipment*, 636(1):74 – 81, 2011. ISSN 0168-9002. doi: <https://doi.org/10.1016/j.nima.2011.01.124>. URL <http://www.sciencedirect.com/science/article/pii/S0168900211002105>.

- [7] Multicomp. *Peltier Cooler Datasheet - MCPE-071-10-13*. Multicomp, 2015.
- [8] R. Ballabriga and X. Llopart. *Medipix3RX Manual V1.4*. CERN, 2014.
- [9] Atmel. *Atmel 16U4-32U4 7766 Datasheet*. Atmel, April 2016.
- [10] Roelof van Silfhout, Anton Kachatkou, Nicholas Kyele, Peter Scott, Thierry Martin, and Sergey Nikitenko. High-resolution transparent x-ray beam location and imaging. *Opt. Lett.*, 36(4):570–572, Feb 2011. doi: 10.1364/OL.36.000570. URL <http://ol.osa.org/abstract.cfm?URI=ol-36-4-570>.
- [11] Nicholas R. Kyele, Klaas Decanniere, and Roelof G. van Silfhout. A transparent two-dimensional *in situ* beam-position and profile monitor for synchrotron X-ray beamlines. *Journal of Synchrotron Radiation*, 12(6):800–806, Nov 2005. doi: 10.1107/S0909049505031250. URL <https://doi.org/10.1107/S0909049505031250>.
- [12] Altera-Corporation. *The JRunner Software Driver: An Embedded Solution for PLD JTAG Configuration*. May 2006.
- [13] H. H. Rossi and A. M. Kellerer. Roentgen. *Radiation Research*, 144(2):pp. 124–128, 1995. ISSN 00337587. URL <http://www.jstor.org/stable/3579251>.
- [14] M.A. Haidekker. *Medical Imaging Technology*. Springer-Briefs in Physics. Springer, 2013. ISBN 9781461470731. URL <http://books.google.co.uk/books?id=hcg.AAAAQBAJ>.
- [15] P. Kraft, A. Bergamaschi, Ch. Broennimann, R. Dinapoli, E. F. Eikenberry, B. Henrich, I. Johnson, A. Mozzanica, C. M. Schlepütz, P. R. Willmott, and B. Schmitt. Performance of single-photon-counting PILATUS detector modules. *Journal of Synchrotron Radiation*, 16(3):368–375, May 2009. doi: 10.1107/S0909049509009911. URL <https://doi.org/10.1107/S0909049509009911>.
- [16] Delpierreand P, Basoloand S, Berarand Jean, Bordesouleand M, Boudeand Nathalie, Breugnonand Patrick, Caillotand Bernard, Chantepieand B,

- C. Clemens and J. Dinkespiler and B. Hustache-Ottini and S. Meessen and C. Menouni and Mohsine, Morel and Christian, Mouget and C, Pangaud and Patrick, Potheau and R, and Vigeolas and E. Xpad: A photons counting pixel detector for material sciences and small animal imaging. 572:250–253, 03 2007.
- [17] Steadman and Roger, Herrmann and Christoph, Mlhens and Oliver, G. Maeding and Dale, Colley and James, Firlit and Ted, Luhta and Randy, Chappo and Marc, Harwood and Brian, and Kosty and Doug. Chromaix: A high-rate energy-resolving photon-counting asic for spectral computed tomography. *Journal of Electronic Materials*, 7622:762220–762220, 03 2010.
- [18] Fraco Rupcich and Taly Gilant-Schmidt. Experimental study in optimal energy weighting in energy-resolved ct using czt detector. *Proceedings of SPIE*, 03 2013.
- [19] Rafael Ballabriga, Michael Campbell, and Xavier Llopart. Asic developments for radiation imaging applications: The medipix and timepix family. *Nuclear Instruments and Methods in Physics Research Section A: Accelerators, Spectrometers, Detectors and Associated Equipment*, 878(Supplement C):10 – 23, 2018. ISSN 0168-9002. doi: <https://doi.org/10.1016/j.nima.2017.07.029>. URL <http://www.sciencedirect.com/science/article/pii/S0168900217307714>. Radiation Imaging Techniques and Applications.
- [20] R Plackett, I Horswell, E N Gimenez, J Marchal, D Omar, and N Tartoni. Merlin: a fast versatile readout system for medipix3. *Journal of Instrumentation*, 8(01): C01038, 2013. URL <http://stacks.iop.org/1748-0221/8/i=01/a=C01038>.
- [21] Rafidah Zainon, Anthony Butler, Nick Cook, J.S. Butzer, Nanette Schleich, N De Ruiter, L Tlustos, Michael Clark, R Heinz, and Philip Butler. Construction and operation of the mars-ct scanner. *University of Canterbury*, 2, 01 2009.
- [22] N. G. Anderson, Butler A. P., Scott N. J. A., Cook N. J., Butzer J. S., Schleich N., and Butler P. H. Spectroscopic (multi-energy) ct distinguishes iodine and barium contrast material in mice. *European Radiology*, 20(9):2126–2134, Sep 2010.

- [23] Ponchut et. all. C. Smartpix a photon-counting pixel detector for synchrotron applications based on medipix3rx readout chip and active edge pixel sensors. *16th INTERNATIONAL WORKSHOP ON RADIATION IMAGING DETECTORS*, 2015.
- [24] Wangand Jin, Soodand Ajay K., Satyamand Parlapalli V., Fengand Yiping, Wuand Xiao-zhong, Caiand Zhonghou, Yunand Wenbing, and Sinhaand Sunil K. X-ray fluorescence correlation spectroscopy: A method for studying particle dynamics in condensed matter. *Phys. Rev. Lett.*, 80:1110–1113, Feb 1998. doi: 10.1103/PhysRevLett.80.1110.
- [25] Nicholas R. Kyele, Klaas Decanniere, and Roelof G. Van Silfhout. A transparent two-dimensional in situ beam-position and profile monitor for synchrotron x-ray beamlines. *Journal of Synchrotron Radiation*, 12(6):800–806, 11 2005. ISSN 0909-0495. doi: 10.1107/S0909049505031250.
- [26] E.W. Bogaart, W Hoekstra, I.M. Peters, Agnes Kleimann, and J.T. Bosiers. Very low dark current ccd image sensor. *Electron Devices, IEEE Transactions on*, 56:2462 – 2467, 12 2009.
- [27] Alan Hoffman, Markus Loose, and Vyshnavi Suntharalingam. Cmos detector technology. *Experimental Astronomy*, 19(1):111–134, Jan 2005. ISSN 1572-9508. doi: 10.1007/s10686-005-9013-2. URL <https://doi.org/10.1007/s10686-005-9013-2>.
- [28] LHCb Collaboration. Lhcb velo upgrade technical design report. *CERN*, 13, "Nov" 2013.
- [29] D. Pennicard, B. Struth, H. Hirsemann, M. Sarajlic, S. Smoljanin, M. Zuvic, M.O. Lampert, T. Fritzsche, M. Rothermund, and H. Graafsma. A germanium hybrid pixel detector with 55 μ m pixel size and 65,000 channels. *Journal of Instrumentation*, 9(12):P12003, 2014. URL <http://stacks.iop.org/1748-0221/9/i=12/a=P12003>.
- [30] D. Pennicard, S. Smoljanin, I. Sheviakov, Q. Xia, A. Rothkirch, Y. Yu, B. Struth, H. Hirsemann, and H. Graafsma. High-speed readout of high-z pixel detectors

- with the lambda detector. *Journal of Instrumentation*, 9(12):C12014, 2014. URL <http://stacks.iop.org/1748-0221/9/i=12/a=C12014>.
- [31] Thomas Koenig, Julia Schulze, Marcus Zuber, Kristian Rink, Jochen Butzer, Elias Hamann, Angelica Cecilia, Andreas Zwerger, Alex Fauler, Michael Fiederle, and Uwe Oelfke. Imaging properties of small-pixel spectroscopic x-ray detectors based on cadmium telluride sensors. *Physics in Medicine and Biology*, 57(21):6743, 2012. URL <http://stacks.iop.org/0031-9155/57/i=21/a=6743>.
- [32] K Rink, T Koenig, M Zuber, A Zwerger, A Fauler, M Fiederle, and U Oelfke. Saturation effects of cdte photon counting detectors under high photon fluxes. *Journal of Instrumentation*, 8(01):C01026, 2013. URL <http://stacks.iop.org/1748-0221/8/i=01/a=C01026>.
- [33] Hugh T Philipp, Mark W Tate, and Sol M Gruner. Low-flux measurements with cornell’s lcls integrating pixel array detector. *Journal of Instrumentation*, 6(11):C11006, 2011. URL <http://stacks.iop.org/1748-0221/6/i=11/a=C11006>.
- [34] P. Kraft, A. Bergamaschi, Ch. Broennimann, R. Dinapoli, E. F. Eikenberry, B. Henrich, I. Johnson, A. Mozzanica, C. M. Schlepütz, P. R. Willmott, and B. Schmitt. Performance of single-photon-counting PILATUS detector modules. *Journal of Synchrotron Radiation*, 16(3):368–375, May 2009. doi: 10.1107/S09090495090009911. URL <https://doi.org/10.1107/S09090495090009911>.
- [35] S Vhnen, T Tick, and M Campbell. Low-cost bump bonding activities at cern. *Journal of Instrumentation*, 5(11):C11008, 2010. URL <http://stacks.iop.org/1748-0221/5/i=11/a=C11008>.
- [36] R. Ballabriga, J. Alozy, M. Campbell, E. Frojdh, E.H.M. Heijne, T. Koenig, X. Llopart, J. Marchal, D. Pennicard, T. Poikela, L. Tlustos, P. Valerio, W. Wong, and M. Zuber. Review of hybrid pixel detector readout asics for spectroscopic x-ray imaging. *Journal of Instrumentation*, 11(01):P01007, 2016. URL <http://stacks.iop.org/1748-0221/11/i=01/a=P01007>.

- [37] Tuomas Sakari Poikela. Readout architecture for hybrid pixel readout chips. *CERN*, 2015.
- [38] Gregor Hülsen, Christian Broennimann, Eric F. Eikenberry, and Armin Wagner. Protein crystallography with a novel large-area pixel detector. *Journal of Applied Crystallography*, 39(4):550–557, Aug 2006. doi: 10.1107/S0021889806016591. URL <https://doi.org/10.1107/S0021889806016591>.
- [39] R.I. de Vries, S. Weijers, K. Bethke, V. Kogan, J. Vasterink, A. Kharchenko, M. Fransen, and J. Bethke. Medipix 2 in x-ray diffraction. *Nuclear Instruments and Methods in Physics Research Section A: Accelerators, Spectrometers, Detectors and Associated Equipment*, 576(1):164 – 168, 2007. ISSN 0168-9002. doi: <https://doi.org/10.1016/j.nima.2007.01.175>. URL <http://www.sciencedirect.com/science/article/pii/S0168900207002355>. Proceedings of the 8th International Workshop on Radiation Imaging Detectors.
- [40] D Turecek, L Pinsky, J Jakubek, Z Vykydal, N Stoffle, and S Pospisil. Small dosimeter based on timepix device for international space station. *Journal of Instrumentation*, 6(12):C12037, 2011. URL <http://stacks.iop.org/1748-0221/6/i=12/a=C12037>.
- [41] I. Sikharulidze, R. van Gastel, S. Schramm, J.P. Abrahams, B. Poelsema, R.M. Tromp, and S.J. van der Molen. Low energy electron microscopy imaging using medipix2 detector. *Nuclear Instruments and Methods in Physics Research Section A: Accelerators, Spectrometers, Detectors and Associated Equipment*, 633(Supplement 1):S239 – S242, 2011. ISSN 0168-9002. doi: <https://doi.org/10.1016/j.nima.2010.06.177>. URL <http://www.sciencedirect.com/science/article/pii/S0168900210013677>. 11th International Workshop on Radiation Imaging Detectors (IWORID).
- [42] John Vallerger, Jason McPhate, Anton Tremsin, Oswald Siegmund, Bettina Mikulec, and Allan Clark. Optically sensitive medipix2 detector for adaptive optics wavefront sensing. *Nuclear Instruments and Methods in Physics Research Section A: Accelerators, Spectrometers, Detectors and Associated Equipment*, 546(1):263 – 269, 2005. ISSN

- 0168-9002. doi: <https://doi.org/10.1016/j.nima.2005.03.102>. URL <http://www.sciencedirect.com/science/article/pii/S0168900205006686>. Proceedings of the 6th International Workshop on Radiation Imaging Detectors.
- [43] Katsuyuki Taguchi and Jan S. Iwanczyk. Vision 20/20: Single photon counting x-ray detectors in medical imaging. *Medical Physics*, 40(10):100901–n/a, 2013. ISSN 2473-4209. doi: 10.1118/1.4820371. URL <http://dx.doi.org/10.1118/1.4820371>. 100901.
- [44] J Zemlicka, J Jakubek, M Kroupa, D Hradil, J Hradilova, and H Mislerova. Analysis of painted arts by energy sensitive radiographic techniques with the pixel detector timepix. *Journal of Instrumentation*, 6(01):C01066, 2011. URL <http://stacks.iop.org/1748-0221/6/i=01/a=C01066>.
- [45] G. Ottaviani, C. Canali, and A. Alberigi Quaranta. A review of some charge transport properties of silicon. *IEE Trans. Nucl. Sci.*, (NS-22), 1975.
- [46] G.F Knoll. Radiation detection and measurement. 1999.
- [47] et al R. Ballabriga. The medipix3rx: a high resolution, zero dead-time pixel detector readout chip allowing spectroscopic imaging. *INTERNATIONAL WORKSHOP ON RADIATION IMAGING DETECTORS*, July 2012.
- [48] F. Krummenacher. Pixel detectors with local intelligence: an ic designer point of view. *Nuclear Instruments and Methods in Physics Research Section A: Accelerators, Spectrometers, Detectors and Associated Equipment*, 305(3):527 – 532, 1991. ISSN 0168-9002. doi: [https://doi.org/10.1016/0168-9002\(91\)90152-G](https://doi.org/10.1016/0168-9002(91)90152-G). URL <http://www.sciencedirect.com/science/article/pii/016890029190152G>.
- [49] R. Szczygiel. Krummenacher feedback analysis for high-count-rate semiconductor pixel detector readout. *Proceedings of the 17th International Conference Mixed Design of Integrated Circuits and Systems - MIXDES 2010*, pages 412–415, June 2010.
- [50] B Mikulec. Single photon detection with semiconductor pixel arrays for medical imaging applications. *CERN*, CERN-THESIS-2000-021, June 2000.

- [51] Patrick Takoukam Talla, Peter Bartl, Thilo Michel, Jrgen Durst, and Gisela Anton. A modified spectrum reconstruction method for the charge summing mode of medipix3. *Nuclear Instruments and Methods in Physics Research Section A: Accelerators, Spectrometers, Detectors and Associated Equipment*, 633(Supplement 1):S128 – S130, 2011. ISSN 0168-9002. doi: <https://doi.org/10.1016/j.nima.2010.06.144>. URL <http://www.sciencedirect.com/science/article/pii/S0168900210013343>. 11th International Workshop on Radiation Imaging Detectors (IWORID).
- [52] R. Ballabriga, M. Campbell, E. H. M. Heijne, X. Llopart, and L. Tlustos. The medipix3 prototype, a pixel readout chip working in single photon counting mode with improved spectrometric performance. *2006 IEEE Nuclear Science Symposium Conference Record*, 6:3557–3561, Oct 2006. ISSN 1082-3654.
- [53] E. N. Gimenez, R. Ballabriga, G. Blaj, M. Campbell, I. Dolbnya, E. Frodjh, I. Horswell, X. Llopart, J. Marchal, J. McGrath, D. Omar, R. Plackett, K. Sawhney, and N. Tartoni. Medipix3rx: Characterizing the medipix3 redesign with synchrotron radiation. *IEEE Transactions on Nuclear Science*, 62(3):1413–1421, June 2015. ISSN 0018-9499. doi: 10.1109/TNS.2015.2425227.
- [54] Vytautas et. all. Astromskas. The influence of operating conditions on schottky cdte medipix3rx spectroscopic pixel detector performance. *10th International Conference on Position Sensitive Detectors*, 2015.
- [55] et al Elias Hamann. Performance of a medipix3rx spectroscopic pixel detector with a high resistivity gallium arsenide sensor. *IEEE TRANSACTIONS ON MEDICAL IMAGING*, 2014.
- [56] Texas Instruments. *TPS7A7200 2-A, Fast-Transient, Low-Dropout Voltage Regulator*. Texas Instruments, 2015.
- [57] Jr. William A. Campbell and Richard S. Outgassing data for spacecraft materials. *J NASA Reference Publication 1124*, 1987.
- [58] Rogers-Corporation. Low outgassing characteristics of rogers laminates approved for spacecraft applications. *Rogers Corporation*, .

- [59] Rogers-Corporation. Ro4000 series high frequency circuit materials. *Rogers Corporation*, .
- [60] Intersil-Corporation. Carrying the heat away from power module pcb designs. *Intersil Corporation*.
- [61] Thermagon. Thermally conductive printed circuit board materials, the t-iam system. *Thermagon Inc*.
- [62] F. Sarvar, N. J. Poole, and P. A. Witting. Pcb glass-fibre laminates: Thermal conductivity measurements and their effect on simulation. *Journal of Electronic Materials*, 19(12):1345–1350, Dec 1990. ISSN 1543-186X. doi: 10.1007/BF02662823. URL <https://doi.org/10.1007/BF02662823>.
- [63] Application Report. An-1520 a guide to board layout for best thermal resistance for exposed packages. *Texas Instruments*, 2013.
- [64] White Paper. An 479: Design guidelines for implementing lvds interfaces in cyclone series devices. *Altera Corporation*, 2013.
- [65] Altera-Corporation. *Cyclone V device Datasheet*. December 2016.
- [66] Texas-Instruments. *AM335x Sitara Processors*. April 2016.
- [67] Hamann et. all. Elias. Performance of a medipix3rx spectroscopic pixel detector with a high resistivity gallium arsenide sensor. *TRANSACTIONS ON MEDICAL IMAGING*, 2014.
- [68] Quantum Detectors. *Merlin Technical Datasheet*. Quantum Detectors, 2015.
- [69] White Paper. Application tips, dc or pwm. *RMT Ltd*, 2013.
- [70] et all Schelle Donald. Buck-converter design demystified. *Maxim Integrated Products*.
- [71] et all S. Mouhadjer. Comprehensive and field study to design a buck converter for photovoltaic systems. *Revue des Energies Renouvelables Vol. 15 N2*, 2012.
- [72] Naeim Safari. Design of a dc/dc buck converter for ultra-low power applications in 65nm cmos process. 2012.

- [73] Vijayaraghavan G Madhuravasal. *Extreme temperature switch mode power supply based on vee-square control using silicon carbide, silicon on sapphire, hybrid technology*. Oklahoma State University, 2009.
- [74] White Paper. Avalon interface specifications. *Altera Corporation*, 2017.
- [75] et. all. Walsh, M.F. Improving and characterising the threshold equalisation process for multi-chip medipix3 cameras in single pixel mode. *Nuclear Science Symposium Conference Record*, 2011.
- [76] Jean Rinkel, Debora Magalhes, Franz Wagner, Erik Frojdh, and Rafael Ballabriga Sune. Equalization method for medipix3rx. *Nuclear Instruments and Methods in Physics Research Section A: Accelerators, Spectrometers, Detectors and Associated Equipment*, 801(Supplement C):1 – 6, 2015. ISSN 0168-9002. doi: <https://doi.org/10.1016/j.nima.2015.08.029>. URL <http://www.sciencedirect.com/science/article/pii/S0168900215009638>.
- [77] E Frojdh, R Ballabriga, M Campbell, M Fiederle, E Hamann, T Koenig, X Llopart, D de Paiva Magalhaes, and M Zuber. Count rate linearity and spectral response of the medipix3rx chip coupled to a 300 μ m silicon sensor under high flux conditions. *Journal of Instrumentation*, 9(04):C04028, 2014. URL <http://stacks.iop.org/1748-0221/9/i=04/a=C04028>.
- [78] E. N. Gimenez, R. Ballabriga, G. Blaj, M. Campbell, I. Dolbnya, E. Frojdh, I. Horswell, X. Llopart, J. Marchal, J. McGrath, D. Omar, R. Plackett, K. Sawhney, and N. Tartoni. Medipix3rx: Characterizing the medipix3 redesign with synchrotron radiation. *IEEE Transactions on Nuclear Science*, 62(3):1413–1421, June 2015. ISSN 0018-9499. doi: 10.1109/TNS.2015.2425227.
- [79] Michael F. Walsh. Spectral computed tomography development. *PHD Thesis*, 2014.
- [80] H. Saisho and Y. Gohshi. *Applications of Synchrotron Radiation to Materials Analysis*. Elsevier Science, 1996.
- [81] Oliver Bunk, Franz Pfeiffer, Marco Stampanoni, Bruce D. Patterson, Clemens Schulze-Bries, and Christian David. X-ray beam-position monitoring in

- the sub-micrometre and sub-second regime. *Journal of Synchrotron Radiation*, 12(6):795–799, Nov 2005. doi: 10.1107/S0909049505028189. URL <https://doi.org/10.1107/S0909049505028189>.
- [82] Thierry Martin, G Baret, F Lesimple, and P.P. Jobert. semi-transparent x-ray beam monitor based on nanometric phosphor powder deposited on thin carbon plate. *Nuclear Science, IEEE Transactions on*, 55:1527 – 1531, 07 2008.
- [83] Anton Kachatkou, Nicholas Kyele, Peter Scott, and Roelof van Silfhout. *In situ* X-ray beam imaging using an off-axis magnifying coded aperture camera system. *Journal of Synchrotron Radiation*, 20(4):596–602, Jul 2013. doi: 10.1107/S0909049513011060. URL <https://doi.org/10.1107/S0909049513011060>.
- [84] P. Revesz and J. A. White. An X-ray beam position monitor based on the photoluminescence of helium gas. *Nuclear Instruments and Methods in Physics Research A*, 540:470–479, March 2005. doi: 10.1016/j.nima.2004.11.040.
- [85] A. Oed. Position-sensitive detector with microstrip anode for electron multiplication with gases. *Nuclear Instruments and Methods in Physics Research Section A: Accelerators, Spectrometers, Detectors and Associated Equipment*, 263(2):351 – 359, 1988. ISSN 0168-9002. doi: [https://doi.org/10.1016/0168-9002\(88\)90970-9](https://doi.org/10.1016/0168-9002(88)90970-9). URL <http://www.sciencedirect.com/science/article/pii/0168900288909709>.
- [86] Petr Ilinski. Residual gas x-ray beam position monitor for petra-iii. *AIP Conference Proceedings*, 01 2010.
- [87] Chris Bloomer, Jose Brandao-neto, Guenther Rehm, and C Thomas. Dual beam x-ray beam position monitor. *DIPAC 2009 - 9th European Workshop on Beam Diagnostics and Instrumentation for Particle Accelerators*, pages 4–6, 01 2009.
- [88] J.-R. Chen, T. S. Ueng, G. Y. Hsiung, T. F. Lin, C. T. Lee, S. L. Tsai, and S.-L. Chang. A synchrotron radiation beam-position

- monitor at the Taiwan Light Source. *Journal of Synchrotron Radiation*, 5(3):621–623, May 1998. doi: 10.1107/S0909049597018207. URL <https://doi.org/10.1107/S0909049597018207>.
- [89] E. D. Johnson and T. Oversluizen. Compact high flux photon beam position monitor. *Review of Scientific Instruments*, 60(7):1947–1950, 1989. doi: 10.1063/1.1140896.
- [90] R. W. Alkire, G. Rosenbaum, and G. Evans. Design of a vacuum-compatible high-precision monochromatic beam-position monitor for use with synchrotron radiation from 5 to 25keV. *Journal of Synchrotron Radiation*, 7(2):61–68, Mar 2000. doi: 10.1107/S090904959901568X. URL <https://doi.org/10.1107/S090904959901568X>.
- [91] P. Bergonzo, D. Tromson, and C. Mer. Radiation detection devices made from cvd diamond. *Semiconductor Science and Technology*, 18(3):S105, 2003. URL <http://stacks.iop.org/0268-1242/18/i=3/a=315>.
- [92] P. Bergonzo, D. Tromson, and C. Mer. CVD diamond-based semi-transparent beam-position monitors for synchrotron beamlines: preliminary studies and device developments at CEA/Saclay. *Journal of Synchrotron Radiation*, 13(2):151–158, Mar 2006. doi: 10.1107/S0909049505032097. URL <https://doi.org/10.1107/S0909049505032097>.
- [93] Kewin Desjardins, Denis Duran, Stphanie Hustache, Michal Pomorski, and William Shepard. Characterisation of cvd diamond devices as xbpms at soleil. *Journal of Physics: Conference Series*, 425(21):212004, 2013. URL <http://stacks.iop.org/1742-6596/425/i=21/a=212004>.
- [94] Anton Kachatkou, Nicholas Kyele, Peter Scott, and Roelof van Silfhout. Real-time in-situ x-ray beam diagnostics. *Journal of Physics: Conference Series*, 425(4):042002, 2013. URL <http://stacks.iop.org/1742-6596/425/i=4/a=042002>.
- [95] Manuel Guizar-Sicairos, Samuel T. Thurman, and James R. Fienup. Efficient subpixel image registration algorithms. *Opt.*

- Lett.*, 33(2):156–158, Jan 2008. doi: 10.1364/OL.33.000156. URL <http://ol.osa.org/abstract.cfm?URI=ol-33-2-156>.
- [96] Y. Feng, J. Goree, and Bin Liu. Accurate particle position measurement from images. *Review of Scientific Instruments*, 78(5):053704, 2007. doi: 10.1063/1.2735920.
- [97] Tim Short Mark R. Shortis, Timothy A. Clarke. Comparison of some techniques for the subpixel location of discrete target images. *Proc.SPIE*, 2350:2350 – 2350 – 12, 1994. doi: 10.1117/12.189136. URL <http://dx.doi.org/10.1117/12.189136>.
- [98] Anton Kachatkou and Roelof Van Silfhout. On the resolution and linearity of lensless in situ x-ray beam diagnostics using pixelated sensors. *Optics express*, 21:4291–4302, 02 2013.
- [99] J.L. Gaines, L.D. Kissel, H.C. Catron, and R.A. Hansen. Scattering of x rays from low-z materials. *Lawrence Livermore Lab*, 12, 08 1980.
- [100] R. G. van Silfhout. A high-precision X-ray beam-position and profile monitor for synchrotron beamlines. *Journal of Synchrotron Radiation*, 6(6):1071–1075, Nov 1999. doi: 10.1107/S0909049599010596. URL <https://doi.org/10.1107/S0909049599010596>.
- [101] Klaus D Mielenz. On the Diffraction Limit for Lensless Imaging. *Journal of Research of the National Institute of Standards and Technology*, 104(5), Oct 1999.
- [102] S. Feuerlein et al. Multienergy photon-counting k-edge imaging: potential for improved luminal depiction in vascular imaging. *Radiology*, 249:1010, 2008. URL <http://dx.doi.org/10.1148/radiol.2492080560>.
- [103] R. Zainon et al. Atherosclerotic plaque composition: analysis with multi-color ct and targeted gold nanoparticles. *Radiology*, 256:774, 2010. URL <http://dx.doi.org/10.1148/radiol.10092473>.

- [104] D.P. Cormode et al. Spectral ct of carotid atherosclerotic plaque: comparison with histology. *Eur. Radiol.*, 22:2581, 2012. URL <http://dx.doi.org/10.1007/s00330-012-2538-7>.
- [105] S Procz, K A Wartig, A Fauler, A Zwerger, J Luebke, R Ballabriga, G Blaj, M Campbell, M Mix, and M Fiederle. Medipix3 ct for material sciences. *Journal of Instrumentation*, 8(01):C01025, 2013. URL <http://stacks.iop.org/1748-0221/8/i=01/a=C01025>.
- [106] K Rajendran, M F Walsh, N J A de Ruiter, A I Chernoglazov, R K Panta, A P H Butler, P H Butler, S T Bell, N G Anderson, T B F Woodfield, S J Tredinnick, J L Healy, C J Bateman, R Aamir, R M N Doesburg, P F Renaud, S P Gieseg, D J Smithies, J L Mohr, V B H Mandalika, A M T Opie, N J Cook, J P Ronaldson, S J Nik, A Atharifard, M Clyne, P J Bones, C Bartneck, R Grasset, N Schleich, and M Billinghamurst. Reducing beam hardening effects and metal artefacts in spectral ct using medipix3rx. *Journal of Instrumentation*, 9(03):P03015, 2014. URL <http://stacks.iop.org/1748-0221/9/i=03/a=P03015>.
- [107] R Aamir, A Chernoglazov, C J Bateman, A P H Butler, P H Butler, N G Anderson, S T Bell, R K Panta, J L Healy, J L Mohr, K Rajendran, M F Walsh, N de Ruiter, S P Gieseg, T Woodfield, P F Renaud, L Brooke, S Abdul-Majid, M Clyne, R Glendenning, P J Bones, M Billinghamurst, C Bartneck, H Mandalika, R Grasset, N Schleich, N Scott, S J Nik, A Opie, T Janmale, D N Tang, D Kim, R M Doesburg, R Zainon, J P Ronaldson, N J Cook, D J Smithies, and K Hodge. Mars spectral molecular imaging of lamb tissue: data collection and image analysis. *Journal of Instrumentation*, 9(02):P02005, 2014. URL <http://stacks.iop.org/1748-0221/9/i=02/a=P02005>.
- [108] Thomas Koenig, Elias Hamann, S Procz, Rafael Ballabriga, Angelica Cecilia, Marcus Zuber, X Llopart, Michael Campbell, Alex Fauler, Tilo Baumbach, and Michael Fiederle. Charge summing in spectroscopic x-ray detectors with high-z sensors. 60:4713, 12 2013.
- [109] Markus Firsching, Patrick Takoukam Talla, Thilo Michel, and Gisela Anton. Material resolving x-ray imaging using spectrum reconstruction with medipix2.

- Nuclear Instruments and Methods in Physics Research Section A: Accelerators, Spectrometers, Detectors and Associated Equipment*, 591(1):19 – 23, 2008. ISSN 0168-9002. doi: <https://doi.org/10.1016/j.nima.2008.03.017>. URL <http://www.sciencedirect.com/science/article/pii/S0168900208003926>. Radiation Imaging Detectors 2007.
- [110] J. Paul Ronaldson, Rafidah Zainon, Nicola Jean Agnes Scott, Steven Paul Gieseg, Anthony P. Butler, Philip H. Butler, and Nigel G. Anderson. Toward quantifying the composition of soft tissues by spectral ct with medipix3. *Medical Physics*, 39(11):6847–6857, 2012. ISSN 2473-4209. doi: 10.1118/1.4760773. URL <http://dx.doi.org/10.1118/1.4760773>.
- [111] R E Alvarez and A Macovski. Energy-selective reconstructions in x-ray computerised tomography. *Physics in Medicine & Biology*, 21(5):733, 1976. URL <http://stacks.iop.org/0031-9155/21/i=5/a=002>.
- [112] Anthony P.H. Butler, Jochen Butzer, Nanette Schleich, Nicholas J. Cook, Nigel G. Anderson, Nicola Scott, Niels de Ruiter, Raphael Grasset, Lukas Tlustos, and Philip H. Butler. Processing of spectral x-ray data with principal components analysis. *Nuclear Instruments and Methods in Physics Research Section A: Accelerators, Spectrometers, Detectors and Associated Equipment*, 633(Supplement 1):S140 – S142, 2011. ISSN 0168-9002. doi: <https://doi.org/10.1016/j.nima.2010.06.149>. URL <http://www.sciencedirect.com/science/article/pii/S0168900210013392>. 11th International Workshop on Radiation Imaging Detectors (IWORID).
- [113] X. Wang, D. Meier, K. Taguchi, D. J. Wagenaar, B. E. Patt, and E. C. Frey. Material separation in x-ray ct with energy resolved photon-counting detectors. *Proc.SPIE*, 7961:7961 – 7961 – 7, 2011.
- [114] Kishore Rajendran, Caroline Löbker, Benjamin S. Schon, Christopher J. Bateman, Raja Aamir Younis, Niels J. A. de Ruiter, Alex I. Chernoglazov, Mohsen Ramyar, Gary J. Hooper, Anthony P. H. Butler, Tim B. F. Woodfield, and Nigel G. Anderson. Quantitative imaging of excised osteoarthritic cartilage using spectral ct. *European Radiology*, 27(1):384–392, Jan 2017.

- [115] N. G. Anderson, A. P. Butler, N. J. A. Scott, N. J. Cook, J. S. Butzer, N. Schleich, M. Firsching, R. Grasset, N. de Ruiter, M. Campbell, and P. H. Butler. Spectroscopic (multi-energy) ct distinguishes iodine and barium contrast material in mice. *European Radiology*, 20(9):2126–2134, Sep 2010.
- [116] Ryan K. Roeder, Tyler E. Curtis, Prakash D. Nallathamby, Lisa E. Irimata, Tracie L. McGinnity, Lisa E. Cole, Tracy Vargo-Gogola, and Karen D. Cowden Dahl. Nanoparticle imaging probes for molecular imaging with computed tomography and application to cancer imaging. *Proc.SPIE*, 10132:10132 – 10132 – 8, 2017.
- [117] Koenig Thomas, Hamann Elias, Procz S, Ballabriga Rafael, Cecilia Angelica, Zuber Marcus, Llopart X, Campbell Michael, Fauler Alex, Baumbach Tilo, and Fiederle Michael. Charge summing in spectroscopic x-ray detectors with high-z sensors. 60:4713, 12 2013.
- [118] M. Ramyar, C. Leary, A. Raja, A. P. H. Butler, T. B. F. Woodfield, N. G. Anderson, and Tracy E. Kirkbride. Establishing a method to measure bone structure using spectral ct. *Proc.SPIE*, 10132:10132 – 10132 – 9, 2017. doi: 10.1117/12.2255616. URL <http://dx.doi.org/10.1117/12.2255616>.
- [119] *AM335x PRU-ICSS Reference Guide*. October 2014.

Appendix A

Medipix3RX information

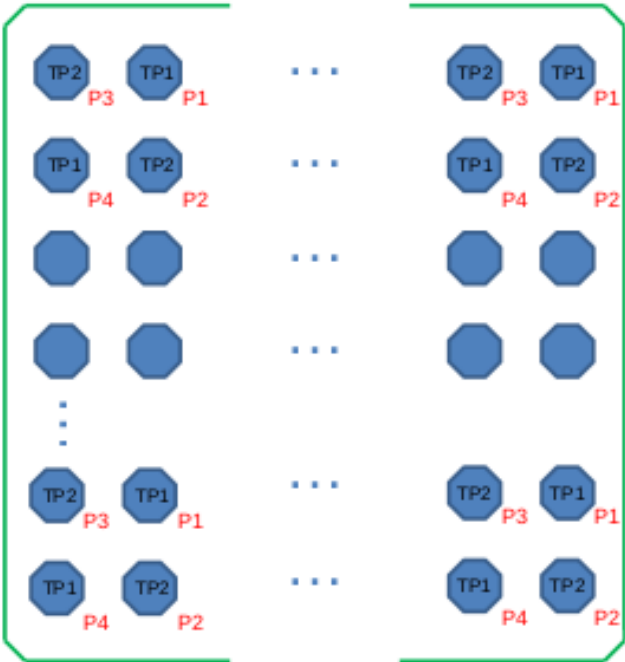


Figure A.1: Checker board pattern of the test pulses in the Medipix3RX matrix. [8]

DAC Name	DAC Code	DAC Register <LSB:MSB>	Length [bits]	DAC Range	Mid Range Value (After Reset)	DAC Step	Ext DAC Range [0 to 1 V]
Threshold[0]	00001	<30:38>	9	0 to 2.04 μ A SHGM: 0..10.4 Ke- HGM: 0..19.6 Ke- LGM: 0..28.6 Ke- SLGM: 0..37.8 Ke-	1.024 μ A (1.05 V) SHGM: 5.2 Ke- HGM: 9.8 Ke- LGM: 14.3 Ke- SLGM: 18.9 Ke-	4 nA SHGM: 20 e- HGM: 38 e- LGM: 56 e- SLGM: 74 e-	2 μ A/V SHGM: 10 Ke-/V HGM: 19 Ke-/V LGM: 28 Ke-/V SLGM: 38 Ke-/V
Threshold[1]	00010	<39:47>					
Threshold[2]	00011	<48:56>					
Threshold[3]	00100	<57:65>					
Threshold[4]	00101	<66:74>					
Threshold[5]	00110	<75:83>					
Threshold[6]	00111	<84:92>					
Threshold[7]	01000	<93:101>					
I_Preampl	01001	<102:109>	8	0 to 5.1 μ A	2.56 μ A (355 mV)	20 nA	1 V/V
I_Ikrm	01010	<110:117>	8	0 to 60 nA	30 nA (970 mV)	234 pA	1 V/V
I_Shaper	01011	<118:125>	8	0 to 1.02 μ A	512 nA (1.03 V)	4 nA	1 V/V
I_Disc	01100	<126:133>	8	0 to 2.04 μ A	1.024 μ A (0.84 V)	8 nA	1 V/V
I_Disc_LS	01101	<134:141>	8	0 to 1.02 μ A	512 nA (270 mV)	4 nA	1 V/V
I_Shaper_test	01110	<142:149>	8	0 to 1.02 μ A	512 nA (1.03 V)	4 nA	1 V/V
I_DAC_Discl	01111	<150:157>	8	0 to 48 nA	24 nA (1.25 V)	187 pA	48 nA/V
I_DAC_test	11110	<158:165>	8	0 to 48 nA	24 nA (1.25 V)	187 pA	48 nA/V
I_DAC_DisclH	11111	<166:173>	8	0 to 48 nA	24 nA (1.25 V)	187 pA	48 nA/V
I_Delay	10000	<174:181>	8	0 to 204 nA	102.4 nA (1.02 V)	800 pA	1 V/V
I_TP_BufferIn	10001	<182:189>	8	0 to 10.2 μ A	5.12 μ A (1.12 V)	40 nA	1 V/V
I_TP_BufferOut	10010	<190:197>	8	0 to 255 μ A	128 μ A (1.04 V)	1 μ A	1 V/V
V_Rpz	10011	<198:205>	8	0 to 1.5 V	640 mV	5 mV	1 V/V
V_Gnd	10100	<206:213>	8	0 to 1.275 V	640 mV	5 mV	1 V/V
V_Tp_ref	10101	<214:221>	8	0 to 1.275 V	640 mV	5 mV	1 V/V
V_Fbk	10110	<222:229>	8	0 to 1.275 V	640 mV	5 mV	1 V/V
V_Cas	10111	<230:237>	8	0 to 1.275 V	640 mV	5 mV	1 V/V
V_Tp_refA	11000	<238:246>	9	0 to 1.275 V	640 mV	2.5 mV	1 V/V
V_Tp_refB	11001	<247:255>	9	0 to 1.275 V	640 mV	2.5 mV	1 V/V

Figure A.2: Table of DACs used in the Medipix3RX. [8]

Name	Bits	Default	Description
M[0:2]	0:2	000	Operation mode selection: 000: Read CounterL 001: Read CounterH 010: Load CounterL 011: Load CounterH 100: Load DACs 101: Load CTPR 110: Read DACs 111: Read OMR and ChipID
CRW_SRW	3	0	0: Sequential Read Write 1: Continuous Read Write
Polarity	4	1	0: Electron collection mode 1: Holes collection mode
PS[0:1]	5:6	00	00: DataOut[0] 10: DataOut[0..1] 01: DataOut[0..3] 11: DataOut[0..7]
Disc_CSM_SPM	7	0	Selects which Discriminator output is used during the 24-bit mode, CRW or Equalization operation modes 0: Selects DiscL 1: Selects DiscH
Enable_TP	8	0	1: Enable internal Test pulse 0: Disable external Test pulse
CountL[0:1]	9:10	00	Selects the counter depth: 00: 2x 1-bit 10: 2x 6-bit 01: 2x 12-bit 11: 1x24 bit
ColumnBlock[0:2]	11:13	000	Selects the matrix columns to be readout if ColumnBlockSel is high <div style="display: flex; align-items: center;"> <div style="margin-right: 10px;"> 000 100 010 110 001 101 011 111 </div> <div style="font-size: 3em; margin-right: 10px;">}</div> <div>See 7.6.2.1</div> </div>

Figure A.3: First section of the Operation Mode Register of the Medipix3RX. Default column shows the bit value after a reset. [8]

ColumnBlockSel	14	0	0: All columns are read out 1: Matrix columns selected by ColumnBlock[0:2] are read out
RowBlock[0:2]	15:17	000	Selects the matrix rows to be readout if RowBlockSel is high. See 7.6.2.1. 000: Row [0] 100: Row [0:1] 010: Row [0:3] 110: Row [0:7] 001: Row [0:15] 101: Row [0:31] 011: Row [0:63] 111: Row [0:127]
RowBlockSel	18	0	0: All rows are read out 1: Matrix rows selected by RowBlock[0:2] are read out
Equalization	19	0	Selects if the chip is in Threshold Equalization Mode (see chapter 8.4) 0: Equalization OFF 1: Equalization ON
ColourMode	20	0	0: Fine Pitch Mode (55µm x 55µm) 1: Spectroscopic Mode (110µm x 110µm)
CSM_SPM	21	0	0: Single Pixel Mode 1: Charge Summing Mode
InfoHeader	22	0	0: No Info header added 1: Info header (OMR bits + chip ID) added before the DataOut stream in Data_Out[0]
FuseSel[0:4]	23:27	000000	Selects Fuse to be burned
FusePulseWidth[0:6]	28:34	0000000	Set the programming pulse width to burn the selected e-fuse 0000_000: No pulse 1000_000: 1024 clocks width 1111_111: 523264 clocks width
GainMode[0:1]	35:36	00	00: Super-High Gain Mode (SHGM) 10: High Gain Mode (HGM) 01: Low Gain Mode (LGM) 11: Super-Low Gain Mode (SLGM)
SenseDAC[0:4]	37:41	0_0000	Selects DAC to be sensed through DACOUT pin
ExtDAC[0:4]	42:46	0_0000	Selects DAC to be externally imposed through EXTDAC pin
ExtBGSel	47	0	0: Internal Band-Gap is used 1: External Band-Gap used through EXTBG pin

Figure A.4: Second section of the Operation Mode Register of the Medipix3RX. Default column shows the bit value after a reset. [8]

B0	B1	B2	B3	B4	B5	B6	B7	B8	B9	B10	B11
MaskBit	ConfigDiscL[0]	ConfigDiscL[1]	ConfigDiscL[2]	ConfigDiscL[3]	ConfigDiscL[4]	ConfigDiscH[0]	ConfigDiscH[1]	ConfigDiscH[2]	ConfigDiscH[3]	ConfigDiscH[4]	TestBit

Figure A.5: Configuration bits per pixel in the Medipix3RX. The configuration matrix is the combination of the configuration bits for all the pixels. [8]

Appendix B

Interface board information and FPGA configuration

Parameter	Bit values	Configuration
Analog output voltage range	XX00	2.5[V]
	XX01	5[V]
	XX10	7.5[V]
	XX11	10[V]
EEPROM write protect	X0XX	Write disabled
	X1XX	Write enabled
Polarity	0XXX	Unipolar
	1XXX	Bipolar

Table B.1: DIP switch configuration on the Interface board.

LED position	System status	
	LED on	LED off
1	Temperature control enabled	Temperature control disabled
2	Vacuum error	Correct Vaccum
3	High Voltage enable	High Voltage disable
4	Medipix3RX driver busy	Medipix3RX driver waiting command

Table B.2: Information shown in frontal LEDs of the Interface board. The positions are given in descending order.

B.1 Configuring the FPGA using the PRU-ICSS subsystem

Embedded systems and FPGA devices is a combination that is being used more and more commonly on modern designs. The high processing speed, versatility and possibilities to implement parallel design on the FPGA, makes it a excellent platform for numerous applications. The use of an ARM processor, that allows to run a Linux operative system, is of common combination with the FPGA. The Linux system can make all the slow tasks that do not require fast processing but do require a complex file system and communication protocols. One of the main issues with this combination, is the possibility to reconfigure the FPGA remotely, using the ARM processor.

One of the possibilities for configuring the Altera Cyclone V FPGA , is to use Jrunner. Jrunner is a C program that runs on the AM335x processor and uses four lines to communicate with the JTAG interface in the Cyclone V. Jrunner is a software designed by Altera and distributed as an open source. The original source can be find in the Altera website with some implementation information. The given code by Altera is made to run under a Windows Operating System, so some of its functions are environment dependant. The Jrunner version used in this project is based on the Altera code but has been modified to work in the AM335x using a Linux distribution. The output and input functions had been modified to work under Linux and the relationship to physical pins in the AM335x has been correctly assigned in relationship to the physical connection in the ARMflash Mini board, for the AM335x lines with the Cyclone V configuration lines.

The AM335x processor, used in the LancelotRX, come with a Programmable Real-Time Unit and Industrial Communication Subsystem (PRU-ICSS), which have two 32-bit RISC cores (Programmable Real Time Units) , shared data and instruction memories, internal peripheral modules and interrupt controller (INTC) [119]. Between the applications for which these PRUs were designed are the possibility to implement power saving techniques, specialized data handling and DMA operations , possibility to access pins and events, implement fast real-time responses , offloading operations from other processor cores and implementing custom peripheral interfaces.

B.1.1 Communication PRU to Cyclone V

The PRU communicates with the Cyclone V by using the physical pins on the AM335x, this require to set the pinmux of the processor from a device tree overlay. The architecture of the PRU-ICSS allows to access the GPIO control registers from the PRU core. To do this, it is necessary to use the L3 interconnect together with the Open Core Protocol (OCP) master port, which allow the PRU core to to access the data bus that interconnects all peripherals on the processor. By doing this, is possible to control the pins required to pass the configuration data to the Cyclone V. In Figure B.1, a diagram of the data flow is shown.

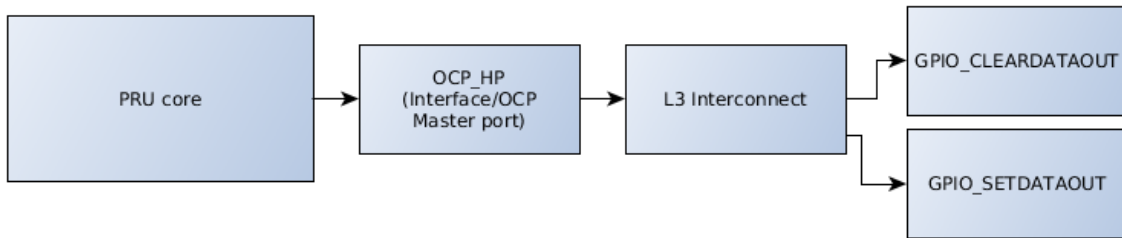


Figure B.1: Block diagram of the connections necessary to control the pins from PRU core without the use of Enhanced GPIO.

B.1.2 Jrunner design flow and modifications for using the PRU

Figure B.2 shows a block diagram of Jrunner and the files it require. Jrunner reads from a CDF file the information it needs to make the configuration. This file tells Jrunner what action is going to be made, with which FPGA its working and where is the configuration data that is going to be used. A list containing the information about each FPGA is used, information like that size, ID numbers, and so on.

The program flow of the Jrunner from its original source can be seen in Figure B.3 . The program starts by reading the CDF file given to it, and by checking the communication with the FPGA. Then the device ID is compared with the device list that the program has. If the action selected is to configure the FPGA, the program now opens the configuration file, gets the file size and resets the counters. The data is sent bit by bit, and the clock line toggles for each bit, this is all made in software.

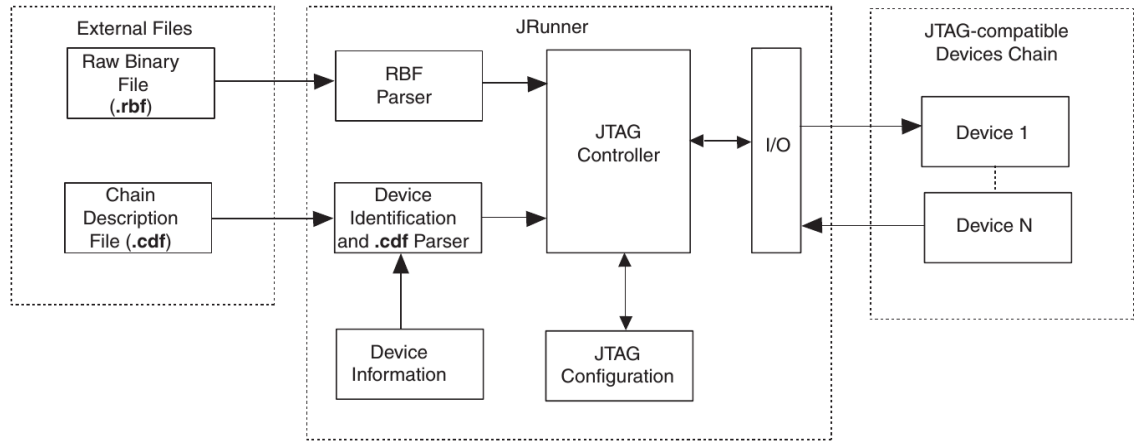


Figure B.2: Block diagram of Jrunner software [12].

After all the bits have been sent, the software checks the status of *conf_done* line. The *conf_done* is high when the FPGA has been correctly configured. If an error happened, the software attempts to configure the FPGA again. If there are no more devices to configure, the program closes.

In the current implementation, Jrunner runs in the main core of the processor and the data transfer to the FPGA is executed by the PRU core. The byte sending process of the Jrunner was modified to call a program that runs on the PRU core and performs the bit-banged communication, while toggling the clock line. The main processor, where the Jrunner is executed, waits until the PRU lets it know that the process has finished. The PRU core uses interrupts to communicate the status of the execution to the processor. Figure B.4 shows the original program flow of the Jrunner and the modification made to use the PRU cores for the bit banded communication.

The PRU program was implemented using data bursts, in which the main processor can copy a section of the configuring data for the Cyclone V, into the shared memory, so the PRU program can access it with one clock cycle reads. The C program fills the shared memory with configuration data and calls the PRU program. The PRU program reads this data from the shared memory and uses L3 to control the registers to set the pins outputs. This way, the PRU uses the L3 only for controlling the GPIO, and the bus is not busy. After the data block has been send by the PRU, the main processor sets a new data block and the process is repeated until all the configuration data had been passed. Figure B.5 shows the program flow of the implementation in the PRU.

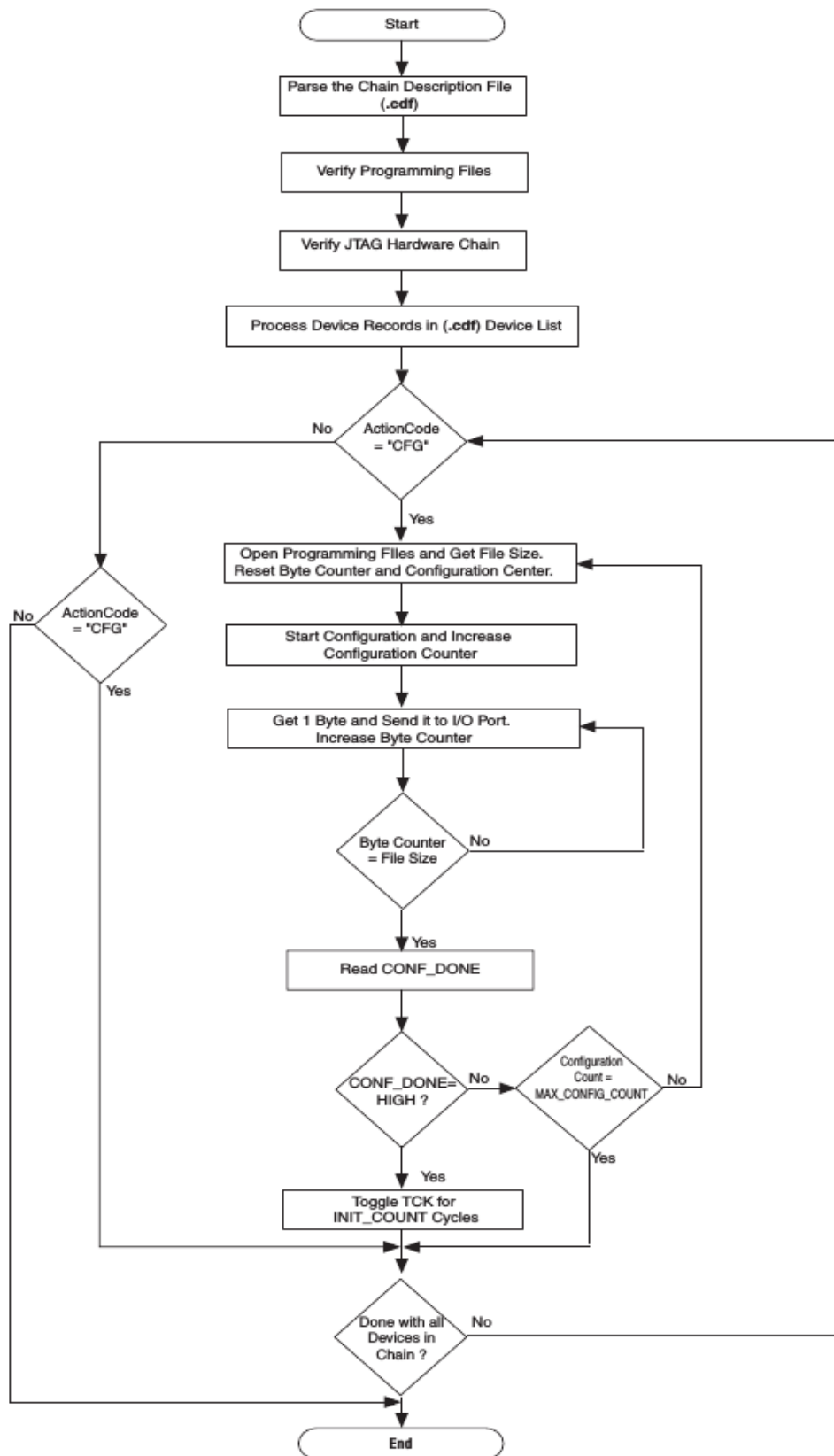


Figure B.3: Original Jranner program flow [12].

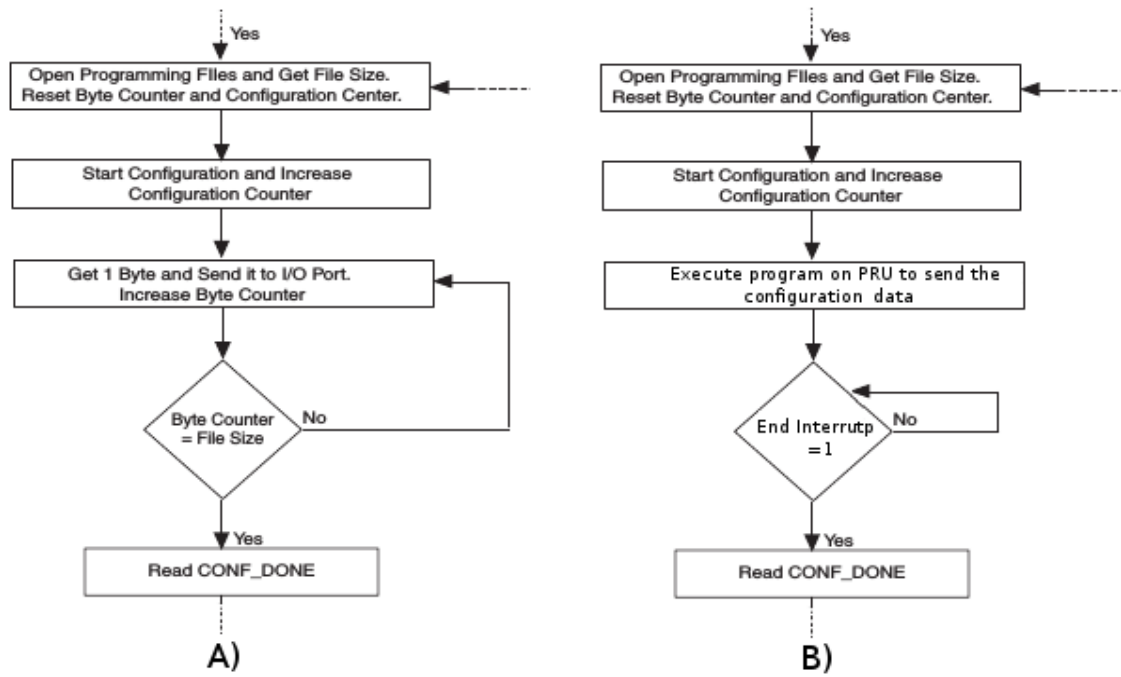


Figure B.4: Modification to the program flow of Jrunner to use the PRU core for the bit banded communication. A) Image is the original program flow, and B) shows the modification made to use the PRU core. Modified from [12].

The program on the PRU implements the bit banded communication. The program reads a 32-bit register from the Shared memory, using a mask obtains the value of the first bit, sets that value into the set or clear control registers for the pin that is connected to the T_{DI} line of the FPGA. After the value is set, the program toggles the clock line TCK, using the control registers of the pin. Then the mask is shifted, the next bit of the read memory register is obtained and the process starts again until all the bits have been sent. The program then asserts the end of program interrupt and exits.

The current LancelotRX is using the Jrunner with the bit banded communication implemented on the ARM processor. Future implementations can make use of the PRU cores using the proposed implementation. Future designs should interconnect PRU specific pins with the FPGA configuration lines.

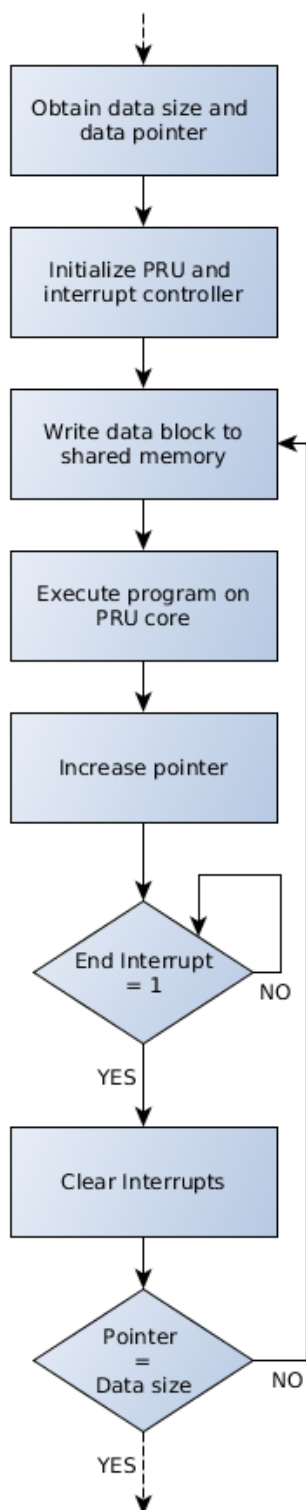


Figure B.5: Program flow of the C program that calls the PRU to write the configuration data in bursts.

Appendix C

MATLAB functions

Command name	Command Description
<i>connect_merlin(host, cmd, data)</i>	Start a connection to the LancelotRX system
<i>dac_read(merlin)</i>	Returns the voltage of the selected DAC by <i>dac_readselect</i> using the ADC from the interface board
<i>dac_readselect(dac_number, merlin)</i>	Sets the acquisition time, returns 0 on success
<i>DAC_Scan(strt, stp, stp, merlin, n)</i>	Run a DAC scan from DAC start to DAC stop in increments of DAC step
<i>data_grabber(merlin)</i>	Connect and grab whatever data is being sent over the data port, 5 second
<i>decode_frame_header(header)</i>	Decode the frame header from the obtained data
<i>decode_response(command, response)</i>	Decode the obtained response from the system
<i>get_acq_time(merlin)</i>	Returns the current acquisition time as a double
<i>get_ChargeSumming(merlin)</i>	Gets the Charge Summing mode set or not
<i>get_ColourMode(merlin)</i>	Gets the Colour mode set or not
<i>get_Counter(merlin)</i>	Gets the counter set to be read ,0 for Low and 1 for High
<i>get_DACs(merlin)</i>	This function returns the currently set value of the DACs as an array
<i>get_DISC_CSM_SPM(merlin)</i>	Gets the <i>disc_csm_spm</i> bit on the OMR to choose which discriminator to read on COUNTERL when Equalization bit is set

Table C.1: List of the individual scripts developed under the MATLAB environment as part of the client. The first column shows the name of the script as well as the arguments taken, the second column shows a brief description of the script. The argument named 'merlin' represents the TCP/IP communication object.

Command name	Command Description
<i>get_num_frames_to_acq()</i>	Returns the current number of frames to acquire as a double
<i>get_Peltier(merlin)</i>	Gets the Peltier pwm value
<i>get_PeltierFANtmp(merlin)</i>	Gets the starting temperature for the Medipix3RX fan
<i>get_PeltierPID(merlin)</i>	Gets the Peltier PID values
<i>get_PeltierPIDOn(merlin)</i>	Gets the Peltier PID control on or off
<i>get_PeltierPIDtmpStep(merlin)</i>	Gets the maximum temperature error pass to the PID controller
<i>get_PeltierPIDwup(merlin)</i>	Gets the Peltier PID windup limit
<i>get_PeltierTempMax(merlin)</i>	Gets the maximum temperature on the Peltier hot side before stopping the Peltier
<i>get_pixel_config_load_filename()</i>	Returns the most recent filename and path used to load the pixel config
<i>get_pixel_config_load_filepath()</i>	Returns the most recent filename and path used to load the pixel config
<i>get_pixel_config_save_file()</i>	Returns the filepath where the pixel config was last saved
<i>get_pixel_config_save_filepath()</i>	returns the filepath where the pixel config was last saved
<i>get_TestPulse(merlin)</i>	Gets the Test Pulse control on or off
<i>get_TestPulseNumber(merlin)</i>	Returns the current number of Test Pulses as a double
<i>get_THScan(merlin)</i>	Gets the number of Threshold that will be scanned trough using DACSCAN
<i>get_tmp(merlin)</i>	This function returns the currently get the value of the temperatures on Lancelot-Rx
<i>load_bpc(filename, merlin)</i>	Takes a bpc file on the local pc and streams it to the Merlin host
<i>load_mask(mask_matrix, merlin)</i>	Send a 256,256 matrix of 1 or 0 to the mask bits of the merlin host
<i>load_test(test_matrix, merlin)</i>	Send a 256,256 matrix of 1 or 0 to the test bit of the merlin host
<i>merlin_command(command, merlin)</i>	Sends the desired command to the Merlin host, returns 0 or value on
<i>load_trims(trim0, trim1, merlin)</i>	Loads two 256 square matrices of Medipix3RX trim values to trim0 and trim1s

Table C.2: List of the individual scripts developed under the MATLAB environment as part of the client. The first column shows the name of the script as well as the arguments taken, the second column shows a brief description of the script. The argument named 'merlin' represents the TCP/IP communication object.

Command name	Command Description
<i>obtain_trim_fromBPC(bpcmat, trim)</i>	Read the bpc matrix and return the values of either TrimL or TrimH
<i>read_bpc(filename, uint16_native)</i>	Read a bpc file and output raw data as an array
<i>read_response(merlin)</i>	Read the raw response from the sensor to the last sent command
<i>save_bpc(fn, trimL, trimH, msk, tbit)</i>	Save a bpc file using an incoming matrix of 256*256
<i>set_acq_period(acq_time, merlin)</i>	Sets the acquisition time, returns 0 on success
<i>set_acq_time(acq_time, merlin)</i>	Sets the acquisition time, returns 0 on success
<i>set_ChargeSumming(on, merlin)</i>	Sets the Charge Summing mode on or off
<i>set_ColourMode(on, merlin)</i>	Sets the Colour mode on or off
<i>set_Counter(on, merlin)</i>	Sets the counter set to be read ,0 for Low and 1 for High
<i>set_CounterDepth(counter, merlin)</i>	Sets the Counter Depth for the images to be read on the Medipix3RX
<i>set_DAC(dac_name, value, merlin)</i>	Set the value of a specific DAC
<i>set_DACs(DACs, merlin)</i>	Set the DACs as an array of 27 values for the Medipix3RX
<i>set_DISC_CSM_SPM(on, merlin)</i>	Sets the <i>disc_csm_spm</i> bit on the OMR to choose which discriminator to read on COUNTERL when Equalization bit is set
<i>set_Equalization(on, merlin)</i>	Sets either enable or disabled the equalization bit
<i>set_gain(gain, merlin)</i>	Sets the acquisition time, returns 0 on success
<i>set_HVon(on, merlin)</i>	Sets either enable or disabled the HV
<i>set_HVvalue(voltage, merlin)</i>	Sets the acquisition time, returns 0 on success
<i>set_num_frames_to_acq(n, merlin)</i>	Set the number of frames to be acquired in next acquisition
<i>set_PELTENABLE(on, merlin)</i>	Sets either enable or disabled the Peltier
<i>set_PeltierFANtmp(temp, merlin)</i>	Sets the starting temperature for the Medipix3RX fan
<i>set_PeltierPID(kp, ki, kd, merlin)</i>	Sets the parameters for the PID temperature control
<i>set_PeltierPIDOn(on, merlin)</i>	Sets the PID control on or off
<i>set_PeltierPIDtmpStep(step, merlin)</i>	Sets the maximum temperature error passed to the PID controller
<i>set_PeltierPIDwup(wup, merlin)</i>	Sets the PID cmax windup

Table C.3: List of the individual scripts developed under the MATLAB environment as part of the client. The first column shows the name of the script as well as the arguments taken, the second column shows a brief description of the script. The argument named 'merlin' represents the TCP/IP communication object.

Command name	Command Description
<i>set_PeltierTempMax(temp, merlin)</i>	Sets the maximum temperature on the Peltier hot side before stopping the Peltier
<i>set_PeltierTempTarget(temp, merlin)</i>	Sets the acquisition time, returns 0 on success
<i>set_pixel_config_load_filepath(path)</i>	Set the filename and path of the pixel config file to load and apply it to
<i>set_pixel_config_save_filepath(path)</i>	Save the current pixel config to the specified path
<i>set_scan_dac(merlin, dac_scan)</i>	Set which of the 8 DACs will be scanned
<i>set_TestPulse(on, merlin)</i>	Sets either enable or disabled the Test Pulse
<i>set_TestPulseNumber(n, merlin)</i>	Sets the amount of test pulses to be used on the acquisition
<i>set_THScan(threshold, merlin)</i>	Sets the number of Threshold that will be scanned trough using DACSCAN. The values are 0 to 7
<i>startacquisition(merlin)</i>	Send the start acquisition command
<i>stopacquisition(merlin)</i>	Stop the acquisition process

Table C.4: List of the individual scripts developed under the MATLAB environment as part of the client. The first column shows the name of the script as well as the arguments taken, the second column shows a brief description of the script. The argument named 'merlin' represents the TCP/IP communication object.

Appendix D

Medipix3RX equalization and energy calibration

D.1 Island phenomenon

For the CSM, errors in equalization of the lower threshold can generate a wrong assignment of the arriving photon to the pixel that has the highest energy. The wrong assignment of the pixel error can become a big problem if the SPM equalization is not precise.

If one pixel has a lower threshold than all its neighbours for the low discriminator, and this difference is big enough, then when the photon arrives and the charge is shared between different pixels, the low discriminator of this pixel will generate a longer duration output pulse than the others. This behaviour will cause the assignment logic to count this photon for that pixel. These assignment errors can be seen in the sensor output as one pixel with very high counts surrounded by pixels with low counts, generating an ‘island phenomenon’. As shown in Figure D.1, the central pixel has a higher value than the surrounding pixels.

Masking a pixel with a threshold offset big enough in comparison to its neighbouring pixels to generate the ‘island phenomenon’ presents a difficult scenario to realize automatically. The threshold offset is found on the low discriminator, which was equalized in SPM, and in this mode this phenomenon does not exist, making it hard to detect. At the same time, if the low discriminator in SPM was equalized using electronic noise as a source, it is possible that this behaviour was not present with the

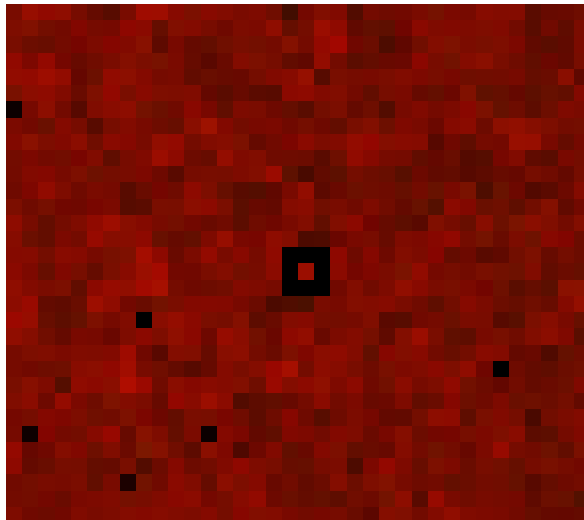


Figure D.1: Island phenomenon generated by the CSM if the thresholds of the low discriminator are not correctly equalized. The sporadic black pixels are either non responsive pixels or masked ones.

electronic noise, but appears as the detected energy goes higher and the gain mismatch between pixels increases the threshold offset. Even if the low discriminator was equalized with another method that would allow compensation for the gain mismatch, for correct reconstruction on CSM, the lower discriminator has to be set to one quarter of the energy that is being detected. This would force the equalization to be done for this low energy, complicating the compensation for the gain mismatch. The only reliable method to detect the ‘island phenomenon’ and mask the central pixel is to flood the sensor with x-rays at the desired energy for experiments, look for this pattern, and find pixels to mask.

D.2 Pixel parameters based equalization method

Each equalization method is completed for a specific energy. If using electronic noise as a source, then the energy is the zero level, if using injected pulses, it depends on the amplitude of the pulses, and if using x-rays, it depends on the energy of the x-rays. For the sources of x-rays and pulses, it is possible to vary the amplitude of the pulses or the energy of the x-rays to generate equalization matrices for different energies, but this is an intensive, time-consuming process.

This is a problem for the end-user, using a detector that requires constant equalization every time the energy of the experiment is changed. This is not optimal, especially

in experiment facilities like a Synchrotron where the beam time is highly valuable.

A possible solution to save equalization time for the user of the system, is to have stored several equalization matrices, but this requires too much space in memory. These two problems, processing time and data storage, become worse as a system using several Medipix3RX sensors is contemplated. To reduce these problems and aiming for a compromised approach between time and stored data, an equalization procedure named ‘Parameters Equalization’ is proposed.

D.2.1 Objective of the parameters equalization

The principle of the parameters method is to obtain parameters from each pixel that would be able to describe an approximation of how the pixel behaves, what the threshold deviation is and how it is affected by the added threshold offset. These parameters’ information is stored and can be used to generate an equalization matrix for a specific energy. Because the saved information are generalized parameters of each pixel, the total amount of storage required is less than if all the possible equalization matrices were saved. An equalization matrix can be processed from the parameters without the need to obtain new images from the sensor, this increments the speed at which a new equalization matrix can be generated. The generation of the equalization from parameters could be implemented on the FPGA to further increase the processing speed.

D.2.2 The parameters model equalization method

This method uses injected pulses as a source of counts for the equalization. Figure D.2 shows a sequence of ‘S’ profiles for a given pixel to different values of amplitude of pulses. By changing the value of the amplitude of the pulses, the value of the threshold DAC where the second fall of the ‘S’ profile happens is shifted. From each profile a th^* is computed and these values are stored as parameters of the pixel.

Figure D.3 shows a plot of the obtained values of th^* per pulse amplitude. The values have been fitted to a straight line, showing how linear the behaviour of the th^* is to the pulse amplitude. This line can be moved in the threshold spectrum by a adding threshold offset, using the LDAC_DISC and the trim bits. Two more lines,

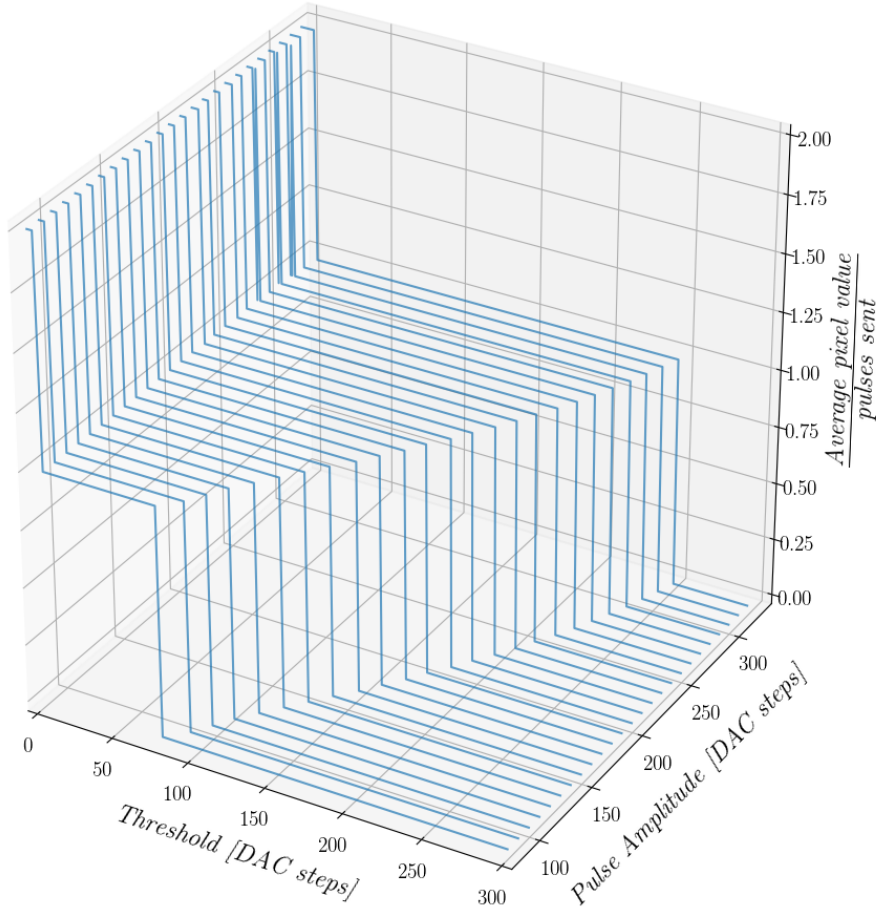


Figure D.2: Profiles of one pixel for a scan of the threshold DAC on a non-equalized sensor, using pulses to generate counts. The profiles are repeated for different amplitude values of the pulses.

with a positive and negative threshold offset are displayed for comparison as well.

Using the fitted linear function to the th^* values for pulse amplitude without an added threshold offset, values of the gain and original threshold offset can be computed. Using the fitted lines when a positive or negative threshold offset has been added, the relation of threshold DAC value changes to trim bits and LDAC_DISC can be obtained. Assuming that the behaviour of LDAC_DISC and the trim bits is linear, a factor named *trim_factor* per pixel is obtained with the following equation:

$$trim_factor_i = \frac{added_offset_i}{LDAC_DISC * added_trim_i} \quad (D.1)$$

Where: the $added_offset_i$ has been calculated using the linearly fitted th^* lines

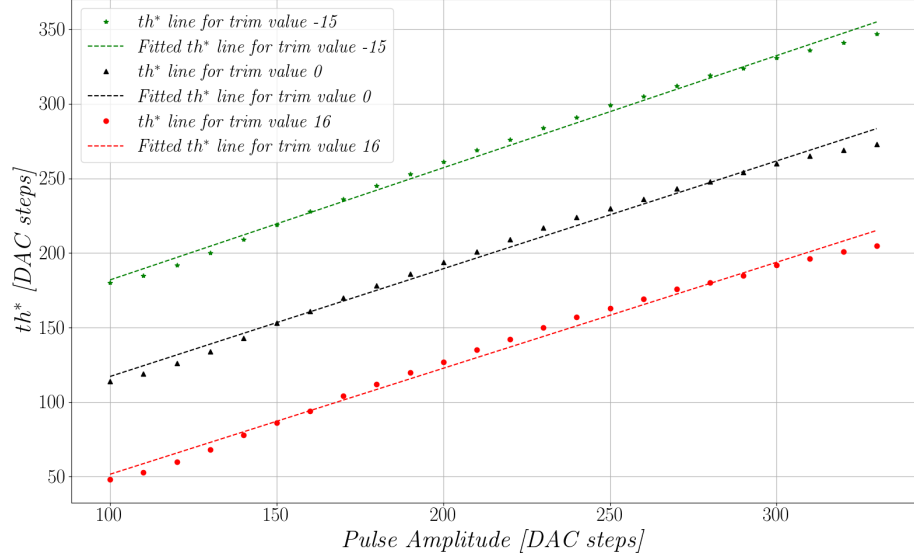


Figure D.3: th^* values per pulse amplitude for a specific pixel. The response is shown without an added threshold offset, with a positive offset and with a negative offset. The values of th^* lines have been fitted to obtain its parameters.

to pulse amplitude. The $added_trim_i$ value is the difference of the relative trim values used between the two th^* lines acquisitions. The $trim_factor_i$, the $gain^*$ and the th^*_offset are obtained from all the pixels of the matrix and the dispersion on gain and on the original threshold offset can be measured. Figure D.4 shows the line of th^* to pulse amplitude for 9 different pixels without an added threshold offset.

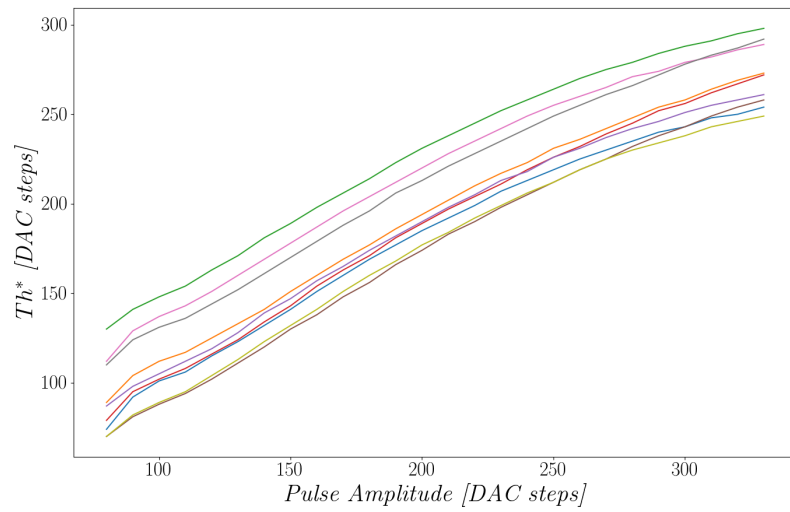


Figure D.4: th^* to pulse amplitude line for 9 neighbouring pixels. No correction has been added and it is possible to see the gain mismatch and original threshold dispersion.

From the parameters of all the pixels, the average threshold offset without correction is computed, this offset will be called threshold offset target, and will be used as the value to which all the pixels will be equalized. Following the same method, the average gain is computed and will be denoted as $gain_{target}$. To generate an equalization matrix, the first step is to create an error distance matrix, where the distance from the th^* to the target th for the given pulse energy for pixel i can be obtained as:

$$error_distance_i = gain_{target} * (PA) + th_{offset_target} - gain_i^* * (PA) + th_{offset_i}^* \quad (D.2)$$

Where: PA is the pulse amplitude, $gain^*$ is the computed effective gain for each pixel and th^*_{offset} is the computed effective threshold offset for each pixel.

Using the $error_distance$ matrix and the previously obtained $trim_factor$ the maximum added threshold is computed. The value of I_DAC_DISC to use is the absolute value of the maximum error distance divided by 16, which is the maximum possible trim. With the I_DAC_DISC calculated, the trim values for each pixel can be obtained with

$$Relative_trim_i = (gain_{target} - gain_i^*) * PA + \frac{th_{offset_target} - th_{offset_i}^*}{I_DAC_DISC * trim_factor_i} \quad (D.3)$$

In Figure D.5, the plot of the equalized response of the same 9 pixels as shown in Figure D.4 for two different pulse amplitudes is shown. The selected pulse amplitudes are the limits of the spectrum to show clearly how the equalization is done for a specific energy or pulse amplitude. This shows that equalization can be generated by the parameters method.

D.2.3 Results with the parameters model equalization method

The method presented is capable of generating an equalization, based on previously collected parameter information from the pixels, for different energies without the need of taking new images from the sensor. This speeds up the equalization process for the user allowing changes of energies in the experimental set up.

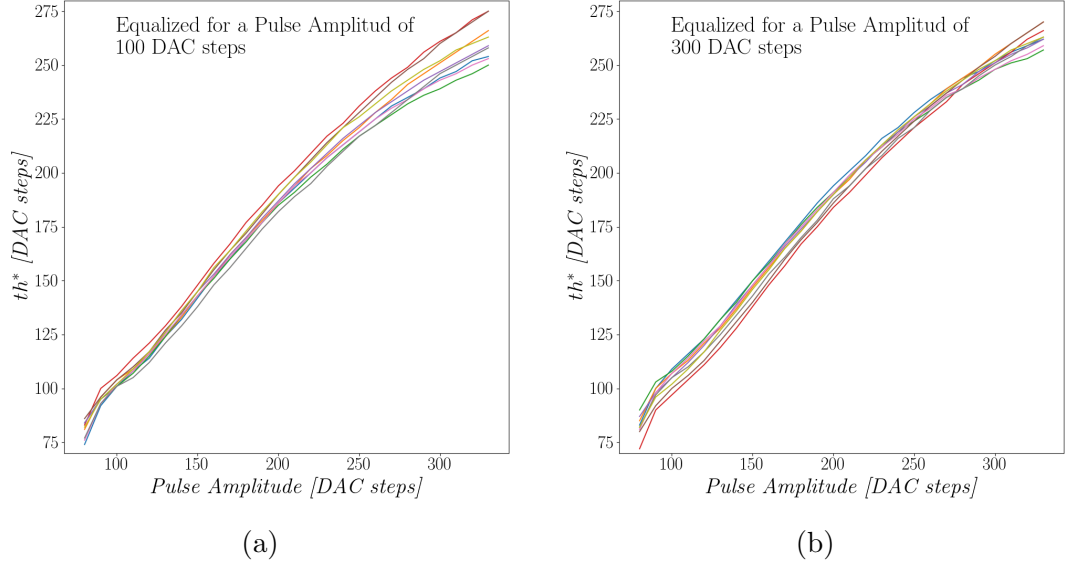


Figure D.5: th^* to pulse amplitude lines for 9 neighbouring pixels after equalization. The equalization has been done for a pulse amplitude of 100 and 300, respectively.

In order to minimize the amount of stored information and to speed up processing, a number of simplifications have been made, particularly considering linear behaviours from the sensor. The actual behaviours differ from being perfectly linear, and this introduces errors in the equalization process. Therefore, the final equalization matrix does not give results as good as the ones that can be achieved through methods that are more data and time consuming.

Because the equalization method with parameters could be embedded into the FPGA processing, the system could equalize the sensor without requirement of knowledge for the user, the only information needed is the energy of the x-rays.

The method is based on injected pulses as a source of counts for the equalization, which means that it is subject to errors generated by the dispersion of the values of the test injection capacitors on the Medipix3RX. When the method was tested against x-rays, it was not possible to reconstruct the energy peak. The method showed good results when tested with injected pulses, it is only when tested with x-rays that the method did not worked.

The parameters values could be obtained using x-rays instead of injected pulses, but this is a long process and requires access to an x-ray source with a high flux and the possibility to change the x-ray energy.

	SPM		CSM	
Gain Mode	Gain[DAC.u./keV]	Offset[DAC. u.]	Gain[DAC.u./keV]	Offset[DAC. u.]
SLGM	3.05	5.02	1.31	12.39
LGM	4.09	1.99	1.85	10.52
HGM	5.45	4.95	2.72	8.94
SHGM	9.00	9.52	-	-

Table D.1: Energy calibration results. The gain and offsets were obtained by a linear fitting with measurements from energies of 6.4, 8, 9.7, 15.7 and 17.4 keV.

D.3 Energy calibration

The energy calibration is an experimental method to obtain the relation between the energy of the x-ray photons and the value of the threshold DAC. A linear relationship is expected due to the amplifiers of the Medipix3RX, which have a linear gain. To find the relationship, a scan of the threshold DAC is executed at different x-ray energies. For each energy, the energy peak is found by fitting the response to a Gaussian function. The obtained energy peaks in DAC values and the tested x-ray energies are used as points to fit a linear equalization. The result of the linear fitting is a gain and an offset.

In the LancelotRX, the energy calibration was done using five different energies. The energies were obtained from x-ray fluorescence, using the elements: iron ($K_\alpha=6.4$), copper ($K_\alpha=8.04$), gold ($L_\alpha=9.71$), zirconium ($K_\alpha=15.77$) and molybdenum ($K_\alpha=17.48$). The obtained gains and offsets for SPM and CSM are shown in Table D.1.

Appendix E

LancelotRX design for vacuum

Due to requirements of beamline I24 in Diamond Light Source, a parallel design of LancelotRX was made for a in-vacuum XBPM application. Beamline I24 has a micro-focused beam for Macromolecular Crystallography. The experiments are conducted in vacuum, and the XBPM was required to work inside the vacuum chamber used for experiments. For this purpose, a ‘vacuum’ design of LancelotRX was made, using a tube to set the scattering foil into the beam’s path. The vacuum design is explained in this Appendix.

E.1 Mechanical design

The mechanical parts for the vacuum design are shown in Figure E.1. The mechanical parts for the vacuum design are divided in two sections, the sensor section, which is inside the vacuum, and the electronics section which is in air. The division between the two sections is connected using a vacuum tight D-sub feed through.

A tube has been used to set the scattering foil at the height where the x-ray beam will pass. The scattering foil is placed on a foil holder which also carries the aperture holder that clamps the sheet with the pinhole. The foil and the holders are placed at one end of the tube as shown in Figure E.1. The tube has three vertical countersunk slits at 120 degree angles, which are used to set the height of the Medipix3RX sensor. The sensor will be placed on a copper puck that is fixed to a specific position by screws passing through the slits on the tube. This design allows to move the puck and sensor along the tube and set a fix position, the position used will affect the magnification

of the beam image. The other end of the tube is clamped to a base mount which is screwed to the plate used for the vacuum tight seal.

The electronics are encased by an aluminium box. Rails are used on the sides of the box to hold into position the PCBs, which are then clamped by the lateral faces of the box. The lateral faces of the box have the free spaces for the connections to the D-sub feed through on one side, and the connections for power and communication on the other. The top of the box is a sliding plate that is held into position by the lateral faces.

E.1.1 Heat dissipation

To ensure that the temperature in the electronics box stays within the working limits of the electronics, a fan is used to cool down the PCBs. The sliding top panel is designed with slits to allow air flow. Two sections of air vents are used, a circular section where the fan is positioned and a second section where the air can enter the electronics box. This generates an airflow along the electronics box.

To dissipate the heat generated by the Medipix3RX sensor a cylindrical piece of copper has been used. The copper puck, shown in Figure E.2 is used to keep in position a Peltier thermoelectric cooler, also used as a base for the PCB where the Medipix3RX sensor is wire-bonded and used to dissipate the heat generated. The puck is embedded inside the anodize aluminium tube, which will also help to dissipate the heat.

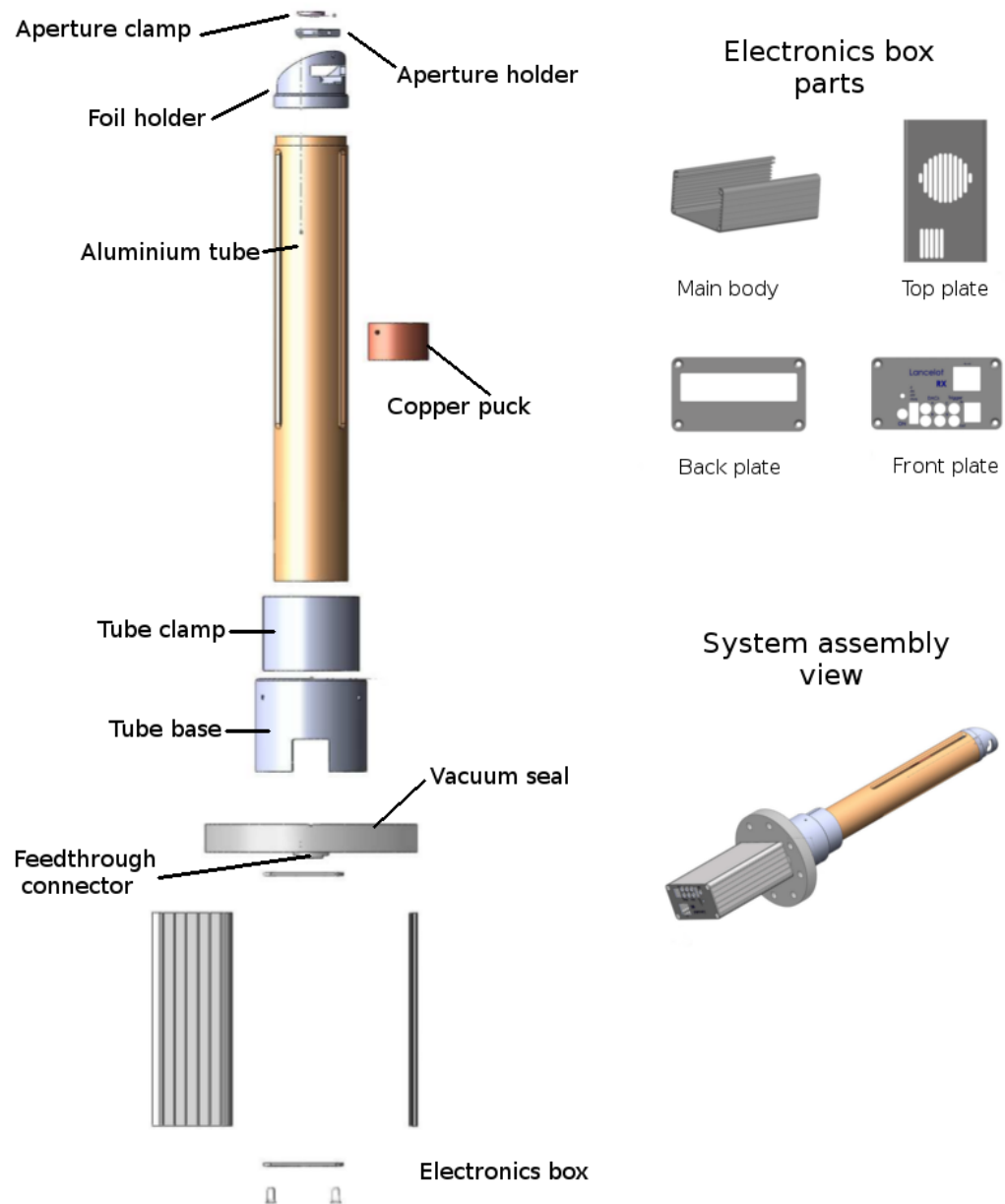


Figure E.1: Housings and mechanical design of the vacuum system for the XBPM vacuum application.

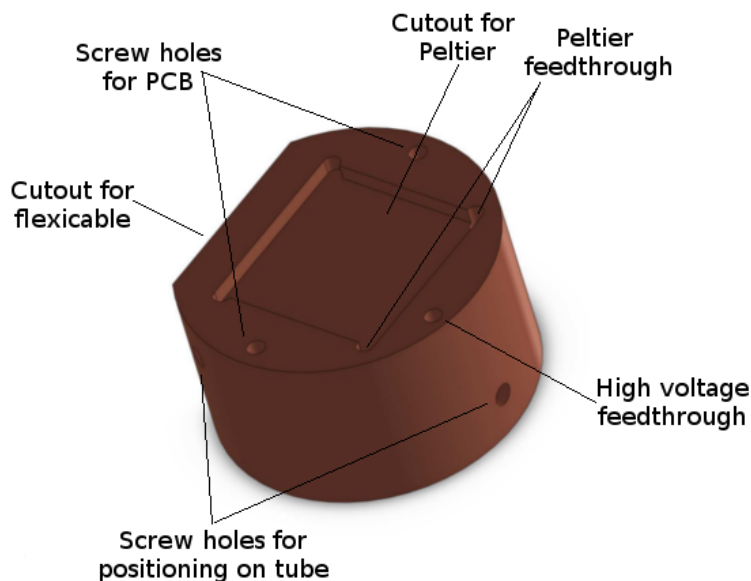


Figure E.2: Cylindrical copper piece used to hold the sensor electronics into position and to aid the heat dissipation. The copper puck is hold into position by 3 screws.

E.2 Electronics

The electronics of the vacuum design are the same as the LancelotRX, with the exception of the Sensor board. For the vacuum design, the Sensor board was designed using both flexible segments and rigid segments. The area where the Medipix3RX sensor is placed is a rigid PCB, but the signals expand out of this PCB on a flexible part, as showed in Figure E.3. Using a flexible PCB segment provides a smaller footprint on the Sensor board than using a connector.

As showed in Figure E.3, on one end of the flexible part the sensor PCB is placed, and on the other end there is a rigid part to solder the D-SUB connector. It was required to use a rigid part to solder the true hole D-SUB connector to ensure that movement would not break the solder points. The sensor assembly on the vacuum design can be moved up and down the Z axis, concentric to the tube, to change the magnification ratio of the pin hole camera. The flexible board will bend to fit in the available space, this is shown in Figure E.4. The flexible part has a 230 mm length.

To implement the temperature control, a similar design to the LancelotRX is used.

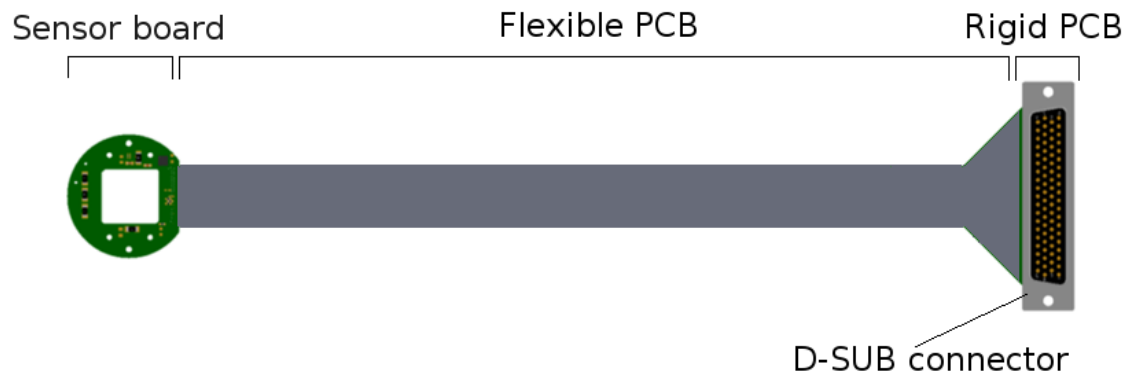


Figure E.3: Flexible board designed to interconnect the Interface and Sensor boards on the vacuum design. The flex part of the board is attached to the FR4 rigid material parts of the PCB.

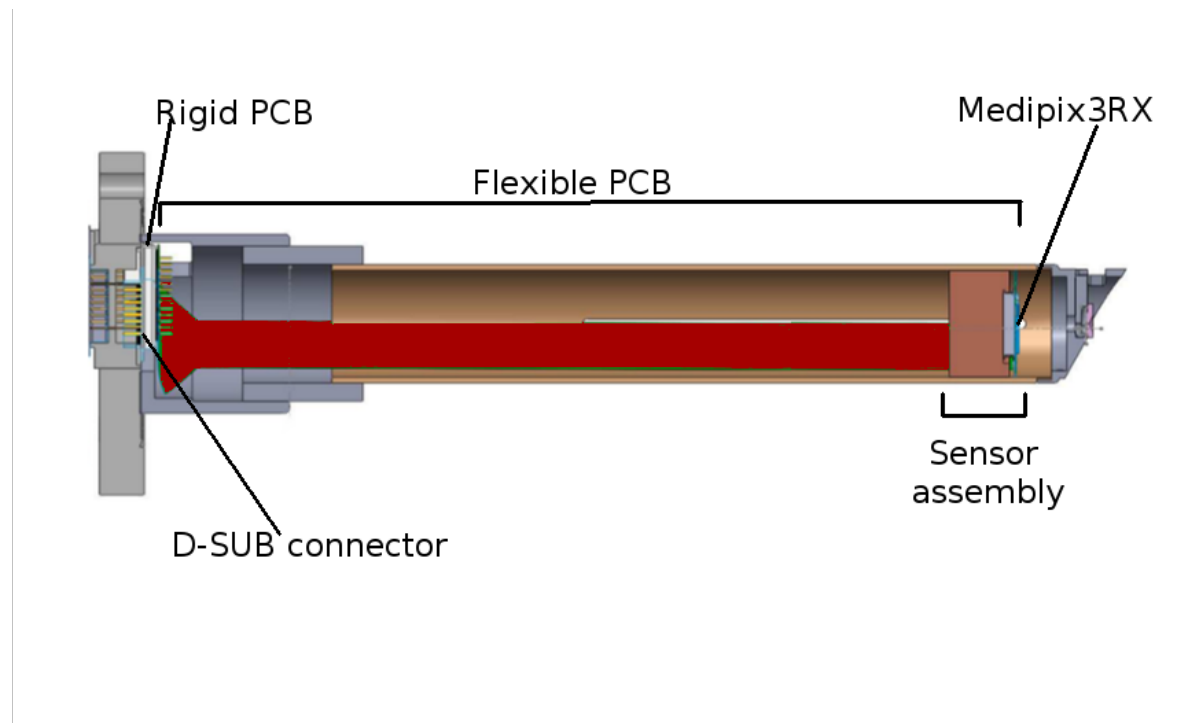


Figure E.4: Placement of the flexible board used to interconnect the Interface and Sensor boards on the vacuum LancelotRX system. The flexible segment of the PCB has been coloured in red to help visualization.

In Figure E.5 the sensor stack is shown. The Medipix3RX is glued to a copper block, which is in contact with the Peltier. The Peltier pumps heat from the copper block to the copper puck. A temperature sensor placed on the back of the Sensor PCB, touching the copper block, is used to determine the temperature of the Medipix3RX. The heat pumped into the copper puck is dissipated into the aluminium tube.

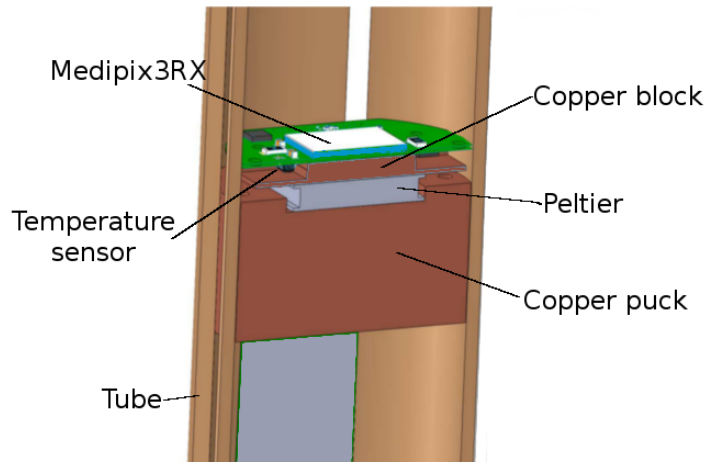


Figure E.5: Cross section of the relevant parts for the temperature control in the vacuum design. The heat generated by the Peltier is dissipated into the copper puck.

E.3 System assembly

A full assembly of the parts of the vacuum design is presented on Figure E.6. The system was fully tested, obtaining similar results to the ones obtained with the LancelotRX.

1	Pinhole clamp
2	Pinhole holder
3	Foil holder
4	Tube
5	Peltier
6	Copper puck
7	Sensor board
8	Tube clamp
9	Tube base
10	Feedthrough
11	Back plate
12	Top plate
13	Box body
14	Fan
15	Interface board
16	Processor board
17	Front plate

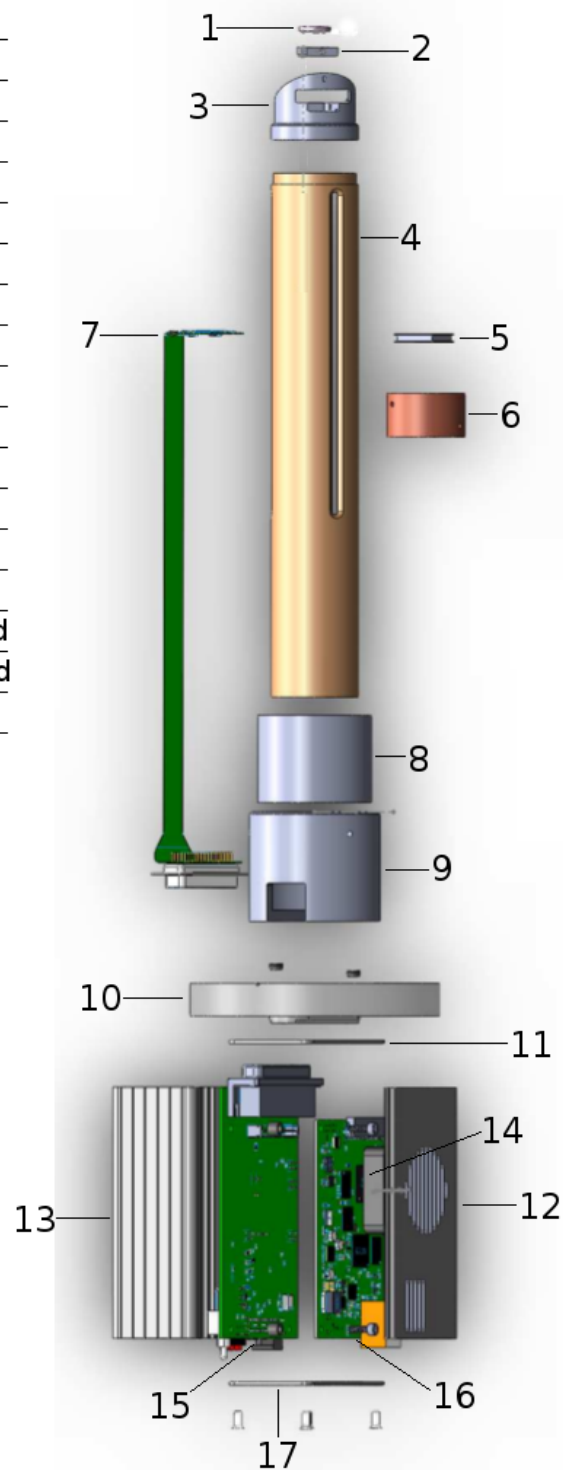


Figure E.6: Full system explode for the components of the vacuum LancelotRX system.